DOCTORAL THESIS

Modelling of plasma-antenna coupling and non-linear radio frequency wave-plasma-wall interactions in the magnetized plasma device under ion cyclotron range of frequencies

by:

LingFeng Lu

Board of examiners for public PhD defence on December 2nd, 2016

Prof. Michel Vergnat	Chair-ULorraine
Prof. Rik Van de Walle	Co-chair-UGent
Prof. Nong Xiang	Referee-ASIPP
Prof. Daniel De Zutter	Referee- UGent
Dr. Annika Ekedahl	Referee-HDR Aix-Marseille U
Dr. Dirk Van Eester	Examiner-ERM/KMS
Dr. Philippe Jacquet	Examiner-CCFE
Dr. Laurent Colas	Supervisor-HDR ULorraine
Prof. Jean-Marie Noterdaeme	Supervisor-UGent/MPI
Prof. Kristel Crombé	Thesis promotor-UGent/ERM
Prof. Stéphane Heuraux	Thesis promotor-ULorraine

Acknowledgement

Thanks to the support from Erasmus Fusion-DC program, I had the opportunity to conduct a thesis in France and Belgium under the guidance of an international committee. I am greatly thankful to my four supervisors, Dr. Laurent Colas (IRFM, CEA), Prof. Kristel Crombé (LPP, ERM/KMS), Prof. Stéphane Heuraux (IJL, Université de Lorraine) and Prof. Jean-Marie Noterdaeme (IPP Garching). Your profound knowledge and conscientious attitude towards scientific work always encourage me and set an example for my future research career.

I spent 2 over the total 3 years in IRFM, which locates in the picturesque countryside of Provence. I would like to thanks all the members of the GCHF group which I affiliated for their company. Special thanks to Walid Helou and Julien Hillairet for the useful technical discussions on RF engineering. I learned a lot from them. Also thanks Annika Ekedahl to be one of my reporters of the thesis defence. Thanks Robert Volpe for the interesting and funny discussions on Asterix and let me know many Italian/French cultures. Besides, I would like to thanks Nathalie Borio, Karine Ruiz for many practical helps. The SSWICH-FW I developed in this thesis is a successor of the previous work did by Jonathan Jacquot. During this thesis, I got many useful suggestions concerning the code development. Also he provided me the field map from his 3D RAPLICASOL code. Many thanks for these helps.

The 6 month's stay in LPP is my busiest time during this 3 years. The lab is compact but really have many talented people. We are lucky to have our Wikipedia André Messiaen with us, who have almost simulated everything. Thanks Fabrice Louche for many beneficial discussions on RF simulations and also Riccardo Ragona who shares the COMSOL workstation with me. I need acknowledge Benedicte schifflers for many practical helps. Finally, many thanks to my co-director in this lab: Dr. Dirk Van Eester, who always have many ideas and show great passion and optimism during the work as well as in the afterwork chat. One of the most fascinating things during my thesis is that I had the honor to work with so many elites that I knew before from reading scientific articles. Dirk is definitely one of them. I also owe my gratitude to Fusion DC administrative staffs, Kathleen Van Oost, Frank Janssens and UGent policy officer Muriel Vervaeke from the Dean's office of faculty of engineering an architecture who helped me solve many practical things concerning cotutelle agreement and the preparations of two doctoral defences.

The 3 month's stay in IJL is short compared to the duration I spent in other labs. I am grateful to Eric Faudot who guided my simulation work on Aline. Our daily discussion let me learn a lot of things beyond Tokamaks. Also thanks Stéphane Devaux who kindly provided me the experimental data.

I would like to thank Prof. Rik Van de Walle (UGent), Prof. Daniel De Zutter (UGent), Dr. Philippe Jacquet (CCFE), Prof. NongXiang (ASIPP) and Prof. Michel Vergnat (ULorraine) who agreed to become my thesis juries. I am also grateful to Tycho Van Noorden from COMSOL support team who gave me a lot of useful tips on numerical implementation.

Finally, I would address my appreciation to the friends who accompanied me in the past 3 years. Thanks Laurent Valade taught me many useful French. I know from many people that as long as I can understand this Parisien, I can understand everyone. The trips we had together in UK and US won't be forgotten all my life. Thanks Hugo Arnichand who is always so hospitable and open mind. The trips to visit Montpellier, Arles and the mountains near your holiday house are my best memories about France. Also thanks Nicolas and Alexandre Fil who watched football and went hiking with me several times. Thanks Charles Ehrlacher

Acknowledgement

telling me many interesting stories during his military service and the history of France. I am also pleased to recognize Jane Ho in Ghent. The food cooked by your father is the best food I ever ate in Belgium. I hope next time when you come to China, I could able to speak Cantonese with you.

Acronyms

AUG: Axially Symmetric Divertor Experiment (ASDEX) Upgrade

DC: Direct current

FS: Faraday screen

ICRF: Ion cyclotron range of frequencies

ICRH: Ion cyclotron resonant heating

IshTAR: Ion cyclotron sheath test arrangement

ITER: International thermonuclear experimental reactor

JET: Joint European Tokamak

LCFS: Last closed flux surface

PEC: Perfect electric conductor

PFC: Plasma facing component

PMC: Perfect magnetic conductor

PML: Perfectly matched layer

RAPLICASOL: Radiofrequency wave coupling for ion cyclotron antenna in scrape off layer

RF: Radio-frequency

SBC: Sheath boundary condition

SOL: Scrape-off layer

SSWICH-FW: Self-consistent sheath and waves for ion cyclotron heating-full wave

SSWICH-SW: Self-consistent sheath and waves for ion cyclotron heating-slow wave

TE: Transverse electric

TM: Transverse magnetic

TOPICA: Torino polytechnic ion cyclotron antenna

TS: Tore Supra Tokamak

WEST: W environment Steady-state Tokamak

Overzicht

Ion cyclotron resonante verhitting (Ion cyclotron resonant heating - ICRH) is één van de belangrijkste verhittingsmethodes in de huidige Tokamaks. De golven worden opgewekt door antennes aan de rand van de Tokamak met frequenties tussen 30 en 80 MHz. Om de plasma's voldoende te kunnen verhitten en de systemen voldoende betrouwbaar te maken voor langdurige steady-state operatie, is het van belang de antenne-plasma koppeling te begrijpen en de nefaste, ongewilde randeffecten van de nabije velden van de radio frequente (RF) golven tot een minimum te beperken.

Een ICRH antenne kan twee types van koude plasma golven uitzenden: de snelle golf (meestal de belangrijkste component) en de trage golf (parasitair). Het eerste deel van deze thesis bestudeert de invloed van een dichtheid die continu afneemt in de antenne en daarbij een resonante laag doorkruist (i.e. de lower hybrid (LH) resonantie), op de nabije RF velden en het koppelen van het vermogen naar het plasma. Hiertoe werd een 2D golf code ontwikkeld, RAPLICASOL, gebaseerd op het COMSOL Multiphysics pakket. Bij dichtheden onder de LH resonantie is het niet-triviaal gebleken om numerieke convergentie te bereiken. Tot de grenzen van het geheugen van de gebruikte computer, blijft het patroon van de velden veranderen met de grootte van het gebruikte rooster. Een fysische interpretatie is dat de trage golf zich kan voorplanten bij deze dichtheden en zeer korte golflengtes kan aannemen, en daardoor gevoelig is voor de parameters van de simulatie, zoals de grootte van het rooster. Echter, een interessante en belangrijke observatie is dat het totale spectrum dat gekoppeld wordt naar het plasma onafhankelijk is van de grootte van de cellen en slechts beperkt wordt beïnvloed door de aanwezigheid van een dichtheidsprofiel in de antenne box, vooral bij een dipool fase spectrum van de antenne. Golven met een dipool fase verschil worden meestal gebruikt voor de plasma verhitting. Voor de studie van de snelle golven en de koppeling is het daarom niet nodig om deze lage dichtheden in de antenne box in rekening te brengen. Bij antenne operatie met een monopole fasering tonen de simulaties dat er tot 20% meer vermogen in het plasma kan terecht komen als rekening wordt gehouden met de lage dichtheden. Het verschil is te verklaren door het feit dat de evanescentielengte van de snelle golf voor lage waarden van $k_{//}$ verandert. Dit heeft tot gevolg dat het modelleren van schema's met lage $k_{//}$ waarbij wordt aangenomen dat de antennes zich in vacuüm bevinden, moet worden herbekeken. De simulaties tonen verder aan dat veranderingen in de dichtheidsgradiënt in de evanescente zone van de snelle golf geen effect heeft op de koppeling van de golven. Het is dus nog steeds mogelijk om de vermogensoverdracht naar het plasma met goede nauwkeurigheid te modelleren ondanks onzekerheden in het dichtheidsprofiel.

Grenslaag ("sheath") effecten aan de antennes worden verantwoordelijk geacht voor het sputteren van onzuiverheden en een overdreven verhitting van antenne oppervlakken en andere componenten die in aanraking kunnen komen met plasma, zoals ook experimenteel wordt waargenomen. Om deze sheath effecten te modelleren in een realistische geometrie op schaal van een ICRH antenne werd al voor de start van deze thesis een code ontwikkeld, de SSWICH-slow wave code (Self-consistent Sheaths and Waves for ICH). Ze koppelt op een zelf-consistente wijze de propagatie van de trage golf en de DC SOL biasing via een niet-lineaire RF en DC sheath randvoorwaarde die wordt toegepast op de interfaces tussen het plasma en de wand. Een eerste versie van SSWICH had een 2D toroïdale en radiale geometry

en rechthoekige wanden die hetzij loodrecht, hetzij parallel waren met het magnetische veld $\mathbf{B_0}$. Het kon enkel een evanescente trage golf modelleren. De snelle golf propageert verder van de antenne dan de evanescente trage golf en kan de SOL wijzigen in regio's die niet bereikbaar zijn voor de trage golf. Daarnaast, als de wanden schuin staan t.o.v. of een scherpe overgang hebben, zoals het geval is in een echte Tokamak omgeving, kan de snelle golf koppelen naar de trage golf bij een reflectie en op die manier bijdragen tot het creëren van RF sheaths. In de eerste versie van SSWICH werd in zekere mate met deze effecten op een verre afstand van de antenne rekening gehouden door het invoeren van een DC stroomtransport.

Het centrale deel van deze thesis behandelt het ontwikkelen van een nieuwe SSWICH versie die ook de snelle golf modelleert, een meer realistische magnetische veld configuratie en gebogen wanden. De SSWICH-Full Wave code is nog steeds in 2D om de numerieke kost te beperken, het heeft een magnetisch veld dat een hoek maakt met het poloïdale en toroïdale vlak. Meer algemene randvoorwaarden voor de RF sheath werden afgeleid en verbeterde formules voor het gelijkrichten van de RF elektrische velden houden op eenvoudige wijze rekening met de helling van $\mathbf{B_0}$. Ze zijn geïmplementeerd langs de gebogen wanden van de SOL regio. De techniek van de perfecte aangepaste laag (Perfectly Matched Layer) werd gebruikt om de snelle golf te dempen. De RF golven kunnen worden geëxciteerd door ofwel een opgelegde stroom in de poloïdale richting ofwel een opgelegd externe veldkaart. SSWICH is op dit moment de enige code in de wereld die in staat is om RF sheaths te simuleren in een tokamak omgeving en daarbij gebruik maakt van een realistische veldkaart gecreëerd door de antenne.

De SSWICH-Full Wave simulaties van typische tokamak experimenten hebben de mode conversie aangetoond, waarbij de snelle golf wordt omgezet in een trage golf, aan scherpe hoeken waarbij de vormen van de wanden sterk variëren. Het heeft ook de sheaths van de verre velden weten te vinden, die voorkomen op de gebogen wanden die een relatief lange magnetische connectie hebben met de antenne. Deze oscillaties kunnen enkel worden opgewekt door een propagerende snelle golf. Door de toroïdale en radiale dimensies van de SOL regio aan te passen, kan men zien dat zowel $|V_{RF}|$ als $|V_{DC}|$ aan de gebogen verre SOL rand verminderd (of vermeerderd) onder een grotere toroïdale (of radiale) afstand van de actieve antenne. Dit gedrag komt overeen met de verwachte eigenschappen van de door de snelle golf veroorzaakte verre veld sheath. Simulaties tonen aan dat een vermindering van de loodrechte DC plasma geleiding in belangrijke mate de verbreding van de radiale V_{DC} kan beïnvloeden in de vrije SOL, zelfs in aanwezigheid van de snelle golf. Dit suggereert dat het DC stroomtransport nog steeds het dominante mechanisme is om de DC plasma verbreding te bepalen. SSWICH-FW/RAPLICASOL simulaties hebben ook een dubbele bult in de poloïdale structuur getoond, zoals experimenteel werd gemeten in de temperatuur en potentiaal kaarten. Simulaties komen beter overeen met de experimentele structuur als alleen met de trage golf wordt gerekend. De trage golf, met een korte evanescentie lengte, is gevoelig voor kleine wijzigingen van de geometrie in de private SOL. De buiging die werd geïntroduceerd in de private SOL is van belang voor de studie van het nabije veld, maar zeer waarschijnlijk is ze niet relevant voor de koppeling van de snelle golf. De snelle golf zelf is gevoelig voor 3D effecten. Niettemin, beide golven blijken een gelijkwaardige rol te spelen op de V_{DC} excitatie in de nabijheid van de antenne. Verder werd ook de hitte flux geëvalueerd langs twee tegenover elkaar opgestelde wanden met een sheath aan eenzelfde antenne. De simulatie onthulde de links-rechtse

asymmetrie die uitgebreid werd geobserveerd in experimenten waarbij een asymmetrie in de antenne strap werd geïntroduceerd. Dit suggereert dat de effecten van een ruimtelijke nabijheid op de excitatie van de sheath, zoals eerder voor de trage golf werd bestudeerd, nog steeds belangrijk zijn in de nabijheid van de antenne rekening houdend met een volledige golf polarisatie.

Hoewel oorspronkelijk ontwikkeld voor de RF sheath studies in Tokamaks, SSWICH-FW heeft bredere toepassingen. Er wordt aangetoond hoe het SSWICH principe kan worden geïmplementeerd in een totaal andere machine dan een Tokamak, wat betreft de geometrie en plasma koppeling regimes. Het Aline experiment is gewijd aan basisstudies van het gedrag van golven in plasma's en ook RF sheaths. Het derde deel van deze thesis gaat over het gebruik van SSWICH voor interpretatieve simulaties van de Aline opstelling. Met de SSWICH code werden zowel een Lower Hybrid golf als een Helicon golf bestudeerd, die beide voorkomen in Aline onder verschillende parameters. De structuur van de velden is echter afhankelijk van een slecht gekende botsingsfrequentie. Verder, aangezien het magnetisch veld in Aline volledig horizontaal is en het feit dat een "trage-golf-achtige" lower hybrid golf de belangrijkste component is die wordt opgewekt in de huidige configuratie, werd in eerste instantie de SSWICH-slow wave (SSWICH-SW) code gebruikt voor het modelleren van de RF sheath. Dankzij een eenvoudige toegang voor diagnostieken, kan in Aline een volledige experimentele floating potential kaart opgemeten worden, die kan worden vergeleken met de SSWICH modellen. De DC plasma potentiaal in de SSWICH-SW simulatie is vrij homogeen aan de antenne, terwijl de experimentele floating potential steeds een piek vertoont bovenaan de antenne. Dit verschil wordt verklaard door het versnellen van de ionen door het radiale elektrische veld aan het bovenoppervlak van de antenne, een eigenschap die niet aanwezig is in SSWICH.

Overzicht

Abstract

Ion cyclotron resonant heating (ICRH) is one of the main heating methods in the present-day Tokamaks. The wave is launched by antennas at the edge of the Tokamak device under the frequency range of 30-80MHz. To achieve a sufficient plasma heating and make the heating system reliable for steady-state operation, one must understand the antenna-plasma coupling and minimize spurious edge effects of RF near field.

An ICRH antenna can emit two types of cold plasma waves: the fast wave (mainly) and the slow wave (parasitically). The first part of this thesis studied the impact of densities that decay continuously inside the antenna and across the Lower hybrid resonance on RF near field and power coupling. A 2D full wave code: RAPLICASOL has been developed based on COMSOL Multiphysics to investigate this topic. It is shown that at densities below the LH resonance, reaching numerical convergence is nontrivial: up to the memory limits of the adopted workstation, the field pattern changes with the grid size. A physical interpretation relies on the fact that propagating slow wave can have very short wavelength and thus it is sensitive to simulation parameters, like mesh size. Interestingly and importantly, however, the total coupled spectrum is independent on the mesh size and is weakly affected by the presence of the density profile inside the antenna box in dipole phasing. Dipole phasing is often used as heating phasing. One can thus drop this low density inside antenna box for the fast wave coupling studies. In monopole phasing, simulation shows there is a maximum 20% of power increase due to the presence of plasma. The distinction comes from the fact that the fast wave evanescence length for low $k_{//}$ is changing. Hence modeling low $k_{//}$ scheme with antenna staying in vacuum may need to be re-considered. Simulation also shows that varying the density gradient in the fast wave evanescence region has no significant effect on wave coupling. One can thus still model the power coupling to plasma in a fairly good precision despite of some uncertainties existing in the density profile.

Sheath rectification is suspected to cause strong impurity sputtering and excessive heat loads on ICRH antenna surfaces and other plasma facing components that have been observed experimentally. In order to model the sheath rectification in a realistic geometry over the size of ICRH antennas, the Self-consistent Sheaths and Waves for ICH (SSWICH)-slow wave code has been developed based on COMSOL before this thesis. It couples self-consistently the slow wave propagation and the DC SOL biasing *via* non-linear RF and DC sheath boundary conditions (SBCs) applied at plasma/wall interfaces. A first version of SSWICH had 2D (toroidal and radial) geometry, rectangular walls either normal or parallel to the confinement magnetic field $\mathbf{B_0}$ and only included the evanescent slow wave. The fast wave propagates further from the antenna than the evanescent SW and could modify the SOL in regions inaccessible to the SW. Besides, when the walls are tilted to $\mathbf{B_0}$ or have a sharp transition as it is in the real Tokamak environment, the FW could couple to the SW upon reflection and thus contribute to the RF sheath excitation. In the first version of SSWICH, these RF-induced remote effects were partially accounted for by DC current transport.

The central part of this thesis is to develop a new SSWICH version which includes the fast wave, a more realistic magnetic field configuration and shaped walls. The SSWICH-Full Wave code, still in 2D to limit the numerical cost, has a magnetic field tilted in poloidal and toroidal plane. More general RF SBCs were derived using all RF field components and improved rectification formulas account for the tilted $\mathbf{B_0}$ in a simple way. They are implemented along the shaped walls of the SOL region. The Perfectly Matched Layer technique was used to damp the FW. The RF waves can be excited either by prescribed poloidal currents

Abstract

on built-in antenna straps or prescribed external field maps. SSWICH is at the present time the only code in the world able to simulate RF sheaths in tokamak environment using realistic antenna field maps.

SSWICH-Full Wave simulations of typical tokamak experiments have shown the mode conversion of FW into SW occurring at the sharp corners where the boundary shape varies rapidly. It has also evidenced "far-field" sheath oscillations appearing at the shaped walls with a relatively long magnetic connection length to the antenna. These oscillations can only be excited by the propagating FW. By tuning the toroidal and radial dimensions of the SOL region, one could see that both the $|V_{RF}|$ and $|V_{DC}|$ at the shaped far SOL boundary decreases (increases) under larger toroidal (radial) distance to active antenna. These behaviors agree with the expected properties of the fast wave induced far field sheath. Simulation shows that decreasing the perpendicular DC plasma conductivity can significantly affect the V_{DC} radial broadening in the free SOL even in the presence of the fast wave. This suggests that DC current transport is still the dominant mechanism to determine the DC plasma broadening. SSWICH-FW/RAPLICASOL simulations have also recovered the double-hump poloidal structure measured in the experimental temperature and potential maps. The simulation matches better with this experimental structure when only the slow wave is accounted for. The slow wave, with a short evanescence length, is sensitive to the small modifications of the geometry in the private SOL. The curvature we introduced in the private SOL is important for the near field study but most probably not relevant for the fast wave coupling studies, while the fast wave is sensitive to the 3D effect. Nevertheless, both of these two waves seem to play a comparable role on V_{DC} excitation in the vicinity of the wave launcher. We further evaluated the heat flux along two opposite sheath boundaries of the same antenna. Simulation revealed the left-right asymmetry that has been observed extensively in the strap dissymmetrization experiments, suggesting that spatial proximity effects in RF sheath excitation, studied for SW only previously, is still important in the vicinity of the wave launcher under full wave polarizations.

Initially developed for the RF sheath studies in Tokamaks, SSWICH-FW has more versatile applications. We have shown how SSWICH principle can be implemented into a totally different machine than Tokamak, in terms of geometry and plasma coupling regime. The Aline device is a dedicated tool to study the basic plasma wave properties and the RF sheath. The third part of this thesis is to use SSWICH to conduct interpretative simulations for Aline device. Using the SSWICH-FW code, we have observed and studied in the simulation both the LH wave and Helicon wave appearing under different Aline parameters. The field structure is however very sensitive to the badly known collision frequencies. Since the magnetic field is totally horizontal in Aline and the fact that the "slow-wave-like" Lower Hybrid wave is the main wave being excited under current status of the Aline device, the SSWICH-SW code is used as the first step to model RF sheath in Aline. Thanks to its easy access for diagnostic, the Aline device can provide experimental floating potential map to be compared with the SSWICH modelling. The DC plasma potential in the SSWICH-SW simulation is quite homogeneous at the antenna, whereas the experimental floating potential always has a peak value above the antenna. This discrepancy is explained by the acceleration of the ions by the radial electric field at the top surface of antenna, a phenomenon not present in SSWICH.

Contents

Contents

Contents

Contents

Chapter 1   Background of this thesis

This chapter introduces the general background of this thesis. It starts from a description of the thermal nuclear fusion, and introduce the most common fusion reactor, the so-called Tokamak. Radio frequency wave heating systems are often used to provide supplementary heating. This thesis focuses on the ion cyclotron resonant heating (ICRH). An overview of the ICRH wave launchers used in the Tore Supra Tokamak is given. The final part presents some challenges that the present-day ICRH systems still face as a motivation of this thesis.

1.1   Thermal nuclear fusion as a promising future energy source

The world's energy consumption could possibly double in the next 50 years. Yet more than 80% of our current energy is from fossil origin. According to the current consumption rate, the depletion time for oil, coal and gas are approximately 40, 200 and 70 years [Shafiee 2009]. This means fossil resources would be used up by the end of next century. Moreover, CO_2 emission from fossil fuel contributes to climate change and has raised huge political dispute and public concerns.

Nuclear power has come into people's sight since 1940s. By Einstein's mass-energy equation $E = mc^2$, huge amount of energy can be released from the mass loss during a nuclear reaction. The present day nuclear power stations are based on nuclear fission reaction: a heavy radiative atom, for example, uranium-235 absorbs a neutron and splits into several lighter atoms. The kinetic energy carried by the products is then turned into electricity through driving a steam turbine. Nuclear fission has created great economy benefits meanwhile keeping a low level of greenhouse gas emission. However, it also receives enormous criticisms over its disastrous accidents and potential risks of waste pollution. Thus a cleaner and safer power source is needed for the future. Nuclear fusion, the reaction powering the sun and stars, is the most promising candidate so far.

Nuclear fusion is the reverse process of fission. It is a process where two or more lighter atoms collide and combine to form a heavy atom. In atomic physics, the nuclear cross section [Clayton 1983] is used to characterize the probability that a nuclear reaction will occur. It is often quantified in terms of a "characteristic area" where a larger area means a larger probability of reaction. *Figure 1.1* shows the cross sections w.r.t the energy level of the atoms in several typical fusion reactions. The abscissa unit is the kilo electron volt (keV), 1eV=1.6×10^{-19}J. One can see that the Deuterium-Tritium (DT) reaction has the largest cross section and it reaches the peak value even before the other reactions. Thus it is considered as the easiest way to be realized on earth and potentially used as an economically viable energy source.

Figure 1.2 shows the details of the DT reaction. Each of this reaction generates 17.6MeV (Mega eV) of power. Among them, 14.1MeV is carried by neutrons. The other 3.5MeV is carried by alpha particle (^{4}He). In a future fusion reactor, the former part of the power is transformed into electricity. The latter part is used for self-sustaining the fusion reaction. Compared to the other power resources, fusion has many remarkable advantages. Firstly, unlike nuclear fission in which the input resource has a very limited reservation on Earth, the reactants of nuclear fusion are plenty. Deuterium is present in the sea water. The radioactive element tritium has limited source naturally but can be produced manually or bred during the fusion reaction by contacting with lithium. Lithium is also widely available in the nature. Secondly, In DT reaction, no carbon is produced and only a tiny amount of tritium will be released to the surrounding

environment. The radioactive wastes produced by neutron activation in DT reaction are less active and have a much shorter half-life, compared to those in fission. Thirdly, in a fission power plant, a chain reaction is developed so the reaction continues even without feeding the fuel. In contrast, fusion reaction can stop instantly as soon as the discharge fueling is interrupted thus it is much safer. Moreover, a fusion power plant is also economical. A 1000MW coal-fired power plant requires 2.7 million tonnes of coal per year, a fusion plant will only need 250 kilos of fuel per year. All these features support nuclear fusion to be a bright energy source for the mankind. The only question is how to make it happen.
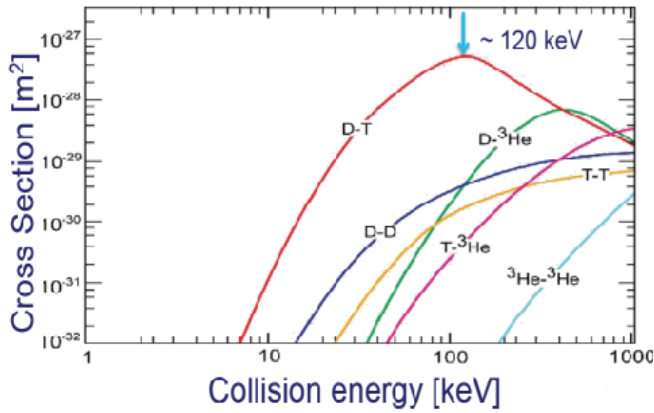
Figure 1.1. Nuclear fusion cross sections of different fusion reactions
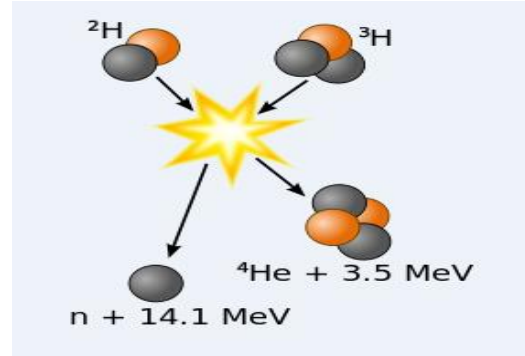
Figure 1.2. A diagram of nuclear fusion reaction

1.2   Magnetically confined torus: the main device to realize fusion on earth

In a real reactor, shortly after deuterium and tritium gas are injected, they are ionized, i.e. the electrons are ripped from the nuclei. The main difficulty to combine two light nuclei together is to overcome the Coulomb repulsion between them. In order to do this, the fuels must be heated to a very high temperature, i.e. 10^8K. At this temperature, the fuel becomes a state called plasma, which by definition, is a quasi-neutral gas of charged and neutral particles. In mathematics, the quasi-neutrality property of the plasma is defined as

$$\sum_{s=1}^{N} Z_s \cdot n_s + n_e = 0 \tag{1.1}$$

Where n_s is the density of ion species s with the number of electric charge Z_s, n_e is the electron density, N is the number of ion species. The charge neutrality, Eq. (1.1) is well fulfilled in a scale larger than the so-called Debye length λ_D[Chen 2016]

$$\lambda_D = \sqrt{\frac{\varepsilon_0 k_B T_e}{n e^2}} \tag{1.2}$$

Where ε_0 is the vacuum permittivity, k_B is the Boltzmann constant, T_e is the electron temperature in Kelvin, n is the plasma density, e is the elementary charge. Under typical fusion plasma parameters, $n = 1 \times 10^{20} m^{-3}$, $T_e = 10^8$ K, this length is about 7×10⁻⁵m. If observing over a scale shorter than this length,

one can see the plasma is oscillating in response to the charge separation. The oscillating frequency is defined as the plasma frequency,

$$w_{ps} = \sqrt{\frac{nq_s^2}{\varepsilon_o m_s}}$$ (1.3)

Where m_s is the mass and q_s is the electric charge of species s, i.e. electron and ion.

In any nuclear fusion device, using input power to generate and maintain the plasma is a-priori before any fusion reaction can happen. Nuclear physicists often use an energy gain factor Q to indicate the ratio between the instant output fusion power and the instant input power. Q=1 limit is called break-even, which means the released fusion power to the plasma equals the input power. $Q \rightarrow \infty$ limit is referred as the ignition condition. It indicates the moment when the energy released by the fusion reaction can solely sustain the plasma such that no external heating is required. In mathematics, the ignition condition is expressed as the so called "Lawson Criterion"[Lawson 1957],

$$nT\tau_E > 3 \times 10^{21} m^{-3} \cdot keV \cdot s$$ (1.4)

Where n is the plasma density, T plasma temperature in *keV*. In plasma physics, many literatures use the electron volt to indicate temperature, ($1keV = 1000eV = 1.16 \times 10^7 \, \mathrm{K}$). In this thesis, the electron volt is used as the unit for temperature. The amount of nuclear power generated by fusion reaction depends on the reaction rate, which is a function of the plasma density and the speed of the ionized particles. The speed of particles is equivalent to its temperature. The plasma suffers continuous energy loss due to conduction, convection, radiation processes, etc. To achieve thermonuclear conditions Eq. (1.4), it is necessary to confine the plasma for a sufficient time. We define the energy confinement time τ_E as the e-folding time in which the total plasma energy decreases to 1/e under zero input power.

There is no existing material can hold on such a thermal fusion plasma. The sun uses gravitational force to confine the plasma However, this approach is impossible to be repeated on the earth since it requires a huge quantity of mass.

One kind of fusion device was developed after the invention of laser. This approach confines the plasma at a very high density ($n \sim 10^{31} m^{-3}$) for a very short time ($\tau_E \sim 10^{-11} s$). It uses high-power (several MW) laser beams to heat and compress a fuel pellet, which typically consists of a mixture of deuterium and tritium. The pellet is expected to encounter nuclear reactions before the fuel escapes. The National Ignition Facility in the USA and Laser Megajoule in France are based on this principle.

Alternatively, when dealing with charged particles, one naturally think about the Lorentz force. In the magnetized plasma, the Lorentz force can act as a confinement force. Charged particles are rotating around the confinement magnetic field in a plane perpendicular to the magnetic field or we say the particles attach to the magnetic field line and thus get confined in the direction perpendicular to the magnetic field. The frequency under which they rotate is called the cyclotron frequency. Each of the plasma particle species has its own cyclotron frequency, which reads,

$$w_{cs} = \frac{q_s B_0}{m_s}$$ (1.5)

Where q_s, m_s are the electrical charge and mass of species s, respectively. Note q_s has signs, e.g. q_s=-e in case of electron. B_0 is the magnitude of the confinement magnetic field **B₀**.

The radius of the particle cyclotron motion is called the Larmor radius,

$$r_s = \frac{m_s v_\perp}{|q_s| B_0}$$
(1.6)

Where $v_\perp$ is the particle velocity component that is perpendicular to the magnetic field.

In the direction parallel to the magnetic field, particles can be confined by bending and closing the magnetic field lines. In the 1950s, scientists from Soviet Union invented a toroidal machine called Tokamak and nowadays it is considered as the main approach to build thermal nuclear reactors on Earth. A sketch of the Tokamak structure is shown in *Figure 1.3*. In order to understand this complex structure, let's firstly define some coordinate conventions.
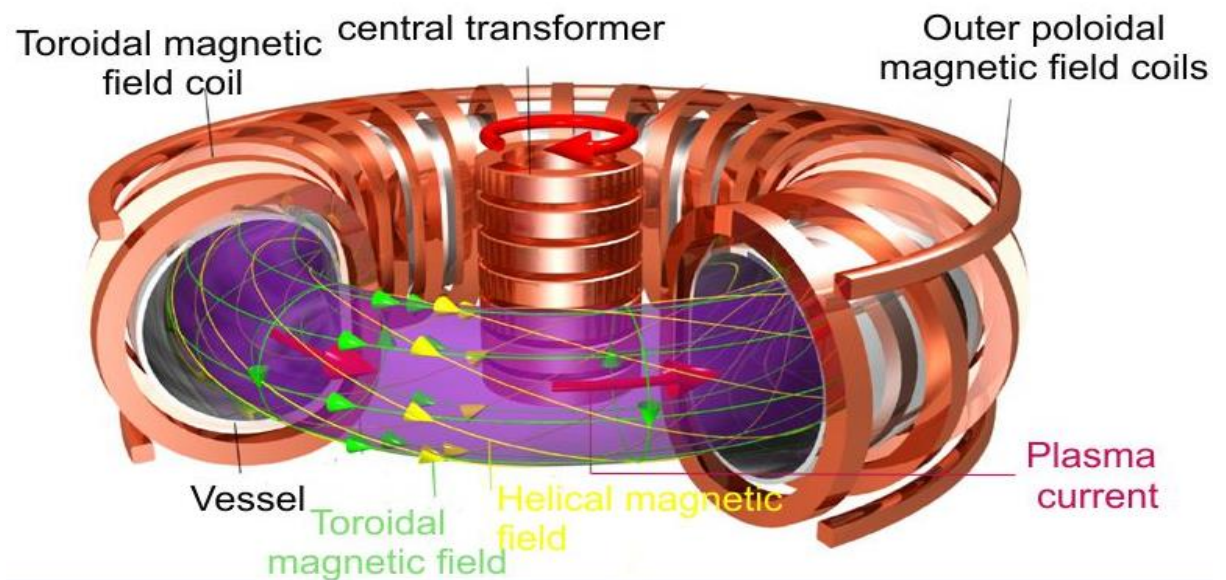
Figure 1.3. Tokamak structure and its magnetic field configuration

To describe the particle and current motion inside a Tokamak, two right-handed coordinate systems are often used at the same time, see *Figure 1.4*. The cylindrical coordinate system (R, φ, Z) is used to describe the overall framework. Here R represents the major radial direction, φ represents the toroidal direction, Z is the vertical direction. R_0 is the major radius. Since the Tokamak geometry is toroidal homogeneous, one could take a poloidal cross-section in one toroidal position. In this cross-section plane, a second coordinate system, the poloidal coordinate system (r, ς, φ) is often used. Here r represents the minor radial direction and ς represents the poloidal direction. r_0 is the minor radius. In this thesis, unless being specified, the radial direction means the major radial direction R.
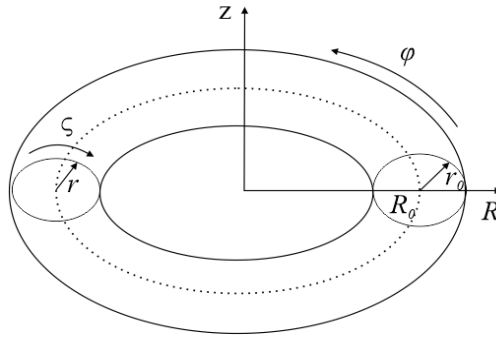
Figure 1.4. A schematic view of the Tokamak coordinate systems

Tokamaks are designed to generate a magnetic configuration that can confine the plasma. The main magnetic field is along the toroidal direction and it is produced by the toroidal magnetic field coils, see *Figure 1.3*. However, the toroidal magnetic field alone is not enough to confine the plasma. This is because there are always some transversal (w.r.t the toroidal magnetic field) plasma drifts occurring due to the presence of curved field lines, which introduces a pressure or current gradient. In order to balance this gradient force, a poloidal magnetic field is needed as well.
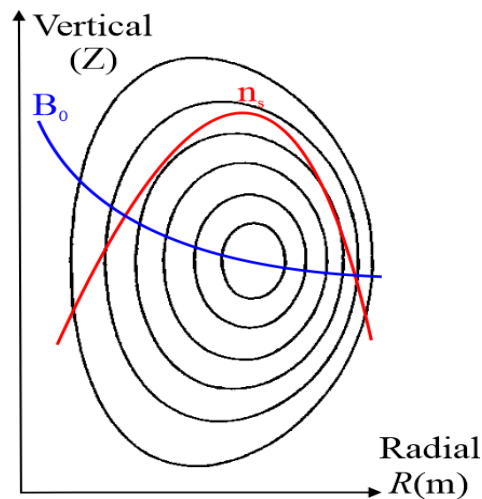
Figure 1.5. Magnetic flux surface in the central plasma, view inside a poloidal cross section. Red curve indicates a typical profile of the plasma density; The blue curve represents the magnetic field profile.

In a Tokamak, the poloidal magnetic field is generated by the plasma current. The plasma current is mainly induced by a central transformer, although there are some alternative current generation methods that will be presented later. The total magnetic field lines in a Tokamak therefore are helical. If one tracks their trajectories, they actually form many stratified surfaces. The field lines lay on these nested magnetic surfaces. Draw in a poloidal cross-section, it is something like many loops circling around the center, shown in *Figure 1.5*. The plasma parameters, i.e. density, pressure, are constant on the magnetic flux surfaces as a consequence of the plasma equilibrium [Grad 1958][Shafranov 1966]. Along the radial directions, the plasma parameters evolve as crossing the magnetic surface. A typical density profile and

magnetic field profile are shown in *Figure 1.5*. The magnetic field strength roughly scales as $1/R$, with R the major radius axis.

Some additional coils are needed to control the plasma shape and position, i.e. the outer poloidal magnetic field coils. For convenience, in Tokamak convention, we also define the parallel direction to be the direction parallel to the confinement magnetic field **B₀**. Similarly, the perpendicular direction is the direction perpendicular to **B₀**.

Tokamak can achieve a significant longer energy confinement time than the lasers. A typical set of parameters in a Tokamak that fulfilling the ignition conditions is: $n = 10^{20}\, m^{-3}, T = 10\, keV$ and $\tau_E = 3s$. Compare to the air ($n=10^{26}$ m^{-3}, T=300K), the Tokamak plasma is rather tenuous and hot.

Over the past 60 years, the Tokamak concept has been tried in many countries around the world. There are hundreds of them in total. The major limitations of the Tokamak concept are the following: at first, Tokamak relies on a strong magnetic field (several Teslas) to confine the plasma. The magnetic field is generated by currents flowing through the compactly winded magnetic field coils. An ordinary coil could produce huge heat which needs much energy to cool down. In 1988, people in France employed superconducting coils and built the world's first supra-conducting toroidal coil Tokamak, Tore Supra. The temperature gradient formed between the central hot plasma (10 KeV) and liquid helium (3.4×10^{-4} eV) used in the superconducting coil is the greatest in the universe. Secondly, Tokamak usually operates in a pulsed mode. This is because the central transformer needs to generate a time-varying magnetic field in order to drive Ohmic plasma current. Once the central transformer current reach its maximum, the pulse will cease. A method to increase the pulse duration is by taking advantage of the non-inductive current. This is one of the applications of the auxiliary heating that will be discussed in section 1.5 .

Table 1-1. Typical parameters for Tore Supra Tokamak and ITER Tokamak

	Tore Supra	ITER
Major radius R_0 (m)	2.5	6.2
Minor radius r_0 (m)	0.7	2
Plasma toroidal current (MA)	1.5	15
Magnetic field **B₀** (T)	3.8	5.3

Another type of machine also using magnetic confinement, the Stellarator [Nuehrenberg 1995], was developed in parallel to the Tokamak. The main advantage of this machine is that it has no net current flowing along the toroidal direction. Consequently, there is no need to have a central transformer and the twisted magnetic field lines are totally created by the external helical coils. It is naturally a good candidate for a steady-state operation. It can also avoid plasma instabilities caused by the current gradient. However, since it relies on extremely dedicated magnetic configuration to balance the gradient force, the manufacturing of such a magnetic coil system is much more complicated than the coils used in Tokamak. In addition, it suffers from a low confinement performance and critical particle losses. Wendelstein 7-X, the world's largest stellarator has just completed its 10 years' construction phase and had its first plasma at the end of 2015.

At the moment, Europe has chosen the magnetic confinement as its main route to fusion power. The International Thermonuclear Experiment Reactor (ITER) - the largest Tokamak in the world and the leading

fusion machine, is currently being built in Cadarache, France. It has an ambitious scientific object: demonstrate the feasibility of fusion power and pave the path for the future commercial fusion reactor. Some major parameters of the Tore Supra Tokamak and the ITER Tokamak are shown in *Table 1-1*.

1.3   At the magnetized plasma edge: the Scrape-Off Layer

The central plasma is the useful part where the nuclear fusion reaction occurs. But one cannot have only the central plasma because the plasma cannot be of infinite size. This is also because one of the main products in DT reaction, helium and other impurity particles (also called as fusion ashes) must be exhausted from the fusion device at the edge in order to avoid plasma dilution. In addition, the output power must be exhausted from the plasma at the edge. Here the edge is defined where the plasma can have interactions with the wall. Unlike in the central plasma, at the edge, the magnetic field lines are open and connect to the wall or other protruding components. The boundary between the closed magnetic flux surface and open magnetic flux is called the Separatrix or the last closed flux surface (LCFS). In the earlier days, a solid surface called limiter was used to interrupt the magnetic field surface. The location of the limiter thus determines the LCFS. In this case, the limiter can be a source of impurity to the plasma because of the sputtering of the limiter surface. Modern-day Tokamaks are more often equipped with an element called "Divertor". The Divertor is usually located at the bottom (in *Figure 1.6*) or at the top of the machine, it is further away from the plasma, compared to a limiter. In a Divertor configuration, the LCFS is solely determined by the magnetic field and its location is manipulable by changing the current in the Divertor's magnetic field coils. Magnetic field lines connect to the Divertor target plates. The fusion ashes are diverted along the open magnetic field lines to the Divertor and then they are being pumped out of the machine.
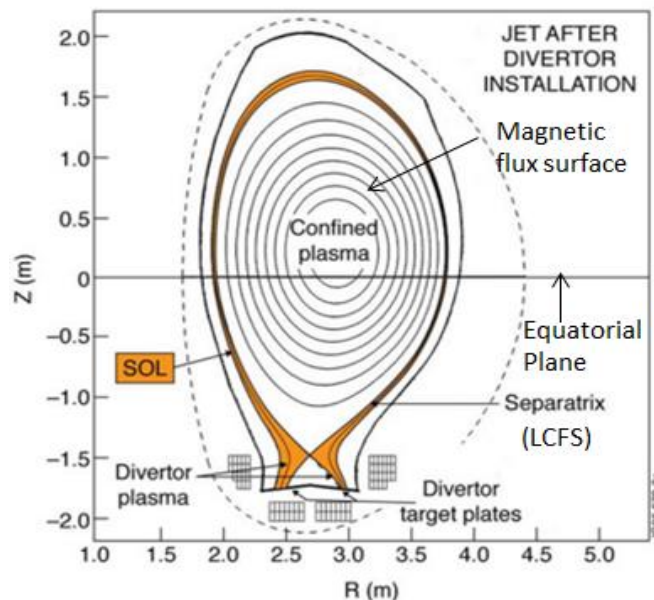

Figure 1.6. Magnetic flux surface in JET Tokamak

What we called as edge in the beginning of this section is the region between the Separatrix and vessel wall. A more definitive name for this region is the scrape-off layer (SOL). It is marked in yellow in *Figure*

1.6. The SOL region is important, because it is the region where the plasma-wall interaction occurs. Understanding the plasma-wall interaction is one of the key tasks in magnetic confinement fusion research. Firstly, as indicated before, the fusion ashes and a part of fusion power must be exhausted through the plasma-wall interaction. Secondly, the plasma-wall interaction affects significantly the plasma confinement at the center. For example, the impurity generated at the edge can be transported to the center, which can reduce the energy confinement time and drop down the temperature.

Therefore, before thinking of making any nuclear reaction, one needs to have a clear view of what is happening at SOL.

1.4   Plasma-wall interactions at the SOL

Many physical processes are occurring at the SOL region. A dedicated study of plasma-wall interaction will cover material science, plasma physics, atomic physics, chemistry, mechanics, et al. Some references dedicated on this topic can be found in [Kirschner 2009][Meade 1974][Reiter 1991][Stangeby 2000]. Here we just mention a few of them that are related to this thesis,

Plasma facing material erosion and re-deposition: During Tokamak operation, plasma facing components suffer constantly high energetic particle flows striking on their surface. This could cause some erosion processes, i.e. sputtering, melting, sublimation and evaporation. Fortunately, a large part of material components released to the plasma by erosion are re-deposited again on the wall surface. This re-deposition process can largely compensate the loss of surface material by erosion.

Sheath excitation: The plasma potential is often positively biased compared to the grounded wall. A thin layer called sheath is formed at the plasma/wall interface. Inside the sheath, the plasma charge neutrality is broken and ions get accelerated. High energy ions then bombard the wall which can cause many deleterious effects, i.e. hot spots at the plasma facing components, impurity production and edge power losses. Understanding the reason of sheath excitation and its effect is the main topic of this thesis.

Sputtering and heat loads: Sputtering is the ejection of the particles from the surface of a solid caused by the bombardment of highly energetic particles, i.e. ions accelerated by sheath. Sputtering can be categorized as physical sputtering and chemical sputtering. For physical sputtering, there is generally an energy threshold below which the sputtering does not occur. High Z material usually has a significant larger energy threshold. For deuterium incident, the energy threshold for Carbon and Tungsten surfaces are 30eV and 214eV [Kirschner 2015], respectively. The sputtering yield is defined as the number of particles being ejected from the surface per incident ion. It is a function of the incident ion energy, the mass ratio between the projectile and target and the surface binding energy of the target particles. A Deuterium plasma with a temperature of 100eV has a sputtering yield of 0.1% for a Tungsten surface and 2% for a Carbon surface [Samm 2015]. The former material has been chosen as the armor of the ITER Divertor. During the ITER operation, it is estimated that the Divertor will suffer around 5-20MW/m^2 steady-state heat flux and 1GW/m^2 instant heat flux [Linke 2015]. As a comparison, the heat flux density at the nozzle of rocket is just around 85MW/m^2. Heat loads on other plasma facing components are less pronounced, but still could produce serious damage on the wall surface.

Impurity transport and radiation: as highly energetic particles incident on the surface, some wall materials can be released to the plasma. They are usually different from the plasma species and thus play as impurities. Some high Z (atomic number) impurities, like Tungsten can be transported to the core plasma and significantly cool down the plasma core by its radiation losses. In some worse cases, it can

further develop instabilities, so called MARFE [Lipschultz 1987] and cause plasma disruptions [Schuller 1995].

1.5   Heating and current drive methods in the magnetic confinement device

1.5.1   Ohmic heating

Once the plasma is created, the ions and electrons are driven by the loop voltage which is produced by the central transformer. They flow along the magnetic field and form a plasma current. In a Tokamak, this current can easily reach several Mega Ampere. The plasma has an electrical conductivity. In the parallel direction, it is expressed by Spitzer conductivity,

$$\sigma_{//,S} = \frac{(0.001Te)^{3/2}}{1.65 \times 10^{-9} \ln \Lambda} \tag{1.7}$$

Where Te is the electron temperature in eV, $\ln \Lambda$ is the Coulomb logarithm whose typical values are between 15 and 20. From Eq. (1.7), the conductivity increases with the electron temperature. So the resistivity and thus the efficiency of Ohmic heating decreases dramatically after the temperature reaches $2.6\text{-}3.5 \times 10^7$ KeV. In order to achieve the ignition temperature, e.g. T=10 KeV, additional heating is needed. There are two major auxiliary heating methods, neutral beam injection and radio frequency (RF) wave.

It's worthwhile to mention that besides providing additional heating, another main purpose of the auxiliary heating is to drive non-inductive current. As indicated before, one of the drawbacks of Tokamak operation is that it is intrinsically pulsed. However, in a real fusion reactor, a steady-state operation is desired for many reasons. This relies on the contribution of non-inductive currents to the total plasma current. A steady state operation of Tokamak requires at least 20% of the total current driven from auxiliary heating & current drive. For ITER, a high fraction of it will come from the bootstrap current [Peeters 2000], which is a naturally occurring current caused by the pressure gradient. Another part will come from the auxiliary heating being discussed in the following.

1.5.2   Neutral beam injection

In a Tokamak plasma, the magnetic field is so strong that any charged particles coming from outside will soon be deflected by the Lorentz force and could not reach the core. In order to heat the core plasma, one can only use neutrals. The structure of a neutral beam system is the following: ions (typically H^+ or D^+) coming out from an ion source are accelerated by electrical grids to highly energetic (100 keV at present) and then they pass through a cold neutral gas where they are neutralized by charge exchange. The remaining ions that have not been neutralized are diverted out by a magnetic field. Finally only the neutral hydrogen atoms are injected into the plasma. Inside the plasmas, the neutrals are ionized again soon (with a typical penetration length of 1m) and then transfer their energy to the plasma through collisions. Neutral beam injection has achieved significant heating in present-days' Tokamak experiments and it is the main heating system in JET and DIII-D Tokamaks. Some references about this heating method can be found in [Hemswoth 2009][McAdams 2014]. In the following sections, we will only talk about the radio frequency wave heating.

1.5.3   Radio frequency wave heating and current drive

The electromagnetic waves are injected through the Tokamak edge. In most media, i.e. water inside food, waves are damped through collisional mechanisms. In fusion plasmas, however, collisions are often too weak so it has to rely on the collisionless mechanism. When the wave frequency matches one of the

cyclotron frequencies, the corresponding charged particle is then accelerated by the oscillating electric field of the wave in the perpendicular direction. Thus the wave energy and momentum could be transferred from the wave to the charged particles. This is the fundamental principle of the so called resonant heating. In the parallel direction, the wave can also be damped through a collisionless mechanism called Landau damping [Landau 1946][Chen 2016]. The thermal velocity of the particles usually follows a distribution, e.g. Maxwellian distribution. Those particles whose thermal velocity are smaller than the wave phase velocity can be accelerated by the wave. On the contrary, the other particles having a velocity larger than the wave phase velocity will be slowed down. If the wave velocity lies on the higher part of the velocity distribution, the particles will then feel a net acceleration. Assuming a plane wave with harmonic oscillations in $\exp(iwt - i\mathbf{k} \cdot \mathbf{r})$. (Note: here we used the engineering convention, as it will be in the rest of this thesis). The above two heating mechanisms are governed by the wave-particle resonance condition,

$$w - k_{//}v_{//s} - Nw_{cs} = 0 \tag{1.8}$$

Where w is the angular frequency, $k_{//}$ the wave vector parallel to the confinement magnetic field, $v_{//s}$ parallel velocity of particle species s, w_{cs} is the cyclotron frequency of s, N is an integer, represents the order of the harmonic.

Depending on the frequency, waves can be categorized as the ion cyclotron range of frequency (ICRF) wave frequency $f = \dfrac{w}{2\pi} \approx 50MHz$, lower hybrid (LH) $f \approx 2GHz$ and electron cyclotron range of frequency (ECRF) $f \approx 100GHz$, see *Figure 1.7*. The ICRF and ECRF waves, as indicated by their names, are damped at the ion cyclotron resonance and the electron cyclotron resonance, respectively.

Although the electromagnetic waves carries negligible momentum, it could achieve current drive by heating particles in one specific direction. The particles that are heated become less collisional than those who are travelling in the opposite direction. Thus a net current is formed. This is the principle of the RF wave current drive.

The lower hybrid wave is generally the most efficient auxiliary method for non-inductive current drive in present-day Tokamak, while the electron cyclotron wave is an ideal tool to provide localized current drive and heating. Some reference about these two waves can be found in [Hoang 2009][Goniche 2013][Prater 2004]. The following text will only focus on the ion cyclotron wave.
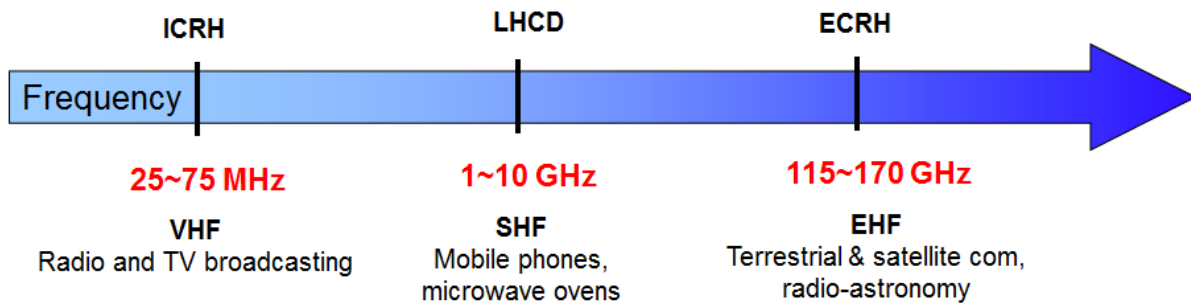
Figure 1.7. Diagram of frequency range of three auxiliary heating and current drive waves

Finally, a list of auxiliary heating powers equipped in the Tore Supra and ITER is shown in *Table 1-2*.

Table 1-2. Quantities of the auxiliary heating power in Tore Supra and ITER Tokamak

Auxiliary heating power	Tore Supra	ITER
ICRH (MW)	12	20
LHCD (MW)	7	0
ECRH (MW)	0.8	20
NBI (MW)	0.5	33

1.6   Ion Cyclotron Resonant Heating: an efficient way to achieve direct ion heating

Among these three wave types, the lower hybrid and electron cyclotron wave mainly damp their waves directly on the electrons (although it can also indirectly heat ions through collisions). However, the fuel of the nuclear reaction is a mixed of Deuterium and Tritium ions. It will be more efficient if one can heat these two nuclei directly. This is where one of the key elements related to this thesis comes into the game: the Ion Cyclotron Resonant Heating (ICRH). At first let us describe the principles of ICRH and its operation scenarios.

A schematic view of ICRH antenna in the WEST (Tungsten (W) Environment in Steay-State Tokamak) tokamak is shown in *Figure 1.8*. WEST is the upgraded version of Tore Supra Tokamak at CEA, which aims at testing actively cooled tungsten divertor. The waves are launched by phased array straps (antenna) at the edge. For ICRH (f=25-100MHz), two types of waves could be excited: the fast wave (FW) and the slow wave (SW), named by the relative scales of their phase velocities. The fast wave can propagates across the whole plasma and thus it is the main heating wave. The ICRH antenna is designed for exciting this wave. The slow wave is excited parasitically by the antenna and it is widely blamed for causing some deleterious wave-SOL interaction, i.e. radio frequency sheath that will be introduced in the next section.
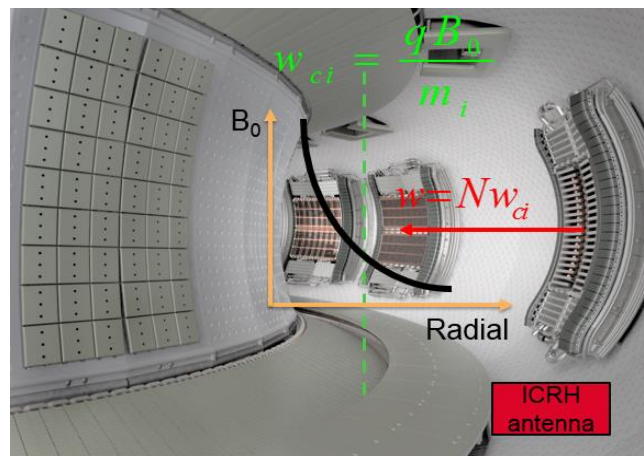
Figure 1.8. The WEST Tokamak vacuum vessel and ICRH antenna. Note: the ICRH antenna here does not reflect the final design that will be used actually in WEST

ICRH has a variety of heating scenarios and relatively cheaper to build, making it a very popular auxiliary heating method. Here are some of its main heating scenarios,

- Wave absorption at the fundamental resonant frequency (N=1): This looks like the most straightforward way to have ion heating. Observing along the direction of the magnetic field, the

ions rotate left-handedly along the magnetic field line. If an incident wave having the same polarization and the same frequency as ion cyclotron motion, then the oscillating electric field of the wave is in phase with the ion motion. Over one cyclotron period, the ions feel a net acceleration. But this is not going to happen in single-ion-species plasma. This is because the fast wave is right-handed at the fundamental resonance of ions, see chapter 2, section 2.1.4.

- Wave absorption at the harmonic frequency (N>1): The polarization problem can be avoided by working at the harmonics of the cyclotron frequency. Let's take N=2 for example. The wave electric field varies two times faster than the ion cyclotron frequency. If the wave electric field is uniform, then there is no net acceleration for ions. On the contrary, if the wave electric field is higher on one side than the other side, then the ions experience a net acceleration over one period. Similarly, higher harmonic resonant heating requires the existence of non-vanishing higher derivatives of the electric field. The efficiency of harmonic wave heating decreases with harmonic number.

- Minority heating: Another way to avoid the polarization problem is to use multiple ion species. For example, put a small amount of hydrogen in a majority of deuterium plasma. The polarization is determined by deuterium but the wave is damped at the fundamental hydrogen resonance. In this case, the fast wave has a left-hand electric component and thus could heat the hydrogen ions, which then transfer their energy to other majority deuterium particles, or electrons through collisions.

- Mode-conversion can take place if several ion species co-exist in the plasma. Each of two ion species pair could create an ion-ion hybrid resonance. The fast wave is mode converted to other waves, i.e. ion Bernstein wave at this resonance. The converted waves are damped on the electrons through Landau damping. A further details of this mechanism can be found in [Lu 2013]

Most of the present-day Tokamaks use the minority heating as the main ICRH heating scenario. ITER will use the second harmonic of Tritium and ^{3}He minority heating.

Figure 1.9. 4 straps ICRH antenna in the KSTAR Tokamak (left); 2 straps ICRH antenna in the ASDEX-Upgrade Tokamak (right)

Different ICRH antennas have been used in many machines. But all of them have some features in common. Firstly, the straps are placed along poloidal direction. This is because the wave that is expected to be excited by the straps has a large poloidal electric field. Secondly, in order to have different spectra
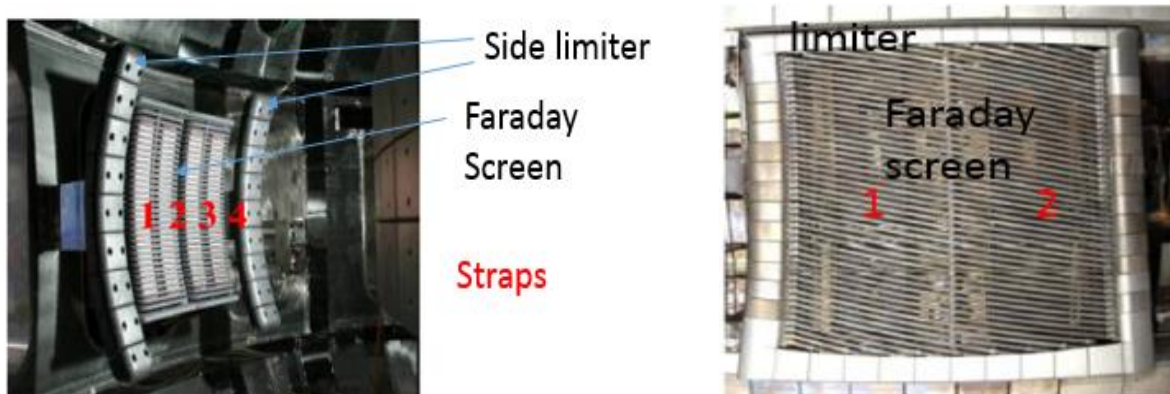
for multiple purposes, the antenna usually contains multiple straps with different phasings. Thirdly, the antenna includes some protecting components, like side limiters and one Faraday Screen. The Faraday screen also aims at minimizing the parallel electric field. An example of ICRH antenna in the ASDEX-Upgrade and the KSTAR Tokamak are shown in *Figure 1.9*.

1.7   Overview of ICRH wave launchers on the Tore Supra Tokamak

The ICRH system in Tore Supra Tokamak is designed for 12MW of ICRH power injection in the frequency range of 35 to 80MHz (ion-ion hybrid heating) and 8MW at 120MHz (harmonic cyclotron heating). The power is delivered into Tokamak through three horizontal ports. The total ICRH system thus consists of three wave launchers (4MW per each), six transmission line and six RF generators. Each of the six RF power generators consists of a pilot generator, a modulator, a solid state wideband amplifier and a 3-stage tetrode amplifier. Six 80m long coaxial transmission lines are installed from the generator to the torus hall. They have a diameter of 140/230mm, with a characteristic impedance of 30Ω. Each of the generator and transmission line connects one strap. More references on the transmission line and generator can be found in [Kuus 1988].
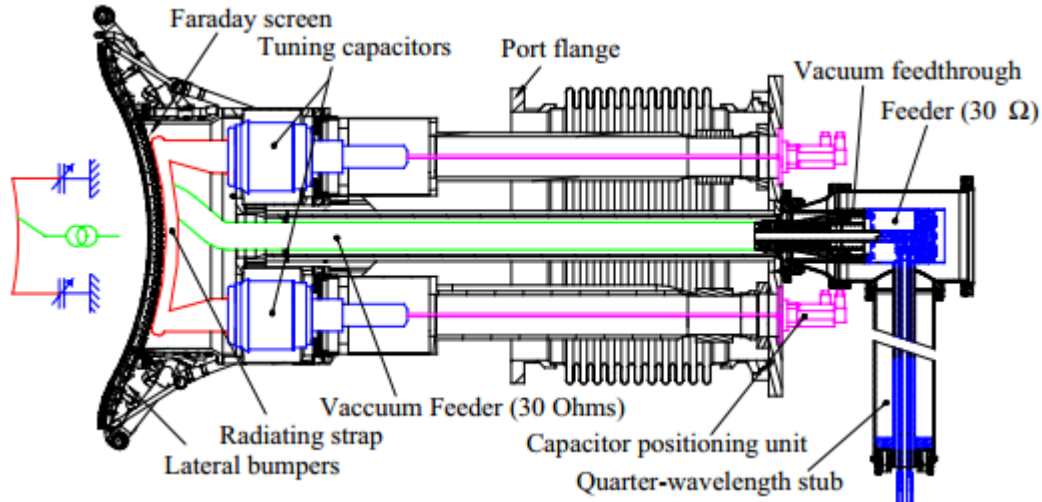
Figure 1.10. Layout of the standard ICRH wave launcher on Tore Supra, cite from [Vulliez 2003]

A cross-section of one of the three wave launchers is shown in *Figure 1.10*. It is about 3m's long in reality. Each of the three wave launchers has two radiating straps (placed side by side in toroidal direction) which are protected by Faraday screen in front of it and lateral bumpers in the poloidal directions. Each radiating strap is based on the resonant double loop concept [Owens 1985]. It is fed at the middle and short-circuited at both ends through two tuning capacitors, which creates a one wave resonator [Colas 2006]. The strap has a large self-inductance, the AC current flowing on its surface varies in time. This is not a lossless resonance loop since it radiates RF waves to the plasma. The energy loss is compensated by the feeder. During the plasma pulse, the plasma resistance (especially the capacitance) is time-varying, the matching is done by changing the capacitance of the resonant circuit. The two capacitors are connected side by side through a bridge. The capacitor consists of two parallel plates, the amount of plate surface which overlaps are controlled by the mechanical tuning bars, i.e. the pink ones in *Figure 1.10*. A quarter-wavelength stub is used at the input of the wave launcher to enable the cooling water cycling through the wave launcher. The port flange connects the vessel port and the wave launcher. During the

operation, the part in front of port range of the wave launch is plugged into the vacuum vessel of the Tokamak. The antenna is hanging on a rollerskate, which allows the antenna moving radially about 10cm along the port axis during Tokamak pulses to achieve more power being transmitted to the plasma.

Figure 1.11 is a picture of the plasma facing part of the ICRH antenna. The classical ToreSupra ICRH antenna [Beaumont 1988] consists of two vertically placed, water cooled rectangular straps made of silver-coated stainless steel, shown in brown. The currents flow along the straps and thus excite mainly the poloidal electric fields, see Figure 1.12. The Tore Supra classical antenna uses two straps. Just like the antenna array used in telecommunication, the direction of emitted wave is determined by the current phasing on the straps. Usually, three current phasings are often used. Dipole phasing [0 π] and monopole phasing [0 0] have antiparallel and parallel currents, respectively. They are frequently used as heating phasings, while the asymmetric phasing [0 π/2] is used mostly for current drive purposes.
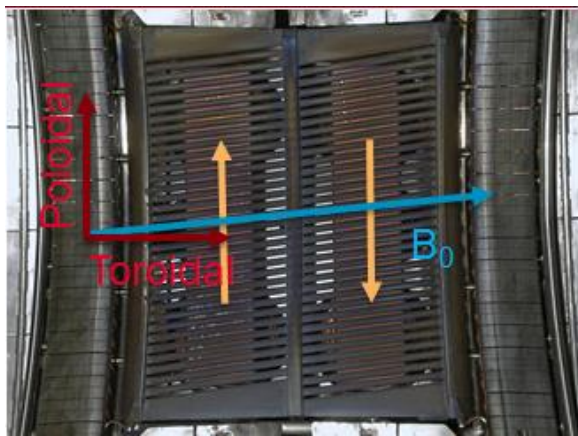
Figure 1.11. ICRH antenna on Tore Supra (view from the plasma side)
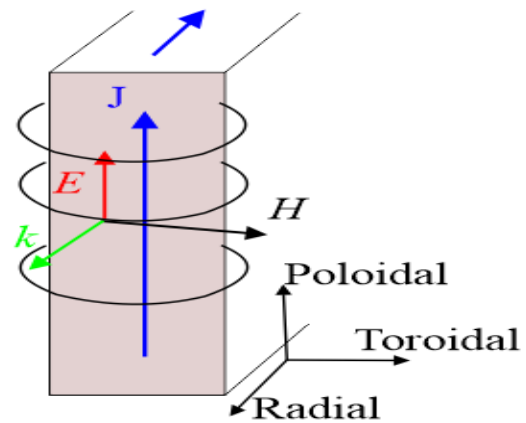
Figure 1.12. The principle of exciting RF field by a poloidal current

The metallic frame with many tilted bars in front of the straps is the Faraday screen. Its dimension is 0.432*0.595 m^2. The bars are oriented roughly parallel to B_0. Initially it is designed to cancel the parallel electric field of the wave and protect the straps from heat flux. The Faraday screen is actively cooled by pressurized water at 150°C behind it and it is coated with boron carbide (B_4C) to limit high Z impurity contamination of the plasma. The two straps are separated by a vertical septum in the middle. At their lateral sides, a curved structure sitting at each side of the antenna is called side limiter. Its main role is to protect the antenna from the heat flux coming from toroidal directions. Like all the other plasma facing components, it is cooled by a water loop beneath it. The side limiter is made of CuCrZr alloy.

1.8   Selected ICRH challenges

Despite the fact that ICRH has many flexible heating schemes and the engineering system is generally reliable during the Tokamak operation, it has some defects which limit its performance. The requirement that a fusion reactor should work in a continuous way imposes a big challenge for the heating system. One must thus optimize the antenna-plasma coupling in a steady-state operation, in the meantime avoiding the spurious effects such as impurity generation, hot spots and anomalous edge heating. Besides, the interactions between different heating systems also need to be accounted for. Here we list several of the main issues related to this thesis.

1.8.1   Plasma intermittence and antenna matching

The plasma property can vary due to some instability events. This will lead to a change of the antenna input impedance seen by the transmission line. If the antenna cannot adjust its load resistance instantaneously to match with the transmission line, the power will be reflected to the RF generators, and subsequently trigger protective power trips, which could possibly shutdown the power supply. To overcome this problem, a real-time matching system, i.e. tuning capacitor (see *Figure 1.10*), is installed behind the antenna which allows antenna matching automatically, following the load change. The reaction time of the mechanical tuning element is typically 100ms (Tore Supra value). This method can handle long-time scale load changes, but the short time scale (~1ms) plasma change is still too fast, so in addition to this, more load-resilient antennas were developed recently using conjugate T junctions or 3dB hybrids techniques [Vuillez 2008][Graham2012], which reduces the voltage standing wave ratio (VSWR) over a wider range of load resistances. It guarantees that the total power transmitted to the plasma can still achieve a high level when the antenna input impedance varies in the designed region. With the dedicated matching system, the reflected power can bounce back to the plasma again, instead of being transmitted back through the feeder. A maximum of 10.4MW of ICRF power into plasma over 12MW input from generator has been achieved in ToreSupra [Colas 2006]. Besides the matching, there are other operational limits. For instance, the RF current on the strap is limited by the thermal issues in critical elements, i.e. matching capacitor. The RF current is proportional to the RF voltage, the latter is limited by the arcing issues.

1.8.2   Antenna-plasma coupling at the edge

The wave coupling property is characterized by the coupling resistance (or the plasma resistance mentioned before), which quantifies how much power is transmitted to the plasma with 1A current on the straps. The details will be given in the next chapter. The main objective when designing any auxiliary heating system is to couple as much power as possible to the plasma. From this point of view, using the IC wave is more problematic than the EC wave. This is because the main heating wave, the fast wave encounters an evanescent region just after it is being excited at the antenna straps. The length of this this evanescent region is the distance between the adjacent cut-off layer and the antenna. The location of the cut-off layer in the plasma depends on the wave frequency, confinement magnetic field and plasma parameters (Details will be given in chapter 2). The fast wave thus suffers a lot of reflection and only a part of the wave can tunnel across the evanescent region and reach the plasma center. This coupling resistance decays exponentially with the length of the evanescence region. In reality, the antenna can move a little bit radially but cannot approach the plasma too much, otherwise it will simply melt. The length of the fast wave evanescent region ranges from several centimeters to tens of centimeters. Furthermore, small scale plasma instability, i.e. turbulence can significantly modify the plasma density in the SOL region. This can also affect the wave coupling.

1.8.3   Radio-frequency sheaths

Another major issue at the SOL is that during the ICRH operations, the antenna surface suffers a large heat flux (of the order of MW/m^2) caused by the bombardment of high-energetic ions. To make things worse, the Direct Current (DC) plasma potential are often enhanced by ICRF waves via a non-linear process called sheath rectification. Consequently, the ions get more significant kinetic energy and lead to more severe damages on the wall surface. Many spurious RF edge effects are suspected to be caused by this sheath rectification process, i.e power losses at the SOL, heat loads deposition on the plasma facing components and impurity production from the wall. As an example, *Figure 1.13* shows a spread of hot

spots observed on the surface of the Faraday screen and side limiters by infrared thermography during Tore Supra ICRH operation.
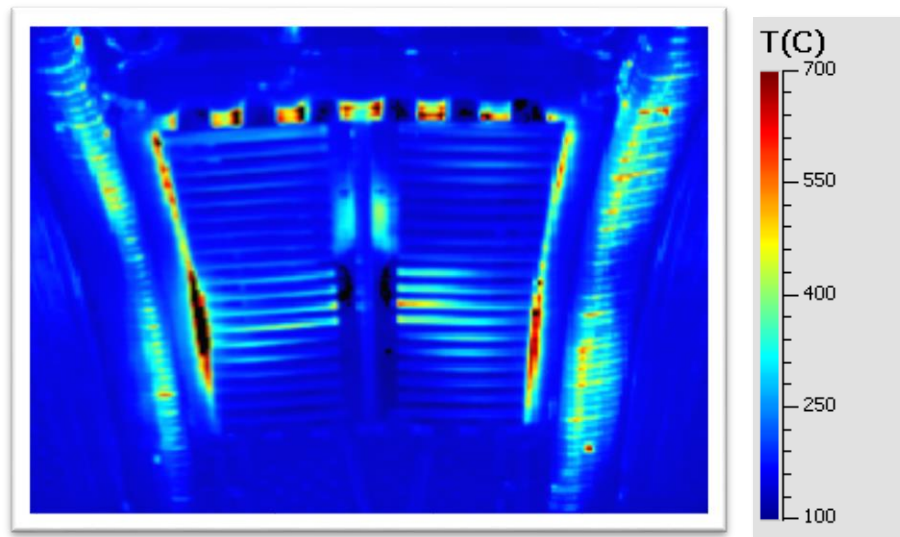
Figure 1.13. Surface temperature map at the front surface of the prototype Faraday screen, obtained by Infrared thermography during ICRH operation

The physics lying behind RF sheath rectification has not been fully understood yet. It is usually modelled in analogy with a double Langmuir probe driven by an oscillating RF voltage (details will be given in chapter 2). The oscillating RF voltage is estimated from a field-line integral of the parallel electric field $E_{//}$, while $E_{//}$ is often pre-calculated in full wave RF simulations without sheath [Perkins 1989]. Their underlying assumption is that the RF sheath rectification is mainly attributed to the parasitically excited slow wave. A prototype Faraday screen designed for reducing RF sheath on its front surface has been tested during ToreSupra 2011 experimental campaign. It is equipped with a slotted frame and cantilevered horizontal bars, aiming at intercepting all parallel RF current paths on its front surface [Mendes 2010]. Surprisingly, compared to the conventional Faraday screen, the prototype exhibited more intense heat loads during the ICRF operations [Colas 2013]. This cannot be explained by the conventional sheath modeling and thus motivated the development of the Self-consistent Sheath & Waves for ICH (SSWICH) code [Jacquot 2014][Colas 2014].

1.9   Dedicated RF sheath test beds

In order to understand RF sheath physics, some specific devices were built. Compared to a Tokamak, they are more flexible to set up relevant parameters, diagnostics and test different antennas. Their geometries are simple for simulations. The experiments on these devices can be much faster as there is no constraints from the Tokamak campaigns. The Ion cyclotron Sheath Test Arrangement (IShTAR) [Crombé 2015] in Ipp Garching and A Linear Experiment (Aline) machine [Faudot 2015] in Institute Jean Lamour are among these dedicated test beds.

The Aline machine has a cylindrical vacuum chamber, which is 1m long and 30cm in diameter, see *Figure 1.14*. It is made by stainless steel. During the experiment, a DC magnetic field can be created by external coils winding around the vacuum chamber. The magnetic field is spatially homogeneous and

aligns along the longitudinal direction. The magnitude of the magnetic field in Aline is rather low (Max 0.1T), compared to the Tokamak (~T). The RF wave is injected into plasmas through a stainless steel disk antenna in the middle of the machine. The antenna disk has a radius of 4cm, and 1cm of thickness, see *Figure 1.15*. In the start-up stage, it also serves to generate the plasma. The details of the excitation will be given in Chapter 2. During the antenna operation, the current flowing on the antenna surface is very low, the electromagnetic field is excited by the voltages. This is called a capacitively coupled plasma. The typical plasma types supported in Aline are Argon (A=40) and Helium (A=4) with a density ranging from 10^{15} to 10^{17} m^{-3}. The RF amplifier has a maximum power of 1100W. The bandwidth covers from 10 KHz to 250 MHz.
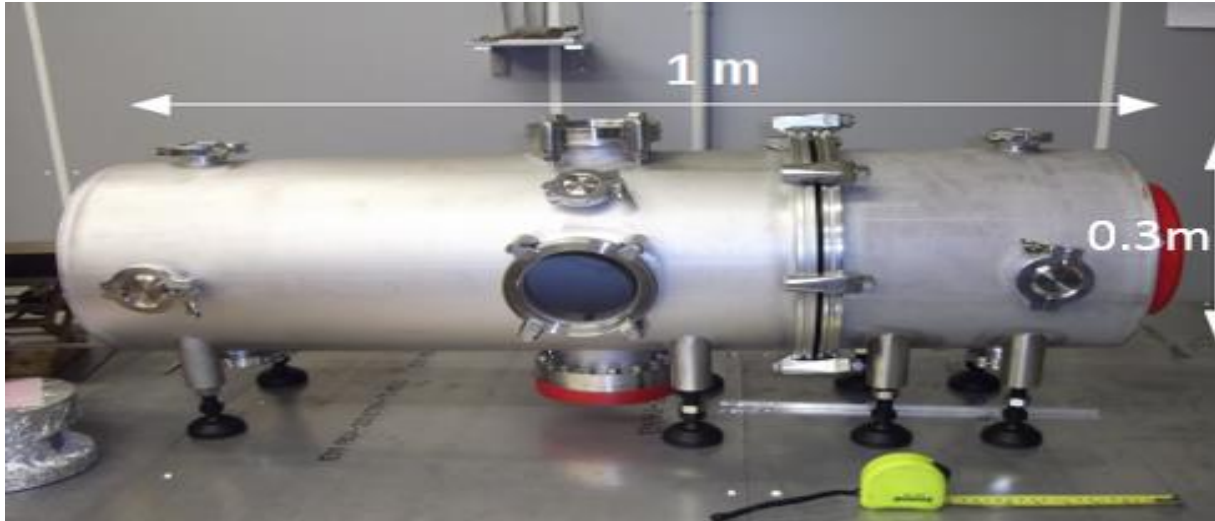
Figure 1.14. A photograph of Aline vacuum chamber without magnetic field coils, cite from [Faudot 2015]

Aline is instrumented with a RF self-compensated Langmuir probe [Sudit 1994]. The main body of the probe is 1.5m long and made by aluminum alloy. In front of the probe is a tungsten cylindrical tip (0.15mm in diameter and 10mm long). The whole probe is mounted on a 3D manipulator, which is able to move in a range of 50cm along the longitudinal direction (cylindrical axis aligned with the applied magnetic field) and 10cm along other two directions. The manipulator is driven by a 10 micrometer accuracy step motors operated by a Labview program. The probe can measure the potential map and other plasma parameters, i.e. temperature, density, etc.
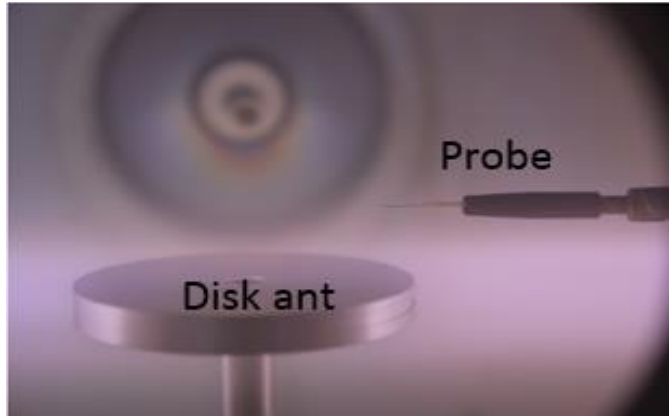
Figure 1.15. Disk antenna and Langmuir probe inside vacuum chamber, cite from [Faudot 2015]

References

[Beaumont 1988] B. Beaumont, G. Agarici, H. Kuus, "Tore Supra ICRH antenna array", Proc. 15th SOFT, page 503, 1988

[Chen 2016] F. F. Chen, "Introduction to plasma physics and controlled fusion", third edition, 2016, Springer International publishing Switzerland

 [Clayton 1983] D. D. Clayton, "Principles of stellar evolution and nucleosynthesis", 1983, the university of Chicago press, Chicago

[Colas 2006] L. Colas et al, "Key results of long pulse ICRH operation in Tore Supra", *Nuclear Fusion* **46**, S500-S513 (2006).

[Colas 2013] L. Colas et al, "RF-sheath patterns modification via novel Faraday screen and strap voltage imbalance on Tore Supra ion cyclotron antennae", *J. Nucl. Mater.* 438, S330-S333 (2013).

[Colas 2014] L. Colas et al, "Self-consistent modeling of radio-frequency sheaths: comparison with Tore Supra measurements and predictability for future machines", Proc. of 25th IAEA fusion energy conference, Saint Petersburg, Russia, October, 2014

[Crombé 2015] K Crombé et al, "Studies of RF sheaths and diagnostics on IShTAR", Proc. of the 21st Topical conference, 030006 (2015)

[Faudot 2015] E. Faudot, S. Devaux, J. Moritz, S. Heuraux, P. M. Cabrera, and F. Brochard, "A linear radio frequency plasma reactor for potential and current mapping in a magnetized plasma", *Rew. Sci. Inst.*, 86 :063502(2015)

[Gonich 2013] M. Goniche et.al, "Lower hybrid current drive at high density on Tore Supra", *Nuclear Fusion* **53**, 033010 (2013).

[Grad 1958] H. Grad and H. Rubin, "Hydromagnetic equilibria and force-free fields", *Proc. 2ⁿᵈ UN Conf. on the peaceful uses of atomic energy*, V31, Geneva: IAEA p.190

[Graham2012] M. Graham et.al, "Implementation of load resilient ion cyclotron resonant frequency (ICRF) systems to couple high levels of ICRF power to ELMy H-mode plasmas in JET", *Plasma Phys. Control. Fusion*, **54**(2012) 074011

[Hemswoth 2009] R. Hemsworth et al., "Status of the ITER heating neutral beam system", *Nuclear Fusion* **49**, 045006 (2009).

[Hoang 2009] G.T. Hoang et al, "A lower hybrid current drive system for ITER", *Nuclear Fusion* **49**, 075001 (2009).

[Jacquot 2014] J. Jacquot et al, "Radio-frequency sheaths physics: Experimental characterization on Tore Supra and related self-consistent modeling", *Phy. Plas*. 21, 061509 (2014)

[Kirschner 2009] A. Kirschner et al., "Estimations of erosion fluxes, material deposition and tritium retention in the divertor of ITER", *J. Nucl. Mat.,* **390-391,** 152 (2009).

[Kirschner 2015] A. Kirschner, "Erosion and Deposition mechanisms in fusion plasmas", Proc. 12ᵗʰ Carolus Magnus summer school on plasma and fusion energy physics, P218-232, 2015

[Kuus 1988] H. Kuus, G. Agarici, B. Beaumont, R. Brugnetti, "The ICRH system for Tore Supra", Proc. 15th SOFT, page 508, 1988.

[Landau 1946] L. Landau, "On the vibrations of the electronic plasma", *J. Phys*, **1**(1946)

[Lawson 1957] J. D. Lawson, "Some criteria for a power producing thermonuclear reactor", *Proc. Royal Phys. Society*, B2:7, 1957

[Linke 2015] J. Linke, "High heat flux performance of plasma facing materials and components under service conditions in future fusion reactors", Proc. 12th Carolus Magnus summer school on plasma and fusion energy physics, P260-269, 2015

[Lipschultz 1987] B. Lipschultz, "Review of MARFE Phenomena in Tokamaks", *J. Nucl. Mater.*,145-147, 15 (1987).

[Lu 2013] Theoretical analysis and numerical calculation of mode conversion efficiency of fast wave, *Acta Physica Sinica* 62(7) 2013 (In Chinese)

[McAdams 2014] McAdams et al, "Beyond ITER: Neutral beams for a demonstration fusion reactor (DEMO)", *Review of Scientific Instruments* **85**, 02B319 (2014).

[Meade 1974] D.M. Meade, "Effect of high-Z impurity on the ignition and Lawson conditions for a thermonuclear reactor", *Nuclear fusion* **14**, 289 (1974).

[Mendes 2010] A. Mendes, L. Colas, K. Vulliez, A. Ekedahl, A. Argouarch and D. Milanesio, " Reduction of RF-sheaths potentials by compensation or suppression of parallel RF currents on ICRF antennas", *Nuclear Fusion* 50, 025021 (2010)

[Nuehrenberg 1995] J. Nuehrenberg, W. Lotz, P. Merkel and T. Hayashi, "Overview on Wendelstein 7-X theory", Fusion technology, 27, 1995

[Owens 1985] T.L. Owens, F.W. Baity and D.J. Hoffman, "ICRF antenna and feedthrough development at the Oak Ridge National Laboratory", Proc. 6th Topical Conf. on RF Plasma Heating pp 95–8, 1985

[Peeters 2000] A.G. Peeters, "The bootstrap current and its consequences", *Plasma Phys. Control. Fusion* 42 B231 (2000)

[Perkins 1989] F. W. Perkins, "Radiofrequency sheaths and impurity generation by ICRF antennas", *Nuclear Fusion* 29, 583 (1989).

[Prater 2004] R. PRATER, "Heating and current drive by electron cyclotron waves", *Phys. Plasmas*, 11, 2349 (2004).

[Reiter 1991] D. REITER et al., "Helium Removal from Tokamaks", *Plasma Physics and Controlled Fusion* **33** 1579 (1991)

[Samm 2015] U. Samm, "Plasma-wall interactions in magnetically confined fusion plasmas", Proc. 12th Carolus Magnus summer school on plasma and fusion energy physics, P178-184, 2015

[Schuller] F. C. Schuller, "Disruptions in Tokamaks", *Plasma Phys. Control. Fusion*, 37, A135 (1995).

[Shafiee 2009] S. Shafiee and E. Topal, "When will fossil fuel reserves be diminished?", *Energy Policy*, **37** (2009) 181-189

[Shafranov 1966] V. D. Shafranov, "Plasma equilibrium in a magnetic field", *Review of plasma physics,* V2, New York: Consultants bureau, P. 103

[Stangeby 2000] P.C. Stangeby, "The Plasma Boundary of Magnetic Fusion Devices", Plasma Physics Series, IoP Publishing Ltd, Bristol, UK (2000).

[I. D. Sudit 1994] I. D. Sudit and F. F. Chen, "RF compensated probes for high-density discharges", *Plas. Sources Sci. Tech.* **3**(1994) 162-168

[Vulliez 2003] K. Vulliez, G. Bosia, G. Agarici, B. Beaumont, S. Bremond, P. Mollard and B. Cantone, "Tore supra ICRH antenna prototype for next step devices", *Fusion Engineering and Design*, 66-68 (2003) 531-535

[Vulliez 2008] K. Vulliez et.al, "Validation of the load-resilient ion cyclotron resonance frequency antenna concept on Tore Supra plasmas", *Nucl. Fusion* **48**(2008) 065007

Chapter 2   Theoretical basis of this thesis

This chapter introduces all the theoretical ingredients that are needed in order to understand this thesis work. First, we will derive the cold plasma dielectric tensor, which makes it possible to treat the plasma as a specific dielectric. Then we will look at the properties of waves that exist in the cold plasma under Ion Cyclotron Range of Frequencies (ICRF). Their dispersion relation, polarization and the theory of wave coupling are discussed. Then a short introduction on how to model the wave coupling numerically is made. The second part discusses the sheath physics. Some important sheath features under RF and DC regimes are presented, i.e. sheath capacitance and sheath rectification. Finally, an overview of the status of numerical codes on wave coupling and RF sheath before this thesis is given, followed by the motivation and outline of this thesis.

2.1   The physics of cold plasma waves under ion cyclotron range of frequencies

2.1.1   Dielectric tensor under cold plasma approximation

The basic equations describing the electromagnetic waves are the well-known Maxwell's equation [Jackson 1998]. Using Faraday's law and Ampere's law, one can derive the wave equation which is the governing equation of the RF waves. Assume the time-harmonic waves are oscillating as e^{iwt}, where w is the wave angular frequency. The wave equation reads,

$$\nabla \times \overset{=-1}{u_r} (\nabla \times \mathbf{E}) - k_0^2 (\overset{=}{\mathbf{1}} - \frac{i\overset{=}{\sigma}}{w\varepsilon_0})\mathbf{E} = -iwu_0\mathbf{J} \tag{2.1}$$

$\overset{=}{\bar{u}}_r$, $\overset{=}{\bar{\sigma}}$ are the relative permeability, relative permittivity and electric conductivity tensors of the material, i.e. plasma. k_0, ε_0 and u_0 are the wave number, permittivity and permeability in vacuum. In contrast to vacuum where relative permeability, relative permittivity and electric conductivity are all scalars, they are all tensors in plasma. The excitation is done by the external current **J** on the RHS of Eq. (2.1).

Even though the fusion plasma is hot, it has been proved that using a cold plasma approximation [Swanson 2003] could significantly simplify the problem while providing a fairly well description of the RF waves of our concern. Cold plasma means that all the particles have zero thermal energy of their own but could still move in response to the oscillating electric fields of the RF waves. One needs to consider the hot plasma effect only when describing the resonant heating in the regions near the wave-particle resonances (introduced in Chapter 1). Under the cold plasma approximation, the plasma dielectric tensor can be derived from the equation of motion. For a particle species s, it reads,

$$m_s(\frac{\partial \mathbf{v_s}}{\partial t} + (\mathbf{v_s} \cdot \nabla)\mathbf{v_s}) = q_s(\mathbf{E} + \mathbf{v_s} \times \mathbf{B}) \tag{2.2}$$

Where $\mathbf{v_s}$ is the fluid velocity. Please note Eq. (2.2) implicitly assumes that the temperature is zero. A full description considering thermal effect can be done through more complicated fluid description [Swanson 2003] or kinetic description [Brambilla 1998].

We further assume that $\mathbf{v_s}$ is small enough so that the second term on the LHS of Eq. (2.2) could be neglected. Doing this simplification also means the zero-order velocity of the particle flow has been neglected. Eq. (2.2) thus becomes linear. The particle current reads,

$$\mathbf{J} = \sum_s n_s q_s \mathbf{v_s} \tag{2.3}$$

Substitute Eq. (2.2) into Eq. (2.3) and add up all the particle species. After some algebra, the current density $\mathbf{J}$ becomes a linear function of $\mathbf{E}$. By comparing that function to Ohm's law, one immediately obtains the plasma conductivity tensor. The equivalent cold plasma dielectric tensor is a combination of relative permittivity and conductivity tensors. It can be expressed as [Stix 1992]

$$\mathbf{\varepsilon_r} = \overline{\overline{\mathbf{1}}} - \frac{i\overline{\overline{\sigma}}}{w\varepsilon_0} = \begin{bmatrix} \varepsilon_{//} & 0 & 0 \\ 0 & \varepsilon_\perp & i\varepsilon_\times \\ 0 & -i\varepsilon_x & \varepsilon_\perp \end{bmatrix} \begin{matrix} \varphi \\ r \\ \varsigma \end{matrix} \tag{2.4}$$

Where φ, r and ς stand for the Tokamak coordinates defined in Chapter 1. The full derivation of the cold plasma dielectric tensor can be found in [Swanson 2003]. The Tokamak coordinates defined in chapter 1 are used here. Please note in this thesis we use engineering convention, and assume at this moment $\mathbf{B_0}$ is along the toroidal (φ) direction. The tensor we obtained is thus the complex conjugate of the one in [Swanson 2003]. Since the cold plasma dielectric tensor (2.4) is essentially a matrix, hereafter we will use the notation $\mathbf{\varepsilon_r}$. $\varepsilon_{//}$, $\varepsilon_\perp$ and $\varepsilon_\times$ are Stix parameters defined in [Stix 1992]. They are functions of wave angular frequency, plasma frequency and cyclotron frequency,

$$\varepsilon_{//} = 1 - \sum_s \frac{w_{ps}^2}{w^2} \tag{2.5}$$

$$\varepsilon_\perp = \frac{1}{2}(\varepsilon_R + \varepsilon_L) \tag{2.6}$$

$$\varepsilon_\times = \frac{1}{2}(\varepsilon_R - \varepsilon_L) \tag{2.7}$$

$$\varepsilon_R = 1 - \sum_s \frac{w_{ps}^2}{w(w + w_{cs})} \tag{2.8}$$

$$\varepsilon_L = 1 - \sum_s \frac{w_{ps}^2}{w(w - w_{cs})} \tag{2.9}$$

Where w_{ps} and w_{cs} are the plasma frequency and cyclotron frequency defined in chapter 1. The dielectric tensor Eq. (2.4) is invariant under rotations along the magnetic axis, i.e. φ direction. This is called the gyrotropic property of the magnetized plasma. The frequency-dependent property of the cold plasma dielectric tensor indicates that the cold plasma is a time-dispersive material. The waves inside the plasma should be described by the dispersion relation, which gives plane wave vector $\mathbf{k}$ as a function of w.

Eq. (2.4) is the case when the $\mathbf{B_0}$ aligns wth the φ-axis. In a Tokamak edge, $\mathbf{B_0}$ is usually tilted w.r.t the toroidal direction. Now let x be the toroidal direction (φ), y the radial direction (r) and z the poloidal direction (ς). This coordinate is often used in the later simulations, and it corresponds to the equatorial plane in the real 3D Tokamak geometry. We consider a simple case where $\mathbf{B_0}$ has a tilt angle θ at toroidal/poloidal plane, see *Figure 2.1*. This is not the most general case, but it can ease the code development mentioned in the later chapters of this thesis. So now the toroidal direction is no more equivalent to the parallel direction. The dielectric tensor in Eq. (2.4) is valid for the coordinate system shown with dashed lines in *Figure 2.1*. Now it should be rotated to fit the black coordinates.
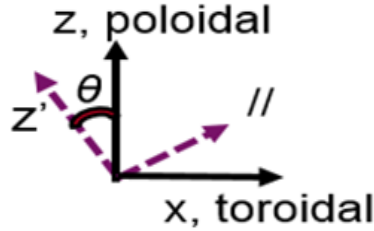
Figure 2.1. Diagram of tilted magnetic field

After conducting a rotational transform to Eq. (2.4), the cold plasma dielectric tensor becomes,

$$\boldsymbol{\varepsilon}_\mathbf{r}(\theta) = \begin{pmatrix} \varepsilon_\perp \sin^2\theta + \varepsilon_{//}\cos^2\theta & i\varepsilon_\times \sin\theta & -\varepsilon_\perp \sin\theta\cos\theta + \varepsilon_{//}\sin\theta\cos\theta \\ -i\varepsilon_\times \sin\theta & \varepsilon_\perp & i\varepsilon_\times \cos\theta \\ -\varepsilon_\perp \sin\theta\cos\theta + \varepsilon_{//}\sin\theta\cos\theta & -i\varepsilon_\times \cos\theta & \varepsilon_\perp \cos^2\theta + \varepsilon_{//}\sin^2\theta \end{pmatrix} \begin{matrix} x \\ y \\ z \end{matrix} \quad (2.10)$$

Throughout this thesis, we will frequently use this form of the cold plasma dielectric tensor. For simplicity, we define hereby the following notations,

$$\varepsilon_{11} = \varepsilon_\perp \sin^2\theta + \varepsilon_{//}\cos^2\theta; \ \varepsilon_{12} = i\varepsilon_\times \sin\theta; \ \varepsilon_{13} = -\varepsilon_\perp \sin\theta\cos\theta + \varepsilon_{//}\sin\theta\cos\theta$$
$$\varepsilon_{21} = -i\varepsilon_\times \sin\theta; \ \varepsilon_{22} = \varepsilon_\perp; \ \varepsilon_{23} = i\varepsilon_\times \cos\theta \quad (2.11)$$
$$\varepsilon_{31} = -\varepsilon_\perp \sin\theta\cos\theta + \varepsilon_{//}\sin\theta\cos\theta; \ \varepsilon_{32} = -i\varepsilon_\times \cos\theta; \ \varepsilon_{33} = \varepsilon_\perp \cos^2\theta + \varepsilon_{//}\sin^2\theta$$

For simplicity, unless being explicitly pointed out, the rest of the theoretical derivations concerning the wave properties in this section will only consider the non-tilted $\mathbf{B_0}$. Given the dispersion relation, the polarization are the intrinsic properties of the plane waves, they should be independent on the coordinate rotation.

2.1.2   Dispersion relations of ICRF waves under cold plasma approximation

In a homogenous, isotropic and infinite extended medium, the solution for Eq. (2.1) is a plane wave oscillating as $\exp(iwt - i\mathbf{k}\cdot\mathbf{r})$. A real fusion plasma is by no means such an ideal medium. Firstly, the plasma density and temperatures are varying spatially and thus the plasma is inhomogeneous. Secondly, due to the presence of the magnetic field, the magnetized plasma is gyrotropic (justified at the end of last subsection). Thirdly, it is bounded by the walls.

However, with an infinite domain and homogeneous (in all dimensions) plasma, it is much easier to derive the dispersion relations for the cold plasma waves. The wave behaviors described by those

dispersion relations are preserved in a realistic fusion plasma. Therefore for the dispersion studies, we assume that the plasma is homogeneous and boundless. We also restrict ourselves to the plane wave solutions. In principle, all the waves can be decomposed by a series of plane waves.

By assuming that the plasma is homogeneous, all the spectral components are independent. One can replace ∇ in Eq. (2.1) by $-i\mathbf{k}$ (engineering convention again). The wave equation under a non-tilted $\mathbf{B_0}$ becomes,

$$\mathbf{k} \times (\mathbf{k} \times \mathbf{E}) + k_0^2 \boldsymbol{\varepsilon_r} \cdot \mathbf{E} = 0 \tag{2.12}$$

It is convenient to express Eq. (2.12) by a non-dimensional vector $\mathbf{n}$, whose magnitude is the refractive index

$$\mathbf{n} = \frac{\mathbf{k}}{k_0} \tag{2.13}$$

It then becomes

$$\mathbf{n} \times (\mathbf{n} \times \mathbf{E}) + k_0^2 \boldsymbol{\varepsilon_r} \cdot \mathbf{E} = 0 \tag{2.14}$$

We assume the poloidal direction (here the z direction) has no derivative, i.e. $n_z=0$. Making use of Eq. (2.4), one can express Eq. (2.14) in a matrix form

$$\begin{bmatrix} \varepsilon_{//} - n_\perp^2 & n_\perp n_{//} & 0 \\ n_\perp n_{//} & \varepsilon_\perp - n_{//}^2 & i\varepsilon_\times \\ 0 & -i\varepsilon_\times & \varepsilon_\perp - n_{//}^2 - n_\perp^2 \end{bmatrix} \begin{bmatrix} E_x \\ E_y \\ E_z \end{bmatrix} = 0 \tag{2.15}$$

Since $\mathbf{B_0}$ is aligned with the toroidal direction, $//$ is equal to the toroidal direction and $\perp$ is the composition of the radial and the poloidal directions. To avoid nontrivial solution, the determinant in Eq. (2.15) must vanish. One thus obtains a fourth-order equation for $n_\perp$,

$$\varepsilon_\perp n_\perp^4 - [(\varepsilon_\perp - n_{//}^2)(\varepsilon_\perp + \varepsilon_{//}) - \varepsilon_\times^2] n_\perp^2 + \varepsilon_{//}[(\varepsilon_\perp - n_{//}^2)^2 - \varepsilon_\times^2] = 0 \tag{2.16}$$

Although Eq. (2.16) is derived under non-tilted $\mathbf{B_0}$, it should be invariant under tilted $\mathbf{B_0}$.

2.1.3   Decoupled dispersion relations for the fast wave and the slow wave

The Eq. (2.16) has two $n_\perp^2$ roots as functions of $n_{//}^2$. Assuming $n_{//}$ is fixed, the dispersion relation provides a picture of how the wave property evolves with the plasma density, magnetic field, etc. In a Tokamak plasma, under ion cyclotron range of frequencies, the two roots can be decoupled (although not always, see subsection 2.1.5) to the fast wave mode and the slow wave mode. The dispersion relation for each of them and their respective plasma conditions are

$$fast\ wave:\ n_{\perp F}^2 = \frac{(\varepsilon_R - n_{//}^2)(\varepsilon_L - n_{//}^2)}{(\varepsilon_\perp - n_{//}^2)}\ \text{with}\,|\,\varepsilon_{//}\,| \geq n_\perp^2, |\,\varepsilon_\perp\,|, |\,\varepsilon_\times\,|, n_{//}^2 \tag{2.17}$$

$$slow\ wave: n_{\perp S}^2 = \varepsilon_{//}(1-\frac{n_{//}^2}{\varepsilon_{\perp}})\ \ with\ n_{\perp}^2 \sim |\varepsilon_{//}| \ge |\varepsilon_{\perp}|,|\varepsilon_{\times}|,n_{//}^2 \tag{2.18}$$

Where the subscript *F* represents the fast wave; *S* represents the slow wave. Knowing the dispersion relation, the wavelength of the waves can be immediately computed. Under a typical Tokamak plasma condition (i.e. $n_e = 1\times10^{19} m^{-3}, \varepsilon_{//} = -2.5\times10^5, \varepsilon_{\perp} = -222$), the slow wave is almost evanescent everywhere in the Tokamak, thus it is convenient to define an evanescence length. At the edge plasma, the second term on the LHS of Eq. (2.18) can usually be neglected. It thus yields to $n_{\perp s} = \sqrt{\varepsilon_{//}} \approx \frac{w_{pe}}{w} i$. The slow wave evanescence length corresponds to the e-fold decay length,

$$l_{\perp s} = \frac{1}{|k_{\perp s}|} = \frac{c}{w|n_{\perp s}|} \approx \frac{c}{w_{pe}} \tag{2.19}$$

In the wave physics, two physical quantities are often used to describe the speed of wave propagation. The phase velocity v_p describes the propagation of the wave front, while the group velocity $\mathbf{v_g}$ indicates the speed of the energy flow. They are defined as

$$v_p = \frac{w}{k} \tag{2.20}$$

$$\mathbf{v_g} = \frac{\partial w}{\partial \mathbf{k}} \tag{2.21}$$

In which $k = |\mathbf{k}|$ is the wave number. It should be noted that although the phase velocity has a direction described by a wave vector **k**, it is not a vector because it does not follow the cosine law [Booker 1984]. The names "fast wave" and "slow wave" come from the fact that the slow wave usually has a larger wave number and smaller phase velocity than the fast wave. A wave is called forward (backward) wave if its phase velocity points the same (opposite) direction as its group velocity. The fast wave is typically a forward wave, while the slow wave is often a backward wave.

The concept of the fast wave and slow wave are initially used to describe the waves in ICRF domain a Tokamaks. For linear machines, as Aline, there are two waves equivalent to the fast wave and the slow wave. They are called differently as helicon wave and lower hybrid wave, respectively. The dispersion relations of them are,

$$Helicon\ wave\ (fast\ wave): w = \frac{\mathbf{k}^2 c^2 (w_{ce}cos\alpha - w)}{w_{pe}^2} \tag{2.22}$$

With ($\alpha \ne 90^0$, $w_{ci} \le w \le w_{ce} \ll w_{pe}$) , α is the angle between wave vector **k** and **B₀**.

$$Lower\ Hybrid\ wave\ (slow\ wave): k_{\perp}^2 = \frac{k_{//}^2 w_{pe}^2 w_{ce}^2}{(w_{pe}^2 + w_{ce}^2)(w^2 - w_{LH}^2)} \tag{2.23}$$

With ($\varepsilon_{\perp} \approx 0$, $w_{ci} \le w \le w_{ce}, w_{pe}$), $w_{LH}^2 = w_{ce}w_{ci}/(1+w_{ce}^2/w_{pe}^2)$

Be aware that Eq. (2.22) excludes the case where the phase velocity is perpendicular to **B₀**, i.e. $\alpha = 90^0$. In that case, the wave is named as ordinary wave Eq. (2.24) and extraordinary wave Eq. (2.25)

$$n^2 = P \tag{2.24}$$

$$n^2 = RL/S = \frac{S^2 - D^2}{S} \tag{2.25}$$

Chen [Chen 2016] gives a simplified introduction of these waves. More elaborate descriptions can be found in [Swanson 2003][Chabert 2011].

2.1.4   Wave polarizations

The wave polarization can be determined from Eq. (2.15). For the fast wave, since $|\varepsilon_{//}| \geq n_\perp^2, |\varepsilon_\perp|, |\varepsilon_\times|, n_{//}^2$, it has a relatively small parallel electric field component $E_{//}$. The main electric components of the fast wave are those perpendicular to **B₀**. Some literatures often call the fast wave as a transversal electric (TE) mode. Here one should note that the polarization is defined, with respect to the direction of **B₀**, instead of the direction of wave propagation. The latter convention is often used in the RF communication.

If we now neglect the parallel electric field component, the matrix Eq.(2.15) can be reduced to 2×2,

$$\begin{bmatrix} \varepsilon_\perp - n_{//}^2 & i\varepsilon_\times \\ -i\varepsilon_\times & \varepsilon_\perp - n^2 \end{bmatrix} \begin{bmatrix} E_y \\ E_z \end{bmatrix} = 0 \tag{2.26}$$

It yields to the fast wave polarization

$$\frac{E_z}{E_y} = \frac{i\varepsilon_\times}{\varepsilon_\perp - n^2} \tag{2.27}$$

One can further computer the ratio of the left-hand to the right-hand components. In case the plasma only has one ion species,

$$|\frac{E_y + iE_z}{E_y - iE_z}| \approx |\frac{w - w_{ci}}{w + w_{ci}}| \tag{2.28}$$

The left-hand component vanishes when $w \approx w_{ci}$. Note that the ion cyclotron motion is left-handed. That explains why the fast wave usually cannot be used as a heating wave at the fundamental resonance in case of single ion species.

For the slow wave, since $n_\perp^2 \sim |\varepsilon_{//}| \geq |\varepsilon_\perp|, |\varepsilon_\times|, n_{//}^2$, it has a relative small poloidal electric field component, E_z. The wave magnetic field component in toroidal direction is zero. So it is approximately a transversal magnetic (TM) mode.

Similarly, under the slow wave condition, the matrix Eq.(2.15) can be reduced to

$$\begin{bmatrix} \varepsilon_{//} - n_\perp^2 & n_\perp n_{//} \\ n_\perp n_{//} & \varepsilon_\perp - n_{//}^2 \end{bmatrix} \begin{bmatrix} E_x \\ E_y \end{bmatrix} = 0 \tag{2.29}$$

It's worthwhile to mention that from Eq. (2.26) and Eq. (2.29), one can immediately obtain the dispersion relations Eq. (2.17) and Eq. (2.18). Using the second row of Eq. (2.29), one gets the Slow wave polarization,

$$\frac{E_y}{E_x} = \frac{n_\perp n_{//}}{n_{//}^2 - \varepsilon_\perp} \tag{2.30}$$

2.1.5   Cut-off and resonance

From this point, we go back to the inhomogeneous plasma, and make a simplification that the inhomogeneity is only present in the radial direction. In the dispersion relation Eq. (2.17) and Eq.(2.18), there are two limiting case where the refractive index $n_\perp^2 \to 0$ and $n_\perp^2 \to \infty$. Here $\perp$ is equal to the radial direction. When the radial refractive index goes to zero, the wave stops propagating in the radial direction. This case is called cut-off. On the contrary, if the radial refractive index goes to infinity, it is called as resonance. In Eq. (2.17) and Eq. (2.18), the cut-off and resonance are just layers. In real fusion plasma, due to the thermal effects, they have a finite width. Waves are being reflected at the cut-off. At the magnetized plasma edge, the R cut-off layer of the fast wave plays an important role in RF wave coupling. Under non-tilted **B₀**, it is defined as

$$n_{//}^2 = \varepsilon_R \tag{2.31}$$
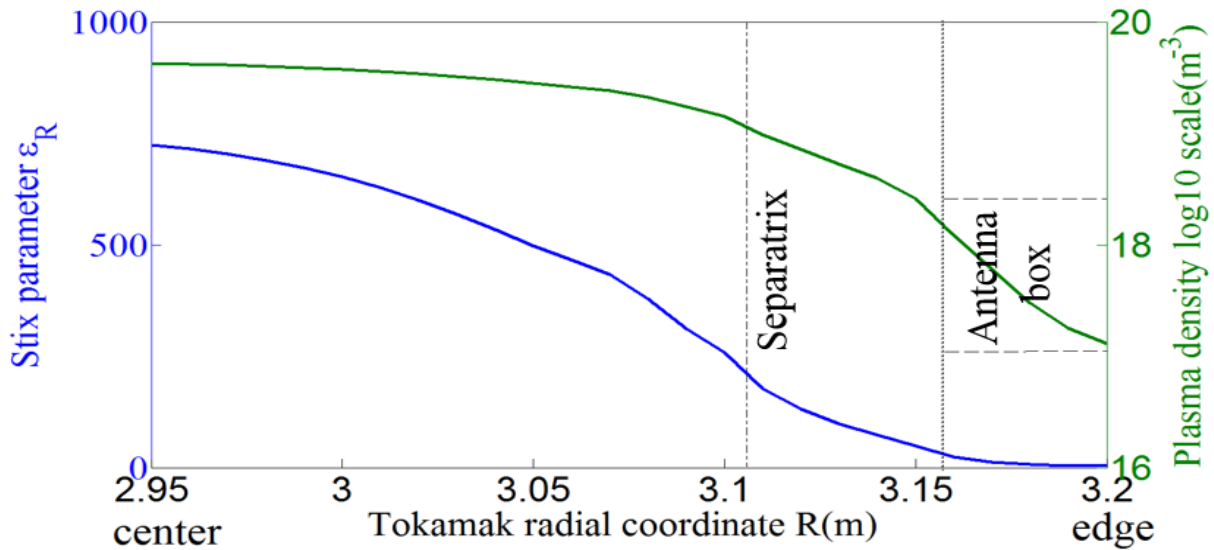
Figure 2.2. Evolution of Stix parameter ε_R and plasma density profile from Tore Supra shot 40574 along the radial distance to the Tokamak center. Magnetic tilt angle $\theta = 0°$ and Tore Supra parameters are used, $n_x=9.14$, $f=w/2\pi=48MHz$, $B_0(R_0=2.4)=3.1T$, full Deterium plasma

The Stix parameter ε_R defined in Eq.(2.8) decreases with the density, or the distance from the center plasma, shown in *Figure 2.2*. The locations of the separatrix and antenna box are also shown in the figure. Thus from Eq. (2.31), one can see with a lower $n_{//}$, the R cutoff layer shifts towards the edge.

In case of a tilted magnetic field, the parallel and perpendicular refractive index can be expressed as

$$
\begin{aligned}
n_\perp^2 &= n_{z'}^2 + n_{y'}^2 = n_y^2 + (n_z \cos\theta - n_x \sin\theta)^2 \\
n_{//}^2 &= (n_x \cos\theta + n_z \sin\theta)^2
\end{aligned}
\tag{2.32}
$$

Insert the above two equations into Eq. (2.17). In case of a 2D geometry, neglecting the poloidal derivative, i.e. n_z=0, finally one obtains

$$
n_y^2 + n_x^2 \sin^2\theta = \frac{(n_x^2 \cos^2\theta - \varepsilon_R)(n_x^2 \cos^2\theta - \varepsilon_L)}{\varepsilon_\perp - n_x^2 \cos^2\theta}
\tag{2.33}
$$

Using the definition of R-cutoff layer, n_y=0, yields to

$$
n_x^2 \sin^2\theta = \frac{(n_x^2 \cos^2\theta - \varepsilon_R)(n_x^2 \cos^2\theta - \varepsilon_L)}{\varepsilon_\perp - n_x^2 \cos^2\theta}
\tag{2.34}
$$

Note Eq. (2.34) falls back to (2.31) in case of $\theta = 0°$.

Figure 2.3 shows the R cutoff density decreases with the increasing tilt angle. This means that the R cutoff layer shifts towards the edge under a higher tilt angle, as its behavior under smaller $n_{//}$.
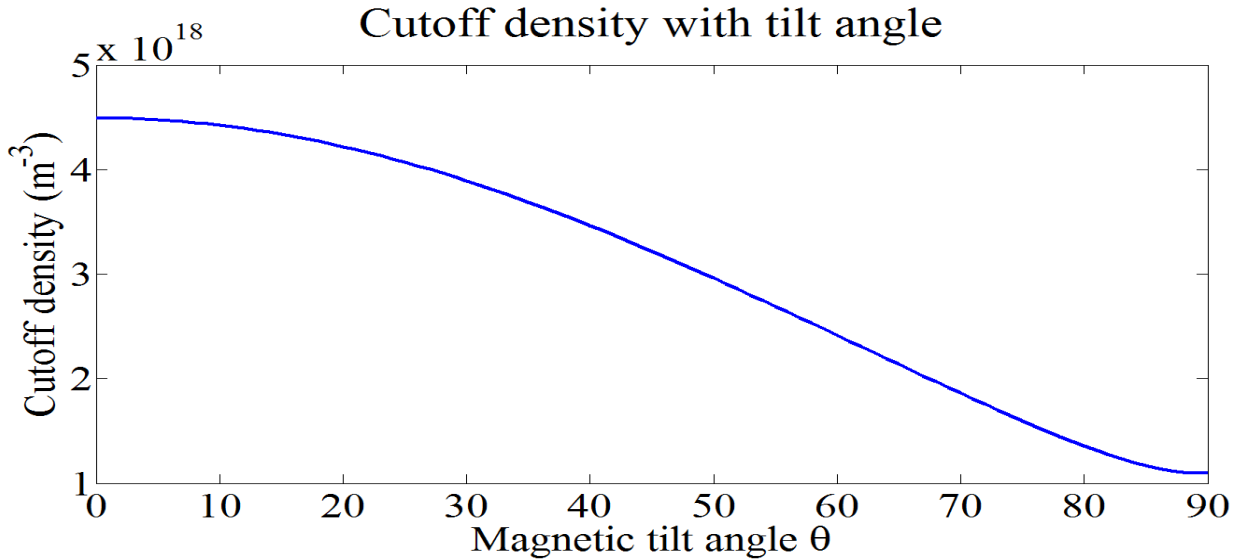
Figure 2.3. Fast wave cutoff density w.r.t the magnetic tilt angle. The same Tore Supra parameters are used as Figure 2.2

On the contrary, Waves are absorbed or being mode-converted at the resonance. For the slow wave, the lower hybrid resonance is defined as

$$\varepsilon_\perp = 0 \qquad (2.35)$$

Please note that the singularity of the dispersion relation Eq. (2.18) occurring at the resonance layer is essentially due to the simplification of the cold plasma approximation. The singularity vanishes when thermal effects are included. Near the resonance, the decoupled dispersion relations of the fast wave Eq. (2.17) and the slow wave Eq. (2.18) are not valid any more. Instead, one should use the fully coupled roots computed directly from Eq.(2.16). The fully coupled roots are [Bellan 1994],

$$n_\perp^2 = \frac{(\varepsilon_\perp - n_{//}^2)(\varepsilon_\perp + \varepsilon_{//}) - \varepsilon_\times^2 \pm \sqrt{[(\varepsilon_\perp - n_{//}^2)(\varepsilon_\perp - \varepsilon_{//}) - \varepsilon_\times^2]^2 + 4\varepsilon_{//}\varepsilon_\times^2 n_{//}^2}}{2\varepsilon_\perp} \qquad (2.36)$$

Where the small root corresponds to the fast wave, the big root is the slow wave. The two decoupled roots as well as the two fully coupled roots w.r.t a range of typical Tokamak densities are drawn in *Figure 2.4*. From this figure, the fast wave is evanescent between the antenna and the R cut-off layer. The length of this layer affects significantly the power coupling to the plasma, details will be given in the next section. On the other hand, the slow wave, almost evanescent everywhere in Tokamak plasma, is however propagating below the Lower hybrid resonance. From its dispersion relation Eq. (2.18), the slow wave naturally has a short-wavelength since $\varepsilon_{//} \geq \varepsilon_\perp$. This feature will cause the numerical modeling of this wave being problematic across and below the lower hybrid resonance.
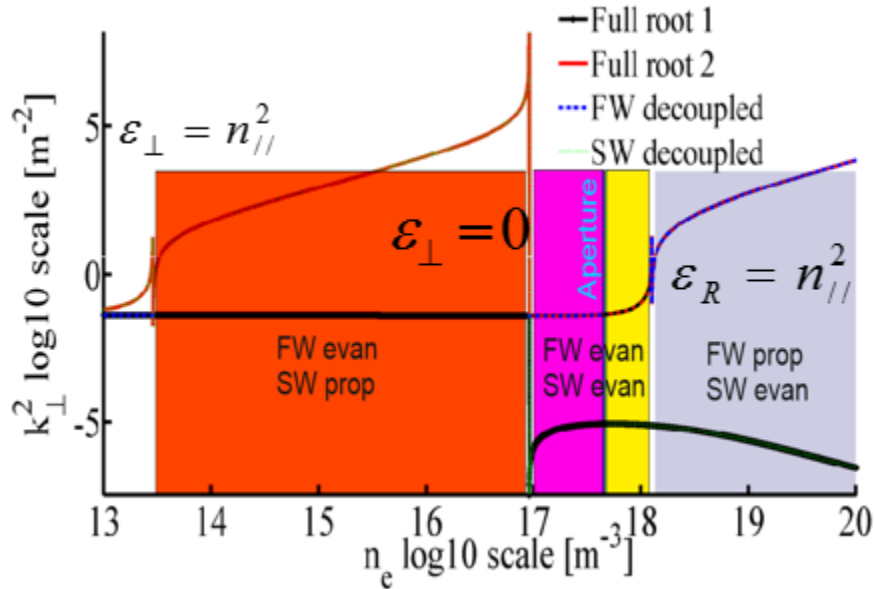
Figure 2.4. A drawing of the dispersion relations of the fast wave and the slow wave in a range of plasma densities and the propagation/evanescence regions for these two waves. Following parameters are used, frequency 48MHz, magnetic field B_0=2.32T at n_e=10^{18}m^{-3}, parallel wave number $k_{//}$=5 m^{-1}, Deuterium plasma

2.1.6   Theory of the fast wave coupling

(a) Wave excitation by phased array straps

We have introduced in Chapter 1 that the ICRH wave is launched by phased array straps. The current flows on the surface of the strap to excite the large poloidal electric field needed by the fast wave. *Figure 2.5* draws the front view of a simplified two-strap array. The two straps are located symmetrically w.r.t. the x=0 axis. The toroidal distance between the two centers of the straps is characterized as e. Each strap has a toroidal width of D. The poloidal length of the strap is L_{strap}. The current density J_0 is assumed to be uniformly distributed on the strap surface. $\varphi 1$ and $\varphi 2$ are the current phasing on the left and right straps, respectively. In the ToreSupra classical antenna, L_{strap}=0.53m, D=0.109m, e=0.224m [Beaumont 1988]. For simplicity, we assume the strap has no radial thickness and infinite poloidal length $L_{strap} \rightarrow \infty$.
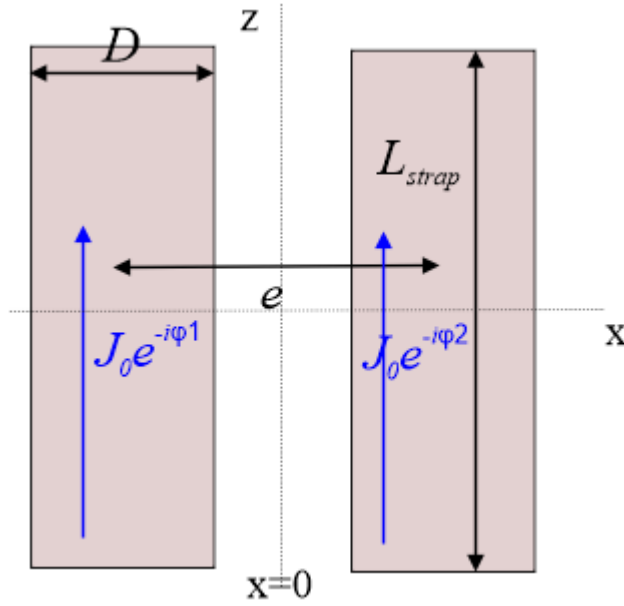
Figure 2.5. A sketch of phased array straps

The dispersion relations solved in section 2.1.3 generally consider a fixed $n_{//}$. It is determined by the antenna structure, current phasing, etc. From the current spectrum, one can have an idea of the values of $n_{//}$. By conducting Fourier transform of the currents on two straps, one can obtain the current spectrum of this two-strap array

$$J_z(k_{//}) = J_0 e^{-i\varphi 1} \int_{-D/2-e/2}^{D/2-e/2} e^{-ik_{//}x}dx + J_0 e^{-i\varphi 2} \int_{e/2-D/2}^{D/2+e/2} e^{-ik_{//}x}dx \tag{2.37}$$

Let $\Delta\varphi = \varphi 2 - \varphi 1$, after some algebra, one gets

$$J_z(k_{//}) = J_0 \frac{2\sin(k_{//}D/2)}{k_{//}/2} e^{-i(\varphi 1+\Delta\varphi/2)} \cos(\frac{k_{//}e}{2} + \frac{\Delta\varphi}{2}) \tag{2.38}$$

A plot of the current spectrum with all frequently used phasing (Monopole phasing [0 0]; Dipole phasing [0 π]; Current drive [0 ±π/2]) is shown in *Figure 2.6*. We used the Tore Supra antenna geometrical parameters. The abscissae $n_{//} = \dfrac{k_{//}c}{w}$ is the parallel refractive index, where f=48×10^6 MHz is the typical operation frequency of Tore Supra antenna.

In monopole phasing, the main lobe of the current spectrum is located at $n_{//}$=0. In reality, dipole phasing is often used as the main heating phasing, which had the main lobe at $n_{//}$=13 for Tore Supra, see the red curve in *Figure 2.6*. This is because the wave absorption by plasma increases with the $n_{//}$ [Lerche 2010], also because more issues related to wave/SOL interaction are usually observed when using monopole phasing. It's worthwhile to mention that this spectrum will shift slightly inside the plasma, see subsection (c).
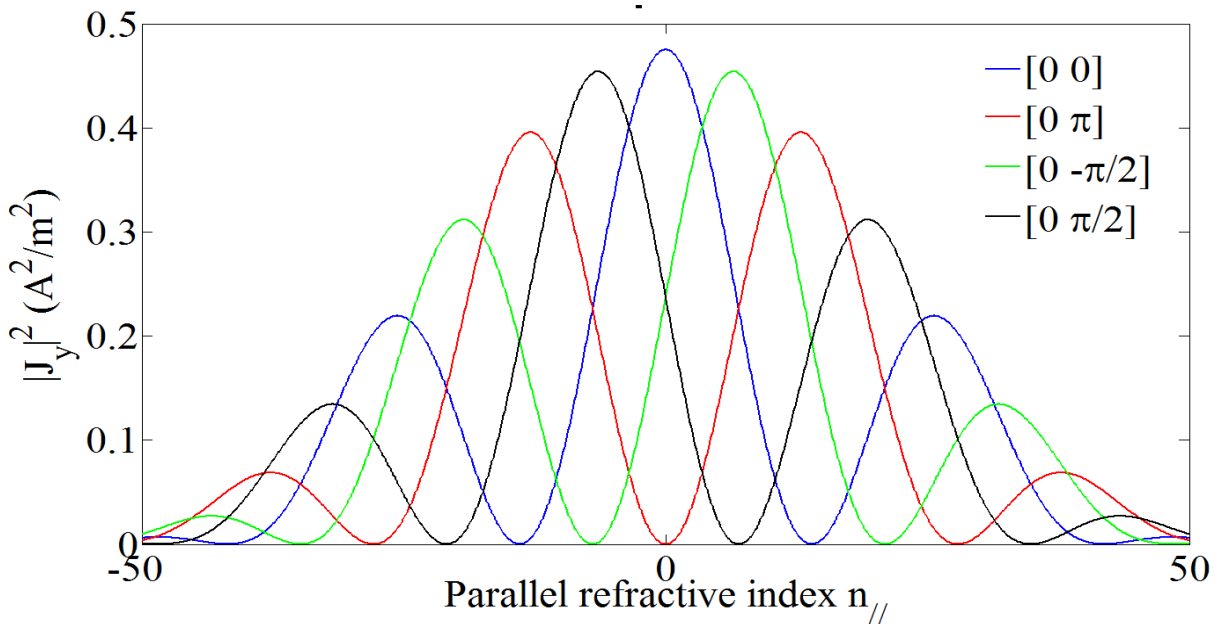
Figure 2.6. Current spectrum with different current phasings. Tore Supra classical antenna parameters are used, D=0.109m, e=0.224m, wave frequency f=w/2π=48×10^{6}Hz, J$_0$=10 A/m

(b) Coupling resistance

Any auxiliary heating system is designed for delivering as much as possible the heating power to the plasma. Wave coupling quantifies with *I*=1A current along 1m of straps, how much power can be transferred to the plasma [Clairet 2004][Goniche 2003].

$$P_t = \frac{1}{2} R_c L_{strap} I^2 \tag{2.39}$$

Where P_t is the power coupled to the plasma, R_c the coupling resistance, expressed in Ω/m. A detailed derivation of Eq. (2.39) can be found in the early work by Bhatnagar [Bhatnagar 1981].

In order to have an approximate mathematic expression for the coupling resistance R_c, we consider a simple three-wave coupling model. The model is shown in *Figure 2.7*. It adopts the simplified Tokamak geometry, where the x is the toroidal direction, y is the radial direction. The poloidal variation and

curvature effects have been ignored. The wave is excited at the antenna with a poloidal electric field whose amplitude E_0 is known. It firstly passes an evanescence region which has a length of y_0. The wave number $k_{\perp 1}$ in this region is thus a pure imaginary number. A part of the wave energy is reflected and the rest is tunneling to the plasma region where the wave becomes propagative. The amplitudes of the poloidal electric fields of the incident wave, the reflected wave and the transmitted wave are marked as E_i, E_R and E_t, respectively. Imposing continuity conditions for the poloidal electric field and the toroidal magnetic field across y=0, and a boundary condition at y=-y₀, the total power transmitted to the plasma can be calculated.
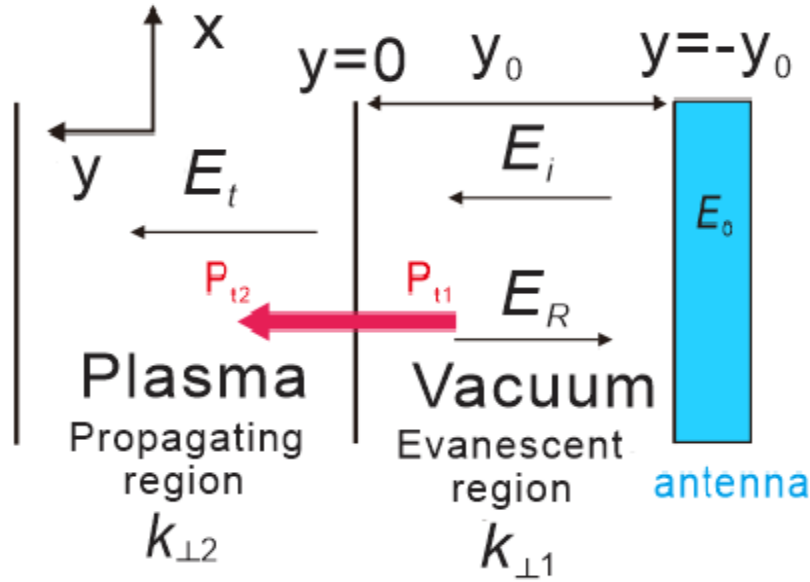
Figure 2.7. A simple three-wave coupling model

$$P_{t1} = P_{t2} = \frac{E_0 E_0^*}{\mu_0 w} \frac{4k_{\perp 2} |k_{\perp 1}|^2}{|k_{\perp 1}|^2 + k_{\perp 2}^2} \exp(-2|k_{\perp 1}|y_0), \quad k_{\perp 1} = i|k_{\perp 1}| \tag{2.40}$$

Where the sign * means the complex conjugate. Comparing Eq. (2.40) and Eq. (2.39) leads to

$$R_c \propto \exp(-2|k_{\perp 1}|y_0) \tag{2.41}$$

With this simple model, we can explain that the power coupling decreases exponentially with the increasing of the length of the evanescence region. Some more elaborate explanations and experimental evidences about the dependence of the power coupling on the evanescence length can be found in [Bilato 2005][Messiaen 2011][Clairet 2004][Mayberry 1990]

(c) Toroidal power spectrum

By Parseval's theorem, the coupled power evaluated in the real space should equal to its counterpart in the frequency space. Thus one could cross-check the simulation results carried out in space domain by analyzing the power in spectral domain. The radial Poynting vector $S_y(x)$ across a 1D toroidal interface (i.e. the leftmost boundary in *Figure 2.7*) reads,

$$S_y(x) = \frac{1}{2} Re(H_x^*(x)E_z(x) - E_x(x)H_z^*(x)) \qquad (2.42)$$

We perform an inverse Fourier transform along the toroidal direction for all the magnetic and electric components contained in Eq. (2.42). The power spectrum comes from integration of S_y from $x \rightarrow -\infty$ to $x \rightarrow +\infty$

$$\int_{-\infty}^{+\infty} S_y(x)dx = \frac{1}{2} Re \left[\int_{-\infty}^{+\infty} dx \int_{-\infty}^{+\infty} dk_x \int_{-\infty}^{+\infty} dk_x' [H_x^*(k_x)E_z(k_x') - H_z^*(k_x)E_x(k_x')] \exp(i k_x x - i k_x' x) \right] \qquad (2.43)$$

Then using the property of Dirac distribution

$$\int_{-\infty}^{+\infty} \exp(ikx)dx = 2\pi\delta(k) \qquad (2.44)$$

And substituting Eq. (2.44) into Eq. (2.43) immediately yields to,

$$\int_{-\infty}^{+\infty} S_y(x)dx = \pi Re \int_{-\infty}^{+\infty} H_x^*(k_x)E_z(k_x)dk_x - \pi Re \int_{-\infty}^{+\infty} E_x(k_x)H_z^*(k_x)dk_x \qquad (2.45)$$

Where k_x is the toroidal wave number. In reality, the length of interface cannot goes to infinity, but it can still be approximated by extending the interface and imposing periodic boundary conditions at its two extremities.

Figure 2.8. Toroidal power spectrum, $f=w/2\pi=48\times10^6$Hz, $n_x = \dfrac{k_x c}{w}$

A graph of the power spectrum of the monopole phasing and dipole phasing is shown in *Figure 2.8*. The electromagnetic fields are taken from the plasma stands radially 50cm away from the straps. The

monopole phasing has the main lobe at n_x=0, whereas the main lobe in dipole phasing are located at $|n_x|$=9. Compared to the current spectrum, which has a main lobe at n_x=13, the power spectrum has a phase shifting towards n_x =0. This is because u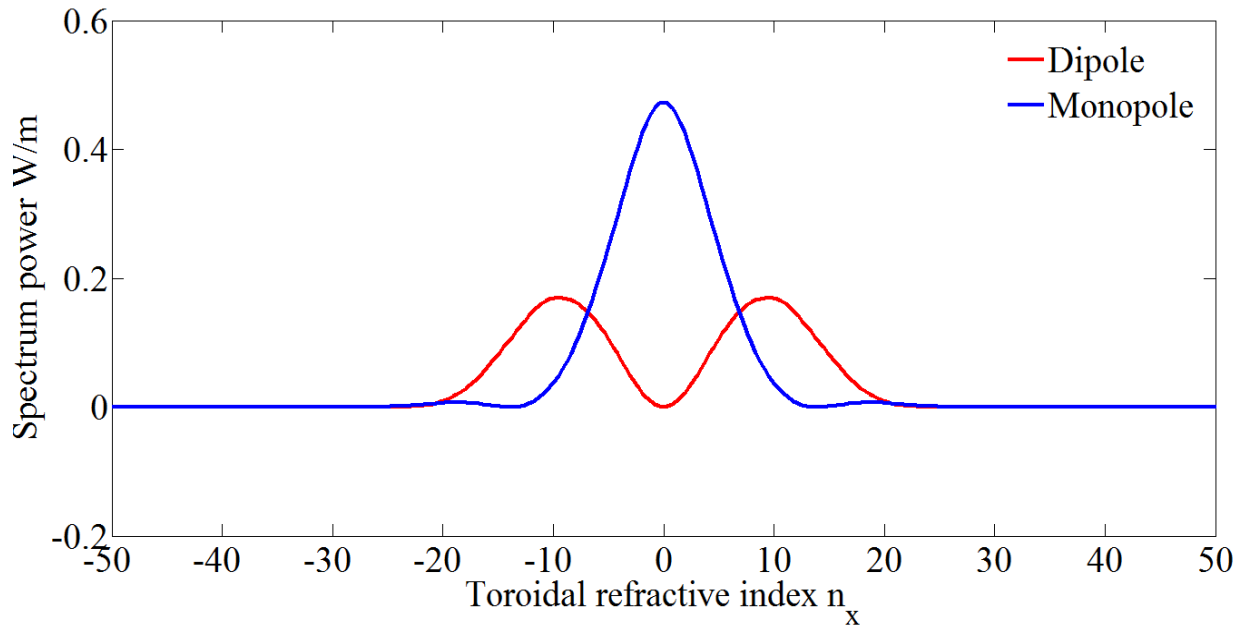nder high n_x, the R-cutoff layer shifts towards the plasma center. The fast wave evanescence length is accordingly getting larger. More power is being reflected and less power is transmitted to the central plasma.

2.2   Numerical techniques used in modelling full wave propagation at the SOL

No analytical solution fulfilling the wave equation Eq. (2.1) exists for an inhomogeneous plasma. Thus one has to rely on numerical methods. Any numerical model for the ICRF wave coupling needs at least two ingredients, the wave excitation and wave damping. Depending on the complexity of the code, the wave can be excited through imposing a current, voltage or external field map on the antenna/sheet/aperture, etc. The wave can be damped by collision or absorbed in an artificially layer, i.e. perfectly matched layer.

2.2.1   Numerical techniques to solve the wave equation

Although no simple solution exists, there are some dedicated methods to do this. Wentzel-Kramer-Brillouin (WKB) method or ray-tracing [Swanson 2003][Van Eester 1989] can give an accurate solution for a single wave in a slowly evolving plasma (invariant over one wavelength). Ray-tracing is a generalized WKB method, it traces the energy fronts of many waves. It is a perfect tool to describe short-wavelength waves. The typical ICRF wavelength (~1cm) is much shorter than the machine size (1m) thus the WKB method is applicable at this point. On the other hand, the WKB approach becomes invalid at the cut-off and resonance layers whereas in the Tokamak edge plasma, this layers are often present. Spectral analysis is capable to model the waves at these special positions and it is cheap in terms of memory. But Fourier transform can be done only with periodic or infinite boundary conditions. A realistic boundary condition can be much more complicated than this. When the geometry has transitions, one needs to perform mode matching at the interface between two geometries. Finite Difference method is convenient when the geometry is regular or can be subdivided by regular domains. In the latter case, the fields need to be matched at each internal boundary. The scope of this thesis is to find a numerical solution to the wave problem in an inhomogeneous plasma with realistic boundary shapes, sophisticated boundary conditions, i.e. sheath boundary conditions. Thus none of the above methods fit our requirements. This thesis uses the finite element solver which is embedded in a commercial software, COMSOL Multiphysics. By adopting the finite element method, one has a great flexibility to set up realistic boundaries and special boundary conditions.

2.2.2   RF wave excitation

There are generally two ways to couple RF waves into a plasma: inductive coupling and capacitive coupling [Chabert 2011] [Lieberman 2005]. In a Tokamak, the RF field is excited by a strong current flowing on the straps, thus it is an inductive coupling discharge. A realistic heating system uses coaxial line to feed the radiating straps. Thus the best way to simulate the wave emission is imposing a voltage drop between the inner conductor and outer conductor of the coaxial line, or simply impose a constant power at the port. *Figure 2.9* shows a part of the TS classical antenna model. The RF field excitation is done by imposing a voltage drop or power at the blue gap of the coaxial line. A current loop is formed flowing from one coaxial feeder to the other (does not show in the figure). However, this treatment requires a 3D geometry. In this thesis, due to the computational memory and time consuming of the simulation, we will only tackle 2D problem, providing everything is infinite and homogeneous in the third (poloidal) direction. In a 2D

model, one generally cuts the strap in one poloidal position and then imposes current or electric field on the obtained rectangular boundaries. Strictly speaking, prescribing a current on the strap is not very self-consistent because the plasma can induce current on the straps too. A better way to model the antenna-plasma coupling more self-consistently is to introduce an electric field map from the 3D solver directly on a prescribed place at the boundary of the 2D simulation domain, i.e. the aperture.
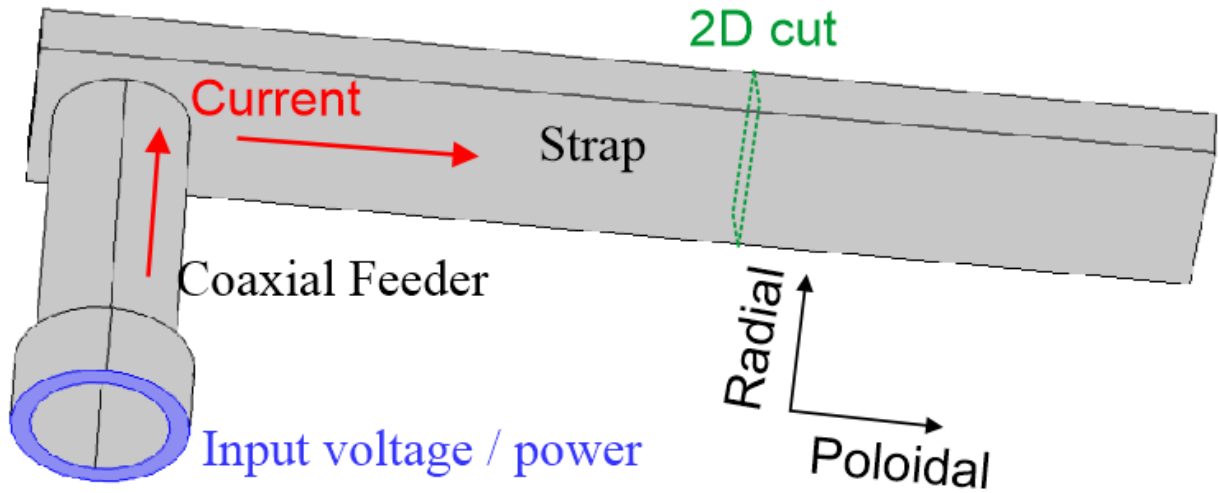
Figure 2.9. A schematic view of RF field excitation in RF modeling for inductive coupling. In a realistic 3D antenna model, voltage/power excitation is imposed at the outer port of the coaxial feeder. Green part shows in case of 2D, strap falls to a rectangle

An example of the antenna aperture is shown in *Figure 2.10*. From the 3D simulation, we could export the field map at one radial position, e.g. at the Faraday screen and then import it into the 2D simulation. The 2D model is a cut in one poloidal position. If one can neglect the poloidal derivative, a 3D results can be done using 2D model through scanning all the poloidal positions with a regular step size. This is called the multiple-2D approach. The straps, side limiters, septum and the thickness of the antenna box are considered as perfect electric conductors and thus are removed in the simulation domain, see the blank ones in *Figure 2.10* (b). The 2D model can be excited either or by field map at the aperture or by imposing currents on the straps. In the former case, choosing the aperture on/above the Faraday screen in the 3D model allows one to avoid implementing tilted Faraday screen bars in the 2D model. In the latter case, the power emanating from the strap should fulfill the following identity

$$-\frac{1}{2}\mathrm{Re}(\int_V \mathbf{E}\cdot\mathbf{J}^*\,dV) = \mathrm{Re}(\mathbf{P}) \tag{2.46}$$

The Left-Hand Side (LHS) is a volume integral to the antenna region with **J** the imposed surface current density on the strap, whereas the Right-Hand Side (RHS) means the real part of $\mathbf{P} = \frac{1}{2}\oint_S (\mathbf{E}\times\mathbf{H}^*)\cdot\mathbf{n}\,dS_a$

i.e. the power flow through a closed surface S_a surrounding the strap.
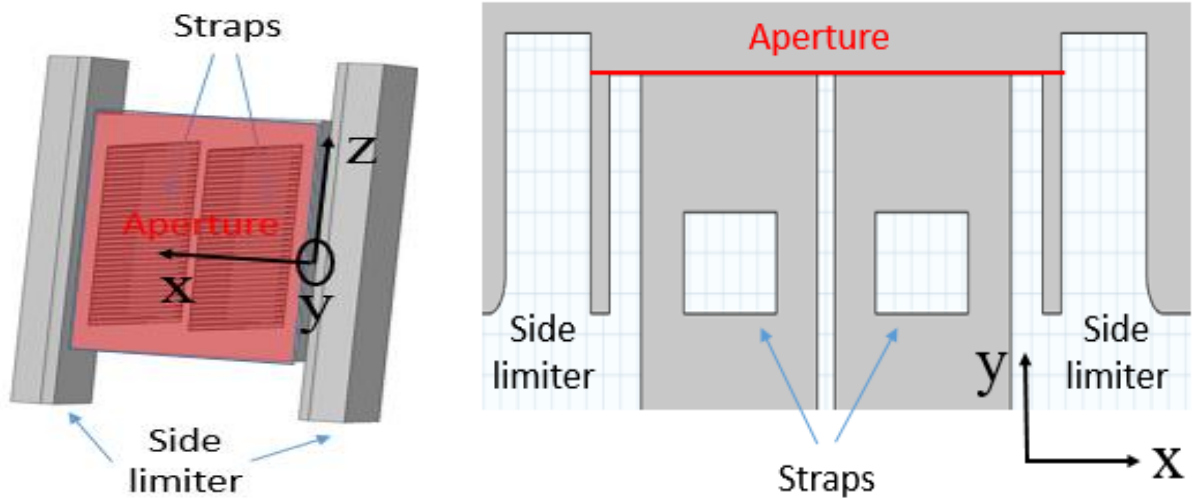
(a) Tore Supra antenna in 3D modelling. Red plane is the aperture.

(b) Tore Supra antenna in 2D simulation. Red curve is the aperture.

Figure 2.10. Typical choices of the aperture in the 3D and 2D simulation

Capacitive coupling is used in Aline [Faudot 2015] at this moment, although it is flexible to change to inductive coupling when needed. The Aline reactor uses a disc antenna to excite the RF fields. The disc antenna is essentially an electrode and the DC current flowing on its surface is negligible. The RF field is consequently excited by the voltage difference between the antenna and the plasma. The feeder of the RF disk antenna, shown in *Figure 2.11* (a) is a solid stainless steel wire, which has a diameter of 6mm. It is further covered by a ceramic ($\sigma = 2 \times 10^{-15}\ S/m,\ \varepsilon_r = 6,\ u_r = 1$) layer (2mm of thickness). The stainless wire is injected into the vacuum vessel, which is indicated by the enclosed dot lines. The upper part of the stainless wire has a metal connection with the disk antenna. Below the stainless wire, there is a copper ($\sigma = 6 \times 10^{7}\ S/m,\ \varepsilon_r = 1,\ u_r = 1$) connection wire (1mm in diameter), which joints together the stainless wire and coaxial cable. The coaxial cable is connected to the RF generator. Under a typical operation frequency w_0= 8.5×10^7 rad/s, the skin depth of stainless steel is 1E-4 m. It is much smaller than the dimensions of disk antenna, i.e. 1cm and the wire, i.e. 6E-3 m. Thus the disk antenna and stainless wire generally can be replaced by Perfect Electric Conductor (PEC) in the simulation, see *Figure 2.11* (b). *Figure 2.11* (b) is a zoom-in of the rectangular region enclosed by dot lines in *Figure 2.11* (a). In 2D modeling, in the same way as imposing the field map at a chosen aperture. The excitation was done by imposing tangential electric field at the bottom of the ceramic layer.

(a)   (b)
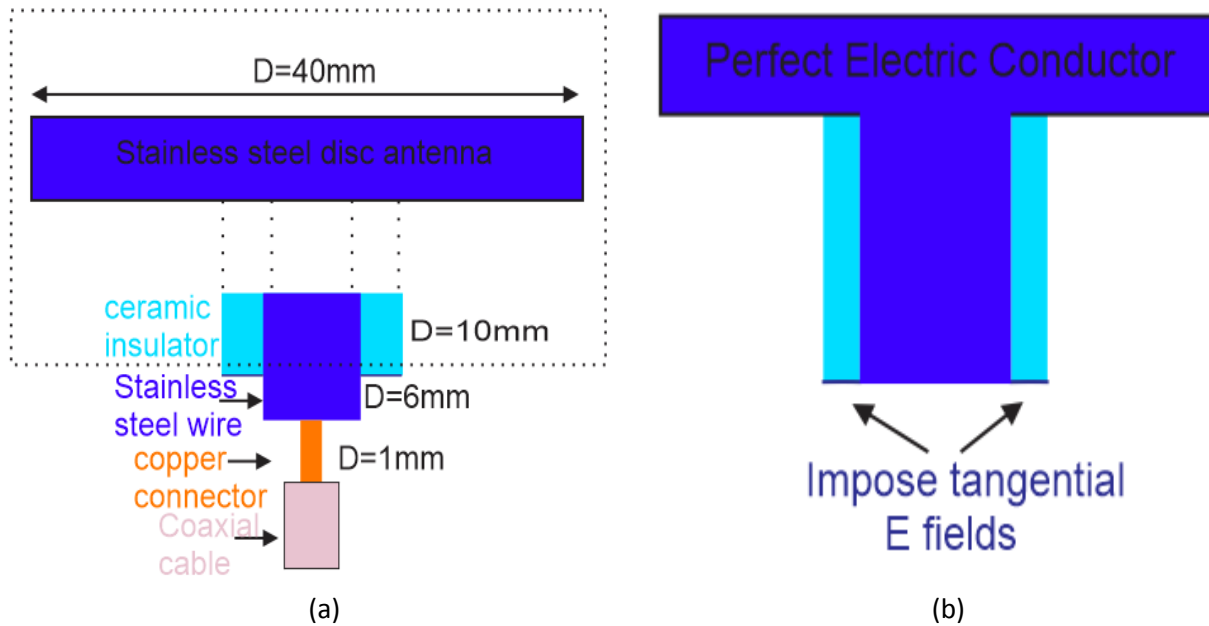
Figure 2.11. A view of the RF field excitation in a capacitive coupling mode (a) A cut of the Aline disc antenna and its feeder. (b) Excitation in the modelling

2.2.3   Wave damping

In fusion devices, the ICRF wave is damped at the cyclotron resonance at the plasma center, but our interested simulation domain is in the scrape-off layer. Besides cyclotron damping is a hot plasma effect that cannot be captured with the adopted cold plasma tensor. In the SOL region, it is needed to introduce other kinds of wave damping, otherwise the wave will bouncing forth and back inside a cavity. Assuming a plane wave that oscillates as $\exp(iwt - i\mathbf{k} \cdot \mathbf{r})$, there are two typical ways to do this.

The perfectly matched layer (PML) emulates radiation at infinity in a bounded simulation domain. The underlying assumption under which the PML technique could work is that wave passing through the plasma never comes back (single pass absorption). The principle of the PML is that it extends the coordinate **r** into the complex domain, i.e. **r**=**r**'-i**r**'', the imaginary part of the coordinate will then damp the propagating wave, the real part of the coordinate will take care of the evanescent one. A detailed description of PML technique applied in the magnetized plasma can be found in [Jacquot 2013]. At this moment, the PML we used can only damp either the forward wave or the backward wave, not both at the same time (the reason is explained in the following page). Thus it is implemented in the region where only the fast wave (forward) is expected to appear, i.e. the slow wave (backward) has decayed to a negligible level. PML can be defined as an artificial material. In case PML is filled by the plasma, the dielectric tensor reads,

$$\boldsymbol{\varepsilon}_{\mathbf{r,PML}} = \begin{bmatrix} \varepsilon_{11} \dfrac{S_y(y)S_z(z)}{S_x(x)} & \varepsilon_{12}S_z(z) & \varepsilon_{13}S_y(y) \\[2mm] \varepsilon_{21}S_z(z) & \varepsilon_{22}\dfrac{S_z(z)S_x(x)}{S_y(y)} & \varepsilon_{23}S_x(x) \\[2mm] \varepsilon_{31}S_y(y) & \varepsilon_{32}S_x(x) & \varepsilon_{33}\dfrac{S_x(x)S_y(y)}{S_z(z)} \end{bmatrix} \tag{2.47}$$

Where the stretching function S_y, S_z and S_z contains complex coordinates. They are defined in Eq. 13 in [Jacquot 2013].

$$S_r(r) = \begin{cases} 1 & 0 \leq r \leq L_r \\[2mm] 1+(S_r' + iS_r'')(\dfrac{r - L_r}{L_{PML}})^{Pr} & L_r \leq r \leq L_\infty \end{cases} \tag{2.48}$$

Here, r represents x, y, and z. L_r is the location of PML. Larger S_r'' and lower P_r could efficiently damp the wave, however it will also produce a steeper density gradient among PML, which needs finer mesh to keep smooth. A compromise is found to be $S_r' = 1$, $S_r'' = 2$ and $Pr = 2$ [Jacquot 2013]. For a forward wave ($k_r > 0$), the reflection coefficient can be derived as $\eta \propto \exp(-k_r S'')$, whereas for a backward wave ($k_r < 0$), it is $\eta \propto \exp(|k_r| S'')$. One can see from here why the PML cannot damp both the forward and backward wave at the same time.

When PML is used in vacuum, one can simply set the non-diagonal terms of Eq. (2.47) to zero in addition with $\varepsilon_{11} = \varepsilon_{22} = \varepsilon_{33} = 1$. Similarly, the magnetic permeability in PML reads,

$$\overline{\overline{u}}_{r,PML} = \begin{bmatrix} \dfrac{S_y(y)S_z(z)}{S_x(x)} & 0 & 0 \\[2mm] 0 & \dfrac{S_z(z)S_x(x)}{S_y(y)} & 0 \\[2mm] 0 & 0 & \dfrac{S_x(x)S_y(y)}{S_z(z)} \end{bmatrix} \tag{2.49}$$

In plasma reactors, i.e. Aline, collision plays an important role for damping the wave. Wave energy can be damped through collisions. This is done by adding a collision term F_{co} in the equation of motion, Eq. (2.2), after linearization

$$m_s \frac{\partial \mathbf{v_s}}{\partial t} = q_s(\mathbf{E} + \mathbf{v_s} \times \mathbf{B}) - F_{co} \tag{2.50}$$

Considering collisions with neutrals, the simplest expression for the collision term is $F_{co} = m_s \mathbf{v_s} w_{co}$, where w_{co} is the collision frequency. Move the collision term to the left side, and repeat the steps of deriving dielectric tensor. Now in the new dielectric tensor, the wave frequency is extended to a complex

number. For example, Eq. (2.5), Eq. (2.8) and Eq. (2.9) should transform w into (w-iw_{co}) in their original formula.

$$\varepsilon_{//} = 1 - \sum_s \frac{w_{ps}^2}{(w + iw_{co})w} \qquad \varepsilon_R = 1 - \sum_s \frac{w_{ps}^2}{w(w + iw_{co} + w_{cs})} \qquad \varepsilon_L = 1 - \sum_s \frac{w_{ps}^2}{w(w + iw_{co} - w_{cs})}$$

A typical ion-neutral collision frequency is like 10^5 rad/s for Argon plasma [Faudot 2015].

2.3   Sheath properties in DC and RF regimes

Here we start to talk about sheath. Sheath is a thin (<1mm) layer at the plasma/wall interface. Inside the sheath, the charge neutrality breaks down and a separation of electrons and ions occurs. Ion density is generally larger than the electrons. The sheath width is much shorter compared to the ion mean free path. Thus we assume there is no collision inside the sheath. The Direct Current (DC) sheath does not vary in time. Typical DC sheath, i.e. Bohm sheath and Debye sheath, has a thickness of several Debye lengths. The Radio Frequency (RF) sheath is induced by oscillating RF waves. It expands and contracts sinusoidally, following the RF wave oscillation. Although the RF sheath oscillates during the RF cycle, over one period, its net contribution to the DC plasma potential is non-zero. Instead, it often enhances the DC plasma biasing with respect to the wall. The DC plasma potential enhancement by sheath RF oscillations or simply called sheath rectification has long been accused to cause many deleterious RF edge effects. Previous literatures has studied extensively the DC sheath perpendicular to $\mathbf{B_0}$ [Lieberman 2005][Stangeby 2000], while relatively less literatures talk about DC sheath with tilted $\mathbf{B_0}$ [Chodura 1982][Stangeby 2012]. One generally makes an analogy between the RF sheath and a capacitor, which suggests an important characteristic of RF sheath: the sheath capacitance. While the theory of the sheath capacitance has been well established in the case where the $\mathbf{B_0}$ is perpendicular to the wall, there is no theory being developed yet under tilted $\mathbf{B_0}$.

2.3.1   DC sheath ⊥B₀

The DC sheath has been studied for a long time. The physics of DC sheath is well known [Lieberman 2005]. The magnetic field lines are open at the edge and connect to the wall. Particles flow along the magnetic field line. Due to the different mobilities between ions and electrons. The plasma is often positively biased with respect to the grounded wall. A voltage drop is thus created between the plasma and the wall. This voltage in turn accelerates ions and repels electrons, see *Figure 2.12*.

In order to form a stable DC sheath, the ion speed at the sheath entrance must exceed the Bohm speed [Bohm 1949] or the sound speed. The Bohm /sound speed reads

$$C_s = \sqrt{\frac{k_B(T_e + T_i)}{m_i}} \qquad (2.51)$$

Where m_i is the ion mass. Some literatures indicate that a pre-sheath [Lieberman 2005] is required to accelerate ions to Bohm speed before entering the sheath. The pre-sheath lies in front of the sheath. The density at the exit of the pre-sheath is consequently the density at the entrance of the sheath. The pre-sheath is much larger than the sheath in scale and charge neutrality is still preserved there. Sometimes it

is simply the plasma itself [Stangeby 2000]. But the density at the exit of the pre-sheath is approximately half the density in the plasma.
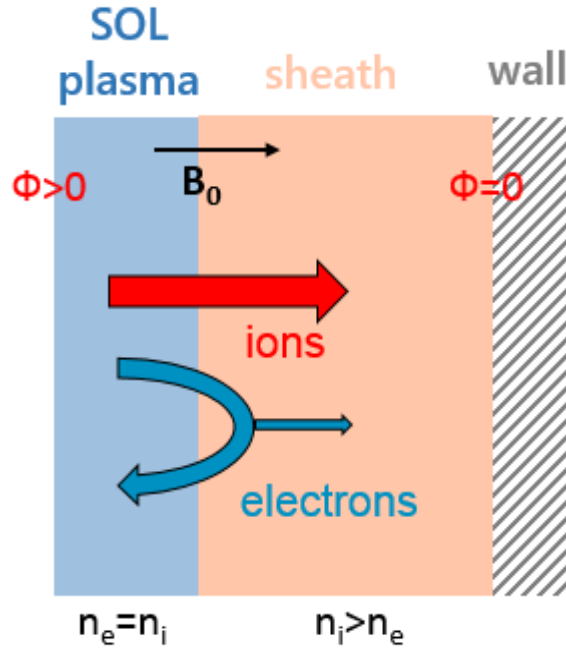
Figure 2.12. A diagram of DC sheath formation

If there is no ionization inside the sheath, the ion current is constant all along the sheath. The current density, also called ion saturation current density, reads,

$$J_{is}^{\perp B} = \frac{n_i}{2} q_i C_s \qquad (2.52)$$

Where n_i is the ion density in the plasma. The superscript $\perp B$ denotes the wall is perpendicular to the magnetic field line.

Inside the sheath, electrons are repelled. One generally assumes that the electron density follows the Boltzmann distribution. Maxwellian distribution is still a good approximation for the election velocity because the directed electron velocity is small in comparison with the thermal velocity [Godyak 1976]. For the Maxwellian electrons, the thermal speed is defined as

$$\bar{v} = \sqrt{8k_B T_e / \pi m_e} \qquad (2.53)$$

Considering the Maxwellian velocity and Boltzmann density, the electron current density inside the sheath has the form

$$J_{electron}^{\perp B} = \frac{n_e e \bar{v}}{8} \exp(\frac{-e\Delta V}{k_B T_e}) \qquad (2.54)$$

Where n_e is the electron density inside plasma, ΔV is the potential drop across the sheath. For a grounded wall, it is equal to the plasma potential V_{DC}. If the wall is floating (i.e. isolated), a steady-state

is reached when the ion flux reaching the wall is equal to the electron flux. The wall potential at this state is called the floating potential. By equaling Eq. (2.52)and Eq. (2.54), one gets the expression of the floating potential V_f,

$$V_f = \frac{k_B T_e}{2e} \ln(\frac{2\pi m_e}{m_i}(1+\frac{T_i}{T_e})) \tag{2.55}$$

In deriving Eq.(2.55) q_i=e is assumed and the plasma neutrality gives n_i=n_e.

The floating potential can be directly measured by a Langmuir probe, a figure of such a probe has been shown in Chapter 1. When a Langmuir probe is inserted into the plasma, a Bohm sheath [Stangeby 2000] is formed at the tip of the probe. Through analyzing the current and voltage picked up by the probe, one can obtain a current-voltage relation, i.e. the I/V characteristic. A typical I/V characteristic from probe measurement is shown in *Figure 2.13*.

In *Figure 2.13*, V_f is the point where the I/V curve crosses zero, corresponding to the case in which no net current is arriving at the probe surface.
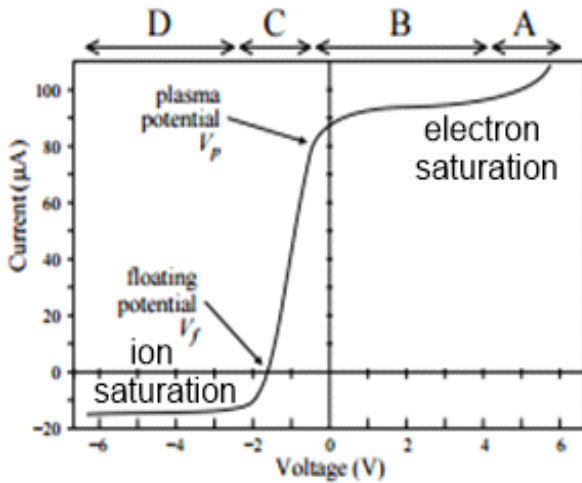
Figure 2.13. Probe I/V characteristic

At the two extremities of the I/V characteristic, there are two parts (B and D) where the current is almost stable. The B part represents the electron saturation regime. It is the state when the probe potential equals to the plasma potential. No sheath is formed at this state. Electrons flow to the probe with a thermal velocity. The corresponding current is called the electron saturation current

$$J_{es}^{\perp B} = \frac{n_e e \overline{v}}{8} \tag{2.56}$$

On the contrary, if the probe potential is much lower than the plasma potential. There is no electrons inside sheath. The probe will only collect the ion current. The current in this case is the ion saturation current. Its expression is shown in Eq. (2.52).

In principle, the plasma potential can also be obtained from the I/V diagram by determining the point with the maximum slop [Chen 2003]. But in reality, with the presence of the magnetic field, the I/V curve will suffer a lot of fluctuations and thus is difficult to determine the plasma potential by this way. A more advanced method is to use the field retarding analyzer [Gahan 2008][Kubic 2013].

The DC sheath has a constant sheath width. It is described by the Child-Langmuir law [Child 1911][Langmuir 1913],

$$\delta_{sh}^{\perp B} = \lambda_{De} (\frac{eV_{DC}}{k_B T_e})^{3/4} \tag{2.57}$$

For a grounded wall, i.e. Tokamak vessel, V_{DC} is the plasma potential. For a floating wall, it is the voltage across the DC sheath. Eq. (2.57) was firstly derived as a voltage-current relation in a thermionic diode which is occupied by electron space charge. Later a similar dependence was found between the sheath width and the magnitude of the DC plasma potential [Chabert 2011].

2.3.2   RF oscillating sheath $\perp B_0$: sheath capacitance

Until now, we did not consider the impact of RF waves on sheath. The interaction between sheath and waves [Noterdaeme 1993] is the key topic of this thesis. RF sheath can be modelled by a circuit model [Chabert 2011], which consists of a constant current source, a reversed diode and a capacitor, see *Figure 2.14*. The ion conduction current flows through the current source whereas the electron conduction current flows through the reversed diode. Due to the inherent time-varying feature of the RF sheath, a displacement current is also present, which passes through the capacitor.
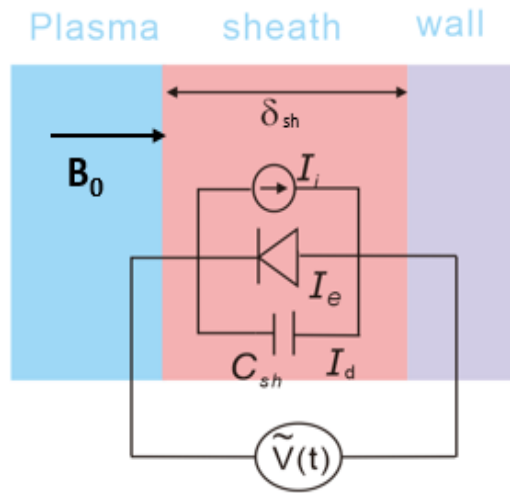
Figure 2.14. Equivalent circuit of RF sheath

We consider a specific regime, (a) the wave frequency is between the ion plasma frequency and the electron plasma frequency, i.e. $w_{pi} < w < w_{pe}$; (b) RF sheath voltage is high, i.e. $V_{sh} >> k_B T_e / e$; (c) No currents enter or exit the sheath at the perpendicular direction. (d) Sheath is electrostatic. Assumption (a) guarantees the ions respond only time-averaged potential, whereas electrons can respond to the instantaneous potential. Assumption (b) suggests that the electron density tends to reach zero in the sheath, and the displacement current is much larger than the conduction current. Assumption (c) ensures the total current is conserved all through the sheath along the parallel direction. Under these assumptions, Chabert [Chabert 2011] proves that a current-driven symmetric double sheath with a constant ion density can be treated as a single capacitor. Lieberman [Lieberman 2005] [Lieberman 1988] further demonstrates that the sheath RF capacitance is still valid in case of an inhomogeneous ion density when the wall is floating. Strictly speaking, the RF capacitance is valid only for a series of two sheaths, shown in *Figure 2.15*. However, at first approximation, we assume that a single sheath can be treated as a capacitor too.
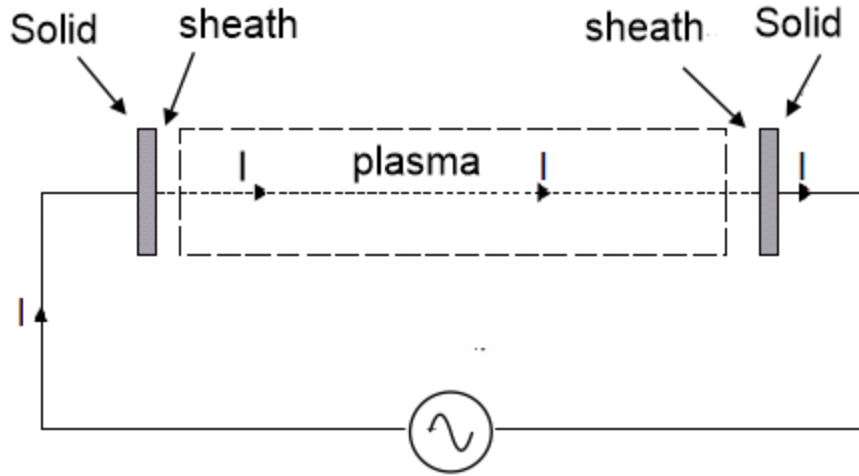
Figure 2.15. A draw of a current-driven symmetric double sheath

Sheath capacitance gives a definition to V_{RF}, which reads

$$V_{RF} = -\frac{D_n \delta_{sh}^{\perp B}}{\varepsilon_{sh}} = \pm \frac{E_{//}\varepsilon_{//}\delta_{sh}^{\perp B}}{\varepsilon_{sh}}$$

(2.58)

where $\delta_{sh}^{\perp B}$, $\varepsilon_{//}$ have been defined in Eq. (2.57), Eq. (2.5) and n represents the normal direction from sheath towards the plasma. The sheath capacitance per unit was used $C_{sh} = \frac{\varepsilon_{sh}}{\delta_{sh}^{\perp B}}$ in deriving Eq. (2.58). When $\mathbf{B_0}$ is perpendicular to the wall, n is also the parallel direction. The constitutive relation links the normal displacement D_n and the parallel electric field $E_{//}$. ε_{sh} is the sheath dielectric permittivity. Opposite signs in the last step accounts for the reversal of the normal direction, + when $e_n \cdot z = -1$ and - when $e_n \cdot z = 1$.

2.3.3   DC sheath rectification $\perp B_0$

In the presence of the RF waves, the plasma potential will be more positively biased w.r.t the wall via a non-linear process called sheath rectification. To understand this process, we write down the averaged current density inside the sheath over one RF period. Please note that the net displacement current vanishes after averaging. Thus only the electron and ion conduction current persist. Combining the ion current Eq. (2.52) and electron current Eq. (2.54), and making use of Eq. (2.55), the DC current density averaged over one RF period T_0 is obtained:

$$< J_{DC}^{\perp B} >= J_{is}^{\perp B}(1 - \min(\frac{J_{es}^{\perp B}}{J_{is}^{\perp B}}, \frac{1}{T_0}\int_{t}^{t+T_0} exp[\frac{e(V_f - V_{tot}(t))}{k_B T_e}]dt))$$

(2.59)

Where

$$V_{tot}(t) = V_{DC} + V_{RF} \cos wt$$

(2.60)

is the instantaneous voltage drop across the total sheath (RF sheath + DC sheath). Here it is implicitly assumed that the RF sheath and DC sheath share the same boundary. This is not true when $\mathbf{B_0}$ is tilted to the wall, see Chodura's model in the next subsection. In Eq. (2.59) we use the electron saturation current as the threshold for the electron conduction current.

The averaging of $V_{RF} \cos wt$ leads to a modified Bessel function of the first kind,

$$I_0(V_{RF}) = \frac{1}{\pi} \int_0^\pi \exp(V_{RF} \cos wt) d(wt) \tag{2.61}$$

Substitute Eq. (2.61) into Eq. (2.59), one gets the final DC current expression when $\mathbf{B_0}$ is perpendicular to the wall,

$$<J_{DC}^{\perp B}> = J_{is}^{\perp B}(1 - \min(\frac{J_{es}^{\perp B}}{J_{is}^{\perp B}}, \exp(\frac{e(V_f + V_b - V_{DC})}{K_B T_e}))) \tag{2.62}$$

Where $V_b = \frac{k_B T_e}{e} \ln[I_0(\frac{e|V_{RF}|}{k_B T_e})]$ is the additional biasing to the DC plasma potential by the oscillating

RF waves. From Eq. (2.62), one can understand although the average of the RF quantities over one period is zero, its net contribution to the DC plasma potential and the DC current is nonzero. This is the so-called DC sheath rectification by RF oscillations.
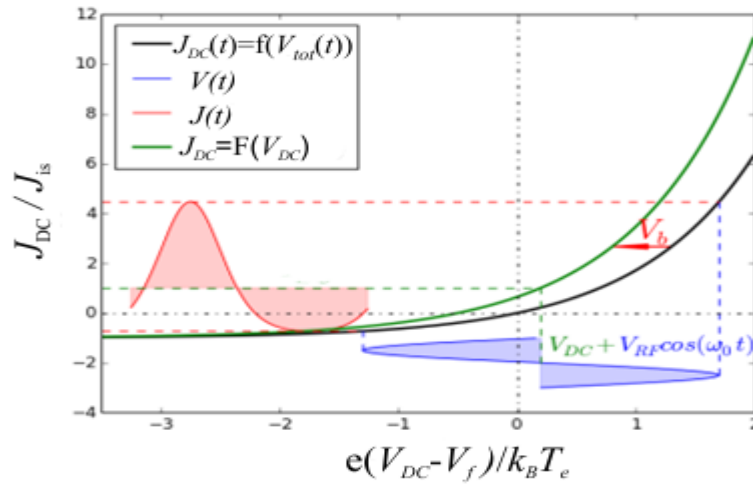
Figure 2.16. An illustration of DC sheath rectification

Figure 2.16 is a graphic view of the DC sheath rectification. The I/V characteristic in this figure stands for the D region in *Figure 2.13.* When there is no wave present, the I/V characteristic is the green curve. The DC plasma potential and current are time independent. With the RF oscillations, the curve is shifted rightwards and the current is a function of the time-dependent potential V_{tot}. After averaging over time, the new current curve is the black one. Consequently, the plasma potential becomes more positive w.r.t the wall potential.

2.3.4   DC sheath under tilted B_0: Chodura's model

A pioneering work on DC sheath under tilted **B₀** is done by Chodura [Chodura 1982] and reviewed by Stangeby [Stangeby 1994][Stangeby 2012]. Chodura's model is shown in *Figure 2.17.* It considers a poloidal-toroidal geometry. **B₀** is tilted as it is in *Figure 2.1*. Under the tilted magnetic configuration, a quasi-neutral region called "Chodura sheath" or "magnetic pre-sheath" will occur, which turns the ion flow from being sonic/supersonic at the parallel-to-**B₀** direction to being sonic/supersonic at the perpendicular-to-wall direction. Chodura sheath has a typical size of ion Larmor radius. Ions then enter into the normal charge separated DC sheath or Debye sheath whose size is a few Debye lengths. Debye sheath can exist without the presence of magnetic field, and the ion motion is dominated by the electric field. Recall Bohm criterion about the sheath formation, ion speed must be no less than the sound speed, which represents the Mach number M=V_z/C_s≥1, at the entrance of Debye sheath. Similar to this, [Chodura 1982] also proved that at the entrance of the Chodura's sheath, the ion parallel velocity should obey $V_{//}$/C_s≥1. To obtain this, a quasineutral pre-sheath region is defined in this model, in this region the electron pressure gradient creates a balanced electric field, which in turn accelerates ions to the sound speed at the entrance of Chodura's sheath. As mentioned in the subsection 2.3.1 , the ion density is half of the plasma density at the pre-sheath boundary. Chodura made an assumption that the plasma flow speed is sonic in the direction of normal to the wall at the exit of the Chodura sheath in order to excite the Debye sheath. However, [Stangeby 2012] shows in a strongly tilted sheath θ~90^0, the ion speed at the Chodura's sheath exit can be subsonic due to the disappearance of the Debye sheath. In this text, we assume that the ion speed $V_{//}$ and V_z equal to the sound speed at the entrance of the Chodura sheath and the Debye sheath, respectively.

With a floating wall, Chodura shows that the total voltage drop across the two sheaths V_{tot} is almost independent on the tilt angle, which is only an approximation for our non-floating case, i.e. the Tokamak wall is grounded.

RF sheath is approximately considered as a plate capacitor, while a capacitor is related to the charge separation, which happened in Debye sheath here. Now we assume all the oscillating RF part is carried by the Debye sheath, i.e. the Chodura sheath is time independent. We extend Chodura DC sheath model given by a collisionless fluid model [Stangeby 2012] into a dynamic model. Adopting the current magnetic configuration, the potential drop at the Chodura's sheath reads

$$V_{CS} = -\frac{k_B T_e}{e} \ln(\cos\theta) \tag{2.63}$$

To be self-consistent, the following V_{DS} is chosen

$$V_{DS}(t) = V_{DC} + \frac{k_B T_e}{e} \ln(\cos\theta) + V_{RF} \cos\omega t \tag{2.64}$$

The ion current density at the wall now is a projection of the total ion current density that is parallel to the tilted magnetic field line at the Chodura sheath entrance, and thus should be multiplied by $\cos\theta$

$$J_{is}^{\theta} = J_{is}^{\perp B} \cos\theta = \frac{n_i}{2} q_i C_s \cos\theta \tag{2.65}$$

Similarly for the electron current density. The $V_{tot}(t)$ in Eq. (2.59) should be replaced by $V_{tot}(t) = V_{CS} + V_{DS}(t)$. Finally the I/V characteristic reads,

$$< J_{DC}^{\theta} > = J_{is}^{\perp B} \cos\theta (1 - \min(\frac{J_{es}^{\perp B}}{J_{is}^{\perp B}}, \exp(\frac{e(V_f + V_b - V_{DC})}{K_B T_e}))) \tag{2.66}$$

Eq. (2.66) gives a similar formula as the I/V characteristic in Eq. (2.62). Thus the form we choose for V_{DS} in Eq. (2.64) is self-consistent. One can see from Eq. (2.63), when magnetic field is non-tilted, the Chodura sheath is disappeared. This corresponds to subsection 2.3.3, where V_{DC} and V_{RF} are defined at the same sheath. Now with the magnetic field tilted, V_{RF} is defined only in the Debye sheath, while the DC voltage is the combination of the Chodura sheath and DC part of the Debye sheath. From Eq. (2.64), we can also derive the displacement current inside the Deybe sheath as

$$J_d^{\theta} = C_{DS}^* \frac{dV_{DS}}{dt} = -C_{DS}^* \omega V_{RF} \sin\omega t \tag{2.67}$$

Where the equivalent capacitance per surface unit is

$$C_{DS}^* = \frac{\varepsilon_{sh}}{\delta_{DS}(\theta)} \tag{2.68}$$

Similar to the Child-Langmuir law for DC sheath, here we assume the Debye sheath width is a function of DC part of $V_{DS}(t)$, which reads

$$\delta_{DS}(\theta) = \lambda_{De}(\theta)(\frac{eV_{DC}}{k_B T_e} + \ln(\cos\theta))^{3/4} \tag{2.69}$$
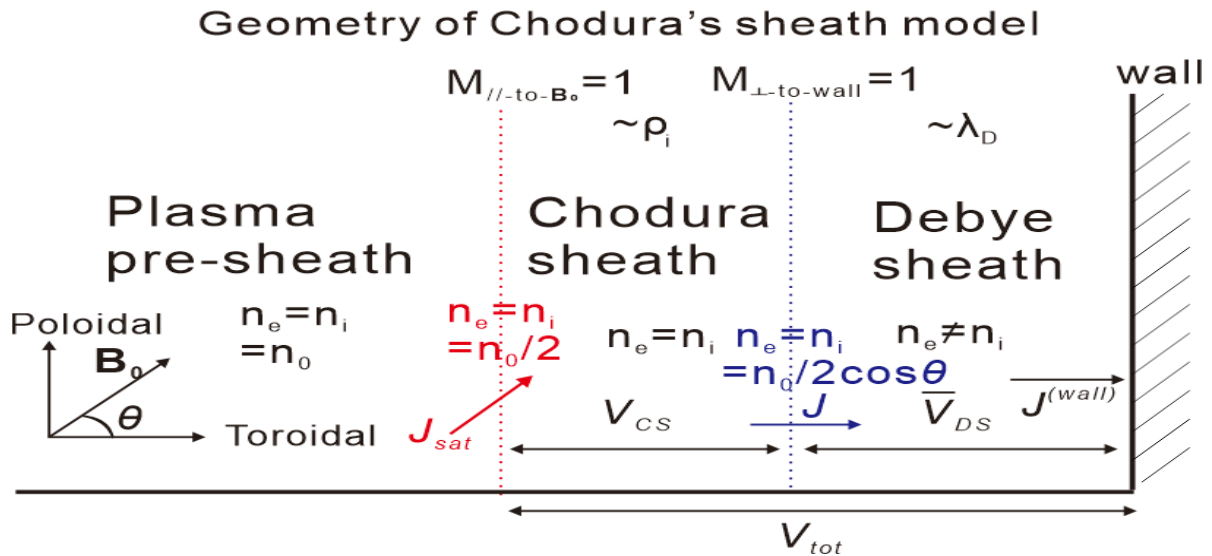

Figure 2.17. Chodura's DC sheath model for a tilted magnetic configuration

Where $\lambda_{De}(\theta) = \lambda_{De} \cos^{-1/2} \theta$. Note that the sheath width depends on the tilt angle. One can see when $\theta=0^o$, it falls back to Eq. (2.57). The Debye length also depends on the tilt angle, since the density at the entrance of Debye sheath contains the tilt angle. However, this formula fail to validate when $\theta\sim90^o$, where sheath width from this formula can be infinite. In such a strongly tilted case, there is a criterion θ_{crit}, above this criterion θ, Stangeby [Stangeby 2012] has proved that $\delta_{DS}(\theta) = 0$. Consistent to this result, a 2D paricle-in-cell (PIC) simulation shows that the rectification of the RF potential is reduced or disappeared when the Debye sheath cease to exist [Heuraux 2015]. Strictly speaking, at the parallel boundaries, the cross field sheath [Moritz 2016] could still appear due to the difference of the Larmor radius between ions and electrons. This specific sheath is not considered in this thesis.

2.3.5   RF sheath under the tilted B$_0$: a simple model and open issues

Very few literatures exist on studying the RF sheath under the tilted **B$_0$**. No literature has proposed an explicit formula for the RF sheath capacitance under the tilted **B$_0$**. Nevertheless, we extrapolate a similar form to Eq. (2.58), but now with the new sheath width obtained from Eq. (2.69). The sheath capacitance under tilted **B$_0$** thus becomes,

$$V_{RF} = -\frac{D_n \delta_{DS}(\theta)}{\varepsilon_{sh}} = \pm\frac{D_z \delta_{DS}(\theta)}{\varepsilon_{sh}} \qquad (2.70)$$

Where D_z is the toroidal displacement. The justification of Eq. (2.70) can only be done through more fundamental physics investigations. Works are still undergoing on exploring the sheath behaviors under tilted **B$_0$** using a PIC code [Verboncoeur 1995] and a 1D Vlasov code [Devaux 2006].

A more generalized form of the sheath capacitance Eq. (2.70) is proposed in [D'Ippolito 2015] in the middle of this thesis. It releases the "immobile ion" assumption and both the resistive and capacitive part of the RF sheath are retained in their new model. This thesis will still keep using the older sheath capacitance Eq. (2.70). Applying the generalized sheath boundary condition is foreseen in the future.

2.3.6   Sheath as a boundary condition

Since sheath is geometrically thin, it is often treated as a boundary condition in the simulation. A well-known RF sheath boundary condition is proposed by Myra and D'Ippolito [D'Ippolito 2006]. It considers an electrostatic and capacitive sheath. The ions are immobile in response to the RF wave pulse, meaning that they are either strongly magnetized or the steady-state magnetic field is normal to the sheath. Under this assumption, the conduction current is much smaller than the displacement current so it can be neglected. In this model, the plasma density has a sharp transition from the plasma to the sheath region [VanEester 2013], which overlooks the possible existence of the lower hybrid resonance inside the sheath. Under these approximation, the resistive part of the sheath is discarded. Making use of the continuity of the normal displacement at the sheath/plasma interface, the electrostatic assumption and sheath capacitance, it leads to a simple formula that the tangential electric fields are equal to the tangential gradient of the RF sheath voltage, at the sheath entrance,

$$E_t = -\nabla_t V_{RF} \qquad (2.71)$$

Where the subscript "t" denote the tangential components.

Efforts are ongoing at LPP Brussels to examine this sheath boundary condition and assess its validity domain by a 1D FORTRAN code [Van Eester 2015]. Success would justify replacing metallic boundary

conditions by this sheath boundary conditions; failure would force one to account for solving multiple basic equations, i.e. Maxwell's equation, equation of motion and continuity equation at differing time scales simultaneously.

2.4   Status of IC wave coupling and RF sheath modeling before this thesis

There are numerous wave coupling and RF sheath modeling codes that existed before this thesis. A good review of numerical modeling tools on these two fields can be found in [Heuraux 2015]. Here we will give a short overview of the status of the modelling codes before this thesis.

2.4.1   Wave coupling codes

Plenty of numerical codes have been developed to study the ICRF wave propagation and coupling. ANTITER II [Messiaen 2010] has a simple antenna geometry consisting of an array of boxes that are recessed in the metal wall. In each of these boxes, the RF field is excited by a thin radiating strap. The antenna is sitting in vacuum. A mode matching technique is used at the plasma/vacuum interface to ensure the continuity of the tangential fields. Calculation by this code is fast but it relies on the input from other codes with more complex geometry. The TOPICA code [Lancellotti 2006] has a so far the most realistic 3D antenna geometry. The code is based on the "method of moment". It has difficulties to include plasma density inside the antenna box and it need to perform an impedance matrix transform at the plasma/vacuum interface. The TORIC code [Brambilla 1998A][Brambilla 2006] solves the differential wave equation using a spectral decomposition by the fast Fourier transform. It is a useful tool to simulate IC wave heating in a thermal plasma. FELICE [Brambilla 1989] solves the same set of equation as TORIC, but the plasma is discretized into a series of slabs. Both the TORIC and FELICE codes treat the antenna as a current sheet. The EVE code [Dumont 2009] simulates the wave coupling in a hot plasma using a variational form of Maxwell's equation. Compared to other codes where the differential operator is used, the main advantage of the variational form approach is that it ensures the energy conservation. This code uses a fixed current on the antenna (sheet) to excite the field, the antenna-plasma coupling is thus not modelled self-consistently. This weakness is overcome by using the boundary element method in ICANT code [Pécoul 2002]. Some of the codes developed from the first principles using FORTRAN or any other basic languages usually restrict themselves in a simplified geometry. Upgrading them to a complex geometry and applying multiple types of finite element shapes would be tough and needs a lot of programming. Recently emerged commercial softwares give unprecedented flexibilities to model wave physics. Most of the code based on CST microwave studio [Louche 2015] and HFSS software [Hillairet 2015] have a problem to implement the off-diagonal term of the plasma dielectric tensor so they lose the typical gyrotropic properties of a magnetized plasma.

A 2D full wave (fast wave + slow wave) coupling code, (name: RAPLICASOL) [Jacquot 2013] with magnetic field either parallel or perpendicular to the wall, dedicated to study of wave coupling problems in a collisionless magnetized cold edge plasma has been developed and tested based on COMSOL Multiphysics finite element solver. During this thesis, this code has been further extended into a tilted magnetic configuration [Lu 2016] and a curved cylindrical geometry [Jacquot 2015]. The details of this code will be presented in the next chapter.

2.4.2   RF sheath modeling codes

The first modelling of the RF sheath rectification was made by Perkins [Perkins 1989]. Following his way of thinking, the oscillating RF voltage is calculated by an integral of $E_{//}$ along magnetic field line, where the $E_{//}$ is generally obtained in the full wave simulation without sheath, i.e. the plasma is in contact with

the metallic wall. This approach has been challenged both theoretically and experimentally. For example, it can hardly explain that opposite variations of sheath effect were observed at the two ends of the same open flux tube in ToreSupra (TS) [Jacquot 2014] and ASDEX Upgrade (AUG) [Bobkov 2015]. One of the main obstacle in modeling the RF+DC problem is that the plasma is a time-dispersive medium, so no single dielectric tensor, Eq. (2.4) or conductivity tensor is valid for all frequencies. Kohno [Kohno 2012] demonstrates the use of the finite element approach of solving plasma waves subject to sheath boundary conditions mentioned in subsection 2.3.6 . However in his paper [kohno 2012A], he avoids computing different time scales by using a crude approach to estimate the rectified potential. A better way is to separate these two time-scales. The Self-consistent Sheath and Waves for ICH (SSWICH) code solves the slow wave propagation, the RF oscillating sheath voltage and the DC plasma potential and then couples these three fields in a loop by non-linear sheath boundary conditions, i.e. sheath capacitance, sheath rectification and the RF sheath boundary condition presented in subsection 2.3.6 . The RF part and DC part are solved in different steps using different conductivity tensors. A first version of SSWICH had 2D (toroidal and radial) geometry, rectangular walls either normal or parallel to the confinement magnetic field B_0 and only included the evanescent slow wave (SW) excited parasitically by the ICRF antenna. It has reproduced qualitatively the poloidal distribution of DC sheath voltage in TS [Jacquot 2014] and AUG experiment [Krivska 2015]. Within this formalism, sheaths at the two ends of the same magnetic field line can oscillate differently, due to the toroidal proximity effects in the sheath excitation by the evanescent slow wave [Colas 2016]. The LPP code [Van Eester 2015] also follows this strategy, it solves self-consistently the interplay between full wave (fast wave + slow wave) and plasma density. The fast time scale modifies the density of the slow time scale via non-linear Ponderomotive effect. An alternative way to model RF+DC problem is used by Smithe [Smithe 2015]. He uses the method of "auxiliary differential equations", which allows frequency dependent materials to be treated in the time domain. Using the same strategy, Faudot [Faudot 2013] develops a 1D time-dependent fluid model which counts for both the transversal RF and DC current. Unlike the first strategy, in their method, the plasma conductivity tensor is replaced by a conductivity operator.

2.5   Motivation for this thesis

This thesis is a part of a working project whose ultimate goal is to minimize deleterious effects of RF near field to have heating system reliable for steady state operation. As a first step to understand the physical reasons behind the RF edge effects mentioned in chapter 1, the RAPLICASOL code and the SSWICH-SW code have been established before the start of this thesis by Jacquot [Jacquot 2014]. Following his work, this thesis focuses on upgrading these simulation tools and using them to investigate the RF wave coupling and DC sheath rectification by RF waves.

This thesis work was conducted in 3 different European labs, the Institute for magnetic fusion research (IRFM) in France, the Laboratory for plasma physics (LPP) in Brussels and the Institute Jean Lamour (IJL) at the University of Lorraine. The works that has been done in these 3 labs are synthesized into three parts.

Most present Ion Cyclotron Resonant Frequency (ICRF) heating codes and antenna codes mentioned in the previous section assume the antenna sitting in a vacuum region and consider the fast wave only, which implicitly performs an abrupt density transition from vacuum to the above lower hybrid (LH) resonance, Eq. (2.35). The impact of the appearance of the LH resonance is entirely overlooked in their simulations. This motivated the first part of this thesis work which was done at LPP, namely, studying the

impact of densities that decay continuously inside the antenna box on near field patterns and power coupling.

The central part of this thesis work was to introduce the fast wave into 2D SSWICH-SW. The 2D SSWICH-SW version has a magnetic field either //**B₀** or ⊥**B₀**. Under such a magnetic configuration, the fast wave which is the main heating wave, is missing in the sheath formation. Besides, measurement in Tore Supra by a retarding field analyzer (RFA) shows that the radial extension of DC plasma potential is far beyond the slow wave evanescence length. At this measurement, the RFA is magnetically connected to the leading edge of one of the antenna's side limiter, see *Figure 2.18* (right), although the length of the magnetic field line between them is 12m. The potential measured by the RFA is thought to represent the potential at that limiter leading edge, see the shading parallelogram in *Figure 2.18* (right). *Figure 2.18* (left) is a differential potential map measured by the RFA. V_{half} is the potential corresponding to half of the ion saturation current and V_{sh} is the time-averaged rectified potential, seen by the RFA. The difference between V_{half} and V_{sh} indicates the broadening of the ion distribution function and thus reflects relatively the DC plasma potential. In this figure, the V_{DC} broadening is approximately 1.5cm, indicated by the blue arrow line in the left figure. Whereas the slow wave evanescence length calculated by Eq. (2.19) is about 5mm. So this V_{DC} broadening cannot be fully explained by the evanescent slow wave. This contradictory was temporarily explained by introducing radial DC current transport, where an ad-hoc plasma perpendicular conductivity was embedded in the equation. One generally assumes that the slow wave propagates along the magnetic field line. So the slow wave could be the reason for the sheath excitation only if the target wall is magnetically connected to the place where the slow wave is excited, which is the case here. But the distance between them is 12m. With typical evanescence length of a few millimeters, the slow wave certainly cannot penetrate such a long distance along the parallel direction.
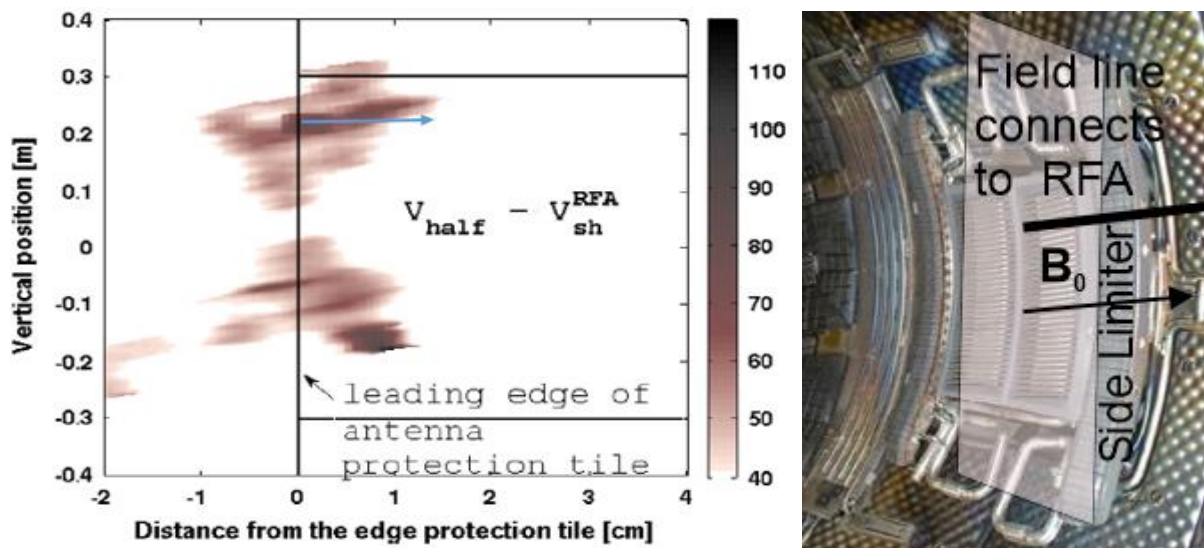

Figure 2.18. Left: Measurement from retarding field analyzer in Tore Supra, cite from [Kubic 2013] Right: ICRF antenna front face, and field line trajectory from the leading edge of the side limiter to RFA. Shading parallelogram is the plane where the 2D measurement (left) represents for.

A large plasma potential (>100V) on field lines that are not connected to the RF antenna has been observed explicitly in the C-mod Tokamak [Ochoukov 2014] and that is explained by the fast wave induced far-field sheath [D'Ippolito 2014]. The fast wave propagates further away from the wave launcher, and thus it can access remote areas that cannot be approached by the slow wave.

In addition, in a realistic Tokamak, the wall is shaped and the magnetic field is tilted to the wall. Under this magnetic configuration, the fast wave is automatically coupled to the sheath boundary conditions and thus contributes to the sheath formation. Besides, previous literature indicates that a sort of "mode conversion" could occur if the magnetic field is tilted to the wall. [D'Ippolito 2008] proves that for an oblique incidence, single reflected wave is not enough to fulfill either the metallic boundary condition or the sheath boundary condition at the wall. Thus the incident fast wave must be converted to the slow wave upon the reflection. A graphic illustration of this mechanism is shown in *Figure 2.19*. One can see these two waves indeed need to be treated simultaneously.

Then the question being asked is "what is the role of the fast wave in the plasma wave interaction". This question motivates one to couple the fast wave into SSWICH modeling. Now with tilted magnetic configuration, it will be shown in Chapter 4 that the fast wave is now being added in the new SSWICH version. The fast wave propagates further away from the wave launcher, and thus it provides a mechanism to excite the far field sheath. Secondly, it may provide an additional mechanism to interpret the V_{DC} radial broadening measured experimentally by RFA. Finally, with the full wave being assembled in the code, the wave coupling and sheath physics could be studied in one single code, that is to say, combine the previous SSWICH code and RAPLICASOL code together.
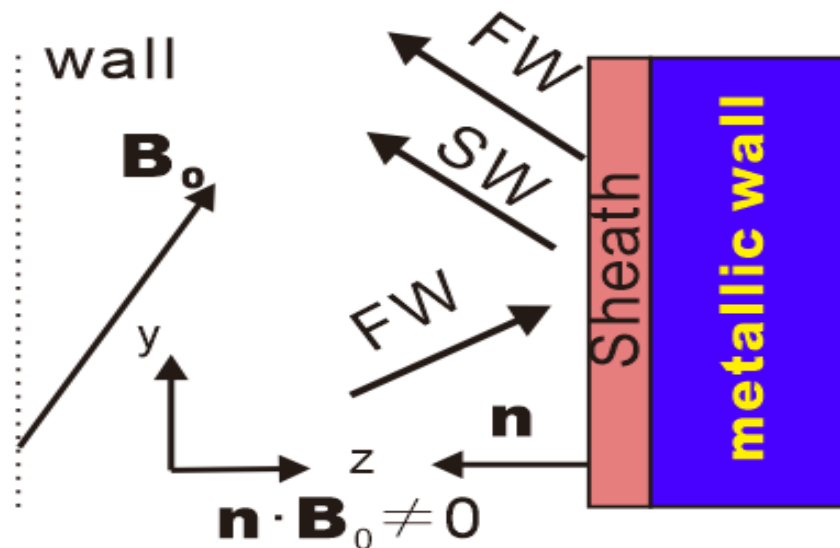
Figure 2.19. Mode conversion mechanism under tilted magnetic configuration

A new code should be able to explain some experimental facts. The first SSWICH version, 2D SSWICH-SW had already made some comparison with measurements from Tore Supra. The new 2D SSWICH-FW code should recover these results and possibly go beyond, i.e. observe the far field sheath. The Aline machine was set into operation during this thesis. It had a first Argon plasma on June 2014. Simulations

are needed to interpret the probe potential measurement and predict the conditions for observing the helicon waves in Aline. The new SSWICH-FW could contribute to these work by conducting dedicated simulations. This motivates the third part of this thesis work: the applications of the 2D SSWICH-FW code.

2.6   Thesis outline

The first two chapters aim at providing the background and theoretical basis for understanding this thesis work. This thesis work is divided into three parts: 1. Upgrading the 2D RAPLICASOL code and deploying it to model wave coupling with a density across the Lower hybrid resonance; 2. Introducing the fast wave, tilted magnetic field and shaped walls into the 2D SSWICH-SW code; 3. Numerical test of the new 2D SSWICH-FW code and performing interpretive simulations for Tore Supra Tokamak and Aline.

Chapter 3 presents the results on wave coupling simulations with a finite, inhomogeneous density inside the antenna box. First of all, specification of the new full wave code with tilted **B₀** is introduced. Then we study the near field pattern above and below the lower hybrid resonance. The last part is to investigate the impact of this low density on power coupling and radiating power spectrum.

Chapter 4 is the technical development of the 2D SSWICH-FW code. The new code combines the sheath physics and wave coupling together. At first, the specifications of the new 2D SSWICH-FW code designed for Tokamak simulation are introduced and the challenges in extension to 3D are pointed out. The second part discusses the numerical issues encountered during the code development. The last part shows the modifications that are needed in order to adopt SSWICH for Aline simulations.

Chapter 5 is the application of the 2D SSWICH-FW code. In this chapter, the questions being asked at the beginning of this thesis: the role of the fast wave is answered by testing this new code and performing direct comparison with the previous "slow-wave-only" version. It further gives a comparison of SSWICH simulation with measurements from Tokamak and Aline. Besides, electromagnetic simulations for helicon and lower hybrid wave in Aline are also presented.

Chapter 6 is the close remark of the whole thesis. Since the summary of the main achievements has been shown in the abstract. Here we will mainly discuss the weakness of the current 2D SSWICH-FW code. In the end, some future improvements and applications are proposed.

Reference

[Beaumont 1988] B. Beaumont, G. Agarici, H. Kuus, "Tore Supra ICRH antenna array", Proc. 15th SOFT, page 503, 1988

[Bellan 1994] P. M. Bellan, "Alfven 'resonance' reconsidered: Exact equations for wave propagation across a cold inhomogeneous plasma", Phys. Plasma 1(11), Nov. 1994

[Bhatnagar 1981] V. P. Bhatnagar, R. Koch, A. M. Messiaen and R. R. Weynants, "A 3-D analysis of the coupling characteristics of ion cyclotron resonance heating antennae", *Nucl. Fus.* V **22**, 2, 1982

[Bilato 2005] R. Bilato, M. Brambilla, D. A. Hartmann and A. Parisot, "Influence of an evanescence layer in front of the antenna on the coupling efficiency of ion cyclotron waves", Nuclear fusion 45(2) 2005

[Bobkov2015] V. Bobkov et al., "Progress in Controlling ICRF-edge Interactions in ASDEX Upgrade", AIP Conf. Proc. **1689**, 030004 (2015)

[Bohm 1949] D. Bohm, "The characteristics of electrical discharges in magnetic fields" editors A. Guthrie and R. K. Wakerling (New York: McGraw-Hill)

[Booker 1984] H.G. Booker, "Cold plasma waves", 1984, Martinus Nijhoff Publishers, The Netherlands

[Brambilla 1989] M. Brambilla, "Finite Larmor radius wave equations in Tokamak plasmas in the ion cyclotron frequency range", Plasma Phys. Control. Fusion 31(723) 1989

[Brambilla 1998] M. Brambilla, "Kinetic theory of plasma waves: homogeneous plasma", first edition, 1998, Oxford university press Inc., New York

[Brambilla 1998A] M. Brambilla, "Electron Landau damping of ion Bernstein waves in Tokamak plasmas", Nucl. Fusion 38 (1998) 1805

[Brambilla 2006] M. Brambilla and R. Bilato, "Simulation of ion cyclotron heating of Tokamak plasmas using coupled Maxwell and quasilinear-Fokker–Planck solvers", Nucl. Fusion, 46(7), 2006

[Chabert 2011] P. Chabert and N. Braithwaite. "Physics of Radio-Frequency plasmas", Cambridge University Press, Cambridge, UK, 2011

[Chen 2003] F. F. Chen, lecture notes on Langmuir probe diagnostics, Mini-course on plasma diagnostics, IEEE-ICOPS meeting, Jeju, Korea, June 5, 2003

[Chen 2016] F. F. Chen, "Introduction to plasma physics and controlled fusion", third edition, 2016, Springer International publishing Switzerland

[Child 1911] C. D. Child, "Discharge from hot CaO", Phys. Rev. (Series I), 32(492) 1911

[Chodura 1982] R. Chodura, "Plasma-wall transition in an oblique magnetic field", Phys. Fluids 25(9) 1982

[Clairet 2004] F. Clairet, L. Colas, S. Heuraux and G. Lombard, "ICRF coupling and edge density profile on Tore Supra", PPCF 46(10), 2004

[Colas 2016] L. Colas, L-F. Lu, A. Krivska, J. Jacquot, J. Hillairet, W. Helou, M. Goniche, S. Heuraux and E. Faudot, "Spatial proximity effects on the excitation of Sheath RF Voltages by evanescent Slow Waves in the Ion Cyclotron Range of Frequencies", submitted to PPCF

[Devaux 2006] S. Devaux and G. Manfredi, "Vlasov simulations of plasma-wall interactions in a magnetized and weakly collisional plasma", Phys. Plas, 13(083504), 2006

[D'Ippolito 2006] D. A. D'Ippolito, J. R. Myra,"A radio-frequency sheath boundary condition and its effect on slow wave propagation", Physics of Plasmas (1994-present) 13(10) - (2006)

[D'Ippolito 2008] D. A. D'Ippolito, J. R. Myra, E.F. Jaeger and L.A. Berry, "Far-field sheaths due to fast wave incident on material boundaries", Phys. Plasm. 15 (2008) 102501

[D'Ippolito 2014] D. A. D'Ippolito and J. R. Myra, R. Ochoukov and D. G. Whyte, "Modeling far-field RF sheaths in Alcator C-Mod", AIP Conf. Proc. 1580(2014) 326

[D'Ippolito 2015] D. A. D'Ippolito and J. R. Myra, "A generalized BC for radio-frequency sheaths", AIP Conf. Proc. 1689, 050001(2015)

[Dumont 2009] R. J. Dumont, "Variational approach to radiofrequency waves in magnetic fusion devices", Nucl. Fusion, 49(7), 2009

[Faudot 2013] E. Faudot, S. Heuraux, M. Kubic, J. Gunn and L. Colas, "Fluid modeling of radio frequency and direct currents in a biased magnetized plasma", Phys. Plas. 20(2013) 043514

[Faudot 2015] E. Faudot, S. Devaux, J. Moritz, S. Heuraux, P. M. Cabrera, and F. Brochard. A linear radio frequency plasma reactor for potential and current mapping in a magnetized plasma. Rew. Sci. Inst., 86 :063502, 2015.

[Gahan 2008] D. Gahan, B. Dolinaj and M. B. Hopkins, "Retarding field analyzer for ion energy distribution measurements at a radio-frequency biased electrode", Rev. Sci. Instrum, 79(033502) 2008

[Goniche 2003] M. Goniche, S. Bremond and L. Colas, "Global analysis of ICRF wave coupling on ToreSupra", Nuclear fusion 43(2), 2003

[Godyak 1976] V. A. Godyak, "Steady-state low-pressure rf discharge", Fiz. Plazmy, 2, 141-151 (1976)

[Heuraux 2015] S. Heuraux et.al, "Simulation as a tool to improve wave heating in fusion plasmas", J. Plasma. Phys. 81(435810503), 2015

[Hillairet 2015] J. Hillairet et.al, "Ion cyclotron resonance heating systems upgrade toward high power and CW operations in WEST", AIP Conf. Proc, 1689, 070005 (2015)

[Jackson 1998] J. D. Jackson, "Classical electrodynamics", third edition, 1999, John wiley & Sons, INC

[Jacquot 2013] J. Jacquot, L. Colas, F. Clairet, M. Goniche, S. Heuraux, J. Hillairet, G. Lombard and D. Milanesio,"2D and 3D modelling of wave propagation in cold magnetized plasma near the Tore Supra ICRH antenna relying on the perfectly matched layer technique", PPCF 55 115004 (2013)

[Jacquot 2014] J. Jacquot, D. Milanesio, L. Colas, Y. Corre, M. Goniche, J. Gunn, S. Heuraux, M. Kubic and R. Maggiora, "Radio-frequency sheaths physics: Experimental characterization on Tore Supra and related self-consistent modeling", Phys. Plasma 21, 061509 (2014)

[Jacquot 2015] J. Jacquot et.al, "Full wave propagation modelling in view to integrated ICRH wave coupling/RF sheaths modelling", AIP Conf. Proc, 1689, 050008 (2015)

[Kohno 2012] H. Kohno, J. R. Myra and D. A. D'Ippolito, "A finite element procedure for radio-frequency sheath–plasma interactions in the ion cyclotron range of frequencies", Comput. Phys. Commun. 183(2012) 2116-2127

[Kohno 2012A] H. Kohno, J. R. Myra and D. A. D'Ippolito, "Numerical analysis of radio-frequency sheath-plasma interactions in the ion cyclotron range of frequencies", Phys. Plas. 19(2012) 012508

[Krivska 2015] A. Krivska, V.V. Bobkov, L. Colas, J. Jacquot, D. Milanesio, R. Ochoukov and ASDEX Upgrade team, "Estimation of sheath potentials in front of ASDEX upgrade ICRF antenna with SSWICH asymptotic code", AIP Conf. Proc. 1689, 050002 (2015)

[Kubic 2013] M. Kubic, J. P. Gunn, S. Heuraux, L. Colas, E. Faudot, J. Jacquot, "Measurement of sheath potential in RF-biased flux tubes using a retarding field analyzer in Tore Supra Tokamak", 438(2013) S509-S512

[Lancellotti 2006] V. Lancellotti, D. Milanesio, R. Maggiora, G. Vecchi and V. Kyrytsya, "TOPICA: an accurate and efficient numerical tool for analysis and design of ICRF antennas", Nucl. Fusion 46(2006) S476-S499

[Langmuir 1913] I. Langmuir, "The effect of space charge and residual gases on thermionic currents in high vacuum", Phys. Rev. 2(450) 1913

[Lerche 2010] E. Lerche et al, "Potential of the ICRF heating schemes foreseen for ITER's half-field Hydrogen phase", 23rd IAEA proceedings, THW/P2-03

[Lieberman 1988] M A. Lieberman, both in "Analytical solution for capacitive RF sheath", IEEE transaction on plasma science 16(6) 1988

[Lieberman 2005] M. A. Lieberman, A. J. Lichtenberg, "Principles of plasma discharges and materials processing", 2nd edition, Wiley 2005

[Louche 2015] F. Louche et.al, "Designing the IShTAR antenna: Physics and engineering aspects", AIP Conf. Proc, 1689, 070016 (2015)

[Lu 2016] L. Lu, K. Crombe, D. Van Eester, L. Colas, J. Jacquot and S. Heuraux, "Ion cyclotron wave coupling in the magnetized plasma edge of Tokamaks: impact of a finite, inhomogeneous density inside the antenna box", PPCF, 58(5) 2016

[Messiaen 2010] A. Messiaen, R. Koch, R. R. Weynants, P. Dumortier, F. Louche, R. Maggiora and D. Milanesio, "Performance of the ITER ICRH system as expected from TOPICA and ANTITER II modelling", Nucl. Fusion, 50(2) 2010

[Messiaen 2011] A. Messiaen, R. Weynants, "ICRH antenna coupling physics and optimum plasma edge density profile. Application to ITER", PPCF 53(8), 2011

[Mayberry 1990] M. J. Mayberry et.al, "Coupling of fast waves in the ion cyclotron range of frequencies to H-mode plasmas in DIII-D", Nuclear fusion 30(4), 1990

[Noterdaeme 1993] J-M. Noterdaeme and G. Van Oost, "The interaction between waves in the ion cyclotron range of frequencies and the plasma boundary", PPCF 35 (1993) 1481-1511

[Ochoukov 2014] R. Ochoukov et.al, "ICRF-enhanced plasma potentials in the SOL of Alcator C-Mod", AIP Conf. Proc. 1580(2014) 267

[Pécoul 2002] S. Pécoul, S. Heuraux, R. Koch and G. Leclert Numerical modeling of the coupling of an ICRH antenna with a plasma with self-consistent antenna currents, Comput. Phys. Commun. 146(166) 2002

[Perkins 1989] F. W. Perkins, "Radiofrequency sheaths and impurity generation by ICRF antennas", Nucl. Fusion, 29(4) 1989

[Smithe 2015] D. N. Smithe, T. G. Jenkins and J. R. King, "Improvements to the ICRH antenna time-domain 3D plasma simulation model", AIP Conf. Proc. 1689, 050004(2015)

[Stangeby 1994] P. C. Stangeby, "The Bohm-Chodura plasma sheath criterion", Phy. Plas. 2(702), 1995

[Stangeby 2000] P.C. Stangeby, "The Plasma Boundary of Magnetic Fusion Devices", Plasma Physics Series, IoP Publishing Ltd, Bristol, UK (2000).

[Stangeby 2012] P. C. Stangeby, "The Chodura sheath for angles of a few degrees between the magnetic field and the surface of divertor targets and limiters", NF, 52 083012 (2012)

[Stix 1992] T. H. Stix, "Waves in plasmas", 1992, AIP Press

[Swanson 2003] D. G Swanson, "Plasma waves", second adition, 2003, IoP Publishing Ltd, Bristol and Philadelphia

[Van Eester 1989] D. Van Eester, "The effect of temperature, oblique incidence and poloidal magnetic field on wave propagation, damping and mode conversion in the ion cyclotron resonance frequency domain", PhD thesis, laboratory of plasma physics, Ecole Royale Militaire, 1000 Brussels, 1989

[Van Eester 2013] D. Van Eester, K. Crombé and V. Kyrytsya, "Connection coefficients for cold plasma wave propagation near metallic surfaces", PPCF, 55 055001 (2013)

[Van Eester 2015] D. Van Eester and K. Crombé, "A crude model to study radio frequency induced density modification close to launchers", Phys. Plas. 22(2015) 122505

[Verboncoeur 1995] J. P. Verboncoeur, A. B. Langdon and N. T. Gladd, "An object-oriented electromagnetic PIC code", Com. Phys. Comm. **87**(1995) 199-211

Chapter 3   Study of wave coupling with density inside ICRF antenna box

3.1   Introduction of this chapter

From chapter 2, we know that the fast wave can propagate into high density plasma, which is why this type of wave is often used as heating wave, whereas the slow wave only propagates in plasmas with fairly low densities**.** Most current-day ICRF heating codes and antenna codes mentioned in section 2.4.1 assume the density close to the antenna is sufficiently low to allow it being neglected altogether, and restrict themselves to the fast wave excitation. In reality, a low but finite density is actually present inside the antenna box and a fast wave antenna parasitically excites the slow wave. So an intriguing question is whether this presence of density profile inside antenna will significantly change the results outside the antenna box. Furthermore, since no accurate density measurement presently exists experimentally inside the antenna box, one may ask whether an accurate density profile is essential. The power carried by the fast wave is the main heating power. For a given $n_{//}$, the fast wave is evanescent below the R cut-off layer (section 2.1.5) and propagating above. The power coupling is sensitive to the fast wave evanescence length (section 2.1.6). For tokamak parameters like those of Tore Supra used in *Figure 2.4*, the R-cut off layer for the main $n_{//}$ of a Tore Supra antenna with antisymmetric (dipole) strap phasing locates at the plasma density close to 10^{18} m^{-3}. For smaller $n_{//}$, the R-cut off layer shifts from the center plasma towards the wall. So another question is how much the density profile inside antenna box can affect R-cut off layer and the coupling power.

The physical behavior becomes more complicated when the Lower Hybrid (LH) resonance (section 2.1.5) appears inside the antenna box. For typical tokamak parameters, i.e. ToreSupra, the LH resonance appears at the plasma density approaching 10^{17} m^{-3}. The density is well beyond the LH resonance at the last closed flux surface but well below it or marginally below it at the position of the straps. Hence the LH resonance is a natural ingredient of wave behavior close to launching structures. Numerous papers have talked about this resonance. Puri [Puri 1973] discovered the collisional energy absorption at the LH resonance leads to a high plasma heating efficiency. Brambilla [Brambilla 1998] points out that the slow wave near this resonance actually shows some properties of the electrostatic waves. Recently, Després and Campos Pinto [Campos Pinto 2016] proposed a new weak formulation to solve the wave equation across the LH resonance. In their method, the specific line in the standard finite element matrix, which reflects the LH resonance is replaced by an integral relation. This method could capture the exact solution even in a relatively coarse mesh in the zero dissipation limits. Somehow at this moment, this method is limited in 1D and deals with the fast wave only. Crombé and Van Eester [Crombé 2014] discussed the wave behavior below the LH resonance, where the slow wave starts to propagate. From its dispersion relation, the slow wave having a nature of short wavelength can be very sensitive to the mesh size in the numerical simulations. Moreover, as the wavelength gets very short, the thermal effect starts to play a role. An unusual situation is met at the LH resonance where the perpendicular wavelength of the slow wave shrinks to zero. One may wonder if it is possible to numerically capture this wave sufficiently accurate. And if it is not as claimed in [Crombé 2014], does a non-converged result inside antenna box significantly affect the results outside the box? It is interesting to know if this thin layer has a global impact

or not. Another question being whether the power carried by the slow wave to this resonance is significant or not.

The 2D RAPLICASOL code [Jacquot 2013] has been used to investigate the radiated electric fields in the presence of a finite, inhomogeneous density inside the antenna box. Essentially, the fields below lower hybrid resonance, and the power coupling property with the appearance of lower hybrid resonance were examined in detail and the results of this study will be discussed in this chapter.

The structure of this chapter is the following: Section 3.2 gives the specifications of the code and the parametric setup for the numerical tests, i.e. density profiles, mesh size, magnetic field tilt angle and phasing. Section 3.3 tunes the PML depth to minimize numerical costs while still guaranteeing a good level of power absorption. Section 3.4 and 3.5 analyze the simulated RF near field pattern inside the antenna box. Section 3.6 shows the radiated power at the antenna mouth and the role of the density gradient in front of antenna straps on the fast wave power coupling. Section 3.7 is the final discussion and conclusion. A simplified version of this chapter was published in [Lu 2016]

3.2   Specifications of the 2D RAPLICASOL code with tilted B_0

To answer the questions being asked in the introduction, we need a dedicated numerical code. It should cover the following physics, a) Fields are excited by a realistic ICRF antenna model includes all the essential elements, antenna box, strap, limiter and so on. b) Fields need to be solved in a tokamak (cold) plasma, which is described by a full dielectric tensor. c) Both the fast wave and the slow wave should be considered simultaneously. d) It should accommodate a continuous and inhomogeneous plasma density across R-cut off layer and LH resonance. e) Fine mesh is needed in order to capture the short wavelength structure. f) As any other numerical code, it should save the computational resource as much as possible. g) At last, for our specific interests, implementing RF sheaths should be easy in a later stage of development.

The 2D RAPLICASOL code [Jacquot 2013] has a realistic 2D geometry, which takes advantage of the finite element solver in COMSOL. It is a cut from the middle plane of the 3D realistic ICRH antenna, see *Figure 3.1*. Using COMSOL allows one cutting down the time spent on the code development. The geometry is shown in *Figure 3.2*, where the x direction corresponds to the toroidal direction, y is the radial direction and z (out of plane component) is the poloidal direction in a Tokamak geometry where the curvature effect has been ignored. The antenna includes two straps, the antenna box, central septum and lateral limiters, indicated as the blank components. All passive metallic elements are treated as Perfect Electric Conductor (PEC): at their interface with the plasma the tangential RF electric field vanishes. The antenna mouth is shown as a dashed line. We will not consider sheath in this chapter, i.e. all the external boundaries are PEC.
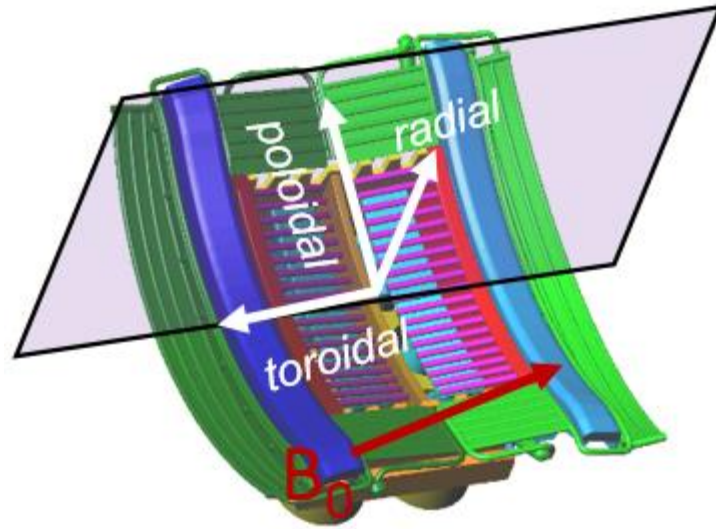
Figure 3.1. A diagram of Tore Supra ICRH prototype antenna. The shading area represents the geometry adopted in the 2D RAPLICASOL modeling
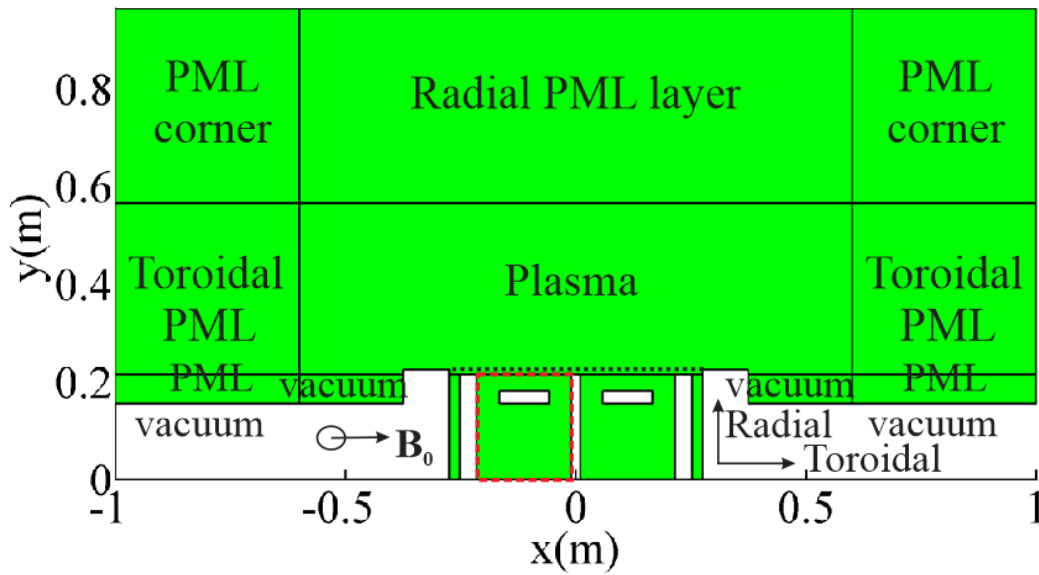
Figure 3.2.Schematic view of 2D RAPLICASOL code in the case of a tilted B_0 in poloidal (z) direction. The computational area is shown in green. Dashed line is the antenna mouth. The red dashed rectangle represents one of the two individual boxes that consists the antenna box.

The magnetic field is tilted as described in *Figure 2.1*. Accordingly, the cold plasma tensor is defined in Eq. (2.10). The tilted magnetic configuration, which did not appear in the previous version of this code, can introduce the fast wave in describing the Direct Current (DC) sheath biasing by RF sheath rectification [Lu 2016]. Thus makes it compatible with the new SSWICH-FW code. To save the computational resource, our simulation domain is radially and toroidally close to the vicinity of a wave launcher. We assume the wave transmitted to the central plasma never comes back to the antenna (single-pass absorption), which could occur in a real hot tokamak plasma. Under this assumption, the Perfectly Matched Layer (PML) is used in the code surrounding the plasma region, to emulate radiating boundary conditions in two

directions. The propagating fast wave is damped artificially in these layers with very low reflections. The PML technique described in [Jacquot 2013] is extended to tilted **B₀** [Lu 2016A] and has been recently further adapted to a curved cylindrical geometry [Jacquot 2015]. In this 2D code, the poloidal geometry is assumed to be infinite and homogenous. As a consequence, the poloidal derivative is set to zero. A 3D simulation tool is developed in parallel with this work in [Jacquot 2015]. It is however extremely memory demanding, and the convergence of the iterative solver is much more difficult to achieve. Thus all the simulations in this paper are done using the 2D code.

In this chapter, we use a plasma solely composed of D ions. Furthermore, the following Tore Supra like parameters are taken [Jacquot 2014]: magnetic field at antenna mouth **B₀**(y=0.224)=2.32T, RF wave frequency 48MHz. The magnetic field strength scales as $1/R_a$, with R_a the major radius axis. In our adopted geometry, R_a=3.382-y. All the simulations in this chapter were done using a dedicated workstation with 64Gb of RAM memory.

Table 3-1. Density profiles used inside the antenna box

Density	Value inside antenna box (m⁻³)	Density at wall (m⁻³)	Location of LH resonance
0	0	0	Not present
1	Extrapolate experiment profile to 10^{17}	1×10^{17}	Not present
2	$n_e=10^{18}$exp(-(0.2195-y)/0.0933)	9.5×10^{16}	Not present
3	$n_e=10^{18}$exp(-(0.2195-y)/0.0477)	1×10^{16}	y=0.1056m
4	$n_e=10^{18}$exp(-(0.2195-y)/0.0318)	1×10^{15}	y=0.1434m

A set of continuous density profiles is used inside the antenna box, the details are shown in *Table 3-1*. *Figure 3.3* is the density profile from Tore Supra shot TS 40574, the same as in *Figure 2.2*, but plotted in the new geometry. It is used outside of the antenna box. *Figure 3.4* is the density profiles inside the antenna box, corresponding to the density profiles listed in *Table 3-1*. For the adopted magnetic field and RF wave frequency, the LH resonance occurs at n_e=9.2×10¹⁶ m⁻³ i.e. at a density crossed by density 3 and density 4. In this chapter, we only consider the cases where the straps locate above the LH resonance and the LH resonance is not crossed anywhere outside the antenna box.
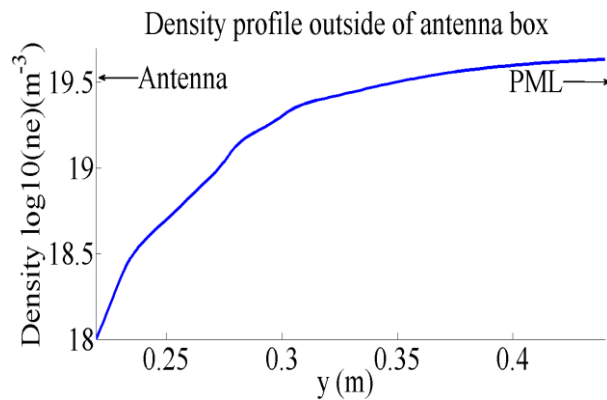
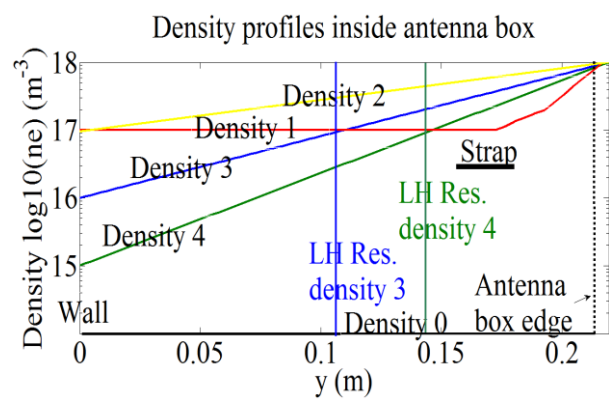*Figure 3.3. Density profiles above the antenna, from TS 40574*

Figure 3.4. Density profiles inside the antenna box. Vertical solid lines indicate the locations of the LH resonance. Vertical dot line specifies the edge of the antenna box.

Our major goal is to investigate the field structure inside the antenna box, where the slow wave may become propagating. As mentioned above, the slow wave generally has a short wavelength. This requires a very fine mesh. In the following simulations, we use four different meshes with triangular shape through all the domain. The details is shown in *Table 3-2*.

Table 3-2. List of meshes used in the simulations

	Mesh 1	Mesh 2	Mesh 3	Mesh 4
Grids size (x, y)	4mm*4mm	4mm*2mm	2mm*4mm	2mm*2mm
Number of grids in each individual box	52*54	52*108	104*54	104*108
Specific refinement	Up to 800*800			

In those regions where the slow wave is supposed to be present, i.e. near the antenna mouth, a mesh refinement is added, generally 4 times or 8 times finer than the other regions. A typical simulation time using the above mesh is around 6 minutes. In case we need to check the convergence with extremely fine mesh, more intensive meshes are used, up to 800*800 grid points in each individual box. A 3D simulation with such a mesh density can easily run out of memory. This explains why we restrict our investigation to two dimensions.

The magnetic field in this code can be tilted continuous from -90º to 90º. We start from non-tilted (0º) case, then pick up a realistic angle (for Tore Supra) 7º and a large angle 60º for all the field analysis. In the power coupling analysis, a scan of tilt angle from -90º to 90º is conducted for the sake of completeness although extreme tilts are clearly unrealistic in tokamaks.

The waves are excited by imposing current on the straps. All the simulations are done with 1A poloidal current imposed on each strap. Both antiparallel strap currents (dipole phasing [0 π]) and parallel ones (monopole phasing [0 0]) are considered in order to change the radiating toroidal spectrum.

3.3   Tuning the PML for implementing good radiation conditions at minimal numerical cost

As having been introduced in Chapter 2, a PML is an artificial lossy medium used to enforce radiation conditions by stretching the spatial coordinates into the complex domain. Three PMLs are used in the radial-toroidal plane, see *Figure 3.2*. Radial PML can stretch its coordinates in the positive vertical direction, while toroidal PMLs can stretch in horizontal directions. Additional PML corners in each upper corner can stretch both in horizontal and positive vertical direction, thus keeping the continuity of stretched coordinates. The spatial extension of this PML is marked by Lpmlt and Lpmlr, shown in *Figure 3.5*. These two parameters need to be determined before doing any wave coupling simulation.
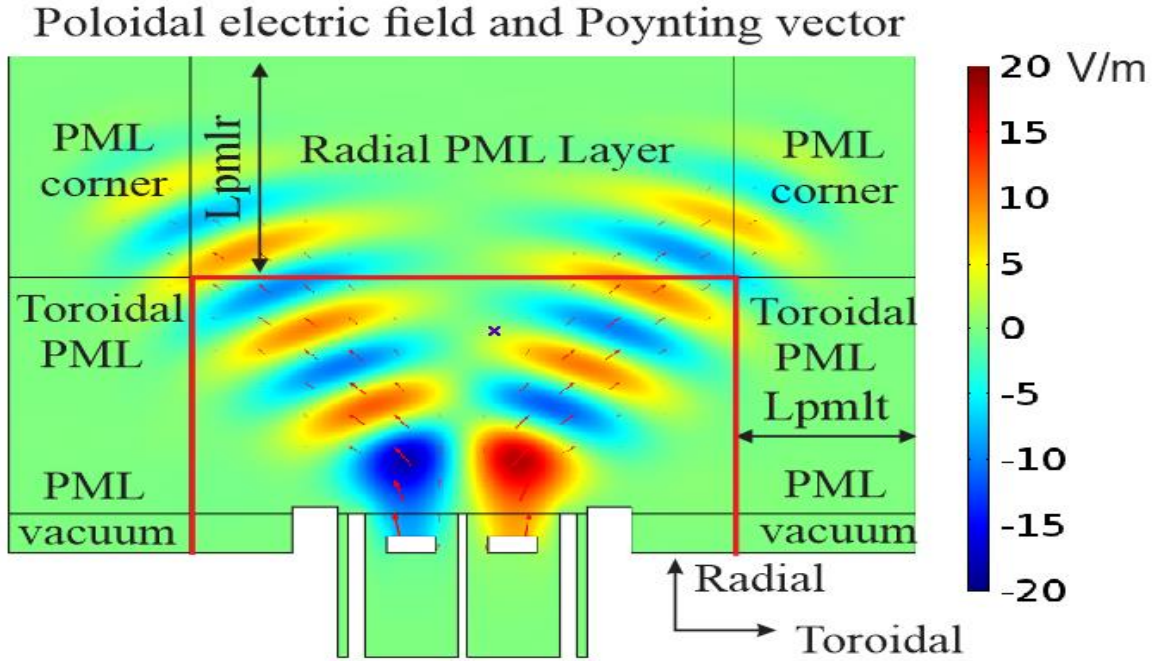
Figure 3.5. 2D map of real part of poloidal electric field in dipole phasing with θ=0º. Arrows represent the Poynting Vector. Density 0 is used in the antenna box. Red lines are defined for the power measurement propose. Lpmlt=Lpmlr=0.4m.

Lpmlt and Lpmlr are chosen according to the following considerations: A. the slow wave should have been evanescent before reaching the radial PML, since this PML cannot describe FW and SW at the same time. B. most of wave power is supposed to be absorbed in the radial PML layer, as wave propagates into the center plasma in real tokamak heating. The analytical reflected coefficient for the propagating plane wave with wave number k_r inside radial PML reads [Jacquot 2013],

$$\eta = \exp(-2k_r \mathrm{Lpmlr} \frac{S_r^{''}}{p_r + 1})\tag{3.1}$$

Where $S_r^{''}$, P_r have been introduced in Eq. (2.48).

Theoretically, any of the results in the main plasma should not be PML dependent. From the numerical point of view, we prefer to have a small PML depth to save memory since the PML also needs to be meshed. Meanwhile, according to Eq. (3.1), a larger PML depth is needed to sufficiently damp the wave. So a scan of each PML depth is conducted to obtain a minimum PML depth that needs a least memory consumption, and keep at the same time the results unaffected.

We chose a small tilt angle, 7º (corresponding to the tilt angle in TS), scan the radial PML depth, Lpmlr, from 1m to 0.09m with step size 0.1m, to examine the fluctuation of the total absorbed power. Power is calculated as the real part of the flux of the Poynting vector through three PML-plasma interfaces (red lines in *Figure 3.5*).
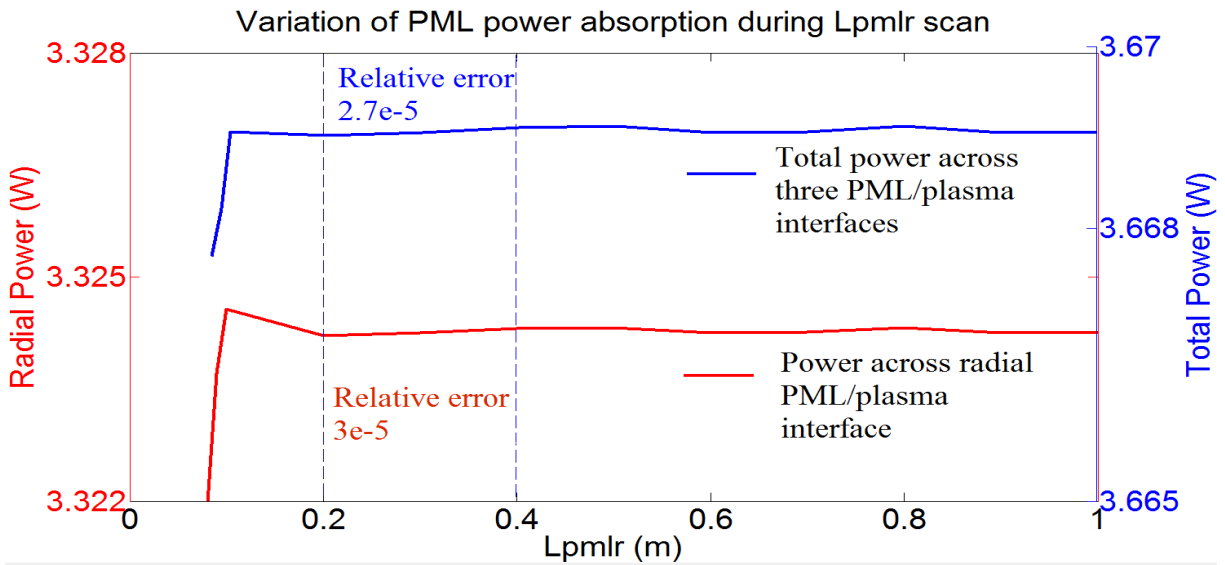
Figure 3.6. A scan of radial PML depth with θ=7°, toroidal PML depth at 0.4m. Criterion PML depth is found at 0.4m, where relative error goes below 1×10⁻⁴

Figure 3.6 compares variations of total radiated power and power crossing the radial PML/plasma interface (the top red line in *Figure 3.5*). It shows that when the PML depth is 0.4m, the power variation is in a scale of 10^{-5}. If we set 1e-4 as a criterion of relative variation, then the criterion value of Lpmlr can accordingly to be put as 0.4m. In *Figure 3.6*, more than 90% of the total radiated power is crossing the radial PML/plasma interface. The same PML criterion depth is found at a large pitch angle, 70°, thus the degree of pitch angle apparently does not significantly affect the PML criterion depth.
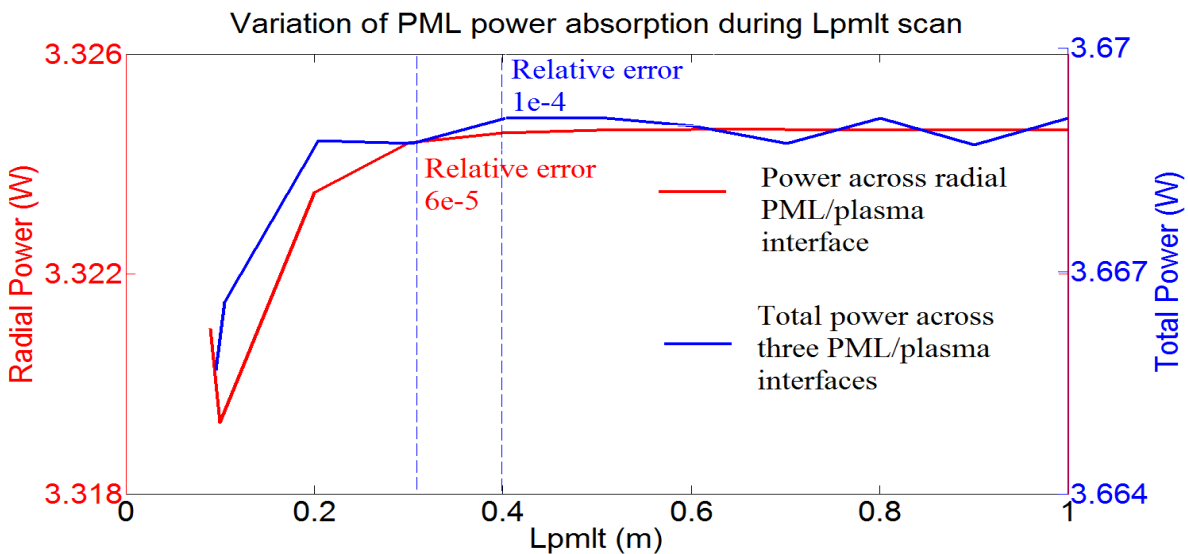
Figure 3.7. A scan of toroidal PML depth with a pitch angle of 7 degree. Radial PML depth is 0.4m. Criterion length is also set at Lpmlt=0.4m

After choosing this Lpmlr criterion depth, we start another scan of the toroidal PML length, Lpmlt. Its criterion depth is also chosen to be 0.4m, see *Figure 3.7*. The simulations of the poloidal electric field and power flow in *Figure 3.5* use these two PML depth. We see the electric field is indeed being sufficiently damped before reaching the metallic boundaries surrounding the PMLs. The criterion PML depth obtained in this section will be used in all of the simulations in this thesis.

3.4   Near field pattern above the Lower Hybrid resonance

This section investigates the RF electric field pattern in the region where the density is above the density at which the lower hybrid resonance condition is satisfied. When the magnetic field is non-tilted, and when the symmetric excitation conditions are used, i.e. dipole and monopole, one can apply "mirror" boundary conditions at the middle of the antenna: perfect electric conductor for dipole and perfect magnetic conductor for monopole. The RF quantities, i.e. poloidal current density J_z, Poynting components S_x and S_y, electric field components E_x, E_y and E_z thus show some symmetric and anti-symmetric properties, see *Table 3-3*. Using this symmetric properties, one can half the simulation domain if rather needed. Often, it provides a quick check of the simulation results. Under tilted magnetic field, these properties are lost.

Table 3-3. Symmetry and anti-symmetry properties of RF quantities dipole phasing and monopole phasing in non-tilted magnetic configuration

Original quantities	Dipole phasing, toroidal $\mathbf{B_0}$	Monopole phasing, toroidal $\mathbf{B_0}$
$J_z(x,y,z)$ or $E_z(x,y,z)$	$J_z(x,y,z)= -J_z(-x,y,z)$ $E_z(x,y,z)= -E_z(-x,y,z)$	$J_z(x,y,z)= J_z(-x,y,z)$ $E_z(x,y,z)= E_z(-x,y,z)$
$E_x(x,y,z)$ and $S_x(x,y,z)$	$E_x(x,y,z)= E_x(-x,y,z)$ $S_x(x,y,z)= -S_x(-x,y,z)$	$E_x(x,y,z)= -E_x(-x,y,z)$ $S_x(x,y,z)= -S_x(-x,y,z)$
$E_y(x,y,z)$ and $S_y(x,y,z)$	$E_y(x,y,z)= -E_y(-x,y,z)$ $S_y(x,y,z)= S_y(-x,y,z)$	$E_y(x,y,z)= E_y(-x,y,z)$ $S_y(x,y,z)= S_y(-x,y,z)$

The power spectrum also exhibits a mirror symmetry property under opposite tilt angles. The toroidal power spectrum shown in *Figure 3.8* is calculated at the radial PML/plasma interface and the magnitude is normalized to satisfy continuous Parseval theorem. In this simulation, the main plasma toroidal width is extended to a large scale, 5m, in order to satisfy periodic conditions presumed by Fourier transformation. It seems the most efficient n_x or the center of main lobe does not change with different pitch angles. The power spectrum concentrates more on one direction when the pitch angle increases, however, it still displays mirror symmetry with $\theta \rightarrow -\theta$ transform.

From the dispersion plot *Figure 2.4*, we know that only the fast wave is propagating in the region above the LH resonance. The fast wave has a large poloidal electric field, thus it is reasonable to look at this electric component. *Figure 3.9* takes density profile 3 in the antenna box. The electric field is anti-symmetric as the magnetic field is non-tilted. One can see the fast wave is propagating in the plasma and being damped inside the PML. The perpendicular wavelength of the fast wave is around 15cm, which is compatible with the calculation from the dispersion relation Eq. (2.17), using a parallel refractive index $n_{//}$=9.14 (main lobe of the spectrum in *Figure 3.8*). The poloidal electric field changes less than 1% when switching from density 0 (vacuum) to density 3 and it varies less than 0.1% between density 3 and density 4 (*Figure 3.10*). *Figure 3.11* shows the differential poloidal electric field taken from two simulations with

different mesh grids, while other parameters are taken the same as *Figure 3.9.* The scale of differential poloidal field in *Figure 3.11* is 3 orders of magnitude smaller than the poloidal field in *Figure 3.9* . *Figure 3.12* is a zoom on the region around the straps surrounded by a red rectangle in *Figure 3.11*. It shows the relative difference of poloidal electric field is less than 10^{-3}. The relative difference is twice larger under large tilt angle, i.e. theta=60º. One may expect in this case the antenna excites a larger part of the slow wave rather than the fast wave (note the slow wave needs a large parallel electric field to be excited, it is the case when the strap orients along the magnetic field). So it will be more sensitive to the mesh.
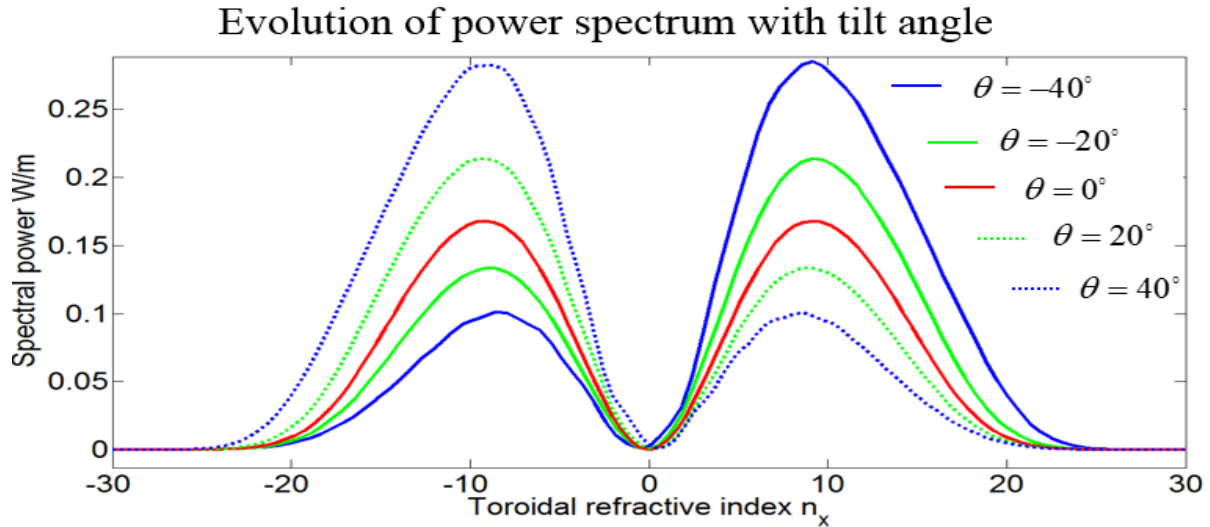

Figure 3.8. Toroidal power spectrum with different tilt angles. Date picks at the radial PML/plasma interface, density 0 inside the box
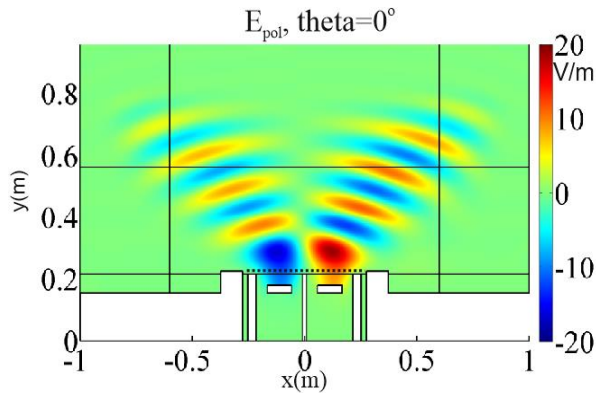
Figure 3.9. Real part of the poloidal electric field, theta=0º, mesh 2, density 3, dipole phasing
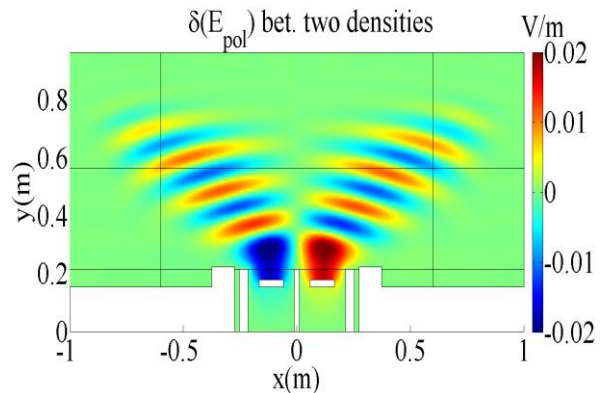
Figure 3.10. Differential field map for the real part of the poloidal electric field, i.e. Epol(density 4)-Epol(density 3)
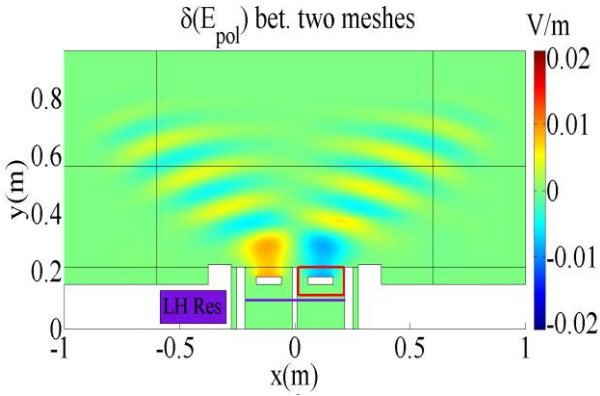
Figure 3.11. Differential field for the real part of poloidal electric field, i.e. Epol(mesh 1)-Epol(mesh 2). Horizontal line: location of LH resonance. Rectangle: box region shown in Figure 3.12
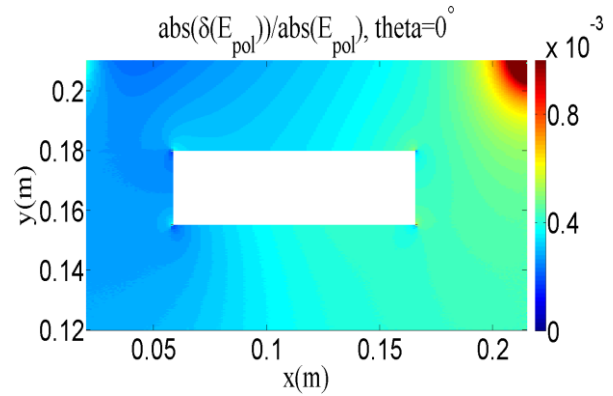
Figure 3.12. Relative error of poloidal electric field. Zoom in the antenna strap's region surrounded by rectangle in Figure 3.11

The radial electric field is also independent on the above mesh sizes outside the antenna box. While inside the antenna box, compared to the vacuum case, new filaments along the toroidal direction appear in both the toroidal electric field and the radial electric field, see *Figure 3.13-Figure 3.14*. Smoothing the corner, imposing different distributions of surface current, i.e. hyperbolic cosine, do not totally remove these filaments.
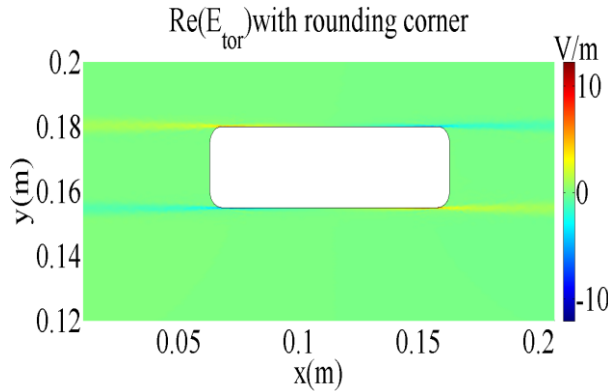
Figure 3.13. Toroidal electric field in the antenna strap region surrounded by rectangle in Figure 3.11, with hyperbolic cosine distribution of RF current over straps with rounded corners
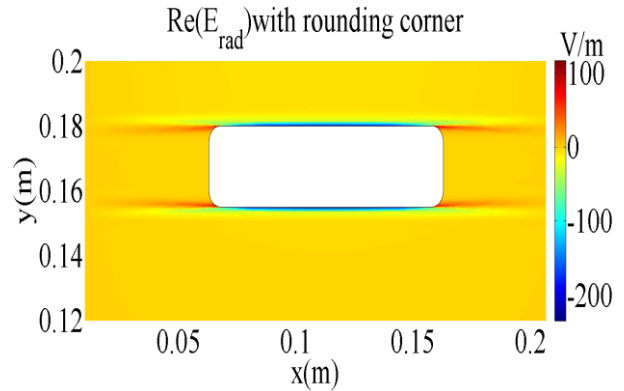
Figure 3.14. Same as Figure 3.13, radial electric field

From *Figure 3.12*, we see that the poloidal electric field is determined by the imposed current and is thus independent on the mesh (size). However unlike in a vacuum antenna, where electric fields on the strap surface normally have a converged solution, further tests show that in a plasma-filled antenna box, it is more difficult to ensure numerical convergence of the toroidal and radial electric field around the strap. A simulation with an extremely intensive mesh shows that the field at the corner points is still not converged, see *Figure 3.15*. This non-converged problem appearing in the neighborhood region of antenna in the presence of plasma [Crombé 2014] is most likely caused by the excitation of the slow wave.

A check of polarization also gives the same indication, that a slow wave fulfills the magnitudes of all the electric components around the strap. Besides, the polarization of the slow wave indicates that the radial electric component of the slow wave is coupled with its parallel electric component [Myra 2010]. The latter is increasing with the tilt angle. Thus one can anticipate that the radial electric field also increases with the tilt angle. Simulation shows that the real part of the radial electric field at theta=20° is indeed twice larger than idem value at theta=0°.
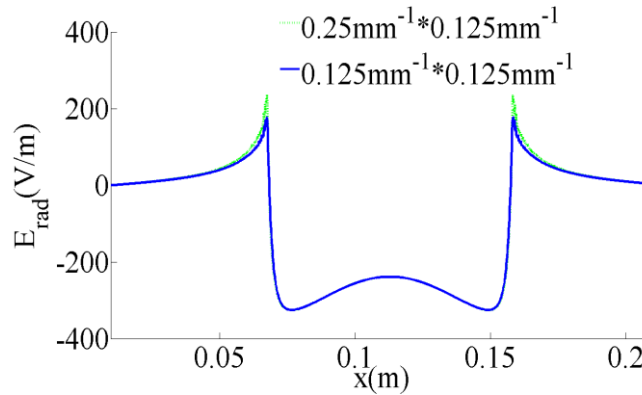
Figure 3.15. Toroidal distribution of Re(E$_{rad}$) on the front face of the right strap, under two very dense symmetric meshes, other conditions are the same with Figure 3.14

COMSOL is unable to go further than the mesh used in *Figure 3.15*, due to the memory limits. Thus a semi-analytical model has been built to further investigate the physics related to the filament. The details can be found in the Appendix A. For simplicity, the field is excited by a sheet of poloidal current in this model. It has a 2D geometry with 3 metallic walls and 1 radiating boundary. By assuming the fast wave and the slow wave are decoupled, one can separate the contribution from the fast wave and the slow wave to the total electric field. This model has successfully reproduced the filament surrounding the current sheet by conducting Fourier analysis for a sufficient large number of plane wave eigenmodes. The spatial resolution is 10 times' finer than *Figure 3.15*. Results show that this filament persists under such a high resolution and it is indeed associated with the slow wave, which demonstrates that a fast wave antenna can excite the slow wave. The slow wave is strongly evanescent here and is sensitive to the stix tensor element $\varepsilon_{//}$. One can estimate that the perpendicular evanescence length is changing with the square root of $\varepsilon_{//}$, see Eq. (2.19). This was confirmed by artificially changing the $\varepsilon_{//}$ value, see the Appendix A.

In realistic 3D simulations, most of the excitation is done through imposing a certain voltage on the straps, thus the currents on the strap are computed self consistently. Unlike we fix the direction of current flow on the antenna here, in a voltage excitation, the tilt angle is relevant w.r.t. the direction in which the current flows on the antenna. Self-consistent computations give rise to image currents on metallic objects and they locally play the role of 'antenna' as well. These may change the slow wave excitation. Besides, a slow wave can also be generated via mode conversion when the geometry has a shape transition [Kohno 2015]. A voltage excitation and curved geometry has been implemented in the 3D RAPLICASOL code [Jacquot 2015].

3.5   Non converged field below the Lower Hybrid resonance

In this section, the fields near and below the lower hybrid resonance are shown. We use the density 3 and density 4, in which the LH resonance is crossed inside the antenna box. As said before, only the slow wave is propagating in this region. Near the LH resonance, the slow wave has a characteristic of an electrostatic wave. Its polarization Eq. (2.30) approximates to

$$\frac{E_{rad}}{E_{tor}} \approx \frac{n_\perp}{n_{//}} \approx \pm\sqrt{-\varepsilon_{//}/\varepsilon_\perp} \tag{3.2}$$
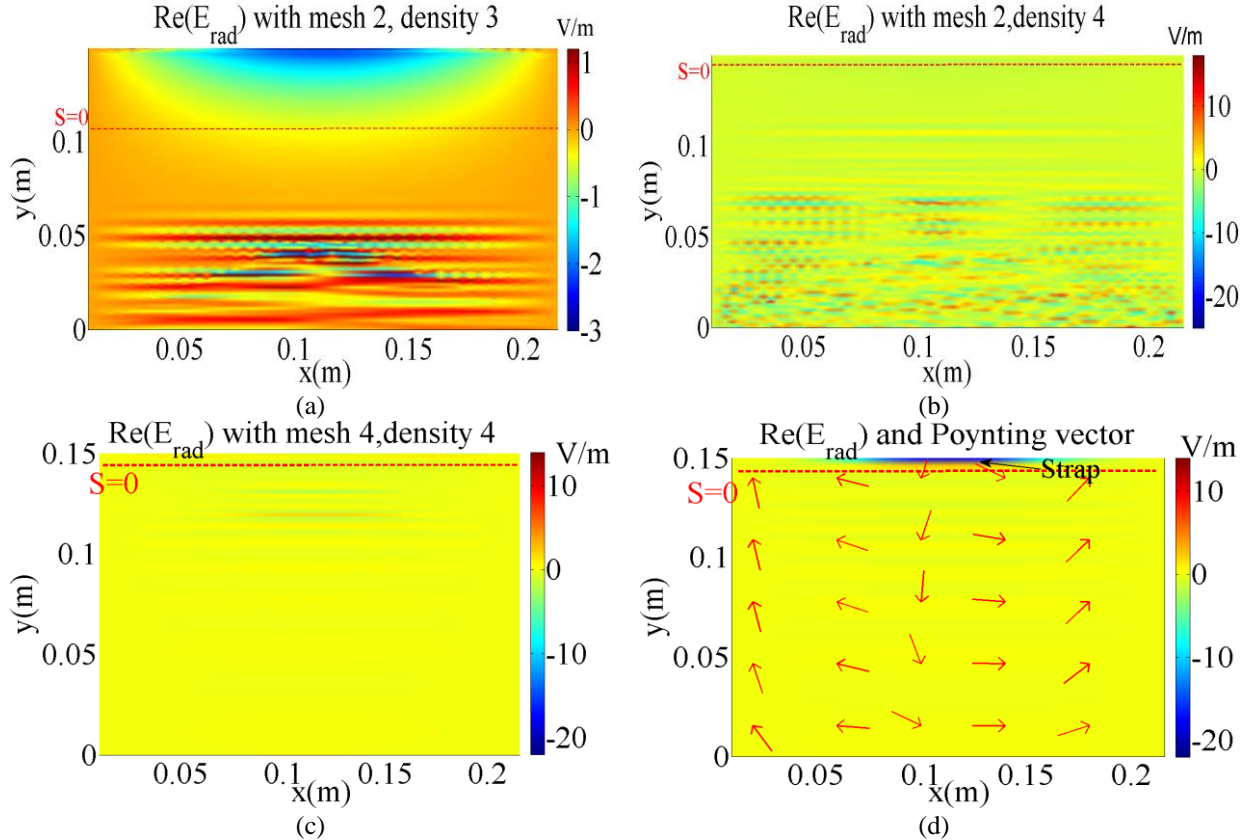
Figures 3.16. *(a)-(b). Real part of the radial electric field with different density profiles, but the same mesh. Dipole phasing, theta=0⁰. (c). the same simulation as (b) but with mesh 4. (d) Radial electric field, using density 4, the same mesh size as mesh 4 but with square grid, instead of triangle. Red arrows indicate the normalized real part of the Poynting vector*

Hence one can know the direction of the phase velocity from the ratio of relevant electric fields. *Figures 3.16* (a)-(b) use exponential density profile 3 and 4 with the same mesh 2. Locations of the lower hybrid resonance are indicated by red dot line, specifically at y=0.1056m and y=0.1434m. One can see below the resonance, new fields start to grow and as the density decreases, more and more modes appear. In dipole phasing, this structure is anti-symmetric between two individual boxes, with respect to the antenna septum, under the condition of a symmetrical mesh. The radial electric field is about 20 times larger than the toroidal electric field, which is consistent with the typical ratio of $\sqrt{-\varepsilon_{//}/\varepsilon_\perp} \approx \sqrt{500/1} \approx 20$, so the phase velocity of the slow wave is mainly in the radial direction. The poloidal electric field is still independent on the mesh in this region.

The slow wave propagates between the lower hybrid resonance ($\varepsilon_\perp = 0$) and $\varepsilon_\perp = n_{//}^2$. One generally considers that the parallel refractive index $n_{//}$ is determined by the antenna geometry and phasing in the main plasma, which can approximately be seen as an invariant spectrum. But this may not be the case in the region below the LH resonance. From *Figures 3.16* (b), one can see the slow wave behaves like cavity modes, where modes with $k_{//} = \frac{2\pi n}{L}$ (with *n* an arbitrary integer and L the toroidal dimension of metallic box) are selected and added up together. Aside from propagating along the radial direction, it bounces between two toroidal metallic walls. The toroidal modulation of the small-scale structure that appears in the lower part of *Figures 3.16* (b) agrees with the grid's size. This suggests that the field structures below the LH resonance are not totally resolved by the present mesh grids.

From the slow wave dispersion relation Eq (2.18), one knows that in its propagating region, for a given $k_{//}$, the perpendicular wave vector $k_\perp$ decreases as the density decreases, see the red line in *Figure 2.4*. This is consistent with *Figures 3.16* (a), where the $\lambda_\perp$ (perpendicular wave length) is increasing as the density decreases from upper to bottom.

Although the propagative region for the slow wave mode is surrounded by 3 metallic walls and one resonance, it is not a lossless resonant cavity for the slow wave. The energy of the slow wave can be transferred through mode conversion to the fast wave at the wall (under tilted magnetic field) or at the LH resonance. Since no damping mechanism is considered in the box, i.e. frequency and all dielectric tensor element have a real value, all the radiative energy (real part of power flow) could finally be transferred to the fast wave, which then carries this power out of the antenna box. This is shown in *Figures 3.16* (d) where the direction of the normalized real Poynting vector indicating the power flow indeed goes to the LH resonance and lateral metallic walls. Although potentially the slow wave can also carry power out of the antenna box, the wave emanating from the box (be it a fast wave, a slow wave or a combination) seems to be essentially the same, i.e. the active power is better converged than the sloshing power. Finally only the slosh power (imaginary part of power flow) remains bouncing inside box.

Given the small radial scales appearing in *Figures 3.16*, one can anticipate that the mesh size near the wall might affect the numerical results. To see this, we check the case where we add a specific mesh refinement in the region within a distance of 0.008m to the antenna box wall. We find that *Figures 3.16* (a) with density 3 changes 10% of values, while *Figures 3.16* (b) with lower density (density 4) changes 200%.

A further test shows that the non-convergence persists up to the memory limits of the adopted workstation (800*800 grid points inside each individual box). This confirms the observation from another finite difference code [Crombé 2014] about the non-convergence behavior of the field below lower hybrid resonance. This instability is increasing under larger tilt angle which again coincides with the fact that the antenna excites more slow wave in that case. No explicit dependence on antenna phasing is observed. This is not surprising for the simulations considered. The straps are housed in individual boxes. The LH resonance is rather deep inside the box. Each slow wave resonant cavity may be therefore mainly influenced by one single strap.

3.6   Power coupling and radiating spectra

One can use Eq. (2.46) to evaluate the total power emitted from the straps. Since we only imposed the poloidal current, the volume integral in LHS can be reduced to a line integral to a scalar product. Since our radiation medium is loss-less, we checked that the power flow at the antenna mouth exactly equals the

line integration at the strap. From *Figure 3.11*, we know that the poloidal electric field is almost independent on the mesh and the current is imposed externally. So the total emanating power as well as the power flow in the plasma is independent on the mesh.

Most antenna design codes assume the antenna is sitting in a vacuum region. It is interesting and important to check how different the power and the electric field near the antenna mouth are when one compares the difference between a plasma-filled and a vacuum antenna box. In the following test, we measure power by doing a line integral of radial power flow, the real part of Poynting vector, across the antenna mouth (dashed line in *Figure 3.2*).
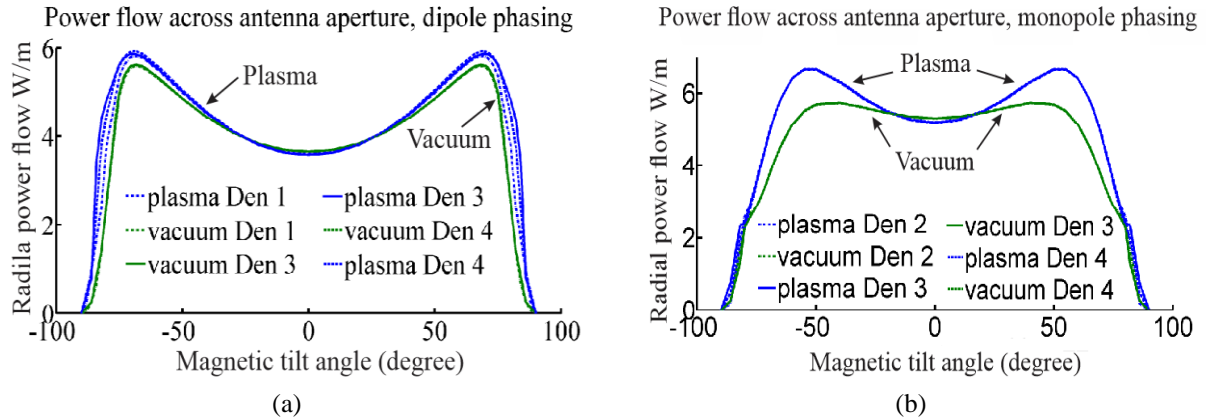
Figures 3.17 . *Radial power flow across the antenna mouth versus the magnetic field tilt angle, (a) dipole phasing with density profiles 1, 3 and 4. (b) Monopole phasing with density profiles 2, 3 and 4. Blue curves indicating plasma-filled antenna box. Green curves show simulations with vacuum in the antenna box.*

Figures 3.17 shows the variation in the radiated power for 1A on the straps, over a scan of tilt angle. Mesh 2 is used. In the simulations with a vacuum antenna box, the density profiles are cut at the antenna box edge, dot line of *Figure 3.4*. In *Figures 3.17*, the power level in monopole phasing is higher than in dipole phasing. This is not surprising since the evanescence region for the fast wave is shorter in monopole phasing than in dipole, thus less power is reflected to the straps. For dipole phasing, power seems independent of whether the antenna is in plasma or in vacuum. For monopole phasing, there is up to 20% difference between the power launched from an antenna immersed in a plasma compared to one sitting in vacuum when scanning over all possible tilt angles. In both cases, power coupling is not sensitive to the density profile shape. In order to check this difference, we plot the toroidal power spectrum (section 2.1.6) obtained by conducting Fourier transform near the antenna mouth at theta=60⁰ where the difference gets largest. We see clearly from the power spectrum, (*Figure 3.18*) that under monopole phasing the power gap between plasma filled-in antenna and vacuum antenna is larger than that in dipole phasing. The farthest lobe we can see in Figure 3.18 is located at the toroidal refractive index n_x=-35, corresponding to a wavelength of 0.006m. As a comparison, our grid size is 2.5×10^{-4}m, so all the spectrum lobes have already been well captured in obtaining the results of *Figures 3.17*.

The drop of the power spectrum at low n_x in monopole phasing can be understood by looking at the fast wave cut-off layer, as introduced in section 2.1.5.
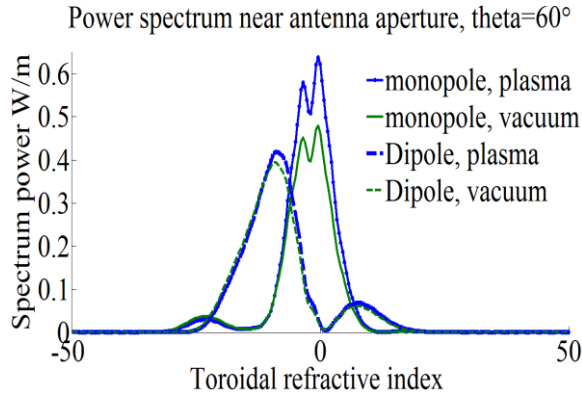
Figure 3.18. Power spectrum at large tilt angle theta=60⁰, plasma density 3 is used for blue curves
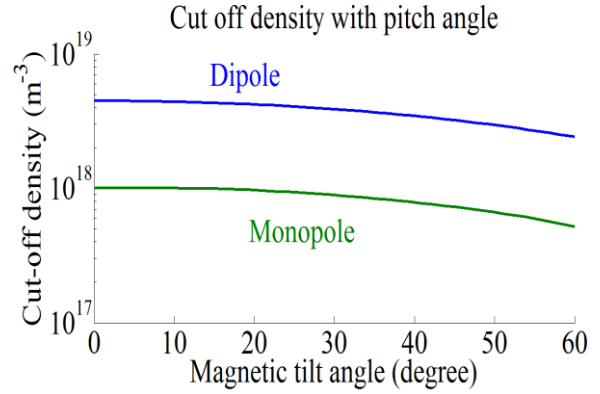
Figure 3.19. Fast wave cut-off density, Dipole phasing n_x=9.14, monopole phasing n_x=4.5 are used

Figure 3.19 plots the fast wave cut off density versus the magnetic tilt angle for two toroidal wavenumbers n_x, characteristic of each phasing. As a reference, the density around the antenna mouth is about $9×10^{17}$ m^{-3}. In dipole phasing, due to the large n_x, the cut-off layer is well above the antenna box, thus the fast wave is evanescent inside the antenna box, no matter the box is in vacuum or filled by plasma. However, in monopole phasing, the cut-off layer is generally inside the antenna box under large tilt angles, thus the fast wave evanescence region is larger in a vacuum antenna than in an antenna filled with plasma. With the increasing of the tilt angle, the cut off layer is shifting to the edge see *Figure 2.3*, in other words the cut off density is decreasing. This explains that the power in *Figures 3.17* is increasing as the evanescent length is decreasing with increasing of the tilt angle. Then under large tilt angle it drops down dramatically as the fast wave antenna changes to a slow wave antenna.

Dipole phasing is used as the main heating phasing in the present ICRH experiments for its better power absorption by the plasma. For this phasing, the effect of the density gradient in the fast wave evanescence region on the power coupling is also studied. We will firstly consider the case in which the densities are both fixed at cut off layer and an extra reference point, i.e. the strap front surface, so that only the density gradient between them is variable. Then we go to a more realistic case that density simply follows an exponential decay, starting from the cut off layer. Please note here we only vary the density gradient below the R-cutoff layer. A sharp density gradient can also happen in the main SOL plasma where it is likely to reflect the propagating fast wave. Some dedicated studies [Messiaen 2011] has been done to investigate the power coupling with varying density gradient in the main SOL plasma. The coupling varies like a tapered line w.r.t the density decay length. The conclusion is that as long as the density decay length exceeds the first maximum, the power variation remains small.

Case 1. Fixed density at the reference point

In this case, we impose an analytical density profile in the fast wave evanescence region, which reads

$$n_e(y) = \frac{n\_co - n\_ref}{1 - \exp(-(y\_co - y\_ref)/L)} (\exp(\frac{y - y\_co}{L}) - 1) + n\_co \qquad (3.3)$$

Where *L* is the exponential decay length; *n_co*, *y_co* are the cut off density and location, which depends on tilt angle. The density at reference point (*y_ref*) is marked as *n_ref*. It takes the same value for all decay lengths. The density in front of the cutoff layer is the experimental profile, i.e. *Figure 3.3*.
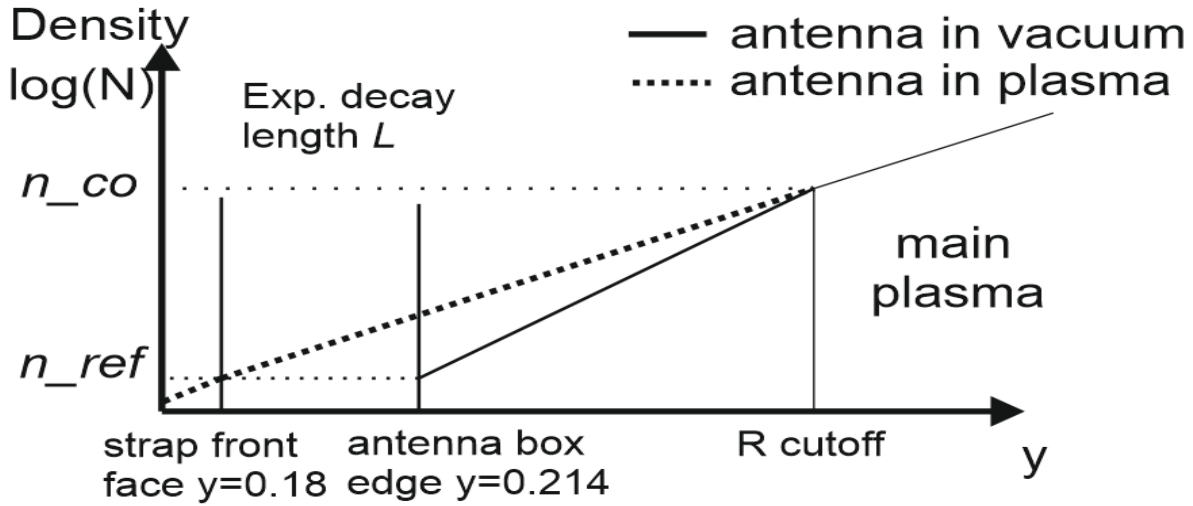
Figure 3.20. Exponential decay density in the fast wave evanescence region

In case of vacuum antenna, the reference point is defined at the antenna box edge, i.e. *n_ref* =1.1164e18 m^{-3} and *y_ref* =0.214m. The density is shown by solid line in *Figure 3.20*.

In case of a plasma filled antenna, we impose the exponential decay density up to the front face of straps. Thus the reference point is defined at the strap front face, i.e. *n_ref* =1.1164e18 m^{-3} and *y_ref* =0.18m. One of the densities is drawn by dashed line in *Figure 3.20*. It takes pre-defined density 3 underneath the strap's front face. *Figure 3.21* shows all the exponential decay lengths we will use in the evanescence region under dipole phasing, theta=0^0.
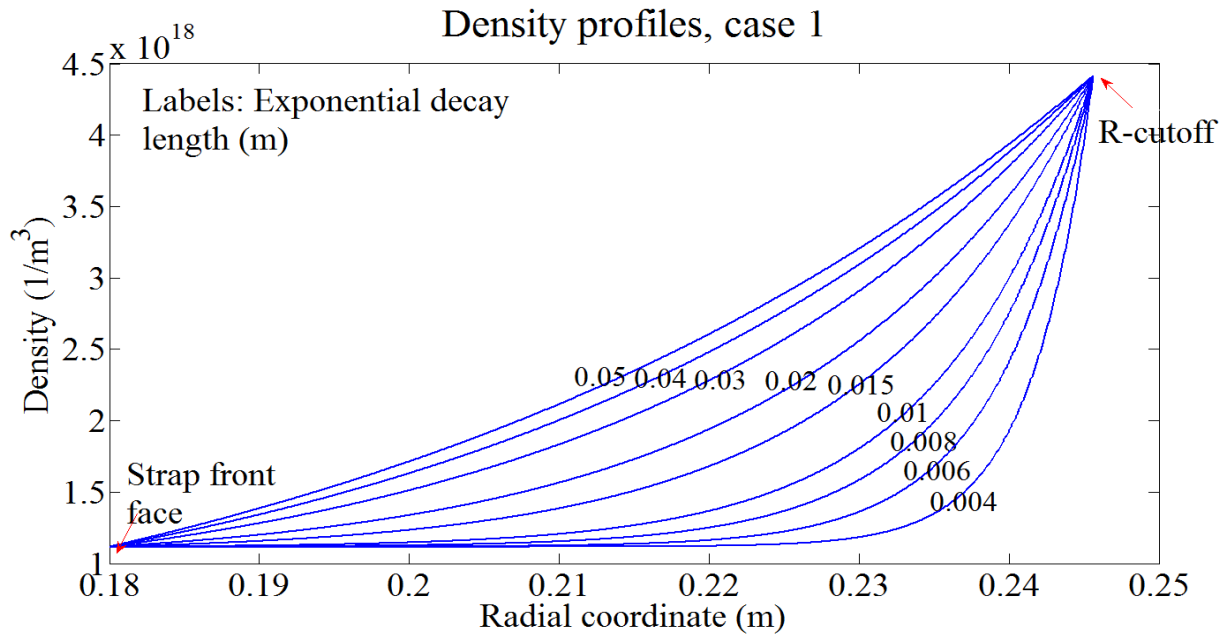
Figure 3.21. A scan of density profiles in the evanescence region, theta=0^0, dipole phasing, plasma filled antenna, n_ref =1.1164e18m^{-3} and y_ref =0.18m

The power flow across the radial PML/plasma interface (top red line in *Figure 3.5*) is measured. The result is shown in *Figure 3.22*. One can see under these three tilt angles, the power has only a 5% of variation with different decay lengths. With larger decay length, the density profiles becomes more 'flat' so that the evanescent lengths for small $n_{//}$ waves become shorter compared to the ones with sharp density profiles, thus slightly increase the power coupling. We also see the presence of plasma inside the antenna box does not modify significantly the power coupling.
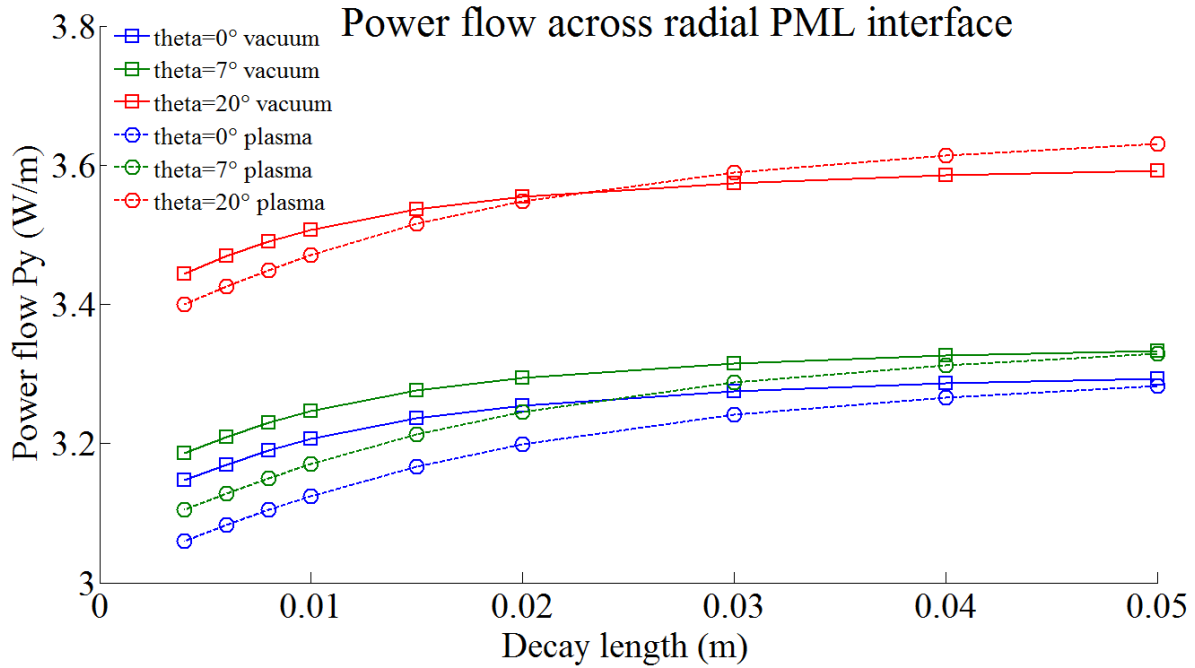
Figure 3.22. Radial power flow w.r.t decay length, case 1

Case 2. Variable density at the reference point

A more realistic case is to release the fixed density at the reference point. In this case, We tested three tilt angles, i.e. theta=0^0,7^0 and 20^0. For each tilt angle, we calculated the *R* cut-off density using Eq. (2.34) and its radial location with our reference density profile (*Figure 3.3*). Then starting from the *R* cut-off, a set of exponential density profiles with different decay lengths was imposed, as shown in *Figure 3.23*. The density is assumed to have the form as following,

$$n_e(y) = n\_co * \exp((y - y\_co)/L) \tag{3.4}$$

Where *n_co*, *y_co* are the cut off density and its location, y the radial coordinate and *L* the density decay length.

Results is shown in *Figure 3.24*. We see that changing density gradient in the fast wave evanescence region can drive power variations up to 5%.
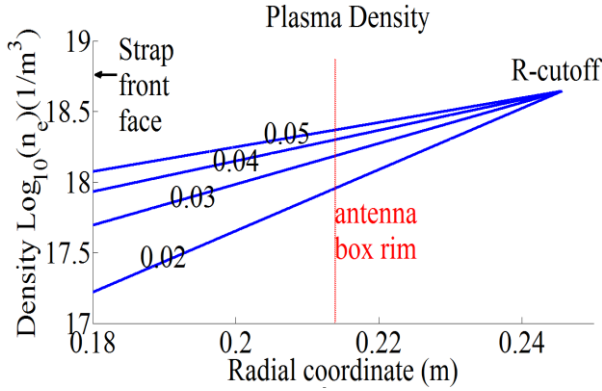
Figure 3.23. Test density profiles in the fast wave evanescence region, theta=0°. Labels indicate the exponential decay length L in meter
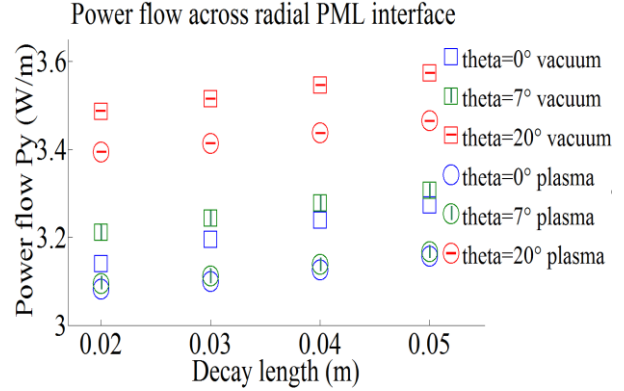
Figure 3.24. Power flow across radial PML interface versus density decay length. In case of a vacuum antenna box, density is cut at antenna box rim, shown in Figure 3.23

3.7   Discussion and conclusion

The presence of a tenuous plasma inside an ICRF antenna box can make the numerical simulation of local RF electric field problematic when the density profile crosses the LH resonance. Up to the memory limits of our dedicated workstation, radial and toroidal RF fields below the LH resonance did not converge with decreasing mesh size. They exhibited sensitivity to small local density changes. This is probably due to the conjunction of short wavelength for the slow wave and the presence of a lossy cavity for this mode inside the antenna box. It is critical to be aware of this non-convergence when studying near field effects inside the antenna box. Another similar case is that a slow wave can also be excited in the vicinity of the straps by a fast wave antenna, however it only causes local numerical instabilities here due to its strong evanescence.

With a dominant poloidal current imposed on the straps, it was shown that the poloidal electric field and thus the total excited power is independent of the mesh even in the presence of the LH resonance behind the straps. This guarantees that the ICRF power transmitted to the main plasma *via* the fast wave is also independent of the mesh or the non-convergence property of the fields inside the antenna box. In a 3D antenna with voltage excitation, this point may need further investigations. With no damping inside the antenna box, all the radiated power carried by the slow wave is transferred out of the antenna box. In a situation where the R-cutoff layer for the fast wave is well outside the box, e.g. in dipole phasing with Tore Supra profiles, the total power coupled to main plasma is indifferent with the plasma density inside the antenna box so that one can drop out the low density inside the antenna box when studying coupling issues. In monopole phasing with Tore Supra density profiles, simulations show that there is a maximum 20% of power increase due to the presence of plasma, for large tilt angles. The distinction comes from the fact that the fast wave evanescence length for low $k_{//}$ changes. Hence modeling low $k_{//}$ scheme with antenna staying in vacuum may need to be re-considered. We did not consider the extreme case in which the strap is below the LH resonance and can excite directly the propagating slow wave. The present model ignores parasitic damping (collisional) and sheath effects. Near the LH resonance, the wavelength become comparable with Larmor radius Eq. (1.6), one may also need to consider the thermal effect or the finite Larmor radius corrections. A situation similar to the LH resonance might arise when peripheral cyclotron layers are located inside the antenna box. The poloidal gradient, which was ignored in our simulations, will likely play a key role at the study of density modifications by ponderomotive force [Van Eester 2013].

Those effects will be left for the future study. The density measurement in the fast wave evanescence region is affected by the largest uncertainty [Milanesio 2013] due to both measurement issues and large fluctuation levels [Clairet 2004]. This is again crucial in determining near field. Nevertheless, changing density gradient in the evanescence region can maximally affect power coupling up to 5%. One can thus still model the power coupling to plasma with a fairly good precision despite some uncertainties in low-density part of the profile. All simulations however stress the need to measure precisely the R-cut off radial position in order to get accurate estimation of ICRF wave coupling properties. This is a strong motivation for implementing density diagnostics as close as possible to the wave launchers.

Reference

[Puri 1973] S. Puri and M. Tutter, "Lower-hybrid-resonance heating of a plasma in a parallel-plate waveguide", Nucl. Fusion, **13**(1), 1973

[Brambilla 1998] M. Brambilla, "Kinetic theory of plasma waves: homogeneous plasma", first edition, 1998, Oxford university press Inc., New York

[Crombé 2014] K. Crombé, D. Van Eester, R. Koch and V. Kyrytsya, "2D modeling of electromagnetic waves in cold plasmas", AIP Conf. Proc. 1580, 318 (2014)

[Lu 2016] L. Lu et al, "Non-linear radio frequency wave-sheath interaction in magnetized plasma edge : the role of the fast wave", 43rd European physics society conference on plasma physics, Leuven, 2016

[Jacquot 2013] J. Jacquot, L. Colas, F. Clairet, M. Goniche, S. Heuraux, J. Hillairet, G. Lombard and D. Milanesio,"2D and 3D modelling of wave propagation in cold magnetized plasma near the Tore Supra ICRH antenna relying on the perfectly matched layer technique", PPCF 55 115004 (2013)

[Jacquot 2014] J. Jacquot, D. Milanesio, L. Colas, Y. Corre, M. Goniche, J. Gunn, S. Heuraux, M. Kubic and R. Maggiora, "Radio-frequency sheaths physics: Experimental characterization on Tore Supra and related self-consistent modeling", Phys. Plasma 21, 061509 (2014)

[Jacquot 2015] J. Jacquot et.al, "Full wave propagation modelling in view to integrated ICRH wave coupling/RF sheaths modelling", AIP Conf. Proc, 1689, 050008 (2015)

[Lu 2016A] L. Lu, K. Crombe, D. Van Eester, L. Colas, J. Jacquot and S. Heuraux, "Ion cyclotron wave coupling in the magnetized plasma edge of tokamaks: impact of a finite, inhomogeneous density inside the antenna box", PPCF, 58(5) 2016

[Myra 2010] J. R. Myra and D. A. D'Ippolito, "Slow-wave propagation and sheath interaction in the ion-cyclotron frequency range", Plas. Phys. Cont. Fus. 52(1), 2010

[Messiaen 2011] A. Messiaen and R. Weynants, "ICRH antenna coupling physics and optimum plasma edge density profile. Application to ITER", Plas. Phys. Cont. Fus. 53(085020), 2011

[Kohno 2015] H. Kohno, J. R. Myra and D. A. D'Ippolito, "Numerical investigation of fast-wave propagation and radio-frequency sheath interaction with a shaped tokamak wall", Phys. Plasmas, **22** (072504) 2015

[Van Eester 2013] D. Van Eester, K. Crombé and V. Kyrytsya, "Ion cyclotron resonance heating-induced density modification near antennas", Plas. Phys. Cont. Fus. 55(2), 2013

[Milanesio 2013] D. Milanesio and R. Maggiora, "Evaluation of the influence of the main plasma density parameters on antenna coupling and radio frequency potentials with TOPICA code", Plas. Phys. Cont. Fus. 55(4), 2013

[Clairet 2004] F. Clairet, L. Colas, S. Heuraux and G. Lombard, "ICRF coupling and edge density profile on Tore Supra", PPCF 46(10), 2004

Chapter 4   SSWICH-FW: self-consistent modeling of full wave propagation and DC plasma biasing by RF sheath

4.1   Introduction of this chapter

Most of the deleterious RF edge effects, including SOL power losses, heat loads on the plasma facing components and impurity sputtering to the main plasma are associated to the DC plasma potential enhancement by RF sheath rectification. In order to model the sheath rectification beyond the traditional double Langmuir probes approach, which has suffered criticism both from experiment and theory, a sheath project under European level has been carried out. It assembles most of the current efforts of RF sheath modelling in Europe. The LPP group focuses on the fundamental physics within the sheath, trying to understand the interplay between RF waves and plasma density by solving iteratively the Maxwell's equation, equation of motions and continuity equations over the spatial scale of the sheath at two different time-scales. The IJL lab in Université de Lorraine studies the fundamental sheath properties by particle-in-cell simulations. They are interested in exploring the behavior of Debye sheath under zero grazing angle of the magnetic field line and the cross field sheath induced by the difference of Larmor radius of the electrons and ions. Both of these two approaches are restricted themselves in a simple geometry with a limited size, which is far from the realistic antennas.

At CEA, our approach is to model RF sheath over a realistic antenna size. Sheath is thus being treated as boundary conditions. The Self-consistent Sheaths and Waves for ICH (SSWICH)-slow wave code was developed in 2013. It couples self-consistently the RF wave propagation and the DC SOL biasing *via* non-linear RF and DC sheath boundary conditions applied at plasma/wall interfaces. The first slow wave version adopts a simple assembly of rectangular elements and the magnetic field is either parallel or perpendicular to the wall. Under this magnetic configuration, the SBCs are only associated with the slow wave. This chapter reports the development of a new SSWICH version, the 2D SSWICH-FW code which includes a more realistic geometry, magnetic configuration, wall shape and full wave (fast wave + slow wave) polarizations. The structure of this chapter is the following: Section 4.2 gives a short overview of the 2D SSWICH-SW code. Section 4.3 illustrates the specifications of the new 2D SSWICH-FW code initially developed for the Tokamak context. Section 4.4 discusses some numerical issues in the 2D SSWICH-FW code. The last section shows how SSWICH principle can be applied in the Aline device in order to provide interpretative simulations.

4.2   Overview of the 2D SSWICH-SW code before this thesis [Jacquot 2012][Jacquot 2013][Colas 2012]

SSWICH-Slow Wave code deals with a simplified 2D geometry in the radial-toroidal plane, it is a cut of one poloidal direction of a real 3D Tore Supra antenna geometry, similarly with the choice of 2D RAPLICASOL code in Chapter 3. Magnetic field line is assumed either perpendicular or parallel to the boundaries. In *Figure 4.1*, blue vertical rectangles represent protruding material objects, e.g. antenna side limiters. They are considered as the walls where sheath can be excited. In reality, sheath is quite thin compared to the simulation domain, their effect is treated through boundary conditions. Numbers 1, 3, 5, 7, 9, 11 are sheath boundaries. They are zoomed in to be visible. No 2, 10 and 4, 8 are outer wall of the machine and leading edge of limiters respectively. No. 12 represents the inner radial boundary. It is a boundary just for the RF field calculation, but not a boundary for the plasma, which will be crossed in the

2D SSWICH-FW code. Antenna part is replaced by imposing field map of $E_{//}$ from any other antenna code [Lancellotti 2006] [Jacquot 2015] at the antenna aperture (No. 6 in Figure 4.1). The antenna straps in those codes need to be tilted in order to generate the field map with a magnetic field tilted to the antenna as in the realistic case and perpendicular to the wall as assumed in the 2D SSWICH-SW code. In reality, the physical aperture is surrounded by metallic walls. So accordingly we implement two metallic boundary conditions at the two extremities of the aperture 6. For simplicity, in the following equations, we use $//\textbf{B}_0$ or $//x$ represent metallic boundaries 2, 4, 8, 10, and $\perp B$ or $\perp x$ represent sheath boundaries 1, 3, 5, 7, 9, 11.
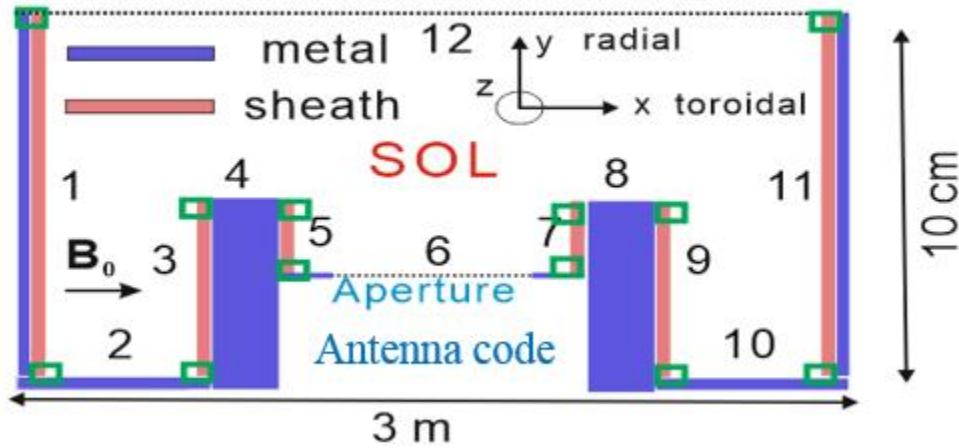
Figure 4.1. Geometry of the 2D SSWICH-SW code. The blue rectangles represent metallic components, red ones correspond to sheath boundaries and green ones indicate sheath corners [Jacquot 2013]

Three scale fields are solved iteratively using the finite element methods (*Figure 4.2*), the parallel electric field $E_{//}$, the oscillating sheath voltage V_{RF} and the DC plasma biasing V_{DC}, respectively. RF quantities $E_{//}$ and V_{RF} are complex scalars, i.e. fields with amplitude and phase, assuming time-harmonic variations as $\exp(iw_0 t)$, following engineering convention adopted in COMSOL software. V_{DC} is real-positive field. Each of these three quantities is calculated within a separated module in COMSOL. They are coupled together by sheath capacitance and sheath rectification. Sheath is treated as a plate capacitor in the $E_{//}$ module by assuming that its resistance can be ignored and electric field is constant with space inside sheath. Sheath capacitance gives a definition of V_{RF}, see Eq. (2.58). Oscillating sheath voltage, although its average amplitude over one RF period is zero, can introduce a biasing voltage in V_{DC} module via sheath rectification. These sheath properties are applied as boundary conditions for three field equations. Now we present the details for each module.

In $E_{//}$ module, the governing equation for the slow wave propagation can be known by manipulating Eq. (2.29),

$$[\varepsilon_{//}\Delta_{//} + \varepsilon_\perp\Delta_\perp + \varepsilon_{//}\varepsilon_\perp(\frac{\omega}{c})^2]E_{//} = 0 \qquad (4.1)$$
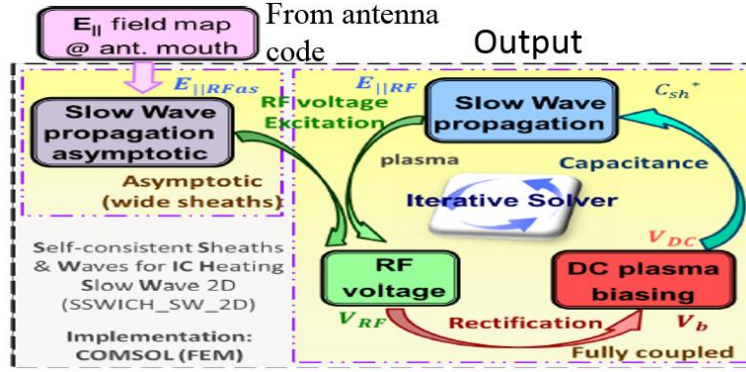
Figure 4.2. Iterative process in 2D SSWICH-SW code [Jacquot 2013]

Please note Eq. (2.29) has used $k_z=0$. In SSWICH-SW, the magnetic field is parallel to the toroidal direction. Thus E_X in Eq. (2.29) is equivalent to $E_{//}$ here. Along the $//\mathbf{B_0}$ boundaries, $E_{//}=0$ is imposed since they are metallic. Along the $\perp\mathbf{B_0}$ boundaries, knowing from the sheath capacitance, the electric field can be represented as a function of the sheath voltage, by introducing a sheath width δ and sheath permittivity ε_{sh}. This can be used as a sheath boundary condition. So the boundary conditions in $E_{//}$ module read

$$\begin{cases} E_{//} = 0 & //\mathrm{B}_0 \ and\ inner\ radial\ boundary \\[2mm] E_{//} = \pm\dfrac{\varepsilon_{sh}}{\varepsilon_{//}\delta}V_{RF} & \perp\mathrm{B}_0 \\[2mm] E_{//}\ from\ antenna\ code & aperture \end{cases} \tag{4.2}$$

The second equation can also be inversely used as a boundary condition for V_{RF}, which will lead to the whole three-field loop run in the opposite direction. Our choice here is first due to a pure computational reason, because the present loop gets a better convergence. Second in the case of large DC biasing, this boundary condition will reduce to $E_{//}=0$, which was justified by the asymptotic analysis in [Colas 2012]. This gives a starting point for running the loop.

In V_{RF} module, the conservation of the displacement ($\nabla\cdot\mathbf{D}=0$) is solved at the sheath-plasma interface. The RF sheath boundary condition Eq. (2.71) gives

$$E_\perp = \nabla_\perp V_{RF} \tag{4.3}$$

Expand the conservation of displacement by the constitutive relation, one gets two terms containing $E_\perp$. The $\nabla\times E_\perp$ term can be neglected by the fact that the slow wave is a transverse magnetic wave. Insert Eq, (4.3) into the $\nabla\cdot E_\perp$ term, one finally obtains a simple relation,

$$\varepsilon_\perp\Delta_\perp V_{RF} = \varepsilon_{//}\partial_{//}E_{//} \tag{4.4}$$

In the original 2D SSWICH-SW version [Jacquot 2013], Eq. (4.4) is solved in all the 2D simulation domain, but V_{RF} only makes sense along sheath boundaries, which could reduce the problem to 1D. The second

equation in (4.2) yields V_{RF}=0 at the two ends of each sheath boundary (green rectangles in *Figure 4.1*) since the tangential **E** along metallic surface is zero. To ease the implementation, we impose V_{RF}=0 at the //**B$_0$** boundaries (This was justified in Section 2.3.4), the inner radial boundary and also the aperture. Doing this does not affect V_{RF} solution at sheath boundaries.

$$V_{RF} = 0 \qquad //\mathrm{B}_0, \textit{inner radial boundary and aperture} \tag{4.5}$$

The last module is the V_{DC} module. It solves the conservation of the DC current ($\nabla \cdot \mathbf{J} = 0$), where

$$\mathbf{J} = \begin{bmatrix} \sigma_{//} & \\ & \sigma_{\perp} \end{bmatrix} \begin{bmatrix} E_{//}^{DC} \\ E_{\perp}^{DC} \end{bmatrix} \tag{4.6}$$

Where the superscript DC is used to distinguish the RF electric field. Making use of the static electric field-voltage relation, one can derive the following equation,

$$\sigma_{//}\Delta_{//}V_{DC} + \sigma_{\perp}\Delta_{\perp}V_{DC} = 0 \tag{4.7}$$

Here, $\sigma_{//}$ and $\sigma_{\perp}$ are the parallel (Spitzer Eq. 1.7) and perpendicular DC conductivities. In the experiment, V_{DC} is observed beyond the side limiter, which is much further than the slow wave evanescence length. To explain this radial extension of V_{DC} phenomenologically, $\sigma_{\perp}$ has to be introduced to allow the radial DC current transport.

In the V_{DC} module, boundary conditions are implemented by assuming transversal current normal to the //**B$_0$** boundaries can be ignored compared to the injection of parallel current at the $\perp$**B$_0$** boundaries, where sheath rectification Eq. (2.62) contributes to the net current. At the inner radial boundary, there is no net current to perturb the core plasma, which means V_{DC} should equal the floating potential V_f.

$$\begin{cases} \mathbf{J} \cdot \mathbf{n} = 0 & //\mathrm{B}_0 \textit{ and aperture} \\ J_n = J_{is}^{\perp B}(1 - \min(\dfrac{J_{es}^{\perp B}}{J_{is}^{\perp B}}, exp[\dfrac{e(V_f + V_b - V_{DC})}{k_B T_e}])) & \perp \mathrm{B}_0 \\ V_{DC} = V_f & \textit{inner radial boundary} \end{cases} \tag{4.8}$$

After solving V_{DC}, the iterative loop is closed by applying the Child-Langmuir law Eq. (2.57) to obtain a new sheath width.

The last thing to think about is how to enter this loop. One may note in the second equation of the boundary condition (4.2), that a prior knowledge of sheath width is needed. But It is supposed to be solved at the last step of this loop. So in order to begin the loop, an asymptotic module that gives a first guess of the sheath width is created (*Figure 4.2*). The asymptotic version solves the three-field in segregated steps instead of using iterative scheme in the fully coupled version. In this version, everything keeps the same, except the second equation of the boundary condition (4.2) is simplified to be $E_{//} = 0$ at $\perp$**B$_0$** boundaries, providing an infinite sheath width[Colas 2012]. Applying the SSWICH-SW code to realistic TS case at MW RF power range shows a finite sheath width is only a small correction to the infinite sheath width [Jacquot 2013A], thus we believe the asymptotic version, where the convergence is faster and guaranteed in contrast to the fully coupled version, can already approximate the final results with a fairly good precision.

The 2D SSWICH-SW version assumes k_z=0 everywhere in the simulation domain. Full 3D version of SSWICH-SW asymptotic code is also developed and its principle is presented in [Colas 2012], where the direction on z is treated in the spectral domain. The SSWICH-SW simulation shows neglecting the poloidal derivatives would leads to a maximum 10% of error for V_{DC} compared with the one has a finite k_z spectrum [Jacquot 2013A]. This may not true when the fast wave is included.

4.3   Specifications of the 2D SSWICH-FW code

In the 2D SSWICH-SW code, **B₀** is either perpendicular or parallel to the metallic walls. Under this magnetic configuration, one can see from above that the sheath boundary condition in the $E_{//}$ module (4.2) and V_{RF} field equation (4.4) only contain the slow wave polarization. Now we consider the same magnetic configuration with the 2D RAPLICASOL code that **B₀** has a tilt angle θ in poloidal-toroidal plane (*Figure 2.1*), like Chodura did, but with another definition of θ in the original paper [Chodura 1982]. This is not the most general case, but under this magnetic configuration, one can keep a similar simulation geometry and at the same time can introduce the fast wave coupling into code.
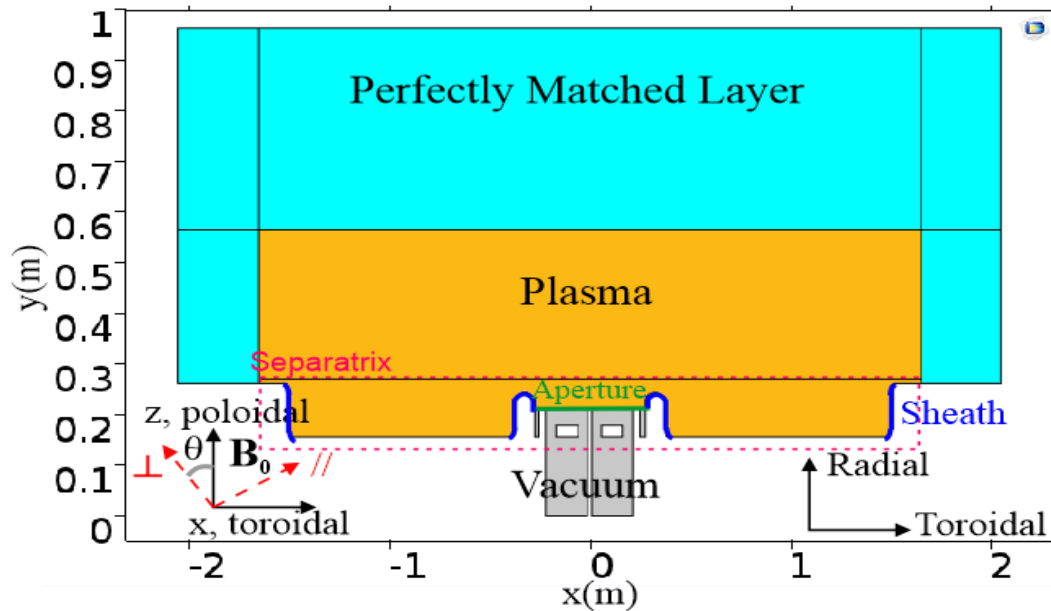
Figure 4.3. Geometry of the 2D SSWICH-FW code. PMLs are implemented to simulate fast wave free propagation. The sheath boundaries are marked in blue. The walls in the SOL region (enclosed by the red dot lines) are shaped

Figure 4.3 shows the new geometry of the 2D SSWICH-FW code. The magnetic field now has a component in the out-of-plane direction. The simulation domain combines the antenna, SOL region and the main plasma, the latter is surrounded by a non-reflecting boundary condition through implementing PMLs, in order to simulate the fast wave propagation and radiation. A realistic density profile can be imported in the model. The antenna is treated in vacuum so as to avoid the LH resonance. One can either excite RF waves by importing two tangential electric field components at antenna aperture, or imposing currents on the straps (a voltage excitation by coaxial line is only available in 3D, see *Figure 2.9*). The sheath boundaries are shaped boundaries locating in the SOL region. It will be shown that curvature is important for RF sheath modelling in Chapter 5.

The structure of the 2D SSWICH-FW code is shown in *Figure 4.4*. We keep three-field structure in the new code. RF fields, V_{RF} and V_{DC} are solved in the same sequence. The RF field module is now vectorial fields and solves both of the polarizations. General formula for sheath capacitance Eq. (2.70), sheath rectification formula Eq. (2.66) and Child-Langmuir law Eq. (2.69) are used in this code (with slightly modifications to include curvature, see details in the next 3 subsections). To save the computational memory, the three fields are solved in different dimensions. Now we will present each module individually.
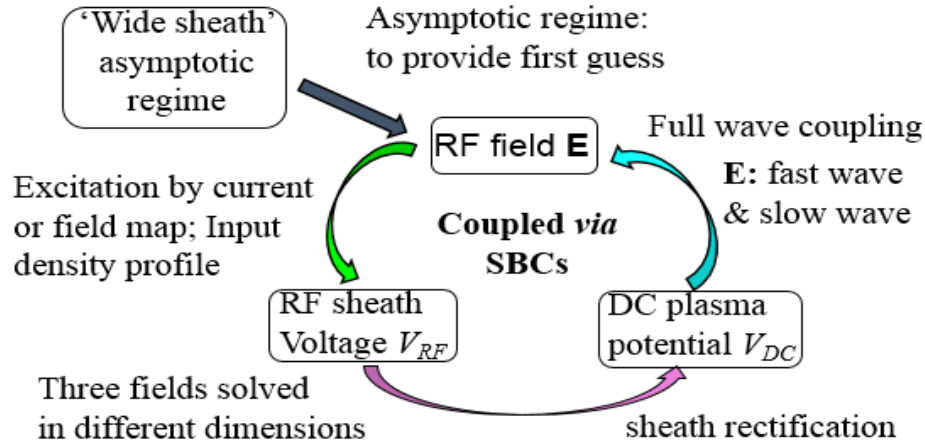
Figure 4.4. Work flow of the 2D SSWICH-FW code

4.3.1   The RF field module

In the presence of tilted magnetic field, the two plasma eigenmodes are likely coupled. The slow wave propagation Eq. (4.1) should be replaced by the vectorial wave equation

$$\nabla \times (\nabla \times \mathbf{E}) - k_0^2 \varepsilon_{\mathbf{r}}(\theta) \mathbf{E} = 0 \tag{4.9}$$

Where **E** is a vector corresponding to the full RF electric fields of the wave; $\varepsilon_{\mathbf{r}}$ is the new dielectric tensor defined in Eq. (2.10); k_0 is the wavenumber in vacuum. Combine Myra and D'Ippolito's boundary conditions Eq. (2.71) and 2D assumption, one has

$$E_z = -\frac{\partial V_{RF}}{\partial z} = 0 \tag{4.10}$$

Another boundary condition for the sheath boundary comes from the sheath capacitance. Starting from Eq. (2.70), accounting for the curvature, one has

$$D_n = \frac{\varepsilon_{sh} V_{RF}}{\delta_{DS}(\theta) \, | \, nx \, |} \tag{4.11}$$

Where *nx* is a COMSOL build-in operator, meaning the x component of the normal direction of the curve. The |nx| is necessary to be included in the new sheath width on the curved boundaries. |nx|=1 on a flat boundary along y direction, and |nx|=0 on a toroidal boundary.

For metallic boundaries, PEC boundary conditions give two tangential components equal to zero. So the whole set of boundary conditions read,

$$\begin{cases} E_z = 0, \; D_n = \dfrac{\varepsilon_{sh} V_{RF}}{\delta_{DS}(\theta) \, | \, nx \, |} & sheath \\[2mm] E_x = E_z = 0 & metal \end{cases} \tag{4.12}$$

Compared with Eq.(4.2), on each boundary, now we need two constraints to solve the vectorial electric field.

4.3.2   The oscillating RF sheath voltage module

a.   Primary approach to evaluate V_{RF}

In the 2D SSWICH-SW code, we worked out a 2nd order PDE for V_{RF} by eliminating SW perpendicular electric fields so that the equation only involves the parallel electric field. This process is not necessary since we are now solving all the three electric components. So one may wondering the V_{RF} does not necessary come from the second order differential equation. V_{RF} is only solved at the sheath boundaries, see *Figure 4.5*. According to the 2D sheath boundary condition given by Myra and D'Ippolito, one has $E_s = -\partial V_{RF} / \partial s$, where E_s the electric field along the direction of arc length (The other relation $E_z = -\partial V_{RF} / \partial z$ has already been used in Eq. (4.10)). So we can simply integrate the tangential electric field along the sheath boundary. This process will not require the derivative of the electric fields. Besides, the first order differential equation only needs one boundary condition at each boundary.
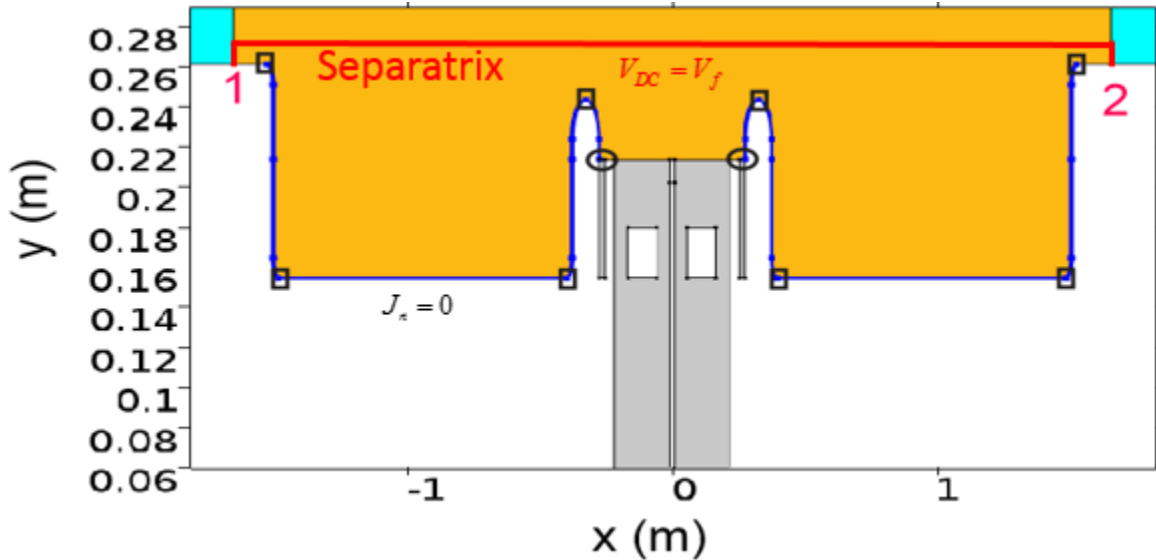
Figure 4.5. Simulation geometry in V_{RF} and V_{DC} modules. V_{RF} solved along 1D sheath boundaries, whereas V_{DC} solved in the 2D SOL domain. The orange color indicates the plasma region; Grey is the vacuum region. Rectangle and ellipse are the boundary points where the RF sheath boundary condition applied in the two approaches; The two identities are the DC sheath boundary condition imposed at the corresponding lines

Following this approach, it is reasonable to choose points sitting furthest away from the wave launcher and assume there V_{RF}=0. Therefore points 1 and 2 are chosen. For simplicity, the line integral takes all the

blue boundaries of *Figure 4.5*, which includes the metallic part between two sheath boundaries, but the metallic boundary has no contribution to V_{RF} since $E_s = 0$.

b. Secondary approach to evaluate V_{RF}

The conservation of RF electric displacement ($\nabla \cdot \mathbf{D} = 0$) is still valid under tilted magnetic field. Due to the curvature, it however needs to be revised to fit in the curvilinear coordinate where the vector basis $(\vec{e}_s, \vec{e}_n, \vec{e}_z)$ is used, with *s* the direction of arc length, *n* normal direction and *z* the out-of plane direction, see *Figure 4.6*. It is obtained by multiplying the Cartesian base vector by a rotation matrix $\overline{\overline{R'}}$

$$\begin{pmatrix} \vec{e}_s \\ \vec{e}_n \\ \vec{e}_z \end{pmatrix} = \begin{pmatrix} tx & ty & 0 \\ nx & ny & 0 \\ 0 & 0 & 1 \end{pmatrix} \begin{pmatrix} \vec{e}_x \\ \vec{e}_y \\ \vec{e}_z \end{pmatrix} = \overline{\overline{R'}} \begin{pmatrix} \vec{e}_x \\ \vec{e}_y \\ \vec{e}_z \end{pmatrix} \quad (4.13)$$

Where $tx = \dfrac{\partial x}{\partial s}, ty = \dfrac{\partial y}{\partial s}, nx = \dfrac{\partial x}{\partial n}, ny = \dfrac{\partial y}{\partial n}$

are all COMSOL build-in operators named as tangential and normal variables.
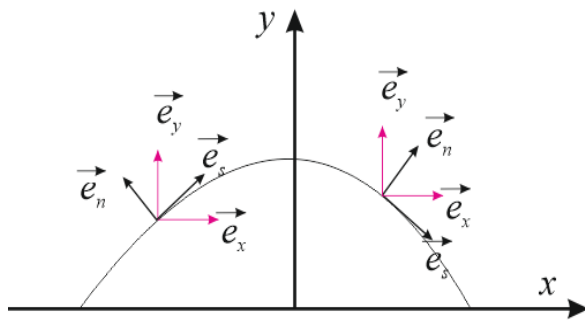
Figure 4.6. Curvilinear base vector Vs. Cartesian base vector

The following relations are naturally fulfilled

$$tx = ny, ty = -nx \quad (4.14)$$

Thus the displacement vector and electric vector in curvilinear coordinate reads

$$\begin{pmatrix} D_s \\ D_n \\ D_z \end{pmatrix} = \overline{\overline{R'}} \overline{\overline{\varepsilon}} \overline{\overline{R'}}^{-1} \begin{pmatrix} E_s \\ E_n \\ E_z \end{pmatrix} = \begin{pmatrix} A_{11} & A_{12} & A_{13} \\ A_{21} & A_{22} & A_{23} \\ A_{31} & A_{32} & A_{33} \end{pmatrix} \begin{pmatrix} E_s \\ E_n \\ E_z \end{pmatrix} \quad (4.15)$$

$$\begin{pmatrix} E_s \\ E_n \\ E_z \end{pmatrix} = \begin{pmatrix} tx & ty & 0 \\ nx & ny & 0 \\ 0 & 0 & 1 \end{pmatrix} \begin{pmatrix} E_x \\ E_y \\ E_z \end{pmatrix} \quad (4.16)$$

where the matrix A is the generalized dielectric tensor expressed in the curvilinear coordinate,

$$A = \begin{pmatrix} A_{11} & A_{12} & A_{13} \\ A_{21} & A_{22} & A_{23} \\ A_{31} & A_{32} & A_{33} \end{pmatrix} = \begin{pmatrix} tx^2\varepsilon_{11} + ty^2\varepsilon_{22} & tx \cdot ty(\varepsilon_{22} - \varepsilon_{11}) - \varepsilon_{21} & tx\varepsilon_{13} + ty\varepsilon_{23} \\ tx \cdot ty(\varepsilon_{22} - \varepsilon_{11}) + \varepsilon_{21} & nx^2\varepsilon_{11} + ny^2\varepsilon_{22} & nx\varepsilon_{13} + ny\varepsilon_{23} \\ tx\varepsilon_{31} + ty\varepsilon_{32} & nx\varepsilon_{31} + ny\varepsilon_{32} & \varepsilon_{33} \end{pmatrix} \text{ (4.17)}$$

Where $\varepsilon_{11} - \varepsilon_{33}$ are defined in Eq. (2.11).

The next step is to rewrite the zero divergence of the displacement into curvilinear coordinate. A mathematical formula concerning the divergence operator under curvilinear coordinate has been derived for this purpose. The details of these derivations can be seen in the Appendix B. Here we just recall the results,

$$\nabla \cdot D = \frac{\partial D_s}{\partial s} + \frac{\partial D_n}{\partial n} + \frac{\partial D_z}{\partial z} + \frac{D_n}{R_c} \text{ (4.18)}$$

Where R_c is the radius of curvature of the curve. It is positive (negative) when its direction is parallel with $\vec{e}_n$ ($-\vec{e}_n$).

Substituting Eq. (4.15) into the zero divergence equation and making use of Eq. (4.18), one can obtain the sheath voltage equation along a curve

$$A_{11}\frac{\partial}{\partial s}(\frac{\partial V_{RF}}{\partial s}) + (\frac{\partial A_{11}}{\partial s} + \frac{A_{21}}{R_c}) \cdot \frac{\partial V_{RF}}{\partial s} = \frac{\partial}{\partial s}(A_{12}E_n) + \frac{\partial}{\partial n}(A_{21}E_s + A_{22}E_n + A_{23}E_z) + \frac{A_{22}E_n}{R_c} \text{ (4.19)}$$

For the flat boundary, it reduces to,

$$\frac{\partial}{\partial y}(\varepsilon_\perp\frac{\partial V_{RF}}{\partial y}) = i\varepsilon_\times sin\theta\frac{\partial E_y}{\partial x} - \frac{\partial}{\partial y}(i\varepsilon_\times sin\theta E_x) + (\varepsilon_{//} - \varepsilon_\perp)sin\theta cos\theta\frac{\partial E_z}{\partial x} + (\varepsilon_\perp sin^2\theta + \varepsilon_{//}cos^2\theta)\frac{\partial E_x}{\partial x} \text{ (4.20)}$$

Again, V_{RF} is solved only at the sheath boundaries. The two metallic boundaries at the bottom of the two far SOL regions in *Figure 4.5* are consequently not involved. Each boundary now needs two boundary conditions at two extremities. Dirichlet boundary condition $V_{RF}=0$ is used at the points surrounded by small rectangles in *Figure 4.5*. The underlying assumption here is that there is no RF sheath at those points. The Neumann boundary condition $\frac{\partial V_{RF}}{\partial y} = \mp\frac{i\varepsilon_{sh}}{\varepsilon_\times\delta(\theta)sin\theta}V_{RF}$ based on sheath capacitance is used at the two points surrounded by small ellipses.

The main difficulty to implement Eq. (4.19) along the 1D sheath boundaries in COMSOL is that Eq. (4.19) contains the normal derivative of tangential/normal variables, such as $\frac{\partial tx}{\partial n}$, whereas those variables are only defined at the boundaries in COMSOL. The problem can be solved using specific COMSOL build-in operators. Alternatively, those partial derivatives can be calculated analytically if we assume the tangential/normal variables are defined in the domain. Appendix C explains these two ways of implementing Eq. (4.19) in COMSOL.

c.   Short remark on these two approaches

This section presents two approaches to evaluate the V_{RF}. The first approach is easy to implement but sometimes it is difficult to choose the starting points of the line integral, e.g. for a vertical boundary, like boundary 1 in *Figure 4.1*, choosing $V_{RF}=0$ at the upper extremity could automatically leads to $V_{RF} \neq 0$ at lower extremity and vice versa. Hence, the "no sheath" assumption cannot be fulfilled at both points. The second approach has no such problem since V_{RF} is constrained at both two extremities of each boundary. But numerical tests show the V_{RF} is not converged to the mesh using this approach, see details in section 4.4.3. Therefore, at this moment, the line integral approach is used as the primary method to computer V_{RF}. If the numerical issues are solved in the future, then the second approach can be a better choice.

4.3.3   The DC plasma potential module

The V_{DC} module also needs to be modified to fit the tilted magnetic configuration. The conductivity tensor in Eq. (4.6) should be converted to fit the new (x,y,z) coordinate. It is done by doing a similar coordinate rotation as the dielectric tensor $\boldsymbol{\varepsilon}_r$, i.e. in Eq. (2.10), replace $\varepsilon_{//}$ and $\varepsilon_{\perp}$ by $\sigma_{//}$ and $\sigma_{\perp}$, meanwhile set $\varepsilon_{\times} = 0$.

$$\boldsymbol{\sigma}_{DC}(\theta) = \begin{pmatrix} \sigma_{\perp} sin^2\theta + \sigma_{//}cos^2\theta & 0 & (\sigma_{//} - \sigma_{\perp})sin\theta cos\theta \\ 0 & \sigma_{\perp} & 0 \\ (\sigma_{//} - \sigma_{\perp})sin\theta cos\theta & 0 & \sigma_{\perp}cos^2\theta + \sigma_{//}sin^2\theta \end{pmatrix} \begin{matrix} x \\ y \\ z \end{matrix} \tag{4.21}$$

As in the SSWICH-SW code, $\sigma_{//}$ takes the Spitzer conductivity Eq. (1.7). The separation of conductivity introduces a badly known parameter $\sigma_{\perp}$, but apparently affects the V_{DC} value in the simulations [Jacquot 2013A]. This uncertainty leads to a weak point of the SSWICH-SW code. At this moment, we still keep using the present conservation of the DC charge equation. DC sheath voltage is solved in the SOL region of *Figure 4.6*.

Besides, sheath rectification should be reconsidered now with the magnetic field tilting. Detailed formulations on the floating potential V_f, RF biasing V_b, saturation current J_{sat} and j_{max} under tilted $\mathbf{B_0}$ have been given in sections 2.33-2.34.

Three types of the boundary conditions are used as seen in Eq. (4.8). We assume there is no perturbation to the main plasma, so $V_{DC}=V_f$ is imposed along the red boundary of Figure 4.6. Since there is no sheath at $//\mathbf{B_0}$ boundary, the zero flux boundary condition is used at the black boundaries. The generalized sheath rectification formula Eq. (2.66) is used along the sheath boundaries. As the boundary is curved, the effective current at the boundary is the normal projection of the toroidal current, which reads,

$$J_n = J_{is}^{\perp B} abs(nx) \cos\theta (1 - \min(\frac{J_{es}^{\perp B}}{J_{is}^{\perp B}}, \exp(\frac{e(V_f + V_b - V_{DC})}{K_B T_e}))) \tag{4.22}$$

The current sheath-rectification formula Eq. (4.22) for RF sheath with tilted $\mathbf{B_0}$ is still simple. It can be further refined when more complete "microscopic" models of the sheaths are available.

4.3.4   The asymptotic version

As mentioned in the Section 4.2, the requirement of a prior knowledge of the sheath width in $E_{//}$ boundaries leads to the development of the asymptotic SSWICH-SW version which is based on the wide

sheath approximation. Simulation by the SSWICH-SW code shows the asymptotic version can already provide a first guess that very close to the final solution. We do the same in the 2D SSWICH-FW code. It means in the boundary condition(4.11), D_n tends to be zero in order to keep V_{RF} finite. Thus the sheath width can be avoided in this boundary condition. This simplification needs to be justified later. Extend $D_n=0$ using the constitutive relation, the sheath boundary condition in Eq. (4.12) can be rewritten as,

$$\begin{cases} E_y = -\varepsilon_{11} E_x / \varepsilon_{12} \\ E_z = 0 \end{cases} \tag{4.23}$$

at the flat boundaries, While

$$\begin{cases} E_x = (\varepsilon_{22} \cdot tx - \varepsilon_{12} ty) \cdot F(ty) \cdot E_y / (\varepsilon_{11} \cdot ty - \varepsilon_{21} \cdot tx) \\ E_z = 0 \end{cases} \tag{4.24}$$

at the curved boundaries, where the dielectric element Eq. (2.11) is used. $F(ty)$ is a smooth function which depends on y component of tangential vector. ty varies from 1 at the vertical sheath boundary to 0 at the toroidal boundaries. In the following tests, we chose hyperbolic tangent function as the smooth function. Physically it means the sheath width has a continuous decay from large width to zero.

$$F(ty) = \text{abs}(\tanh(15 * ty)) \quad ty \in [-1, 1] \tag{4.25}$$

Its role will be further discussed later in 4.4.2.

4.3.5   Progress and challenges towards 3D

The wave equation Eq. (4.9) can be directly implemented in 3D. Work has been done within a European project to develop the 3D RAPLICASOL code with full TS and AUG antenna geometry [Jacquot 2015]. In the future, this code is going to replace the current 2D RF field module in SSWICH-FW code. The problem of memory cost is foreseen. During this thesis, the COMSOL workstation in CEA has been upgraded to 128Gb of memory. A single run of 3D RAPLICASOL costs more than 100 Gb of memory and around 4 hours.

Besides, not all the sheath boundary conditions are ready, at this moment, to be implemented in 3D.

Myra and D'Ippolito's boundary condition [Eq. 2.71] implicitly indicates

$$\frac{\partial E_s}{\partial z} = -\frac{\partial V_{RF}}{\partial z \partial s} = \frac{\partial E_z}{\partial s} \rightarrow \mathbf{n} \cdot (\nabla \times \mathbf{E}) = 0 \tag{4.26}$$

The rotation of the vector field in curvilinear coordinate has been derived in Appendix B. So the boundary conditions for 3D RF field module could be written as,

$$\begin{cases} \mathbf{n} \cdot (\nabla \times \mathbf{E}) = 0, D_n = \dfrac{\varepsilon_{sh} V_{RF}}{\delta_{DS}(\theta) | nx |} \quad sheath \\ Ex = Ez = 0 \qquad\qquad metal \end{cases} \tag{4.27}$$

Eq. (4.26) is equivalent to $B_n=0$. The asymptotic version will thus use $B_n=0$, $D_n=0$ at the sheath boundary. In engineering design, this is called "DB" boundary conditions [Lindell 2009][Bosiljevac 2011]. Lindell proved that for a TE polarized plane wave (w.r.t incidence plane), this boundary condition can be replaced

SSWICH-FW: Self-consistent modelling of full wave propagation and

DC plasma biasing by RF sheath   Chapter. IV

by a PEC, whereas for a TM polarized plane wave, it can be seen as a PMC. He later successfully implemented this type of boundary condition into a circular waveguide [Lindell 2010]. The DB boundary condition is incomplete for a normal incidence plane wave. In this case the plane wave naturally fulfill the vanishing of longitudinal components. So this boundary does not play a role of boundary at all. None of these properties seems to be held in magnetized plasma waves. [Kohno 2012] demonstrates the possibility of modelling RF sheath by this boundary condition. However, constraining the normal electric field in COMSOL turns out to be problematic. Like any other commercial EM modeling software, COMSOL only provides the possibility to set the tangential fields at the boundary. Appendix D provides a promising way to implement DB boundary condition in COMSOL. At this moment, this method is only tested in the free space.

In terms of V_{RF} model, the conservation of displacement is still valid in 3D. But we haven't tested the divergence vector expressed in a 2D curved plane even though its mathematically form is derived in Appendix B. Clearly the primary approach of solving V_{RF} in 1D is not suitable for calculating V_{RF} in 2D plane of the 3D domain.

All the equations in the V_{DC} model can be implemented in 3D.

4.3.6   Parametric setup for numerical tests

Some numerical tests of the 2D SSWICH-FW code were conducted to demonstrate the feasibility and points out the limitations of the code, if there is any. The numerical tests in this chapter use a plasma composed of sole Deuterium. The following TS like parameters are taken: The **B₀** scales as $1/R$, with R major radius axis. **B₀** at aperture (y=0.214)=2.3T, RF wave frequency $f = \frac{w_0}{2\pi} = 48MHz$. A realistic density profile from TS shot 40574 (*Figure 3.3*) is used in the main plasma. The density at the aperture is about 4.5×10^{18}m^{-3}. The RF fields are excited by imposing 1A poloidal current on each strap. Mesh is the densest along the sheath boundary, i.e. 5×10^{-4}m (size), and sparsest inside vacuum antenna, i.e. 5cm (size).

4.4   Numerical issues in the code

This section aims at testing numerically the sheath boundary conditions in the RF field module, Eq. (4.23) and Eq. (4.24). The first part of this section shows the impact of the finite element shape on the RF field simulation. The second part discusses numerical problems at the transition point, i.e. the point where the sheath width varies rapidly, and the mesh dependent behavior of the derivative of the electric field at the sheath boundaries. The last part decreases the magnetic tilt angle gradually, to see how far we can push it to zero while keeping the numerical error of the boundary conditions Eq. (4.23) and Eq. (4.24) in an acceptable level.

4.4.1   The choice of the shape function in solving vectorial wave equation

Unlike solving the classical PDE equations, i.e. Helmholtz or Poisson equations, where the nodal (Lagrange) element are used. For solving the electromagnetic field problems, the vector or edge elements are often adopted. The advantage of the latter is that it releases the continuity condition imposed on the normal components of the EM fields across the interior boundaries between different media. In both cases, using a higher order of the finite element could generally achieve a better accuracy of the solution, given the same mesh size. The vectorial wave equation Eq. (4.9) is implemented in the RF module. It uses by default the vector element, but provides flexibility to change the order of finite element shape. The default one is quadratic. There are also linear and cubic as alternatives.

Firstly we use the quadratic finite element to solve the wave equation and examine the solution at the lower-left boundary in the far SOL region, shown by blue curve in *Figure 4.7* (a). The toroidal length of the far SOL shown in *Figure 4.3* is reduced in order to save memory. The dependence of the RF fields on the dimensional length will be discussed in the next Chapter. The blue line in *Figure 4.7* (c) is E_x imposed by sheath boundary condition, which should in principle match the E_x calculated in COMSOL (green line). But we can see returned E_x has some oscillations meaning that the sheath boundary condition does not behave properly, see *Figure 4.7* (c). The period of the oscillation is correlated to the mesh size which is shown in *Figure 4.7* (b). A similar check in the flat boundary gives a better result. Now we keep everything the same but change the shape function order to cubic and solve the wave equation again. The E_y at the same boundary is shown in *Figure 4.7* (d). We can see the oscillation disappears. But still the left extremities of the curves in (c) and (d) present some discrepancies. They correspond to the transition points shown by red ellipse in (a). We will talk about this problem in the next section.

(a)

(b)

(c)

(d)
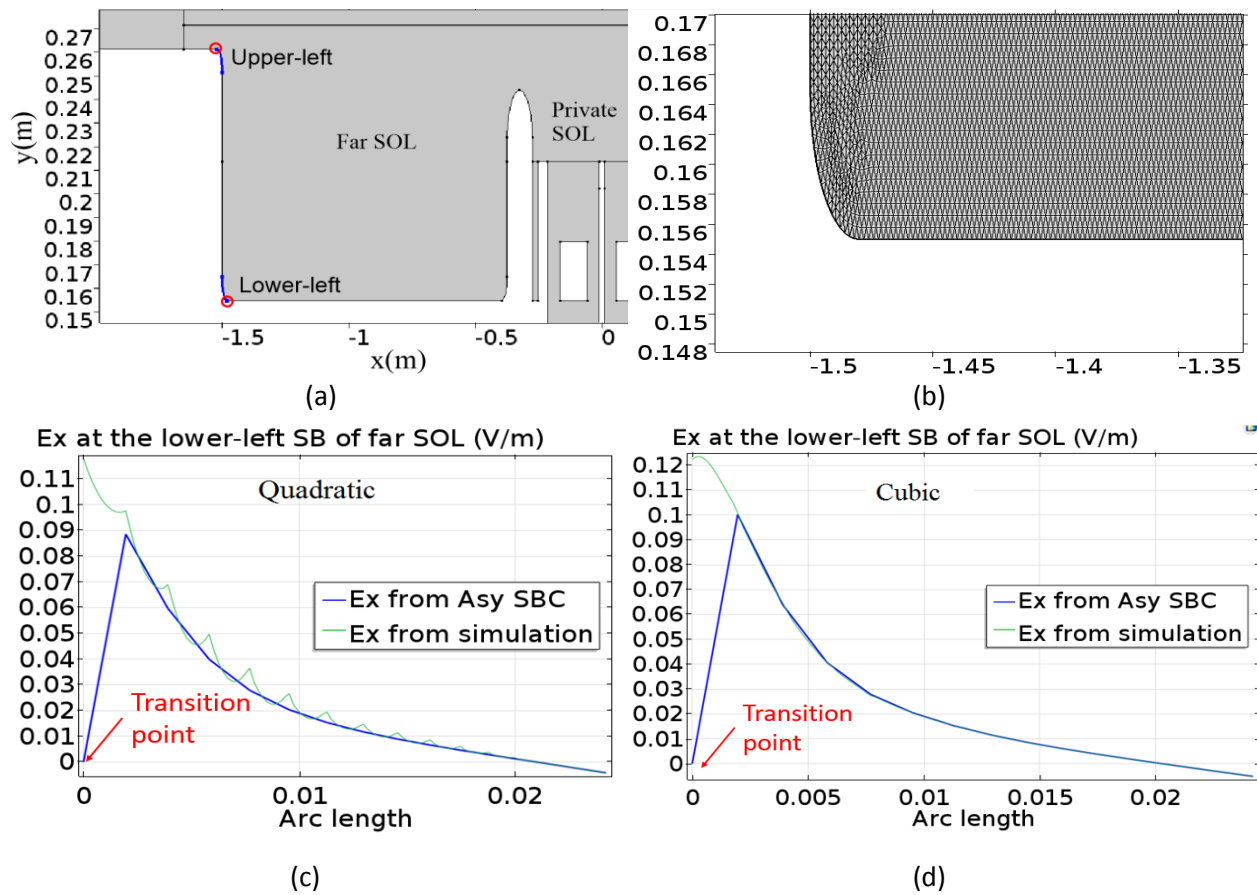
Figure 4.7. Solving the vectorial wave equation using quadratic/cubic shape functions, theta=7°. (a) Choose the lower-left sheath boundary of far SOL region as the target boundary; Red circles show the transition points. (b) shows the mesh around the target boundary; (c) comparison of Ex given by the simulation (Green) using quadratic shape function and Ex given by asymptotic SBC, i.e. the first equation of Eq. (4.24). Arc length goes from the lower-right to the upper-left; (d) comparison of Ex solution using cubic finite shape function with the Ex given by asymptotic SBC at the same boundary as (c)

The cubic finite element shaper can lead to a large memory consumption, typically 40Gb to solve the single wave equation, in contrast to 20Gb when using quadratic element with the same mesh size.

However, another test shows that using quadratic finite element with finer mesh in the SOL region consumes even more memory yet the performance of the sheath boundary condition is worse, see *Figure 4.8*. Hence the cubic finite element is used in RF field module thereafter.
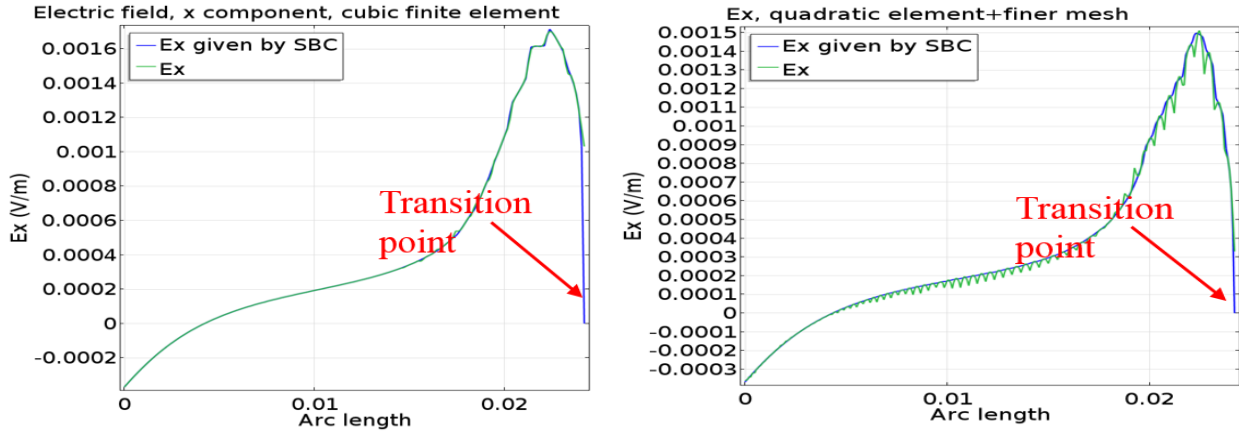
Using cubic finite element, mesh size in sheath region; 1e-3m. Total memory 40Gb, solution time 5mins	Using quadratic + finer mesh, half of the mesh size in SOL region (4 times' of the number of elements). Total memory 80Gb, solution time 10mins

Figure 4.8 . Comparison of the realization of sheath boundary conditions in cubic finite element and quadratic finite element. The upper-left curved sheath boundary of the far SOL region is considered; Arc length goes from lower-right to upper-left.

4.4.2   Discontinuity and mesh dependent behavior at the sheath boundary

Now we will have a special look on the solutions at the transition points. We see in *Figure 4.7* (c)-(d) the E_x calculated in the simulation (green curve) is non zero at the transition point which contradicts with the requirement by the metallic boundary condition or the asymptotic SBC. Furthermore, we tried with different mesh grids, the fields around the transition points are not converged w.r.t the mesh and show some discontinuities, see *Figure 4.9*. The mesh sizes used in these two simulations are extremely fine: 5e-4m^{-1} in x direction and three different sizes in y direction, 5e-4m^{-1} (yscale=2), 2.5e-4 m^{-1} (yscale=3), 1.25e-4 m^{-1} (yscale=4). The smooth function used in the boundary condition(4.24) aims at minimizing the discontinuity occurring at the transition points due to the rapid variation of the sheath width. Without the smooth function, the discontinuity becomes much larger. The discontinuity seems to be a numerical problem. It even appears, but in a much smaller scale, in the case when the asymptotic SBC is switched off. Fortunately both of the mesh-dependent behavior and discontinuity of the RF field only occur locally near the transition points. They should not affect the calculation globally.
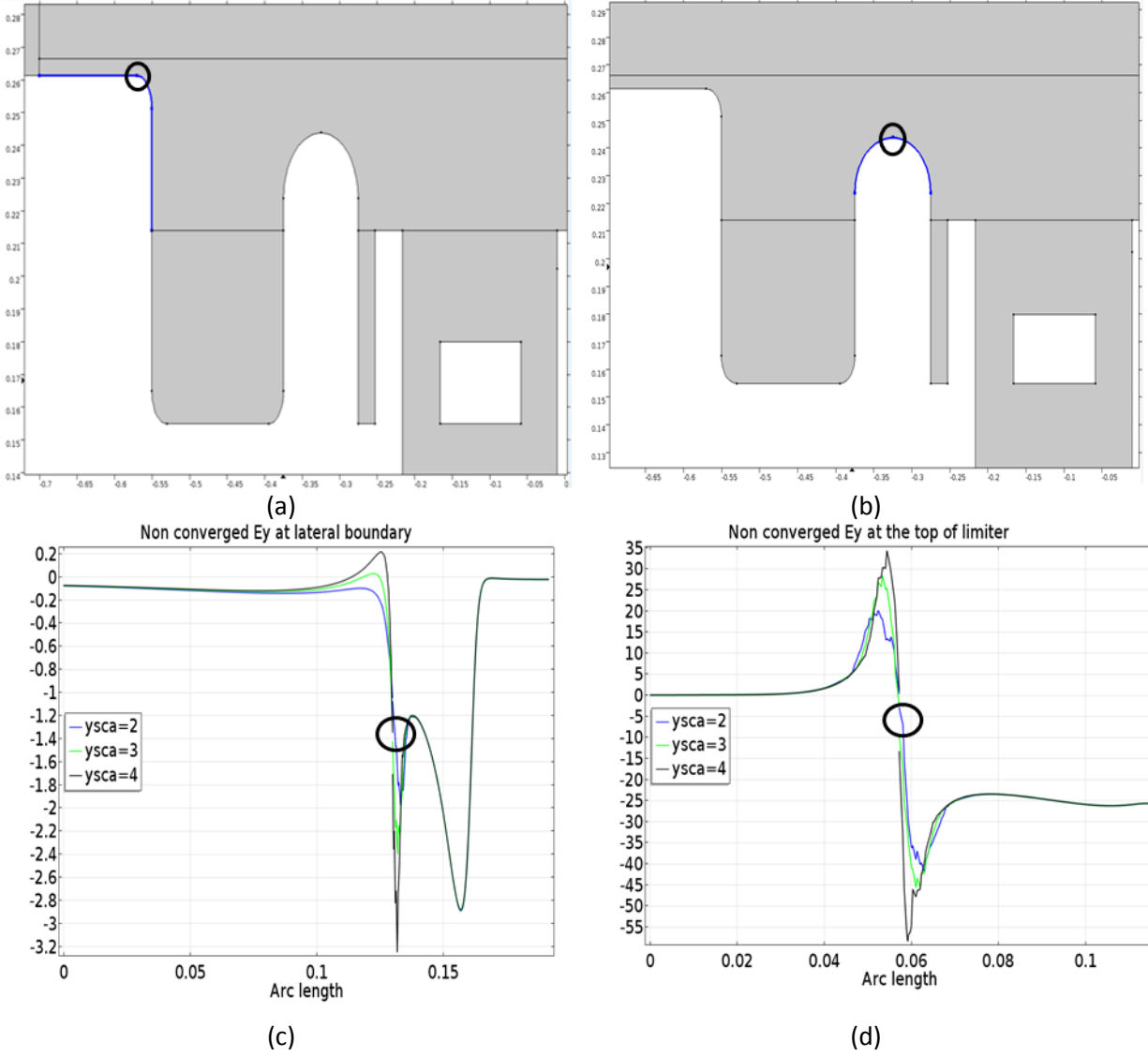
Figure 4.9. (a)-(b) Blue curve Indicates the target boundary while the black circle shows the transition point; (c) Comparison of Ey with three mesh sizes at the boundary in (a). Black circle indicates the transition point; (d) Comparison of Ey with three mesh sizes at the boundary in (b)

Figure 4.10 shows the toroidal and radial electric fields at two sheath boundaries. The boundary elements have a size of 0.5e-4m and 1e-4m in (c) and (d), respectively. We confirms again that excepting some transition points, the fields are generally converged to the mesh size. But even when RF fields are converged, their gradients i.e. E_{xx} (= $\dfrac{\partial Ex}{\partial x}$) are not necessary converged to the mesh size, see (e)-(f). The most problematic place is the upper part of boundary (a). This mesh-dependent behavior also appears in the other derivatives, but E_{xx} is the one most sensitive to the mesh size.

(a) Left sheath boundary

(b) Right sheath boundary

(c) Ex on the boundary (a)

(d) Ey on the boundary (b)

(e) Exx on the boundary (a)

(f) Eyy on the boundary (b)
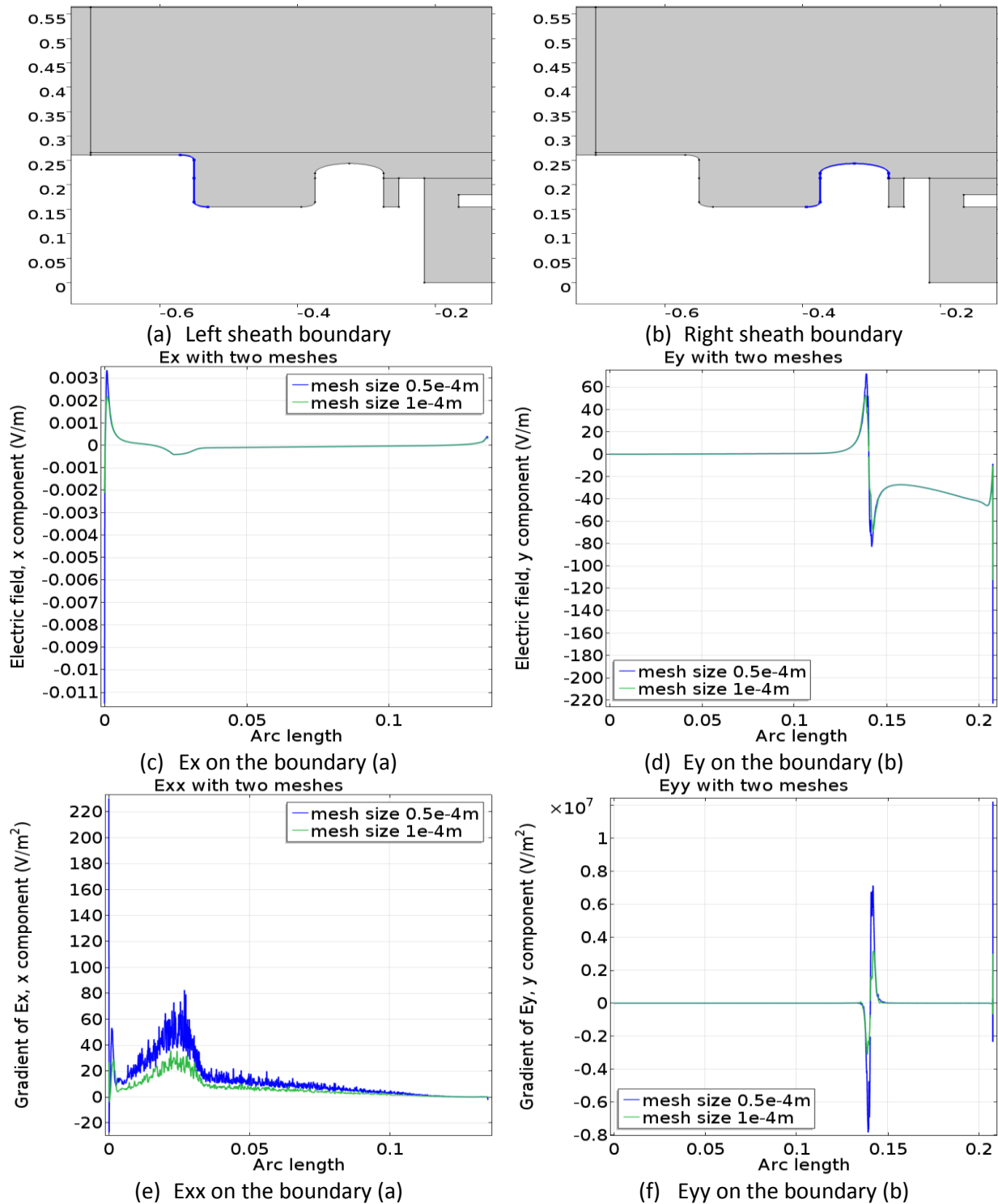
Figure 4.10. A plot of electric field and its derivatives along sheath boundaries, theta=7°; Arc length from left to right

This mesh-dependent of the derivative of the electric field unfortunately dismisses the secondary approach of evaluating V_{RF} as both the Eq. (4.19) and Eq. (4.20) containing the derivatives. Indeed, the comparison of V_{RF} evaluated by this approach shows (*Figure 4.11*) the difference between two different mesh sizes can lead up to 100%.

(a) V_{RF} on the boundary of Figure 4.10 (a)   (b) V_{RF} on the boundary of Figure 4.10 (b)
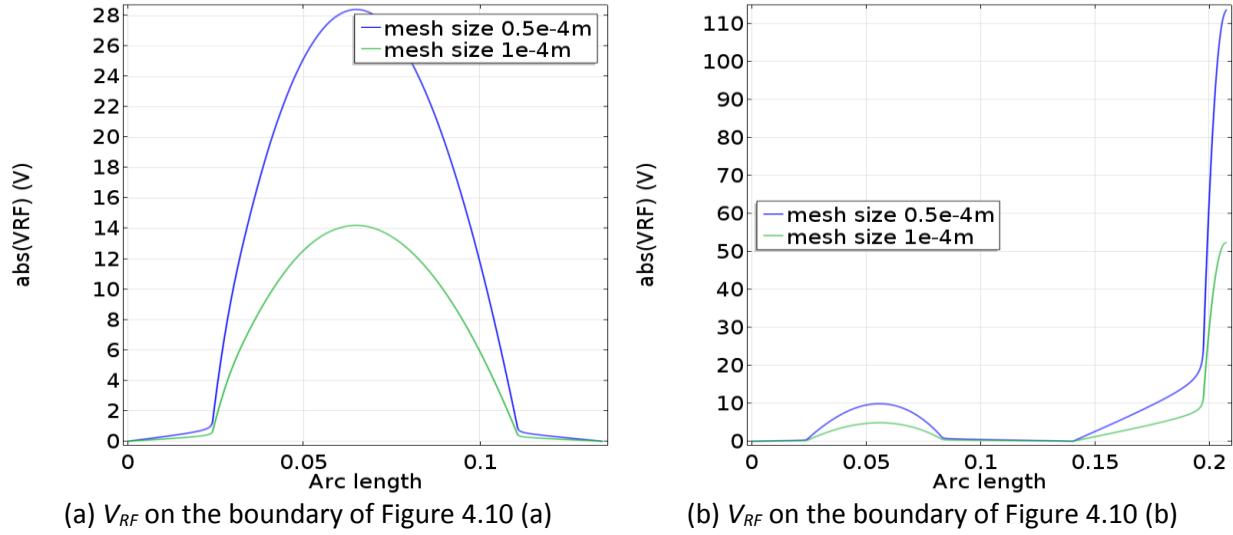
Figure 4.11. Test of V_{RF} with different mesh sizes, 1A current on each strap. Theta=7°

The slow wave propagation equation, i.e. Eq. (4.1) in the SSWICH-SW code uses the Lagrange element and it does not have such a mesh-dependent derivative. Indeed, the vector element method are more sensitive to the element quality than the Lagrange element [Mur 1994]. We will see in the next chapter that using vector element, the derivatives are difficult (but possible with extremely fine mesh size) to achieve convergence even at the metallic boundaries. Things get worse with SBCs. This mesh-dependent derivative of *Figure 4.1* is most probably linked with the compatibility between the vector element used in solving the vectorial wave equation and our choice of the asymptotic SBCs. Work is undergoing to improve the finite element method in solving Maxwell's equation in plasma [Campos Pinto 2016].

4.4.3   Accuracy of the RF field simulation at small magnetic tilt angle

One could note that the current asymptotic sheath boundary condition (4.23) and (4.24) contain $sin\theta$ in the denominator. It is worthwhile to check how small the magnetic tilt angle can go without losing a good numerical accuracy. We will now compare the relative error: dEx/Ex (dEx is the error between Ex imposed by the sheath boundary condition and Ex given by COMSOL calculation) and dEy/Ey.

The first boundary we check is the curved boundary at the lower-left of the far SOL region, the blue boundary in *Figure 4.12* (a). The curvature is introduced by using an ellipse fillet which has semi-axes a=0.02m, b=0.01m. Those lengths are chosen to minimize the numerical errors. For example, using a circle fillet with radius of 0.02m can lead to the relative error of E_x reach 2% when theta=7° and 10% when theta =1°. Using the ellipse, the error has been well reduced, see *Figure 4.12* (b). Sheath boundary condition performs better along the other boundaries, e.g. the flat boundary in *Figure 4.12* (c) and other curved boundaries. If we choose relative error<1% as a criterion, then the minimum angle one can reach is 0.01° along flat boundary and 1° along curved boundary.

(a)

(b)

(c)

(d)
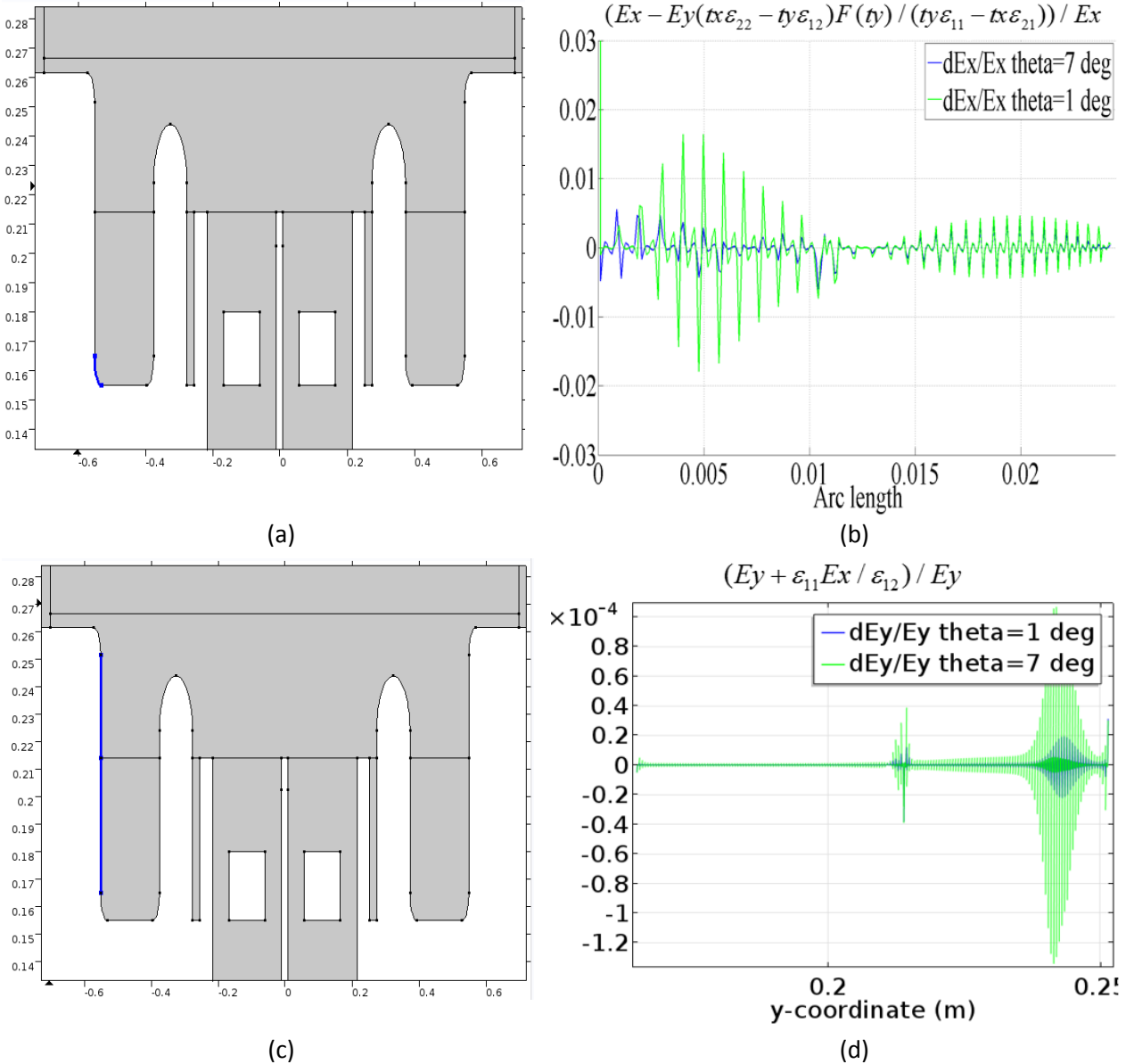
Figure 4.12. Test of the accuracy of the sheath boundary condition at the boundaries. (a) an example of curved boundary; (b) relative error of COMSOL returned Ex at boundary (a) with Ex required by the sheath boundary condition that is imposed at boundary (a) under two magnetic tilt angles; (c) an example of flat boundary; (d) relative error of COMSOL returned Ex at boundary (c) with Ex required by the sheath boundary condition that is imposed at boundary (c) under two magnetic tilt angles

4.5   Adaptations of SSWICH for ALINE simulations

Above, we have mentioned how SSWICH-FW code is implemented for Tokamak simulations. As a general method, it can in principle be used in any device. This section introduces how we transfer SSWICH philosophy into a totally different device, the Aline machine.

As mentioned in chapter 2, there are two waves can exist within Aline operation limits: the Helicon wave and the LH wave. The former corresponds to the fast wave and the latter corresponds to the slow

wave. The Helicon wave is inherently electromagnetic and can only be realized using the full wave simulation. The RF module of the 2D SSWICH-FW code is thus used in this simulation. The simulation is done w/o sheath boundary conditions. The equatorial plane of the realistic ALINE vacuum vessel (*Figure 1.14*) is chosen for our 2D simulation. *Figure 4.13* shows the adapted SSWICH geometry. All the boundaries are flat. The excitation technique introduced in *Figure 2.11* is used, where the antenna and stainless steel wire have been treated as PECs. The metal connection between the stainless steel wire and the disk antenna is not shown since the stainless steel wire is not meshed. The same vectorial wave equation, Eq. (4.9) is solved in this domain.
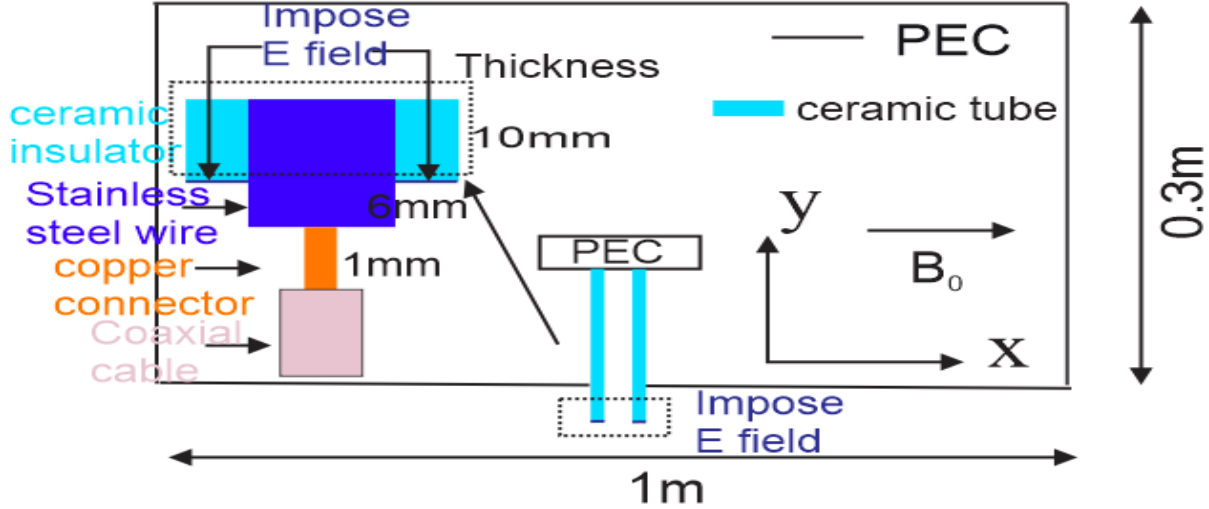
Figure 4.13. 2D SSWICH-FW geometry for Helicon wave Simulations. The feeder structure inserted on the left side is a zoom in the region indicated by the black rectangle;

In order to avoid creating a resonant cavity as being discussed in the chapter 3 where the numerical convergence was not guaranteed, we added a collisional damping. The ionization threshold for Argon is about 15.6eV. Under current energy level of Argon plasma (around Ti=0.026eV, Te=5eV) in Aline, the ionization was very low. The dominant collision was thus the electron-neutral collision. A simple estimation for this frequency could be found in [Chabert 2011].

$$v_m = n_g \overline{\sigma}_{el} \overline{v}_e \qquad\qquad (4.28)$$

Where n_g is the neutral density, $\overline{\sigma}_{el}$ is the cross section, $\overline{v}_e$ is the mean velocity of a Maxwellian electron Eq. (2.53). This electron-neutral collision frequency is added as the imaginary part of the wave frequency in the dielectric tensor as shown in section 2.2.3.

Knowing the typical working gas pressure in Aline (like 10^{-2} mbar or 1 Pascal), the ion-neutral mean free path can be obtained by the following empirical formula that accounts for ionization, ion-neutral elastic collision, excitation [Chabert 2011],

$$\lambda_{i-n}(m) = 0.0042 / P(Pa) \qquad\qquad (4.29)$$

Taking the thermal velocity of ions, one can easily calculate the ion-neutral collision frequency.

The RF sheath is examined separately to the helicon wave simulations. The Aline device has a horizontal magnetic field. Under this **B₀**, the sheath boundary condition only contains the slow wave. Thus we could model RF sheath with 2D SSWICH-SW code. Besides, the slow wave propagation equation, which is a Helmholtz equation, has less numerical instabilities as shown in the previous section and the Appendix A.
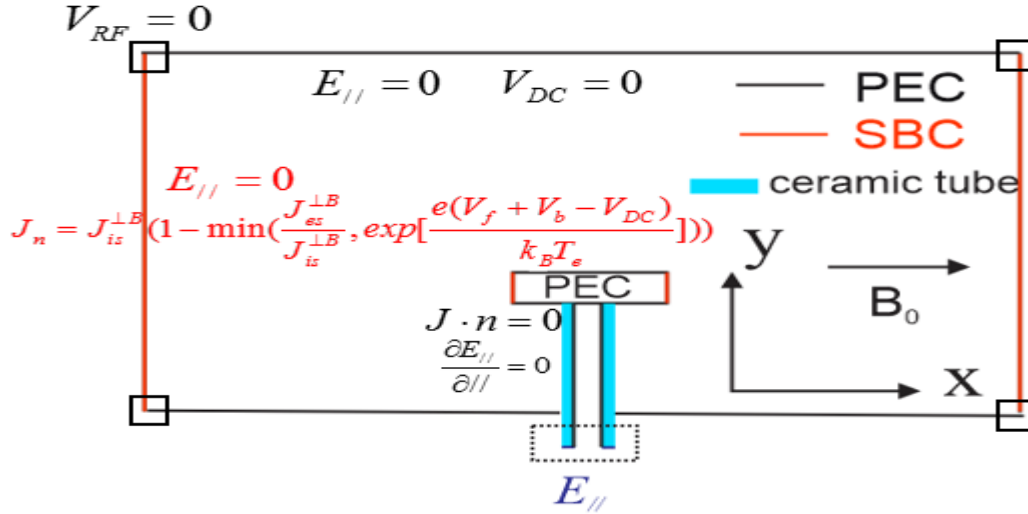
Figure 4.14. Boundary conditions used in SSWICH-SW simulation for Aline

The excitation is the same as shown in *Figure 4.13* where $E_{//}$ field map is imported at the bottom of the ceramic insulator. The slow wave propagation inside ceramic and stainless steel wire can be derived by replacing the plasma dielectric element $\varepsilon_{//}$ and $\varepsilon_{\perp}$ in Eq. (4.1) by $1 - \dfrac{i\sigma}{w_0 \varepsilon_0}$, where σ is the conductivity of the ceramic and stainless steel wire given in section 2.2.2. In the RF field module, PEC boundary condition ($E_{//}$ =0) is used at the parallel boundaries of the antenna and vessel wall. In this case, the asymptotic sheath boundary condition gives the same $E_{//}$ =0 as PEC, see the second equation of equation 4.2 with infinite sheath width. V_{RF} is only solved along the sheath boundaries by Eq. (4.4). At each boundary, V_{RF} =0 is imposed at two extremities. V_{DC} is only solved inside the plasma via Eq. (4.7). The Spitzer conductivity used in SSWICH-FW accounts for electron-ion collisions. This is barely validated in the Tokamak case where the ionization rate is very high. In Aline, the dominant collisions are those with neutrals. The new parallel conductivity accounts for electron-neutral friction, it is proposed by Eq. 2.53 in [Chabert 2011] or the parallel term in the expression 1.3 in [Rozhansky 2008].

$$\sigma_{//} = \frac{n_e e^2}{m_e v_m} \tag{4.30}$$

Where we have set $w = 0$ in the original formula to represent the DC conductivity. Since ions have larger Larmor radius which gives it larger mobility in perpendicular direction than electrons, the perpendicular conductivity thus accounts for the ion-neutral collisions,

$$\sigma_{\perp} = \frac{n_i e^2}{m_i v_i} \tag{4.31}$$

where v_i is the characteristic frequency of ion-neutral collision. For the Argon plasma in Aline, the ions are often not magnetized, meaning that the ion-neutral collision frequency can be larger than the ion cyclotron frequency. Eq. (4.31) can also be obtained by simplifying the perpendicular term in the expression 1.3 in [Rozhansky 2008] under the approximation, $w_{ci} << v_i$.

A typical range of collision frequency can be found in [Faudot 2015]. In the experiment, the outer walls of Aline are connected to the ground. The disk antenna (electrode) can either be grounded or floating via inserting a capacitor in the feeder. In the latter case, the biasing potential at the antenna can be known.

Therefore, the boundary conditions used in the V_{DC} are,

- //$\mathbf{B_0}$ vessel walls: $V_{DC}=0$
- $\perp\mathbf{B_0}$ vessel walls and antenna side boundaries: sheath boundary condition, i.e. second equation of Eq. (4.8)
- //$\mathbf{B_0}$ antenna boundaries: $J \cdot n = 0$
- Ceram/plasma interfaces: $J \cdot n = 0$

4.6   Conclusion of this chapter

In this chapter, we presented the evolution of 2D SSWICH code from the slow wave version to the full wave version. Right now, the SSWICH-FW code has a 2D toroidal/radial geometry and the plasma is assumed only to evolve in the radial direction only. It adopts a tilted B_0 and shaped walls. Under tilted B_0, the formula of sheath capacitance, sheath rectification and Child-Langmuir law all have been revised. Now with the new magnetic configuration, the fast wave is being coupled into the sheath boundary condition. SSWICH-FW is thus able to study the fast wave coupling and sheath physics simultaneously. Compared to the previous slow wave only version, the full wave code has the following new features: 1. The RF field module has a current excitation by realistic antenna geometry, including the antenna box, limiters, septum and straps. The fast wave is damped by an artificial medium, the Perfect Matched Layers. At this moment, a simple generalized form of RF sheath capacitance is used as a boundary condition in solving the Maxwell's equation. 2. The RF sheath boundary condition proposed by [D'Ippolito 2006] is implemented making use of the boundary PDE instead of volume PDE in order to save memory. 3. A generalized form of DC sheath rectification is used in DC plasma potential model. We have also developed the asymptotic version of the SSWICH-FW code, which solves the 3 modules in segregated steps instead of an iterative loop as in the fully coupled version. The asymptotic version assumes the sheath width is infinite. This assumption violates at the transition points where the sheath boundary meets the metallic boundary. Thus a smooth function is included in the sheath boundary condition to gradually decrease the sheath width. The RF field at the sheath boundary likely to have some numerical issues under low order finite element shape. Hence a cubic finite element shape is used in the RF field module. The antenna box is simulated in vacuum so as to avoid the lower hybrid resonance. Due to the limitation of the current sheath boundary conditions, SSWICH-FW code cannot deal with a non-tilted $\mathbf{B_0}$, the minimum tilt angle it can go is 0.01° at the flat boundary and 1° at the curved boundary in order to preserve a fairly good precision level. Several approaches to calculate the oscillating RF sheath voltage have been tried, but only one method (the first approach described in section 4.3.2 a) gives a good numerical stability. The DC plasma potential is still sensitive to the badly constrained parameters, the DC perpendicular conductivity.

The SSWICH-FW code, limited in 2D at this moment for both numerical and physical reason, is initially developed for RF sheath studies in Tokamak. Its philosophy can however be applied to other machines, such as Aline. Application of SSWICH for the Tore Supra ICRH antenna and Aline are illustrated in the next chapter.

Reference

[Bosiljevac 2011] M. Bosiljevac, Z. Sipus, P.S. Kildal and A. A. Kishk, "Modelling EBG surfaces using amended DB boundary conditions", Euro. Conf. on antennas and propagation, 11-15th April 2011, Rome, Italy

[Campos Pinto 2016] M. Campos Pinto and B. Despres, "Constructive formulations of resonant Maxwell's equations", submitted in Feb 2016

[Chabert 2011] P. Chabert and N. Braithwaite. "Physics of Radio-Frequency plasmas", Cambridge University Press, Cambridge, UK, 2011

[Chodura 1982] R. Chodura, "Plasma-wall transition in an oblique magnetic field", Phys. Fluids 25(9) 1982

[Colas 2012] L. Colas, J. Jacquot, S. Heuraux, E. Faudot, K. Crombe, V. Kyrytsya, J. Hillairet and M. Goniche, ,"Self-consistent radio-frequency wave propagation and peripheral direct current plasma biasing: Simplified three dimensional non-linear treatment in the 'wide sheath' asymptotic regime", PoP, **19** 092505 (2012)

[D'Ippolito 2006] D. A. D'Ippolito, J. R. Myra,"A radio-frequency sheath boundary condition and its effect on slow wave propagation", Physics of Plasmas (1994-present) 13(10) - (2006)

[Faudot 2015] E. Faudot, S. Devaux, J. Moritz, S. Heuraux, P. M. Cabrera, and F. Brochard. A linear radio frequency plasma reactor for potential and current mapping in a magnetized plasma. Rew. Sci. Inst., 86 :063502, 2015

[Jacquot 2012] J. Jacquot, D. Milanesio, L. Colas, S. Heuraux and M. Goniche, "Recent advances in self-consistent RF sheath modelling and related physics properties: Application to Tore Supra IC antennae", Proc. 39th EPS conf. & 16th ICPP, Stockholm, Sweden, 2-6th July 2012

[Jacquot 2013] J. Jacquot, L. Colas, F. Clairet, M. Goniche, S. Heuraux, J. Hillairet, G. Lombard and D. Milanesio,"2D and 3D modelling of wave propagation in cold magnetized plasma near the Tore Supra ICRH antenna relying on the perfectly matched layer technique", PPCF 55 115004 (2013)

[Jacquot 2013A] J. Jacquot, PhD thesis, Universite de Lorraine, 2013

[Jacquot 2015] J. Jacquot et.al, "Full wave propagation modelling in view to integrated ICRH wave coupling/RF sheaths modelling", AIP Conf. Proc, 1689, 050008 (2015)

[Kohno 2012] H. Kohno, J. R. Myra and D. A. D'Ippolito, "A finite element procedure for radio-frequency sheath–plasma interactions in the ion cyclotron range of frequencies", Comput. Phys. Commun. 183(2012) 2116-2127

[Lancellotti 2006] V. Lancellotti, D. Milanesio, R. Maggiora, G. Vecchi and V. Kyrytsya, "TOPICA: an accurate and efficient numerical tool for analysis and design of ICRF antennas", Nucl. Fusion 46(2006) S476-S499

[Lindell 2009] I. V. Lindell and A. H. Sihvola, "Uniaxial IB-Medium Interface and Novel Boundary Conditions", IEEE Trans. on antennas and propagation, VOL. 57, NO. 3, MARCH 2009

[Lindell 2010] I. V. Lindell and A. H. Sihvola, "Circular waveguide with DB-boundary conditions", IEEE Trans. on microwave theory and techniques, VOL. 58, NO. 4, April 2010

[Mur 1994] G. Mur, "Edge Element, their advantages and their disadvantages", IEEE trans. on magnetics, v30, N5, 1994

[Rozhansky 2008] V. Rozhansky, "Mechanism of transverse conductivity and generation of self-consistent electric fields in strongly ionized magnetized plasma", 2008, Springer

Chapter 5   Applications of the 2D SSWICH-FW asymptotic code

5.1 Introduction of this chapter

This chapter aims at applying the 2D SSWICH-FW code to do interpretative simulations for Tokamak and Aline device, meanwhile trying to answer the core question being asked in the motivation of this thesis [Section 2.5]: the role of the fast wave in the RF sheath excitation.

In tokamak environment, the suspected role of the fast wave can be summarized as follows: First, the fast wave can mode convert to a slow wave at the walls when the **B$_0$** is tilted to the wall or when the wall has a sharp transition [Kohno 2015]. Besides, the fast wave can induce far field sheath in the region where the wall is not magnetically connected to the wave launcher and locates much further away from the wave launcher than the slow wave evanescence length. Finally, the fast wave may affect the radial extension and parallel prolongation of the V_{DC}. Measurement by the Retarding Field Anaylzer (RFA) shows those lengths are far beyond the slow wave evanescence length. This is currently interpreted by the DC current transport in the SSWICH-SW code. Can the fast wave provide additional mechanism to explain this observation? Can it produce mode conversion and excites the far field sheath in SSWICH-FW simulation? Section 5.2 answers these questions by testing the 2D asymptotic SSWICH-FW code.

A successful model must be able to reproduce and interpret some experimental facts. During operations of TS antennas, the temperature on the antenna surface shows a double-hump poloidal distribution. Left-right asymmetry at the two extremities of the same magnetic field line was observed with asymmetric strap feeding. Section 5.3 shows the comparison of SSWICH-FW/RAPLICASOL simulations with those experimental observations. An ideal model has no uncertainty on the input parameters. This is not the case in SSWICH. The sensitivity of the simulation results on these parameters is addressed.

SSWICH-FW code is also used to conduct electromagnetic simulations for Argon plasmas in Aline. Section 5.4 presents SSWICH-FW simulations on the lower hybrid wave and Helicon wave in Aline. These simulations are conducted without sheath. Section 5.5 studies the RF sheath in Aline using the SSWICH-SW approach, the DC plasma potential from SSWICH simulation is compared to the experimental floating potential map measured by the RF compensated probe.

For the sake of simplicity, only the asymptotic version of SSWICH-FW will be employed for these applications, i.e. the first round in the iterative self-consistent loop. At least in tokamak cases it was verified that the asymptotic results are a fair approximation of the self-consistent results of the fully coupled SSWICH-SW model [Jacquot2014].

5.2 Identifying the role of the fast wave in Tore Supra configuration

SSWICH-FW code is established on the basis of the SSWICH-SW code. Both of the two codes are initially developed for RF sheath studies in Tore Supra Tokamak. Under realistic TS conditions, like density profile in *Figure 3.3*, the typical field pattern is shown in *Figure 5.1*. In this simulation, the excitation is done by imposing 1000A poloidal current with 180° phase difference on the two straps. R cutoff layer locates several centimeters above the antenna aperture (depending on $k_{//}$). The fast wave is propagating above the R-cut off layer and evanescent below. The slow wave is typically evanescent everywhere with an

evanescence length of a few millimeters. Thus it is most concentrated in the private SOL and usually cannot reach the far SOL boundaries (shown by cyan arrow in *Figure 5.1*). The direct excitation of the RF sheath by the evanescent slow wave can be described by the spatial proximity effects, which tells us the emission points which are closer to the sheath wall have a larger contribution to the sheath excitation than those who locate farther away. It is still unclear whether the fast wave also have such a proximity effect.
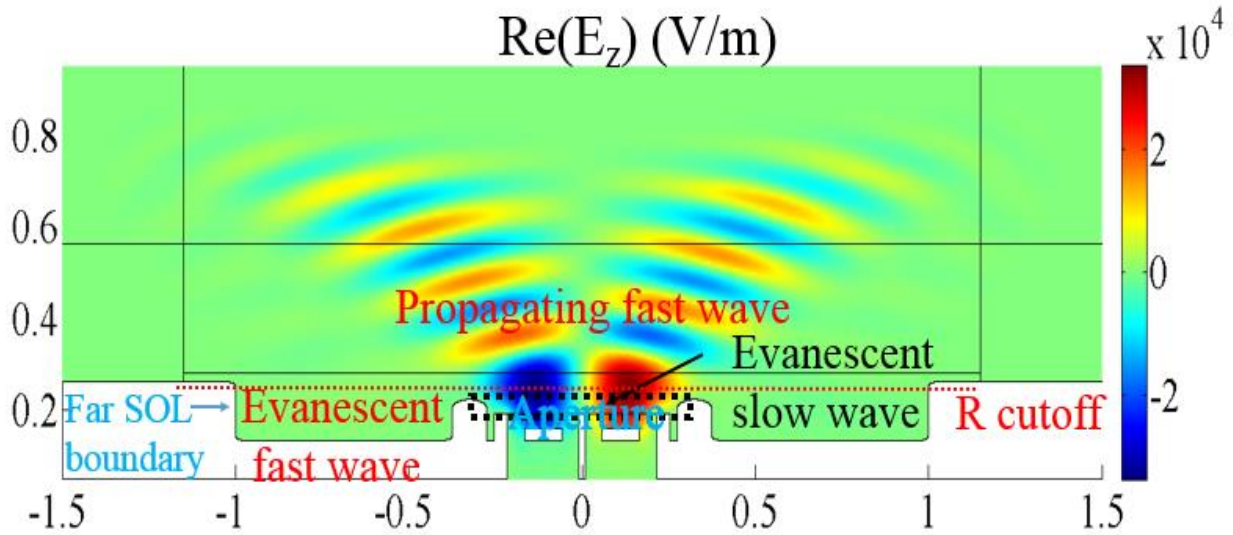
Figure 5.1. The real part of the poloidal electric field obtained in SSWICH-FW under TS configuration. The R-cutoff layer is shown by red dot line. The private SOL is enclosed by black dot rectangle. At its bottom, it is the antenna aperture.

By comparing the SSWICH-FW code with the SSWICH-SW code, one can immediately find out the impact of the fast wave. The first simulation conducted in this section is thus a controlled trial on RF fields. The second test is tuning the dimensional length of the SOL region, trying to see the impact of the dimensional length on the simulation results on one hand, and find evidences of the far field sheath at the far SOL boundaries on the other hand. The last test compares the role of the perpendicular DC conductivity and the fast wave propagation on the radial extension of the V_{DC} structure.

5.2.1 Comparison of RF fields from 2D SSWICH-FW simulations with 2D SSWICH-SW results: observation of mode conversion

The 2D SSWICH-FW solves simultaneously the fast wave and the slow wave polarizations, whereas the slow wave code only solves the slow wave propagation. It's interesting to check the difference of the RF fields from these two codes. To do this, the two codes must have exactly the same geometry and mesh. The following modifications are thus done in the 2D SSWICH-FW code,

1. Tore Supra like geometry, see *Figure 5.1*; The RF Excitation is done by imposing current with dipole phasing on straps.

2. Remove all the curved geometry in the SSWICH-FW code.

3. Remove the vacuum gap between the antenna box and side limiters in the SSWICH-FW code. (It is the two thin rectangular parts hanging below the aperture in *Figure 4.3*).

4. A constant density ($=1.5 \times 10^{18} \text{m}^{-3}$) is assumed all through the private SOL region (the region bounded by two limiters in *Figure 5.1*), in order to get rid of the impact of dielectric tensor evolving with y coordinate in the slow wave propagation. We will only examine the difference of the RF fields in this region.

5. The magnetic tilt angle is set to $\theta=0.01°$ (the limit we can achieve at the flat boundary for which the sheath BC is still working well, see Chapter 4) to match $\theta=0°$ in the SSWICH-SW code.

6. The two wave equations: the vectorial wave equation and the slow wave propagation is implemented sequentially in the same model. The $E_{//}$ field map at the aperture of the SSWICH-FW is used as an input field map to the slow wave code.

The following TS like parameters are used, f=48MHz, density profile TS40574 (*Figure 3.3*), B_0(at aperture)=2.32T. Under this condition, the slow wave has an evanescence length Eq. (2.19) around 3mm in the private SOL region. As a reference, the mesh density here is 0.5mm^{-1}. *Figure 5.2* (a), (c) and (e) show the parallel electric field ($E_{//}$) calculated by the two codes. The relative difference between them is zero at the aperture where they have common fields. Then it increases as the slow wave become evanescent and the fast wave contributes part of $E_{//}$. Finally the propagating fast wave takes over totally and the relative difference of $E_{//}$ consequently becomes very large.

In (a), a large $E_{//}$ pattern appears at the top corners of the side limiters, which does not exist in (c). The slow wave is evanescent before reaching those points, thus we expect it is the fast wave that propagates to that position and mode converts to the slow wave. This observation is similar to the simulations reported in [Kohno 2015], where mode conversion to slow wave occurs when the geometry has a sharp transition.

Figure 5.2 also compares the evolution of $E_{//}$ due to the changing of $\varepsilon_{//}$. The evanescence length of the slow wave Eq. (2.19) is inversely proportional to $\sqrt{|\varepsilon_{//}|}$. Hence reducing $\varepsilon_{//}$ by a factor of 10, the slow wave should propagate further radically. This is confirmed in (d) where the slow wave exceeds the private SOL region. Correspondingly, in (f) the boundary where relative error is less than 1 is shifting upwards. Besides, the $E_{//}$ pattern at the top corners of the side limiters is also increased. (e) has a larger error starting from x=±0.1 and ending at y=0.216. This is because this region is the gap between the main and side lobes where the denominator $E_{//, \text{sw}}$ is small, see (c). Similar to the definition of width of a Gaussian beam, the slow wave evanescence length is defined as the width where the magnitude of $E_{//}$ decreases to 1/e of its maximum value. In log scale, it is the width where the ln(abs($E_{//}$)) decreases 1 unit. *Figure 5.3* shows the slow wave evanescence length is indeed almost 3 times' larger when manually reducing $\varepsilon_{//}$ by a factor of 10.
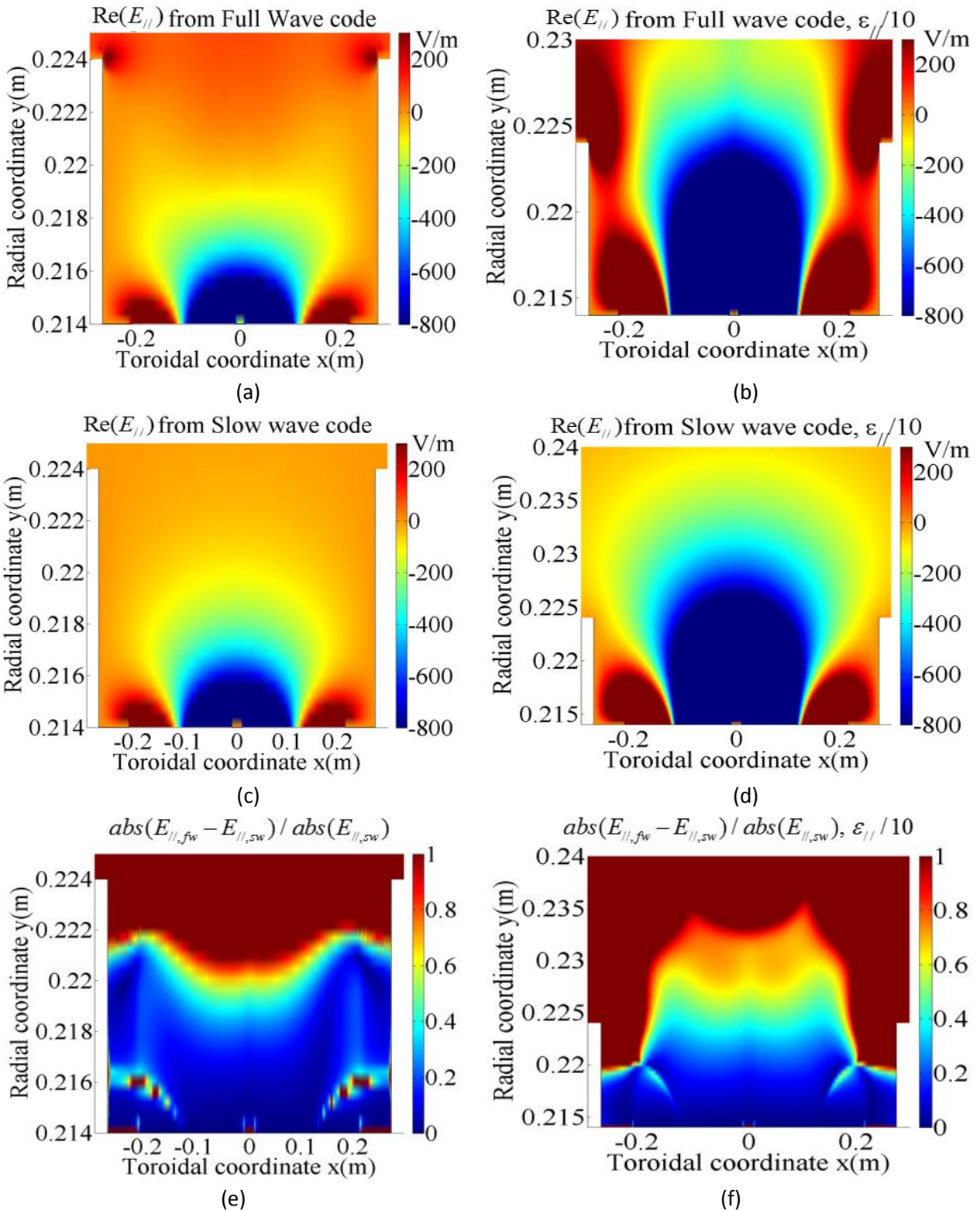
Figure 5.2. Comparison of $E_{//}$ obtained from two codes. (a) , (c), (e) with normal $\varepsilon_{//}$. (b), (d), (f) uses $\varepsilon_{//}/10$. (b) and (d) use the field map from (a) and (c) respectively.
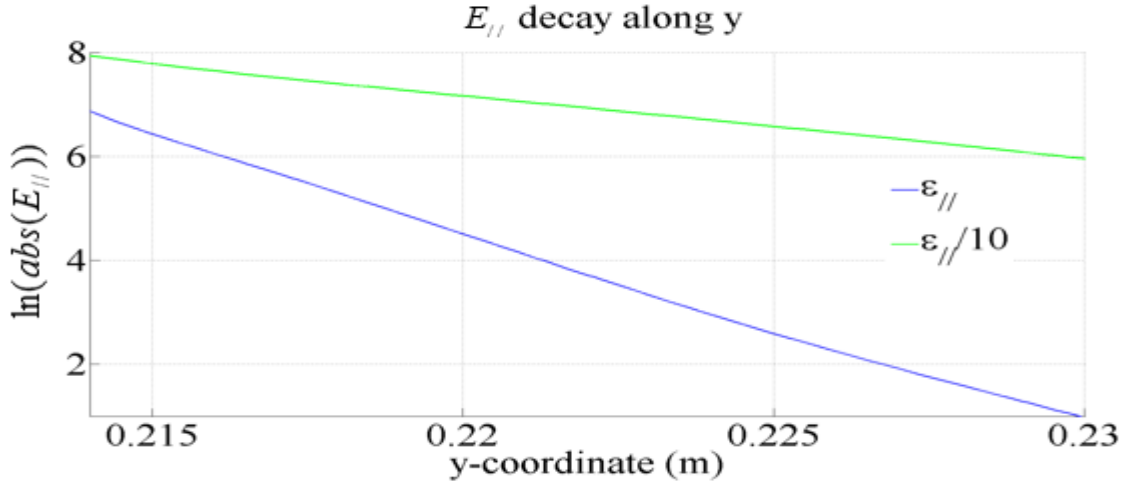
Figure 5.3. $E_{//}$ calculated along a vertical line(x=-0.1m) in the slow wave code

The fast wave dispersion relation Eq. (2.17) can be reformulated as

$$n_\perp^2 = \frac{(n_{//}^2 - \varepsilon_\perp)^2 - \varepsilon_\times^2}{\varepsilon_\perp - n_{//}^2} \text{ (5.1)}$$

From which we see that this wave depends on $\varepsilon_\times$. $\varepsilon_\perp$ is negative above the lower hybrid resonance, thus in the private SOL, the denominator is negative of Eq. (5.1). For our adopted constant density, $\varepsilon_\times = 41$, $\varepsilon_\perp = -14$ and $n_{//} = 10$ (main lobe in dipole phasing, see *Figure 2.8*) in the private SOL. So the numerator is positive and the fast wave is evanescent. Reducing $\varepsilon_\times$ can make the fast wave more evanescent, whereas $\varepsilon_\times$ has no significant impact on the slow wave Eq. (2.18). So changing manually the $\varepsilon_\times$ will only affect the fast wave. Keeping the sheath boundary condition still working correctly, one can investigate how the $E_{//}$ evolves when $\varepsilon_\times$ is changing. Reducing $\varepsilon_\times$ by a factor of 10, the fast wave become more evanescent. This is indicated in *Figure 5.4* where the field structure on the right side is significantly reduced. Note the slow wave code uses the input field map from the output of the full wave code. So even it is only solving the slow wave propagation, the field scale can still be affected by reducing $\varepsilon_\times$ in the full wave code, as seen in *Figure 5.4* (d). The boundary where the relative difference is less than 1, shown in *Figure 5.4*(d) is now changing because both the fast wave and the slow wave are affected. However the slow wave evanescence length should not be affected by varying the $\varepsilon_\times$ in both codes. This is confirmed in *Figure 5.5.*

107
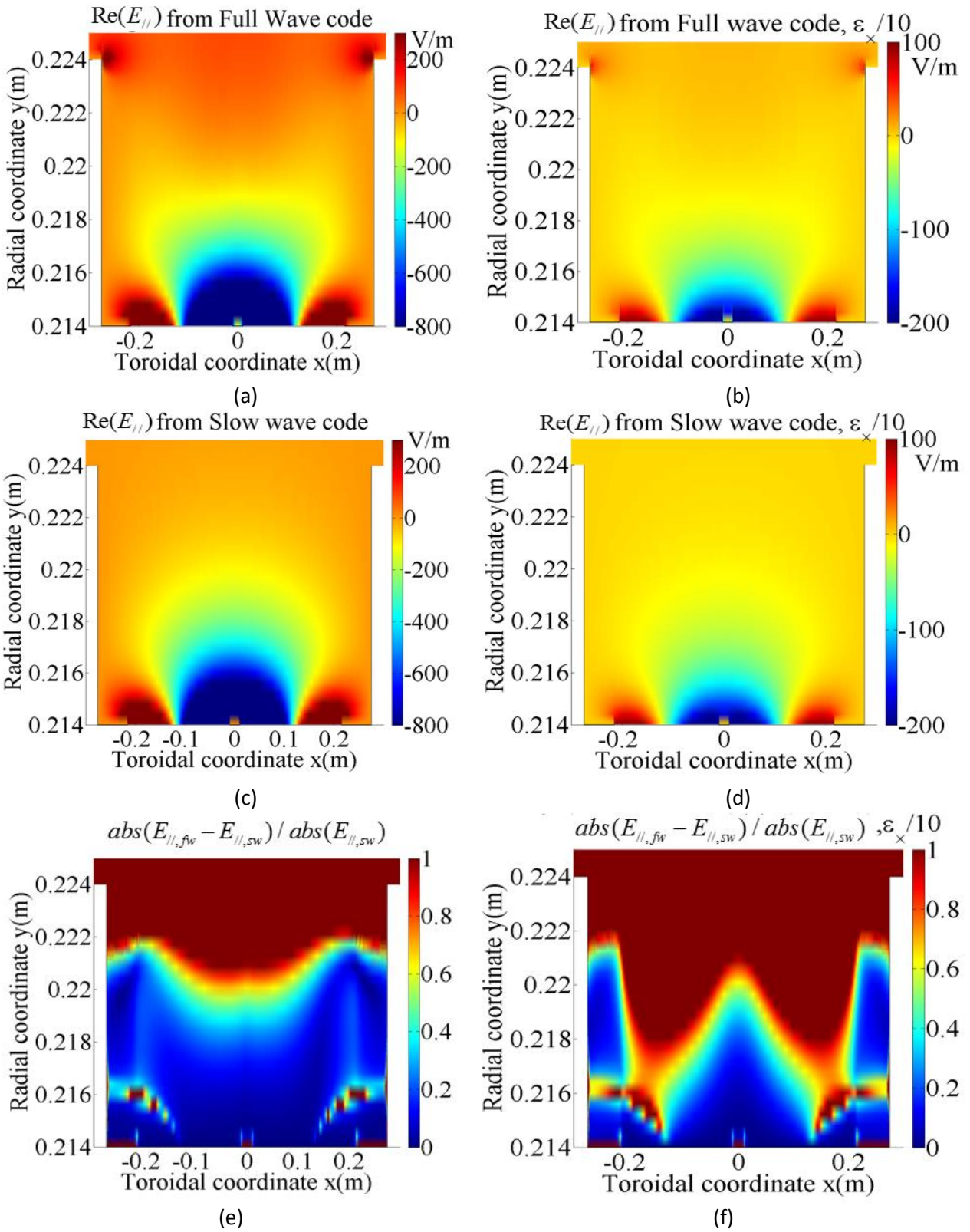
Figure 5.4. Comparison of $E_{//}$. Left: normal parameters Right: $\varepsilon_\times/10$
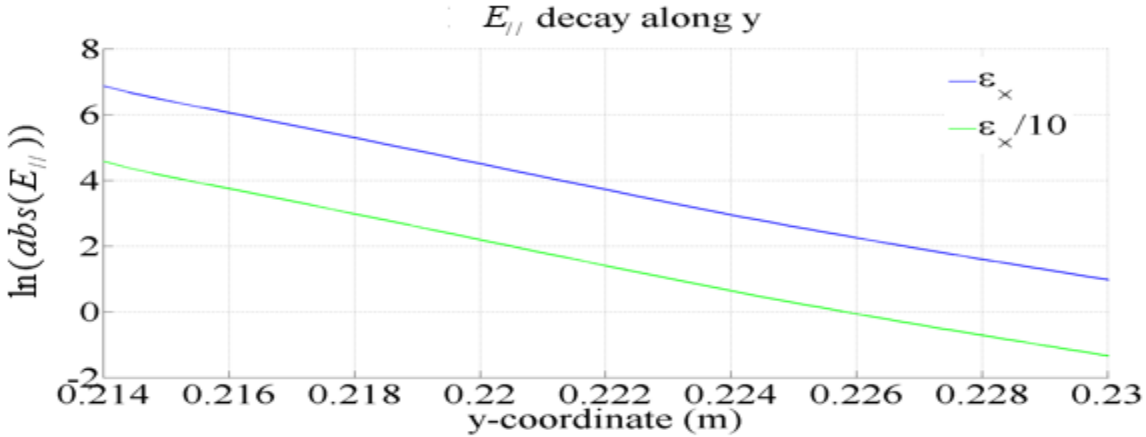
Figure 5.5. Comparison of E$_{//}$ along the same vertical line as Figure 5.3

The next test is change the tilt angle in the full wave code to see the impact on mode conversion. When the magnetic field is tilted to 20º, $E_{//}$ pattern still roughly remain the left-right symmetry. This can be seen from the lower part of the right figure of *Figure 5.6*. Another symmetric check shows the quantity $E_\perp(x) + E_\perp(-x)$ changes from 0 to 3 when the tilt angle increases from 0° to 20°. In other words, the anti-symmetric of $E_\perp$ loses seriously when $\theta = 20^o$. We see in *Figure 5.6* that the $E_{//}$ at the left top of the limiter increases, while decreases at the right top. This opposite variation matches the variation of $E_\perp$ and it also coincides with the fast wave spectrum variation w.r.t the tilt angle *Figure 3.8*.
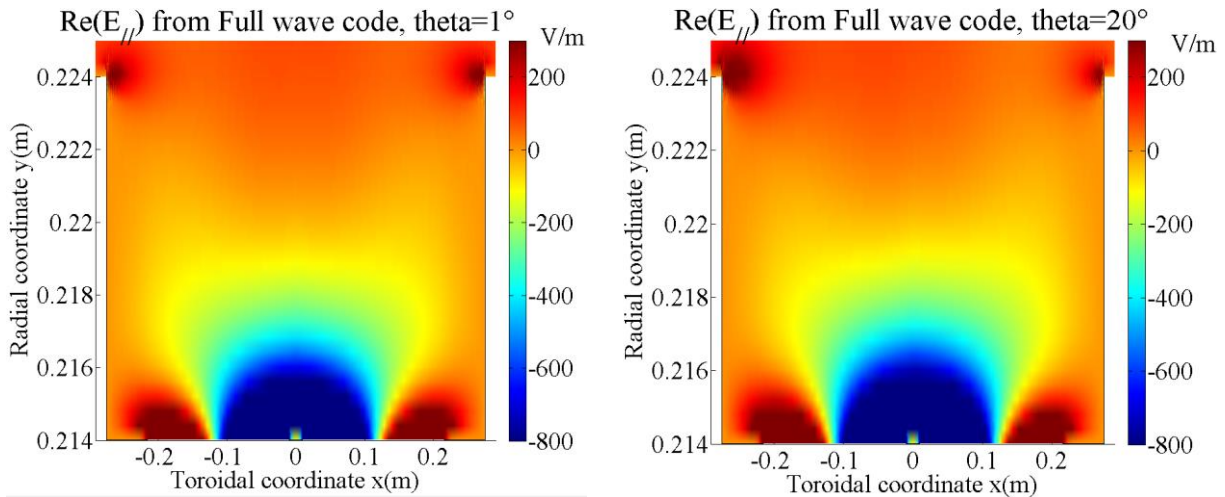
Figure 5.6. The real part of E$_{//}$ from Full wave code with two magnetic tilt angles

5.2.2 Evidence of the far field sheath excitation on remote areas inaccessible to SW emitted by the antenna

In a realistic Tokamak edge condition, the fast wave can propagate much further away from the wave launcher than the evanescent slow wave. The latter should vanish within a few millimeters. In this test, a constant density profile higher than the fast wave R-cutoff density is imposed in the SOL region. So the fast wave can propagate and reach the upper-left boundary of the far SOL region, as shown by the blue

curve in *Figure 5.7*. The magnetic tilt angle is set to $1°$ (minimum angle at the curved sheath boundary to guarantee the sheath boundary condition working correctly, see Chapter 4). The mode conversion is still present at the rounded corners even when $\theta = 0^o$ as the magnetic field is neither perpendicular nor parallel to the curved boundary. V_{RF} is excited preferentially near these rounded corners. This justifies why the intense V_{DC} is observed when the geometry changes rapidly [D'Ippolito 2013]. Here we define two characteristic dimensional lengths, the toroidal and the radial length of the SOL region, $L_{//}$ and $L_{\perp}$, respectively. By tuning the $L_{//}$ and radial $L_{\perp}$, one could see the impact of these lengths on the excited far field sheath. The potential variation at the shaped far SOL boundary (blue curve in *Figure 5.7*) w.r.t. $L_{//}$ and $L_{\perp}$ is examined. Results in *Figure 5.8* (a) and (c) illustrates both $|V_{RF}|$ and $|V_{DC}|$ at that boundary decreases under larger toroidal dimensions. This can be understood from the fast wave field pattern (*Figure 3.5*) that when the toroidal connection length increases, the fast wave passes over the blue boundary and thus only has a smaller contribute to the far field sheath excitation. By the same postulation, increasing the $L_{\perp}$ by shifting downwards the antenna structure could increase the potential as the fast wave can contact with the blue boundary. This is confirmed in *Figure 5.8* (b) and (d) where both $|V_{RF}|$ and $|V_{DC}|$ increases as $L_{\perp}$ getting larger. This observation is prior counter-intuitive: RF sheath excitation gets more intense as the extremity of the wall moves farther from the antenna. It is against the prediction by the spatial proximity effect. Currently, the spatial proximity effect is evidenced only in the evanescent slow wave [Colas 2016]. It is important to assess how this property evolves in the presence of the fast wave. Results in *Figure 5.8* (b) and (d) suggest the fast wave may not have the proximity effects at least in its propagative regions.
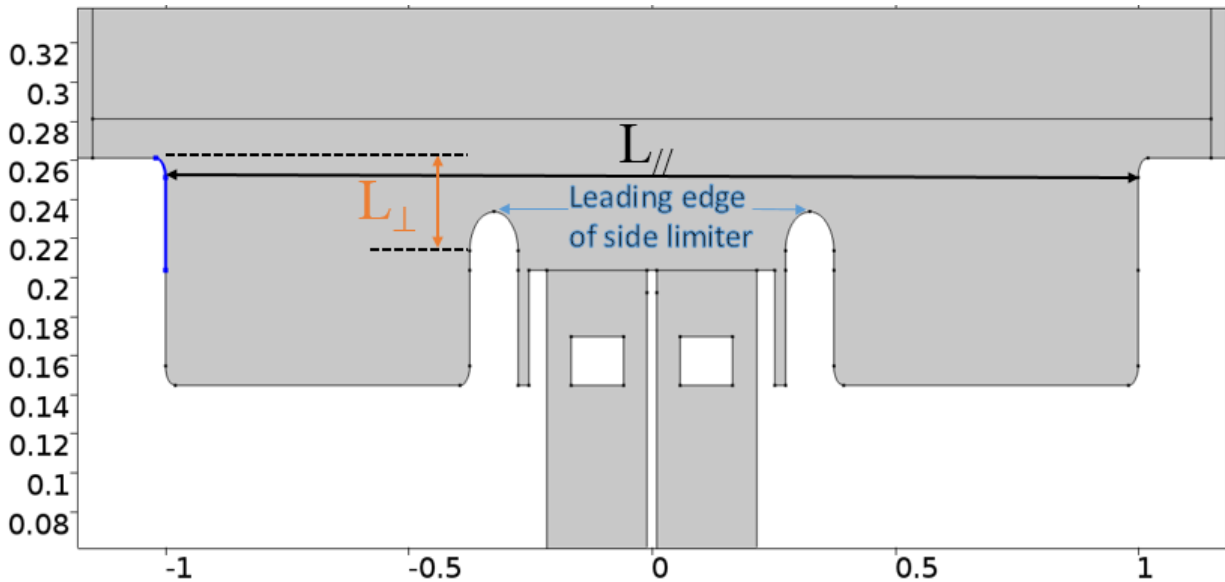
Figure 5.7. The characteristic length $L_{//}$ and $L_{\perp}$ are shown in the geometry; Blue boundary is where V_{RF} and V_{DC} are examined in Figure 5.8

(a) $|V_{RF}|$ at the blue boundary of Figure 5.7 varies with a scan of $L_{//}$, $L_{\perp}$=0.0375m, 1000A current, θ=1°

(b) Variation of $|V_{RF}|$ at the blue boundary of Figure 5.7 with a can of $L_{\perp}$, $L_{//}$=2m, other conditions the same as (a)

(c) V_{DC} at the blue boundary varies with a scan of $L_{//}$, other conditions the same as (a)

(d) *Variation of V_{DC} at the blue boundary with a scan of $L_{\perp}$, other conditions the same as*
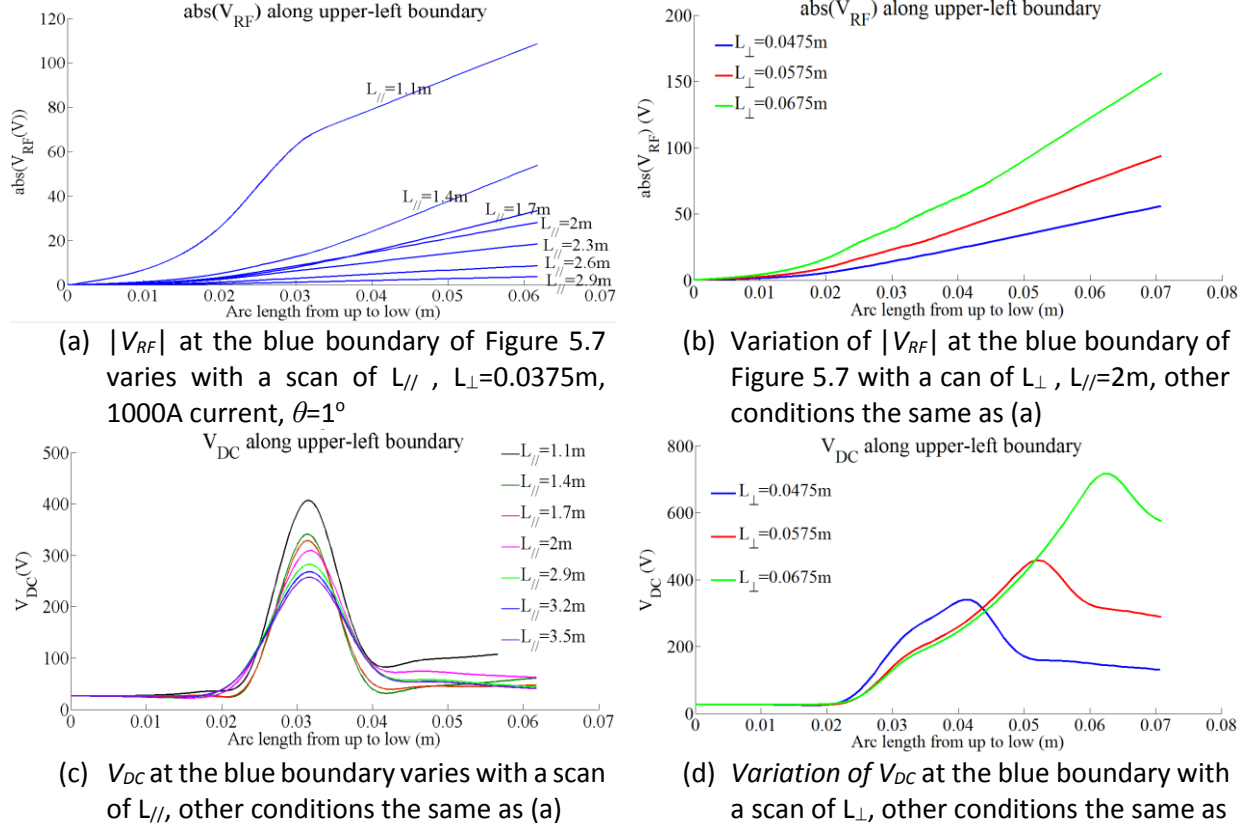
Figure 5.8. V_{RF} and V_{DC} behavior with different dimensional lengths; Data were picked up along the blue boundary of Figure 5.7. A constant density $9\times10^{18}m^{-3}$ at SOL region, f_0=w_0/2π=48MHz, B_0(y=0.214m)=2.3T, $\theta = 1^o$

Finally, we consider the impact of the tilt angle. It affects the V_{DC} structure from two aspects: firstly it changes the fast wave evanescence length and the slow wave excitation. In the extremely case where $\theta = 90^0$, the fast wave antenna excites mainly the slow wave. But under typical TS parameters, the slow wave is always evanescent along the radial direction in the private SOL for whatever tilt angles. On the contrary, the fast wave experiences from evanescent to propagative during the variation of the tilt angle. Thus in the far SOL region, the fast wave may play the dominant role. Secondly, it changes the RF sheath rectification as the RF sheath ceases to exist when $\theta = 90^0$. The dependence of V_{DC} structure at far SOL region on tilt angle is similar to the dependence of the radiating power on the tilt angle (*Figures 3.17*). *Figure 5.9* shows the V_{DC} evaluated at the left boundary of the left side limiter with a full scan of θ. The excitation is done by imposing current on the straps. When the tilt angle is increasing, the V_{DC} is enhanced as the RF field is stronger. After certain points, the second effect become dominant and V_{DC} decreases dramatically to the floating potential.
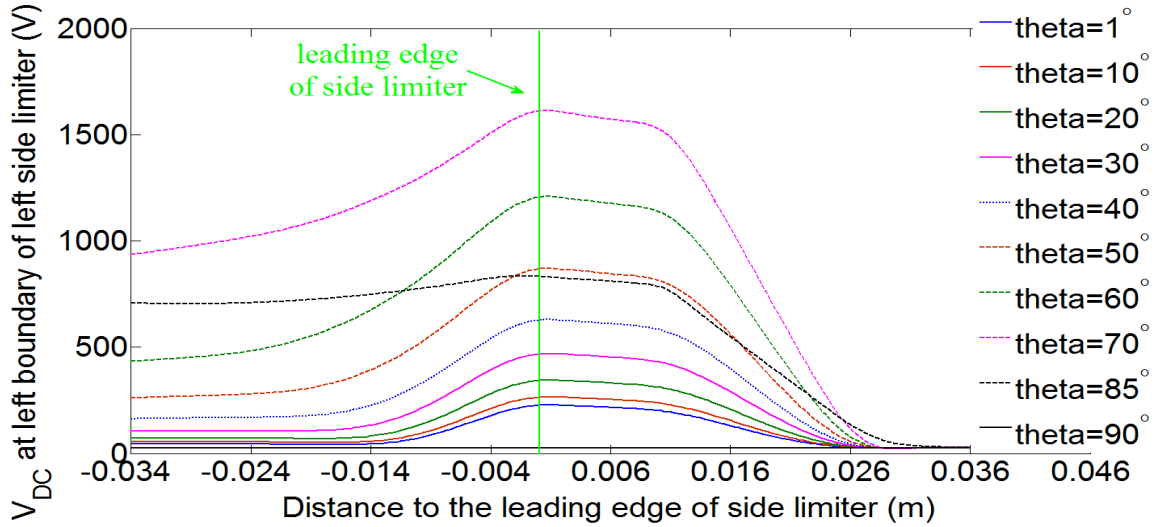
Figure 5.9. V_{DC} at the green line of the left figure of Figure 5.15, w.r.t the magnetic tilt angle. Excitation is done by imposing 1000A current on each strap

5.2.3 Tests of DC plasma potential on DC perpendicular conductivity and Stix tensor: the fast wave plays a supplementary mechanism in V_{DC} radial broadening

The parallel conductivity is described by the Spitzer conductivity, which gives a typical value of $\sigma_{//} = 35714\,S/m$. Two perpendicular conductivities, $\sigma_{\perp,p}$ and $\sigma_{\perp,f}$ are used to distinguish the different turbulence levels in the private SOL and free SOL, respectively. $\sigma_{\perp,p}$ is usually larger than the $\sigma_{\perp,f}$. No precise estimation is available for these two conductivities at this moment. Nevertheless, a domain of these values has been determined by matching the simulation with experimental radial broadening of V_{DC} [Jacquot 2014]. Our goal here is to investigate the role of the fast wave on the V_{DC} radial broadening (Δy in *Figure 5.10* (a)) by reducing the perpendicular conductivity as much as possible. Small value of perpendicular conductivity often leads to convergence problems as the finite element matrix becomes singular during the LU decomposition. The minimum conductivity we can achieve without losing a converged solution is 100 times smaller than the ones used in [Jacquot 2014]. Simulation shows that the radial broadening decreases significantly when the perpendicular conductivity decreases, see from *Figure 5.10*(a)-(b).

Let's now consider an extremely case where $\sigma_\perp$ is zero. In this case, there is no transverse current in the private SOL, the current injects at the left boundary should equal to the current comes from the right, which means

V_{DC} with $\sigma_{\perp p}$=2.6E-6$\sigma_{//}$, $\sigma_{\perp f}$=7.1E-8$\sigma_{//}$

(a)

V_{DC} with $\sigma_{\perp p}$=2.6E-8$\sigma_{//}$, $\sigma_{\perp f}$=7.1E-10$\sigma_{//}$

(b)

V_{DC} with $\sigma_{\perp p}$=2.6E-6$\sigma_{//}$, $\sigma_{\perp f}$=7.1E-8$\sigma_{//}$, $\varepsilon_\times$/10

(c)
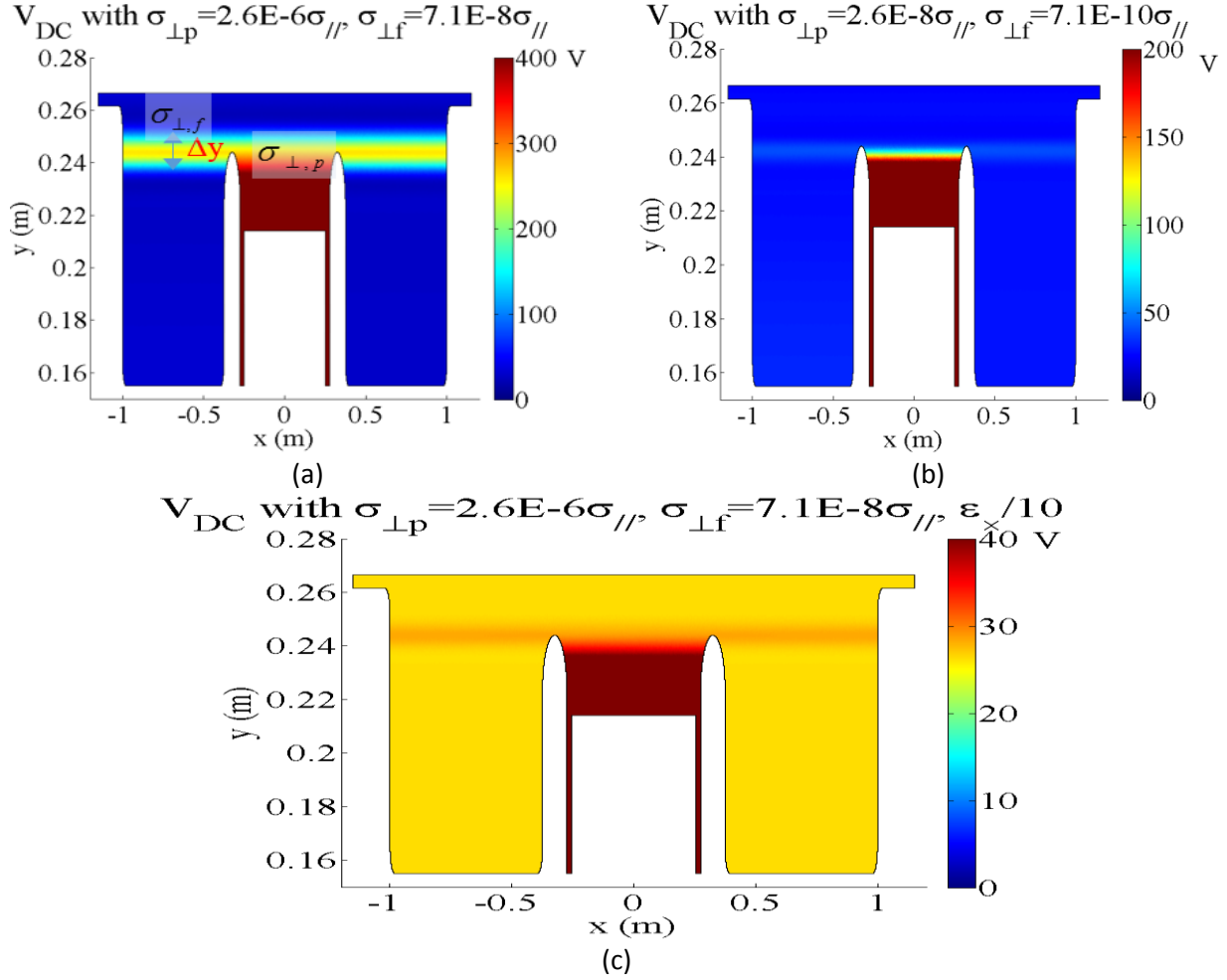
Figure 5.10. Tuning the perpendicular conductivity and off-diagonal term of Stix tensor to see the evolution of V_{DC} radial extension Δy, θ=7°

$$1 - \exp(\frac{e(V_f + V_{b,l} - V_{DC,l})}{k_B T_e}) = \exp(\frac{e(V_f + V_{b,r} - V_{DC,r})}{k_B T_e}) - 1 \tag{5.2}$$

Where the index l, r indicate the left and right sides, respectively.

See from *Figure 5.10* (b), V_{DC} is the same at the right side and the left side of the private SOL. So equal $V_{DC,l}=V_{DC,r}=V_{DC}$ in Eq. (5.2), and use the property of Bessel function: $V_b = \frac{k_B T_e}{e} \ln[I_0(\frac{e|V_{RF}|}{k_B T_e})] < |V_{RF}|$.

After some algebra, one obtains

$$V_{DC} < V_f + \max(|V_{RF,l}|, |V_{RF,r}|) \tag{5.3}$$

In the private SOL of *Figure 5.10* (b), the typical potential values at y=0.226m are: max($|V_{RF}|$) =637V, V_f=26V, V_{DC}=627V. Thus it fulfills the inequality(5.3). Further below this radial position, Eq. (5.3) become invalid because the sheath rectification is so strong that the electron current reaches saturation.

From the fast wave dispersion relation, Eq. (5.1), this wave is sensitive to the change of the off-diagonal term of the Stix tensor: $\varepsilon_\times$. Thus the fast wave contribution to the V_{DC} radial broadening is affected by reducing $\varepsilon_\times$. Compare (c) with (a), the radial broadening only varies slightly. These observations suggest that the DC current transport described by the perpendicular conductivity is still the dominant mechanism for V_{DC} radial broadening.

The two perpendicular DC plasma conductivities in the free SOL and in the private SOL are loosely constrained both in the SSWICH-SW and SSWICH-FW codes. Here are the main points on how V_{DC} evolves with these conductivities: (a) In SSWICH-SW simulations, choosing two different DC conductivities in the free SOL and in the private SOL was found necessary to produce V_{DC} maps with both magnitude and radial extension comparable to the RFA observations on Tore Supra [Jacquot2014]. $\sigma_{\perp,p}$ needs to be larger than $\sigma_{\perp,f}$ to obtain significant V_{DC} in the free SOL; V_{DC} amplitude is intense in the private SOL and lower in the free SOL; (b) V_{DC} at the leading edge of limiter (its location is shown in *Figure 5.7*) increases with $\sigma_{\perp,p}$; (c) With larger $\sigma_{\perp,f}$, the radial broadening of the V_{DC} structure in front of the limiter leading edge at free SOL increases. (a) can be seen in *Figure 5.10*(a)-(b). Indeed, V_{DC} starts from the private SOL and can propagate to the free SOL only if $\sigma_{\perp,p}$ is sufficiently large. The above three observations have similar behaviors in the slow wave code, mainly because SSWICH-SW and SSWICH-FW share similar DC modules. An analytical non-linear diffusion model has been proposed in [Jacquot 2013] to explain them (a simplified model was published in [Jacquot 2014]). It considers a four-region rectangular geometry which covers the private SOL and three free SOL regions. The transversal diffusion length of the V_{DC} is derived, which is proportional to the square root of perpendicular conductivity and the parallel connection length.

$$\lambda = \sqrt{\frac{L_{//}\sigma_\perp k_B T_e}{2eJ_{is}^{\perp B}}} \tag{5.4}$$

Figure 5.8 has shown the dependence of V_{DC} on dimensional parameters. The realistic parallel connection length is about 10m. Modelling such a large scale is certainly out of the memory limits of our working station. But the effect of the dimensional length on the radial extension of V_{DC} structure can be compensated by the choice of perpendicular DC plasma conductivity, i.e. from Eq.(5.4), it is the product of $\sigma_{\perp,f}$ and $L_{//}$ is the parameter that really matters.

(b) can be understood naively that with a larger $\sigma_{\perp,p}$, ∇V_{DC} is smaller to fulfill the conversion of DC current equation. Thus the diffusion length is larger in the private SOL or V_{DC} decreases slower vertically starting from the aperture. Given V_{DC} at the aperture, V_{DC} at the leading edge of the side limiter is consequently larger. *Figure 5.11* shows a scan of V_{DC} at leading edge of the left side limiter with a variety of conductivity. The excitation is done by imposing 1000A current with hyperbolic distribution on each straps. Other parameters are $\theta = 7^o$, $L_{//}$=1.1m, $L_\perp$=0.0375m.

The analytical model can also predict the V_{DC} radial width Δy (width defined between two half maximum). A homogeneous plasma density is assumed to derive analytical solution of Δy. The RF biasing at the walls of far SOL region is assumed to zero, which is barely true when only the slow wave is considered. Following these assumptions, the ratio of Δy over diffusion length λ can be expressed as a function of the magnitude of V_{DC} at leading edge of the limiter, see Eq.(5.5). The right side of Eq. (5.5) is barely constant among the conductivity range of our choice. The radial width is thus increasing with the diffusion length.

$$\frac{\Delta y}{\lambda} = -\int_{V_0/2}^{V_0} \frac{d\Phi}{\sqrt{2(\Phi - 1 + \exp(-\Phi))}}$$
(5.5)

Where V_0 is the normalized V_{DC} at the leading edge of the side limiter, i.e. $V_0 = e\dfrac{V_{DC} - V_f}{k_B T_e}$.
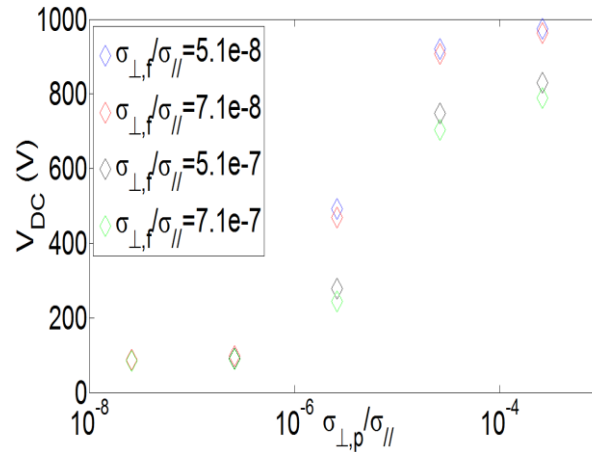

Figure 5.11. Dependence of the V_{DC} at the leading edge of the left side limiter on perpendicular conductivities

5.3 Comparison of SSWICH-FW simulation with Tokamak experiment: V_{DC} vertical structure and left-right asymmetry of the heat flux at the side limiters

The temperature distribution recorded by the infrared thermography over the antenna surface during the RF operation of Tore Supra antennas reflects the intensity of the interactions between SOL plasma and the antenna, see *Figure 5.12*(a). The temperature distribution shows a clear double-hump poloidal structure, which is consistent with the poloidal distribution of the potential measurement by RFA [*Figure 2.18* left]. The enhancement of the DC plasma potential by the RF sheath rectification is widely suspected to be the physics reason behind the intense SOL-antenna interactions. If this is true, V_{DC} should show the similar structures as the temperature. In *Figure 5.12*(b), a differential temperature map is shown. It makes the difference between two RF pulses whose left/right power ratio on the straps are 50%-50% and 63%-37%, respectively. The differential field map shows the temperature is increasing on the left hand side (from the plasma side, strap with higher power) while decreasing on the right hand side (strap with reduced power). This asymmetry cannot be interpreted by the traditional double Langmuir probe approach of RF sheath modelling which characterizes the sheath intensities at both field line extremities with one single parameter (a line-integral of $E_{//}$). Neglecting the transverse heat exchanges in the materials, the temperature measurement in thermal steady-state is a direct indication of the heat flux normal to the antenna surface. Thus we will also examine whether the heat flux in our simulation exhibits left-right asymmetry in case of asymmetric strap feeding. In [Colas 2016], the spatial proximity effect related to the evanescent slow wave is invoked to understand this asymmetry. We do not know yet how this property evolves in the presence of the evanescent fast wave, whose characteristic evanescence lengths are larger than those of the slow wave in the SOL region. This asymmetry property inherently indicates that reducing the power on one strap could mitigate the sheath effect on the side of the antenna that is close to it but

at the same time increase the sheath potential on the other side. This promotes the current effort of using 3 straps antenna in AUG [Bobkov 2016]. Recently results evidenced the sheath effects on both sides of the antenna could be mitigated through using 3 straps antenna.
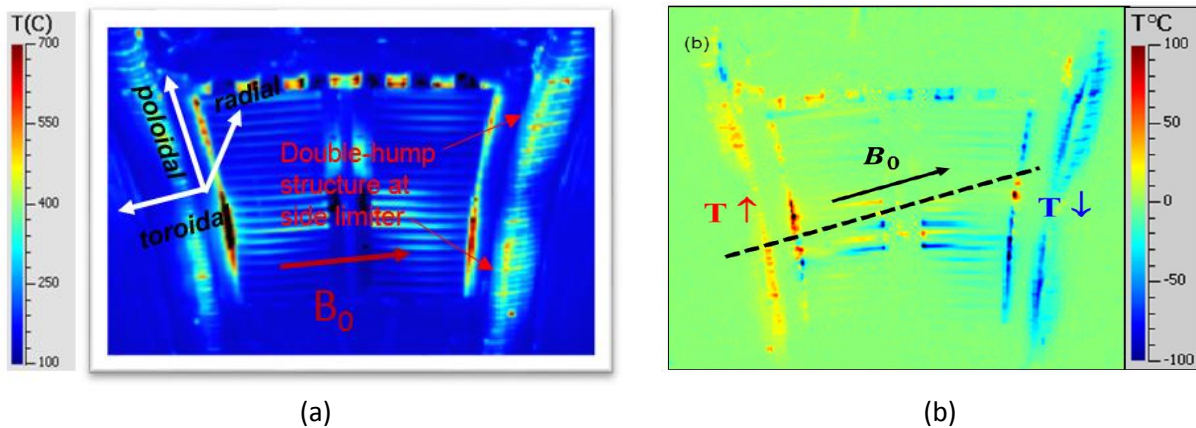

(a)   (b)

Figure 5.12 (a): infrared picture of active ToreSupra ICRF antenna [Corre 2012] shows a double-hump structure at the side limiters (b) differential IR image from subtraction of two RF pulses, where the RF generator power balance is changed from (50% / 50%) to (63% / 37%)[Colas 2013]

The realistic antenna has a poloidal curvature to match the shape of the vacuum vessel, thus the poloidal direction is not exactly vertical. For simplicity, this curvature is not considered in the simulation. SSWICH-FW limited in 2D at this moment, can however produce results on different vertical positions via a multiple-2D approach, exciting several independent 2D simulations with full-wave field maps from the 3D RAPLICASOL code [Jacquot 2015] at different altitudes z. For SSWICH-SW, the multiple-2D approach is shown to be a fairly good approximation of realistic 3D simulations [Colas 2016]. A similar assessment will be made below for the fast wave. The 3D RAPLICASOL code simulates a realistic TS antenna geometry, including the CBSB Faraday screen, see *Figure 5.13* (upper figure). In the simulation model, the Faraday screen bars are recessed by 5mm compared to the edge of the screen box. We found by shifting the bars slightly inward along the radial direction can reduce poloidal oscillations in the electric field at the Faraday screen (here we refer to the radial position of the box, 5mm above the bars). This was done also in the real CBSB FS for some mechanical considerations, see *Figure 5.13* (lower figure). The electric field in RAPLICASOL is solved using the following TS parameters, plasma composition: 95% D and 5% H, B_0 scales as $1/R$, with R major radius axis, B_0 at aperture (y=0.214)=2.9T, RF wave frequency 57MHz, θ=7°. A realistic density profile from TS shot 43026 is used. The density at the aperture is about 1×10^{18}m^{-3}. The slow wave radial evanescence length is about 1cm (value at y=0.224m, $n_{//}$=10). The fast wave R cut-off layer locates at y=0.244m ($n_{//}$=10). The density profile as well as the locations of the antenna aperture, leading edge of the limiter and R-cutoff layer are shown in *Figure 5.14*. The simulation in 3D RAPLICASOL is done with PEC BCs only. It is further normalized to 1MW total coupled power.
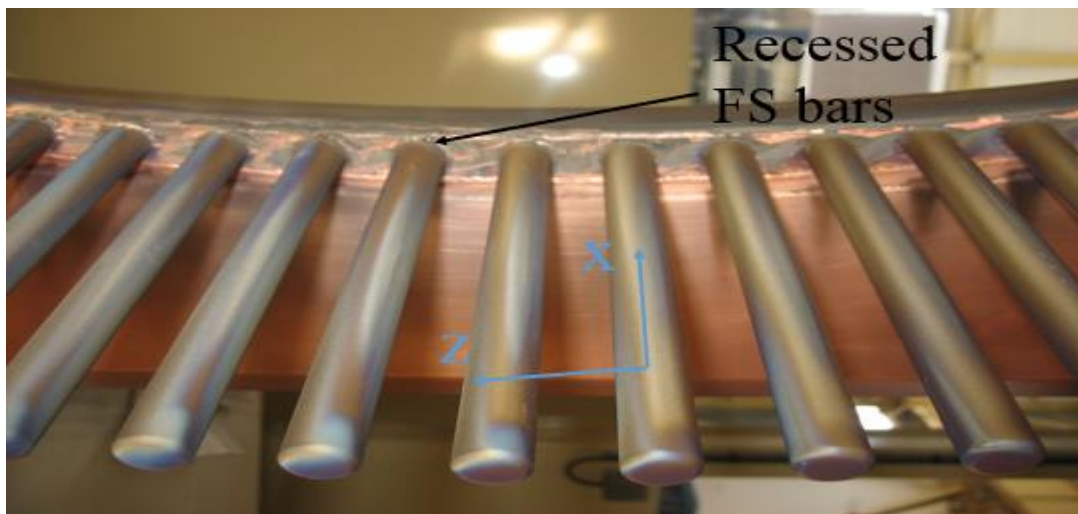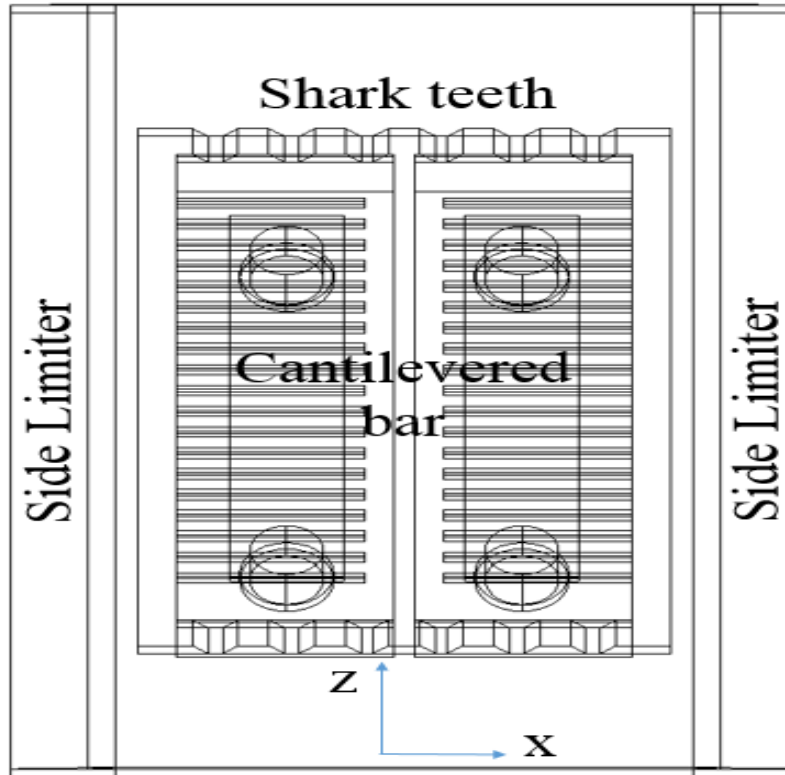
Figure 5.13.Up: RAPLICASOL antenna model with the Cantilevered Bars and Slotted Box (CBSB) Faraday screen; Down: Recessed FS bars in the real CBSB Faraday screen
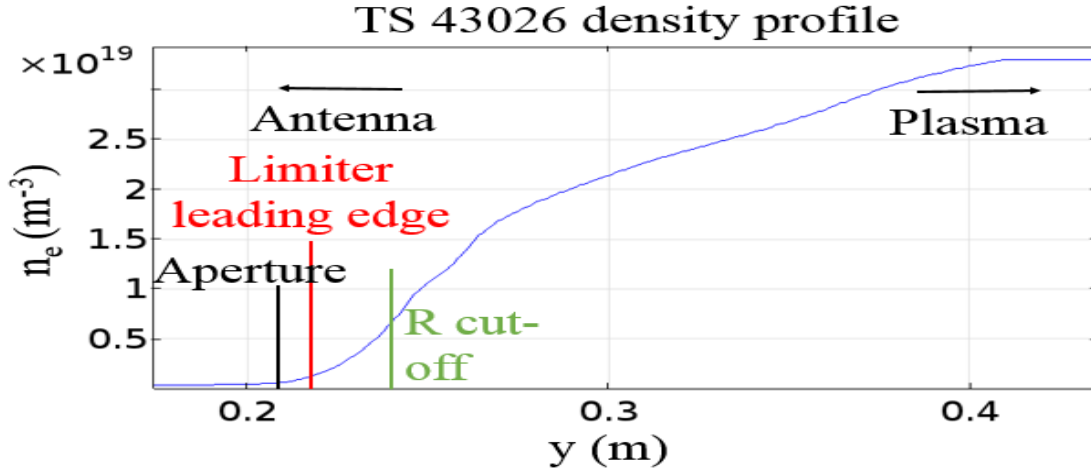
Figure 5.14. Radial density profile and its relative location in the code, data from TS shot 43026

SSWICH-FW simulations are carried out with the same plasma parameters and density profiles as RAPLICASOL runs. In 2D SSWICH-FW code, the top of the limiter is shifted downward to match the realistic value (1cm) of the radial extension of the private SOL (distance between the blue dot line and aperture in the left figure of *Figure 5.15*). The aperture is extended to connect the curved part of the side limiters as it is in 3D RAPLICASOL code. We consider both the cases where the curvature at the side limiter is kept and removed. We chose the parallel connection as large as possible using our dedicated workstation with 128 GB of memory, $L_{//}$ =4.7m. Under typical edge plasma temperature Ti=20eV, Te=10eV, the Spitzer parallel conductivity is around $\sigma_{//} = 35714\,S/m$. The perpendicular DC plasma conductivity $\sigma_{\perp,f} = 10^{-8}\sigma_{//}$ is chosen to match the radial extension of the V_{DC} in free SOL. In the private SOL, the same $\sigma_{\perp,p} = 2.6\times10^{-6}\sigma_{//}$ is used as in [Jacquot 2013].
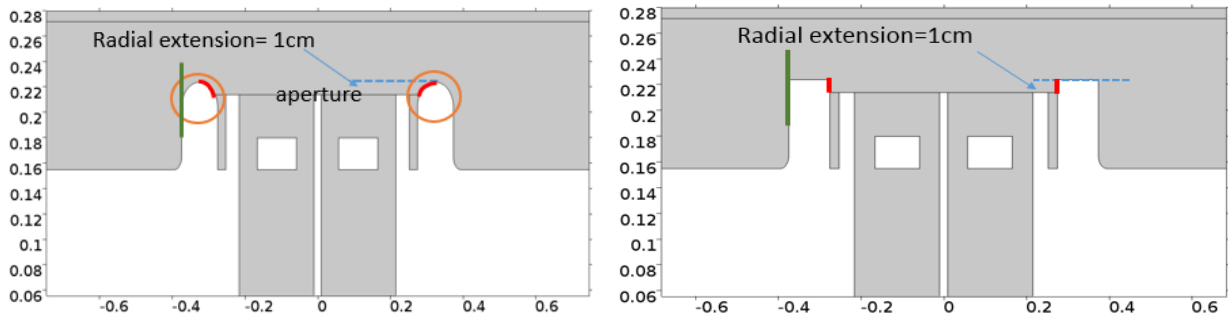
Figure 5.15. Two realistic geometry used in the simulation of this section. Left: the curved part (enclosed by the orange circle) at the top of side limiters is kept but being shifted downwards; The green vertical line is where the V_{DC} data is extracted in Figure 5.17; The two red curves are where the heat flux is examined in Figure 5.20. Right: the curvature part at the top of the side limiters is removed

The multi-2D simulation procedure is the following: scan the vertical positions using 2D SSWICH-FW from -0.376m to 0.378m (bounded by the vertical length of the FS) with a step size of 3mm. In each vertical position, the electric field map tangent to the aperture (containing both the vertical and toroidal field

components) exported from the 3D RAPLICASOL at the Faraday screen (5mm above the bars) in that vertical position is imposed at the aperture of the 2D SSWICH-FW. In 2D SSWICH-FW, we examine the V_{DC} structure at the left edge of the left limiter, shown by the green line in *Figure 5.15*.
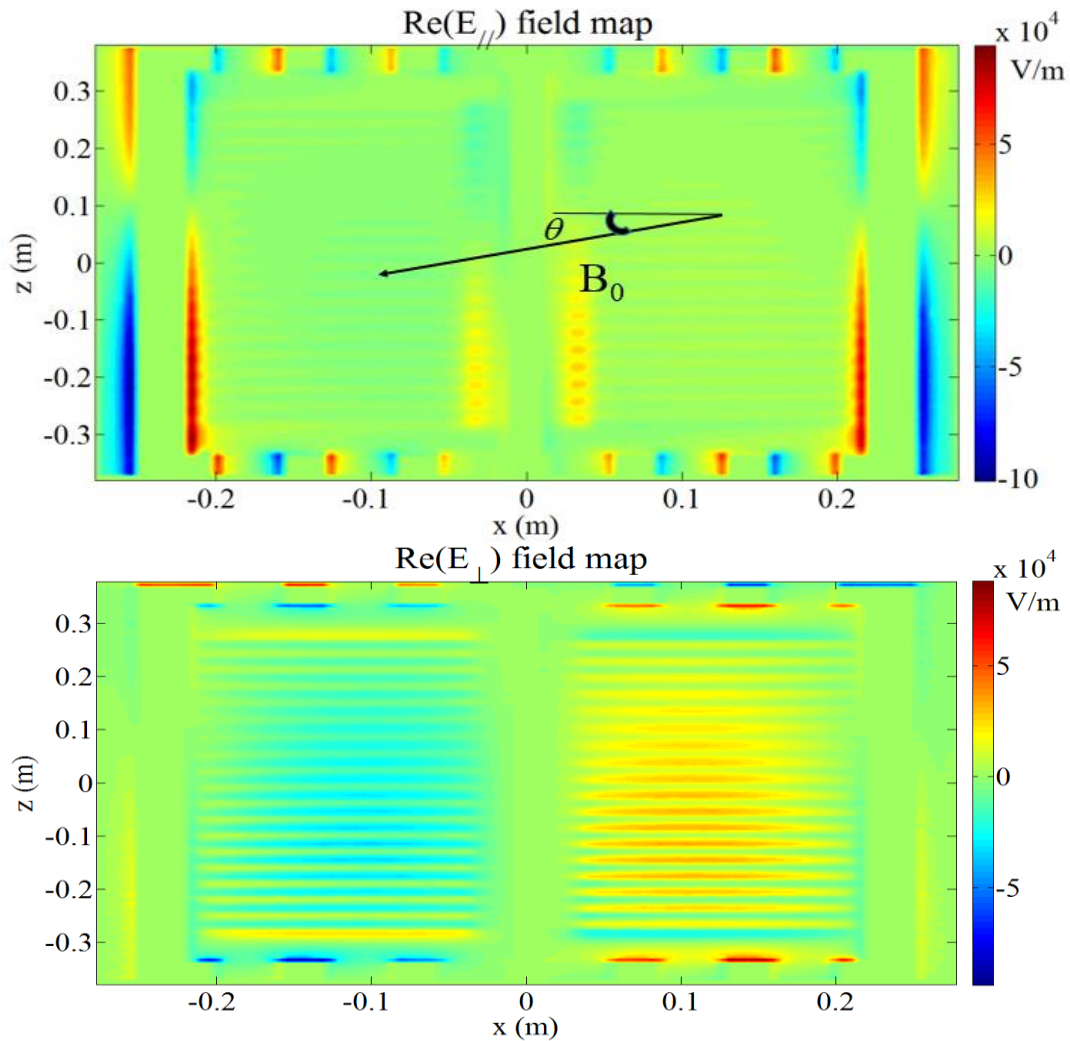
Figure 5.16. 2D field map generated at the Faraday screen of the 3D RAPLICASOL code; Up: the real part of the parallel component; Bottom: the real part of the perpendicular component (the one perpendicular to the radial direction).

In the first approximation for large $|\varepsilon_{//}|$, the fast wave is transverse electric field while the slow wave is transverse magnetic field w.r.t. the direction of the static magnetic field. For $k_z=0$ this also means that the poloidal electric field is negligible in the polarization of the slow wave. These distinct features allow one separating the fast wave and the slow wave on RF excitation. The $E_{//}$ and $E_\perp$ map extracted at the Faraday screen (again 5mm above the bars) of the 3D RAPLICASOL. The direction of the magnetic field depends on the way of looking, i.e. standing at the plasma side facing towards the antenna or the reverse. To ease comparison with experiment, in this section we show the simulation results as if we are looking from the plasma side towards the antenna. So the magnetic field now points from right to the left instead of pointing from left to right as we showed in *Figure 4.3*. We further flip vertically the field maps in order

to match the convention used in the previous simulation in [Jacquot 2013]. The final field maps with the direction of the magnetic field are shown in *Figure 5.16*. The $E_{//}$ map shows a clear double-hump structure at the lateral edges of the side limiters and at the end of the FS bars, whereas the $E_\perp$ has only a single hump and spreads over a large scale. The $E_{//}$ is significantly smaller than the $E_\perp$ at the FS bars (strictly speaking, 5mm above the bars), which is normal since the FS is used for cancelling the $E_{//}$ from the excitation. These field maps are decomposed into the toroidal and vertical components and then imported at the aperture of the 2D SSWICH-FW code.

The vectorial wave equation, the V_{RF} equation ($E_s = -\partial V_{RF}/\partial s$) as well as the asymptotic RF sheath boundary condition Eq. (4.23)-(4.24) are all linear. Thus the RF field and the scale of $|V_{RF}|$ will both respond linearly to the magnitude of the excitation and follow the additivity rules. The sheath rectification formula Eq. (4.22) is intrinsically non-linear and hence the V_{DC} does not follow the additivity rule. These properties are useful when comparing results with different scales of excitations.
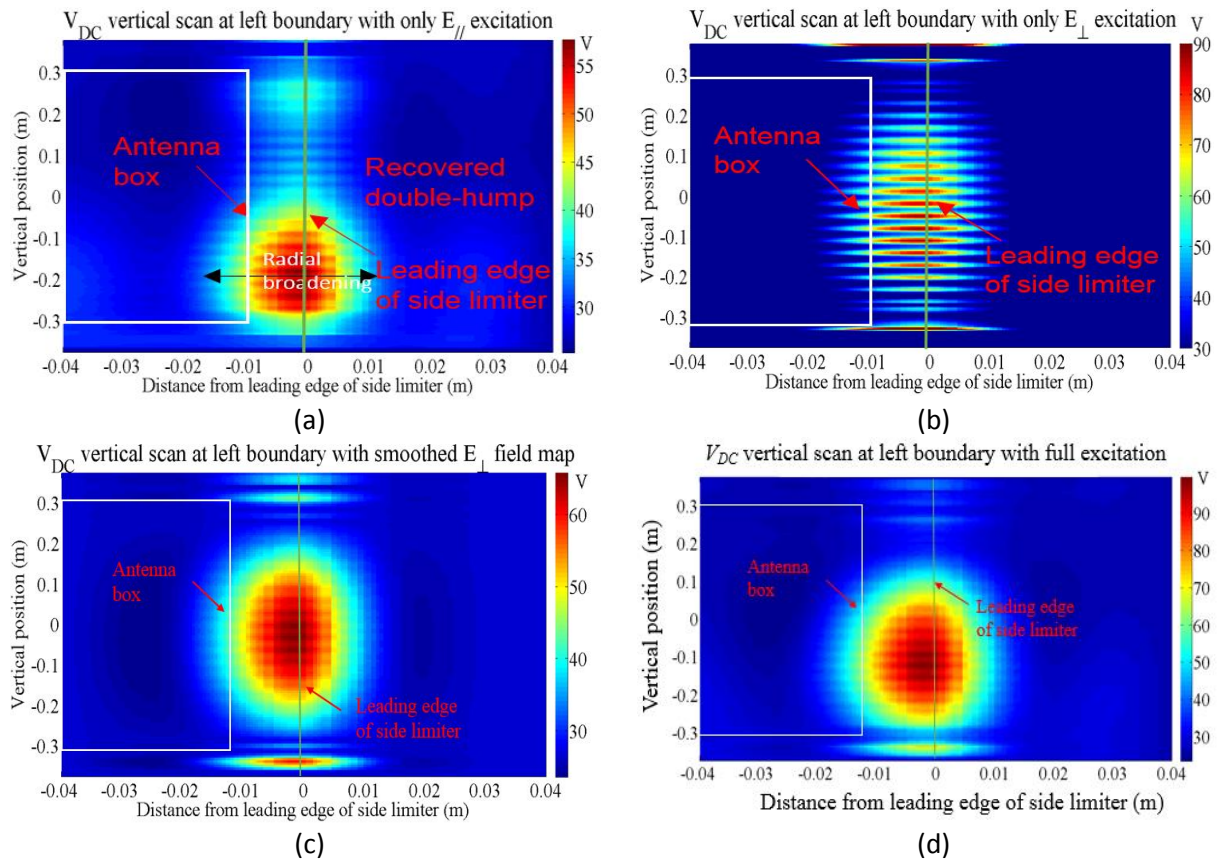
Figure 5.17. V_{DC} vertical scan using field map containing $E_{//}$ only (a), $E_\perp$ only (b), smoothed $E_\perp$ only (c) and both $E_{//}$ and non-smoothed $E_\perp$ (d). Data picked up at the green line of Figure 5.15 (Left)

The first set of simulations excites SSWICH-FW with only the $E_{//}$ component of the RAPLICASOL field map, representing a V_{DC} produced uniquely by the slow wave excitation. The result (*Figure 5.17*(a)) recovers the double-hump shape observed by the RFA measurement and previous SSWICH-SW runs [Jacquot 2014]. With our choice of transverse conductivity, the radial broadening of V_{DC} is about 3cm, which is consistent with the measurement although the parallel connection length in our simulation is

smaller than those in TS free SOL by a factor of 2. The scale of V_{DC} in *Figure 5.17* (a) is however only 40% of the result in [Jacquot 2013]. It is partly because the slow wave is sensitive to the geometry shape of the private SOL. As a reference, the arc length of the curved SBC in the private SOL is 45mm. After removing the curvature, the flat boundary in the private SOL is only 10mm. The value of this arc length in the realistic TS antenna is about 28mm. Simulation shows removing curvature at the top of the side limiters could lead the V_{DC} scale of *Figure 5.17* (a) increasing by 30%. Another part of difference comes from the fact that in [Jacquot 2013], the magnitude of the electric field map is 1.5 times larger than the value used in the simulation here.

The double-hump structure is most probably linked to the slow wave, as it vanishes when only the $E_\perp$ is imposed at the aperture, representing the pure fast wave excitation, i.e. *Figure 5.17* (b)**.** No significant difference is observed on the V_{DC} scale in *Figure 5.17* (b) when removing the curvature of the side limiters. The vertical modulation of V_{DC} in (b) is caused by the Faraday screen bars in the RAPLICASOL code. It can be seen also in the $E_\perp$ field map. However such poloidal modulation is not obvious in the experimental measurements, although its typical period (~3cm) is within the spatial resolution of infrared cameras (the FS bars are clearly visible on the IR pictures). One might look for artefacts in the measurements. Here we rather re-assess for the fast wave the multi-2D approach successfully applied for the SW simulations, looking for a possible over-estimation of the poloidal modulation compared to full-3D calculations.

A typical scale of perpendicular wave number of the fast wave and the slow wave at the green line of *Figure 5.15* can be evaluated from their dispersion relations Eq. (2.17) and Eq. (2.18), i.e. $k_{\perp,fw}^2 = -100 \, m^{-2}, k_{\perp,sw}^2 = -10^5 m^{-2}$. The squared radial wavenumber reads: $k_y^2 = k_\perp^2 - k_z^2$. Our multi-2D approach amounts to taking k_z=0 for all spectral components in the input field map, whereas in real 3D calculations, a finite k_z should be present, whose magnitude ($2\pi/0.03$~200m^{-1} for 3cm modulations) is larger than the $|k_{\perp,fw}|$, while being much less than the $|k_{\perp,sw}|$. Thus the fast wave can be more sensitive than the slow wave to a finite k_z. Adding a finite k_z will make k_y^2 more negative and increases the radial evanescence of the fast wave. Taking as typical radial distance the recess of the side limiters, i.e. δy=1cm, one finds that $k_z\delta y$ ~2 while $k_{\perp,fw}\delta y$ ~0.1. One anticipates a non-negligible attenuation of the FW field modulations between the Faraday screen and leading edge. Correspondingly, the local field structure will become less intense. Thus the amplitude of V_{DC} modulation shown in *Figure 5.17* (b) is probably being overestimated. A way to mitigate the poloidal modulation is to smooth the $E_\perp$ field map. In the following simulation, we average $E_\perp$ over a period of 3cm in the poloidal direction. This can eliminate the fast modulations which has $k_z \geq$200m^{-1}. The result is shown in *Figure 5.17* (c), where the V_{DC} scale indeed decreases by 30%. Comparing the V_{DC} in (c) with (a), one can see that the fast wave changes not only the V_{DC} magnitude in antenna vicinity, but also the poloidal shape.

Although the slow wave only appears in the private SOL, the V_{DC} structure can extend further away toroidally, see *Figure 5.10* (a). This explains why the RFA locating 12m away from the wave launcher can still receive significant signals. *Figure 5.17* (d) shows the V_{DC} distribution over a vertical scan with full (both $E_{//}$ and $E_\perp$) excitation at the aperture. The same smoothed $E_\perp$ field map as in (c) is used. The total V_{DC} is not a simple addition of the two individual contributions from the fast wave and the slow wave since the sheath rectification process is non-linear. The scale of V_{DC} in (d) is comparable with the experimental value (~100 volts), but not really the poloidal shape.

Our latest effort to combine the 3D effect into the simulation is to replace the zero poloidal derivative assumption which was used in deriving RF sheath boundary conditions E_z=0 in Eq. (4.12) by considering all the k_z spectrum. Now if we assume that the plasma parameters have no z-dependence and that the spatial boundaries of the simulation domain are invariant under translation along z. Then we can Fourier transform the RF quantities in z direction and rewrite the RF sheath boundary condition in the spectral domain,

$$\begin{cases} E_s(s,k_z) = \dfrac{i}{k_z} \dfrac{\partial E_z(s,k_z)}{\partial s}, D_n = \pm \dfrac{\varepsilon_{sh} V_{RF}(s,k_z)}{\delta(\theta)} & Sheath \\ E_x = E_z = 0 \quad Metal \end{cases}$$

(5.6)

Where s represents the direction of the boundary arc length, the ansatz $\partial_z.=-ik_z$ and Eq. (4.26) have been used in deriving the first equation.

The ansatz $\partial_z.=-ik_z$ can also be used to extract directly V_{RF} from the vertical RF electric field as

$$V_{RF}(s,k_z) = -\frac{i}{k_z} E_z(s,k_z)$$

(5.7)

In this approach no independent module is needed to compute V_{RF}, contrary to previous formulations. One can also see that in this spectral domain, no boundary condition is necessary to specify V_{RF} (except for k_z=0). In this special case when k_z=0, we checked the convergence of the V_{RF} by decreasing successively k_z. The test is done in a flat SOL geometry, namely removing all the curved boundaries. With curvature, COMSOL still has some difficulties to reach numerical convergence when solving the vectorial equation in the spectral domain at this moment. We plot V_{RF} at the left far SOL boundary, which is the blue boundary in *Figure 4.12 C*. The results is shown in *Figure 5.18*. One can see that as kz decreasing, V_{RF} gets converged. kz=0.01 can already well represent kz=0.

Under wide sheath assumption, the sheath boundary conditions in Eq. (5.6) become linear. Linearity in the first two steps in SSWICH-FW indeed ensures that 2D simulations for each wavevector k_z are independent of each other [Colas2016]. This allows running them sequentially with memory requirements equivalent to a 2D simulation, and running time equivalent to a multi-2D simulation.

The detailed procedures are the following,

1. Fourier transform the input field map, $E_x(x, z)$, $E_z(x, z)$ → $E_x(x, k_z)$, $E_z(x, k_z)$
2. For every k_z, excite electromagnetic fields in spectrum domain using spectral sheath boundary conditions
3. Calculate $V_{RF}(s, k_z)$ in spectrum domain for every k_z
4. Inverse Fourier transform $V_{RF}(s, k_z)$ → $V_{RF}(s, z)$
5. Run V_{DC} module as before

With this new method, one can include all the poloidal derivatives of the RF fields as well as prevent the use of integral constant introduced in the first approach to evaluate V_{RF} (See section 4.3.2 a). This method is promising at those points. However, the assumption we made in order to conduct the poloidal Fourier transform is that the antenna has an unlimited size in the poloidal direction. Test shows that a surface wave is likely to propagate at the outer boundaries of the side limiters under a high kz, see the

wave pattern inside the red ellipses in *Figure 5.19*. In reality, the antenna has a limited size, the surface wave will be bounced back at antenna extremities. This is a clear point suggesting that this spectral method cannot replace the full 3D simulation.

Further testing on this method is restricted by the time duration of this thesis, but this should be a prior improvement to the code when a full-3D SSWICH-FW simulation is out of reach.

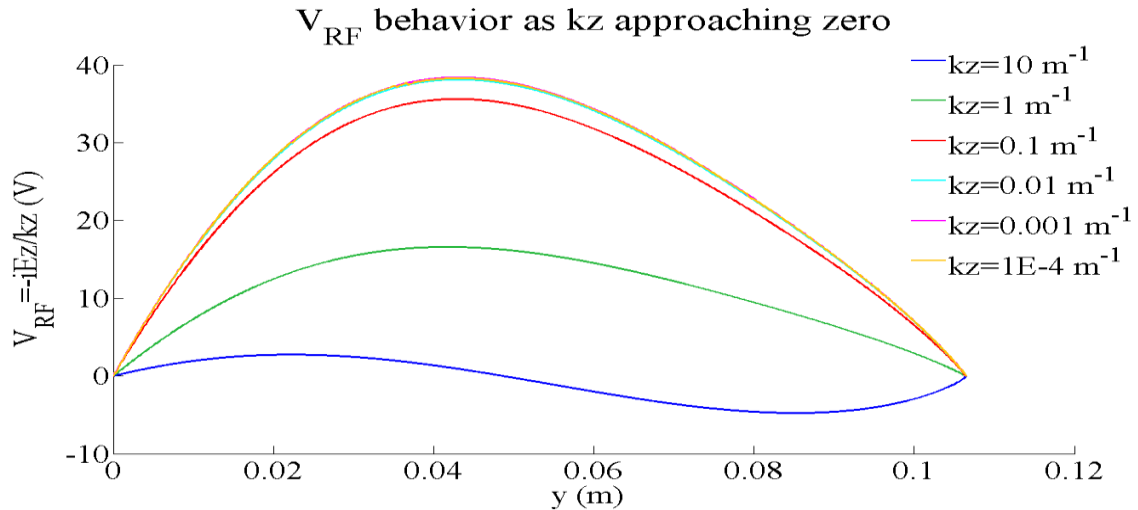*Figure 5.18. Convergence of V_{RF} with tapered kz. Date are picked up at the left far SOL boundary, $\theta=7^o$, freq=57MHz, central magnetic field $B_0=3.87T$, a constant density $ne=1.6\times10^{19}$ m^{-3} is used below the Separatrix*
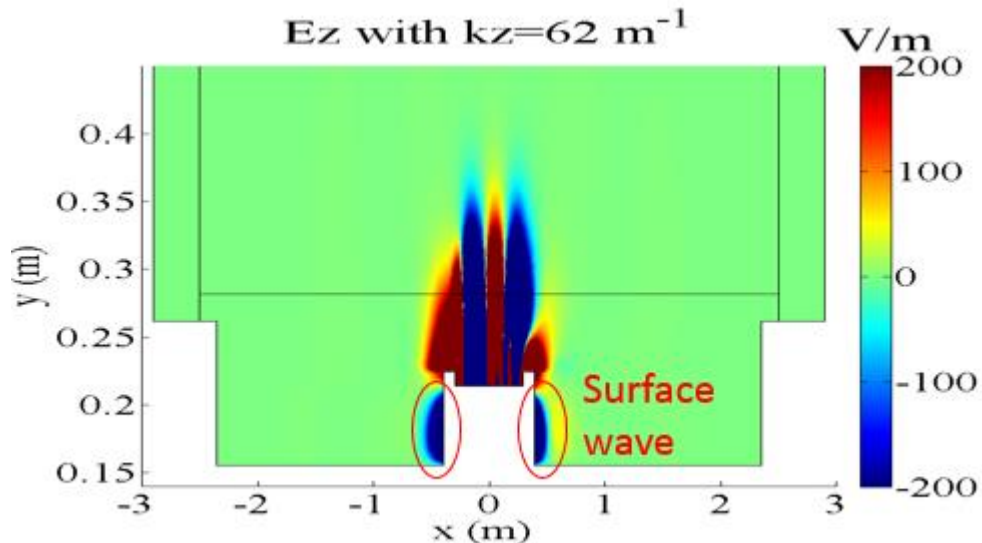

Figure 5.19. Excitation of surface wave in the far SOL under a high kz, other parameters are the same as Figure 5.18

The next step is to calculate the heat flux at the lateral sheath boundary of the private SOL, i.e. the red boundaries in *Figure 5.15*. It is feasible to change the power ratio over the two straps in the 3D RAPLICASOL code. Two tangential field maps with power ratio of 50%-50% and 63%-37% are exported at the Faraday Screen in order to compare with *Figure 5.12*(b). All these maps are not smoothed. The effective heat flux is the one normal to the boundary, which can be determined via the following analytical expression [Jacquot 2013],

$$Q_n = j_{is}^{\perp B}[V_{DC}(x,y)+2.5\frac{k_B T_i}{e}]|\,nx\,|\cos\theta + \frac{2k_B T_e}{e}\,j_{is}^{\perp B}\min\{\frac{j_{es}^{\perp B}}{j_{is}^{\perp B}},\exp[e\frac{V_f+V_b(x,y)-V_{DC}(x,y)}{k_B T_e}]\}|\,nx\,|\cos\theta \quad (5.8)$$

Where the first term is the ion heat flux; the second term corresponds to the electron heat flux. The electron flux reach the maximum when the electron current is saturated, in this case the first term in the bracket is used.

We first evaluate the heat flux at the curved boundary of the private SOL at z=-0.2m, shown in the left figure of *Figure 5.15*. The left-right asymmetry is nicely recovered by SSWICH-FW/RAPLICASOL simulation, see *Figure 5.20*. This left-right asymmetry is a robust invariant property that appears at all vertical positions. This suggests that the spatial proximity effect is still present in the region where the evanescent slow wave and evanescent fast wave co-exist. *Figure 5.20* starting from the aperture, the sheath rectification is so strong that the electron current get saturated. At this stage, the electron saturation current Eq. (2.56) only depends on plasma parameter while it is invariant to the power ratio at straps. Then as moving to the top of the limiter, sheath rectification become moderate so the electron heat flux and thus the total heat flux is correlated with the RF field and thus the power ratio. The sharp drop of the electron flux at the two figures does not occur at the same radial position, this is because the electron current depends on the biased potential V_b and thus the local RF electric fields. Under a tilted magnetic field, the local wave pattern is not exactly left-right symmetric as we have seen in the power spectrum, i.e. *Figure 3.8*. After a certain point, the sheath rectification is so low that the electron heat current is negligible compared to the ion heat flux. The ion heat flux depends on the V_{DC}. But it is not very sensitive to a small change of the power balance. In the simulation, V_{DC} amplitude only changes 4% with these two power ratios. At the leading edge of the limiter, heat flux becomes zero as it is parallel to the magnetic field.
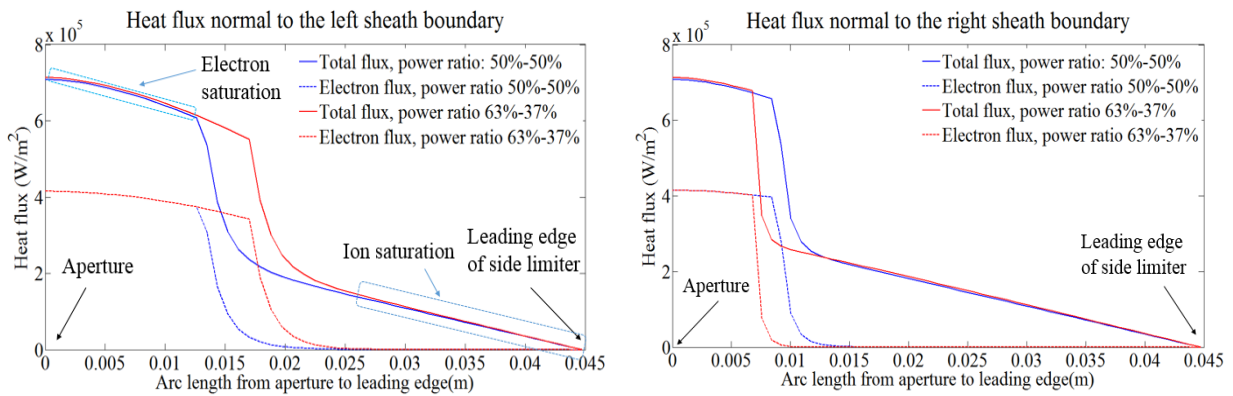
Figure 5.20. Heat flux at the curved boundaries of the private SOL, data picked up at the red boundaries of Figure 5.15 (Left), $\theta = 7^o$, z=-0.2m

The curvature again plays an important role on the scale of V_{DC}. In *Figure 5.21*, the curved part at the top of the limiters is removed. The heat flux still maintains the left-right asymmetry but the magnitude increases 175% compared to *Figure 5.20*. The sensitivity of the magnitude of the heat flux at the private SOL boundary on the curvature suggests the slow wave plays a dominant role on the sheath excitation inside the private SOL. A more realistic curvature will be considered in the future development of the SSWICH code.
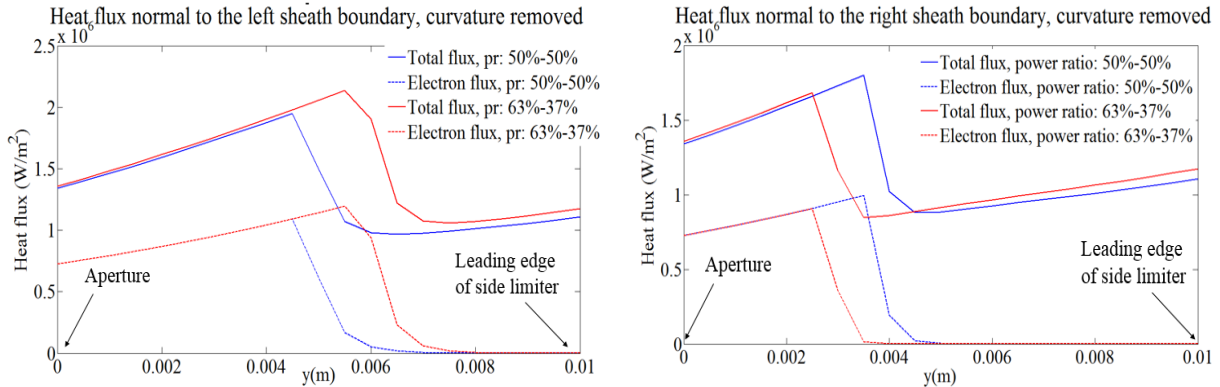
Figure 5.21. Heat flux at the vertical boundaries of the private SOL; Data picked up at the red boundaries of Figure 5.15 (Right), $\theta = 7^{o}$, z=-0.2m

5.4 Electromagnetic simulations for Aline plasma

The Aline device provides a good opportunity to study the physics of the basic plasma waves. One of the short-term scientific goals of the Aline device is to generate the helicon wave. Simulations are thus needed to find out whether the Aline condition could support this wave. Helicon wave is an electromagnetic wave, while the electromagnetic simulations have never been done before in Aline device. This section reports the first electromagnetic simulations for Aline using the 2D SSWICH-FW code without sheath. Both the LH and the Helicon wave are studied.

5.4.1 Simulation of Lower hybrid and Helicon waves for Aline discharge

The first step is to know the typical Argon density profile in Aline. The density is measured by the Langmuir probe, which is shown in *Figure 1.15*. Limited by the Aline window, the probe can only access y=[-50mm 50mm] in the radial direction. The measured density is indicated by the black dot rectangle in *Figure 5.22*. The spatial resolution here is 1mm, corresponding to 100 data points inside the rectangle. Outside of this rectangle, a density with an exponential decay is extrapolated. The combined full density profile is shown by the blue curve in *Figure 5.22*. From the dispersion relation Eq. (2.22), we knows that the helicon wave prefers a high density (so that w_{pe}^2 is larger), low magnetic field (lower w_{ce}) in order to be propagative (a high k^2), whereas the lower hybrid wave appears only when $\varepsilon_\perp \approx 0$. Thus it requires a lower density.

Substituting Aline neutral density (10^{20}m^{-3}), Argon cross-section (10^{-20}m^2), and the experimental electron temperature1.5eV-5eV into Eq. (4.28), yields to the typical electron-neutral collision frequency in Aline: 5×10^6-9×10^6rad/s. The Argon gas pressure is between 10^{-3}mbar (0.1 Pascal) to 10^{-1}mbar (10 Pascal), and the experimental ion temperature is like 0.026eV. Hence by Eq.(4.29), the ion-neutral collision frequency is around 5.2×10^4rad/s-5.2×10^6 rad/s. These values are also mentioned in [Faudot 2015].
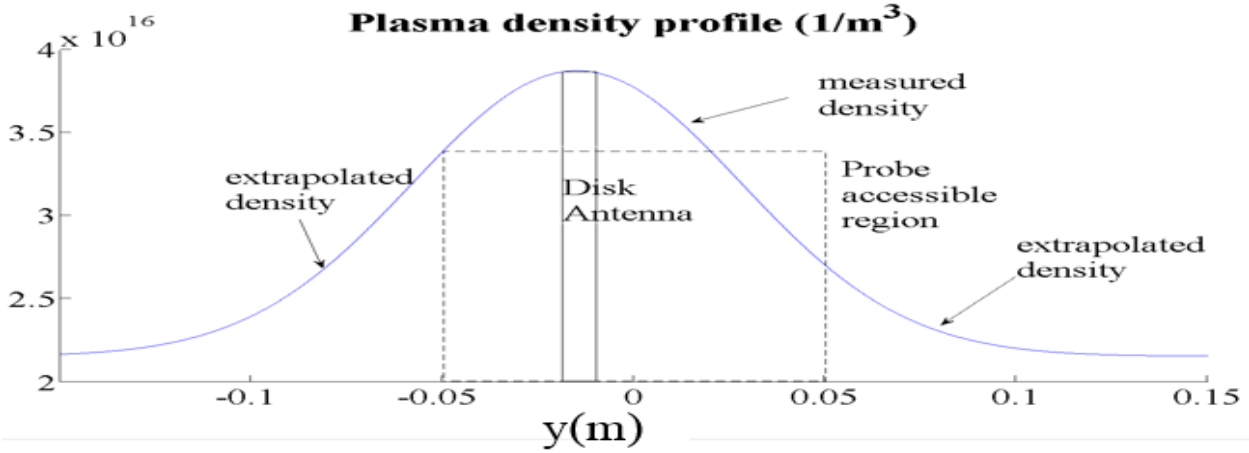
Figure 5.22. Typical density plasma density profile in Aline discharge

Table 5-1. List of parameters for Aline simulation

Argon Plasma	LH wave	Helicon wave
ni=ne (m^{-3}) @ center	10^{15}	10^{18}
Neutral density N (m^{-3})	10^{20}	10^{20}
Magnetic field **B$_0$** (T)	0.05	0.005
Wave frequency w_0 (rad/s)	10^8	6×10^7
Electron-neutral collision frequency v_m (rad/s)	5×10^6	5×10^6
Ion-neutral collision frequency v_i (rad/s)	5.2×10^4	5.2×10^4
Ion cyclotron frequency w_{ci} (rad/s)	1.2×10^5	1.2×10^4
Electron cyclotron frequency w_{ce} (rad/s)	8×10^9	8.79×10^8
Ion plasma frequency w_{pi} (rad/s)	6.59×10^6	2×10^8
Electron plasma frequency w_{pe} (rad/s)	1.78×10^9	5.6×10^{10}
Spitzer parallel conductivity σ$_{//}$ (S/m)	1.2×10^4	1.2×10^4
Perpendicular conductivity σ$_\perp$ (S/m)	0.0074	7.4
Ti (eV)	0.026	0.026
Te(eV)	5	5
$\varepsilon_\perp$ @ center	1+4×10^{-4}i	4×10^3+5.2i
$\varepsilon_{//}$ @ center	-314+31.6i	-8.7×10^5+1.5×10^{5}i
ε_x @ center	-3.6+0.18i	6.0×10^4+5×10^{3}i

The LH wave is an electrostatic wave, it could appear even without the static magnetic field. The current Aline condition can easily excite the Lower hybrid wave. One of the realistic parameter setup is shown in *Table 5-1*. The Helicon wave is electromagnetic. It prefers a higher density and lower magnetic field. Taking the typical density in Aline: 10^{17}m^{-3}, the squared wavenumber of Helicon wave is then $k^2 = k_{//}^2 + k_\perp^2$ =15m^{-2} according to the dispersion relation Eq. (2.22) under **B$_0$**=5mT (here we used $\alpha = 0°$ provided the Helicon wave mainly propagating parallel to **B$_0$** [Chabert 2011])). This corresponds to a

wavelength of 40cm. Note the half-width of the machine is only 50cm along axis. This explains why we proposed a higher density in *Table 5-1* . As a reference, the wavelength of the Helicon wave is about 13cm for $n_e=10^{18}m^{-3}$. Density above $10^{17}m^{-3}$ is impossible before, but now the lab has equipped a new tunable matching box. A density in a scale of $10^{18}m^{-3}$ has been achieved. Different to the Tokamak case, the Argon ion is not really magnetized under the proposed helicon wave condition due to such a low magnetic field (5mT). Note the requirement for magnetized plasma is that the collision frequency of electrons and ions must be lower than their cyclotron frequencies. For the provided ion-neutral collision frequency 5.2×10^4, the lowest magnetic field to have magnetized ion is 0.025T.

Figure 5.23 shows the electric fields of the LH and Helicon waves under the parameters in *Table 5-1* The excitation is done by imposing Ex=±900V/m (900V/m on the right and -900V/m on the left) at the bottom of the ceramic layers, as explained in *Figure 4.14*. Under these parameters, the LH has a wavelength of 7mm (evaluated from Eq. 2.23 with $k_{//}=50m^{-1}$, which is the main lobe of the spectrum). As a reference, the mesh sizes used in the simulation are 1mm in the plasma, 0.2mm in the ceramic layer, i.e. 10 grid points in each layer. Both the helicon wave and LH wave have their energy flow concentrated inside a resonance cone, which are orientated along the field line. This is a significant difference from the fast wave in Tokamak, which usually propagates perpendicular to $\mathbf{B_0}$. The limiting angles between the group velocity and $\mathbf{B_0}$ for these two waves are,

$$\varphi_{LH} = arctan\sqrt{-S/P} \tag{5.9}$$

$$\varphi_{He} = \alpha - arctan(\frac{tan\alpha}{2}) \tag{5.10}$$

The LH wave, like the slow wave in a tokamak plasma, has an ignorable E_z component. The limiting angle of the resonance cone predicted by Eq.(5.9) is about 5°. This value agrees with the observation from E_x and E_y maps shown in *Figure 5.23* (a).

For the Helicon wave, one can immediately see that Eq. (5.10) has a maximum value of 20° at $\alpha = 54^o$. That is to say the Helicon wave only exists inside a resonance cone which has an angle 20°. Beyond this resonance cone, the extraordinary wave could still propagate. This is shown explicitly in the lower part of the E_y map in *Figure 5.23*. According to its dispersion relation Eq. 2.25, the perpendicular propagating extraordinary has a typical wavelength of 3cm. This is consistent with the E_x and E_y maps in *Figure 5.23* (b). Increasing the dissipation (collision) will sufficiently eliminate these modes.

With collision, we can define a damping length where the magnitude of the electric field reduces to a factor of 1/e (e is the natural constant) w.r.t the maximum magnitude. For parallel propagation helicon wave, the parallel damping length can be defined as,

$$L_{He,//} = \frac{1}{|Im(k_{He,//})|} = \frac{c}{w_0|Im(n_{He,//})|} = \frac{c}{w_0|Im(\sqrt{D})|}, \quad (k_{He,//} \gg k_{He,\perp}) \tag{5.11}$$

Take Stix parameters listed in *Table 5-1*, the parallel damping length of this Helicon wave is about $L_{//}=0.5m$.

(a) LH wave, Ex real part

(b) Helicon wave, Ex real part

(c) LH wave, Ey real part

(d) Helicon wave, Ey real part

(e). LH wave, Ez real part

(f). Helicon wave, Ez real part
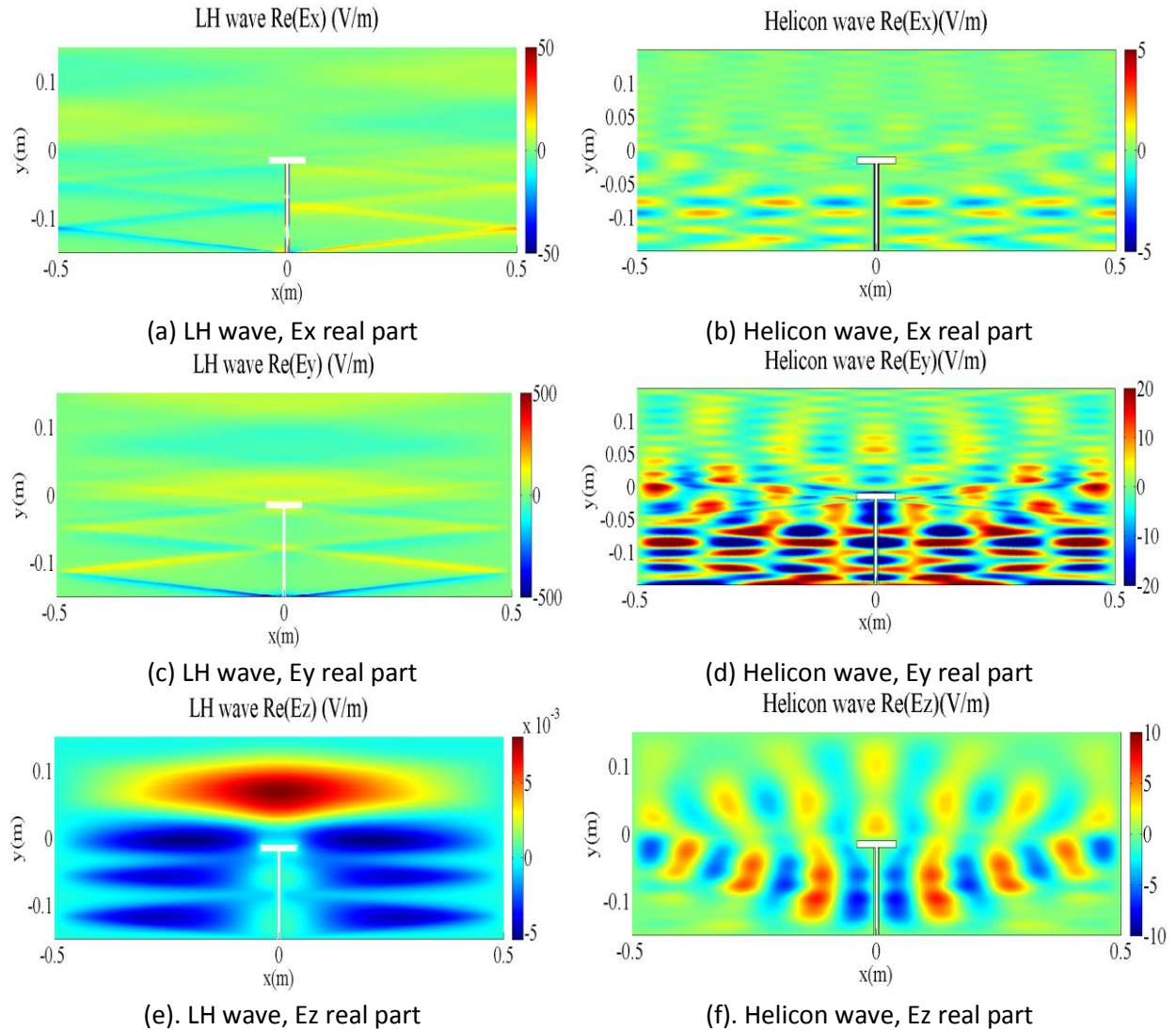
Figure 5.23. Electric fields of the LH and Helicon wave, using the parameters in Table 5-1

In a capacitively coupled plasma, the wave is excited by the displacement current, rather than by the induction current. The ceramic tube is an insulator, thus the induction currents flowing inside it and reaching the disk antenna surface are rather low. The disk antenna and the bottom metallic wall constituted a parallel-plate capacitor. The displacement current flows along the y direction and excites waves. This explains why the electric fields in *Figure 5.23* are more likely to be excited by the feeder than by the antenna itself. Setting perfect electric conductors along with the feeder line could suppress this excitation. This is shown in *Figure 5.24*. Here one can see clearly the limiting angle of the wave propagation (group velocity) in *Figure 5.24* is close to 20°. The distance between two lobes is also consistent with the predicted wavelength, i.e. 13cm.

Helicon wave Re(Ez) with 2 PEC (V/m)
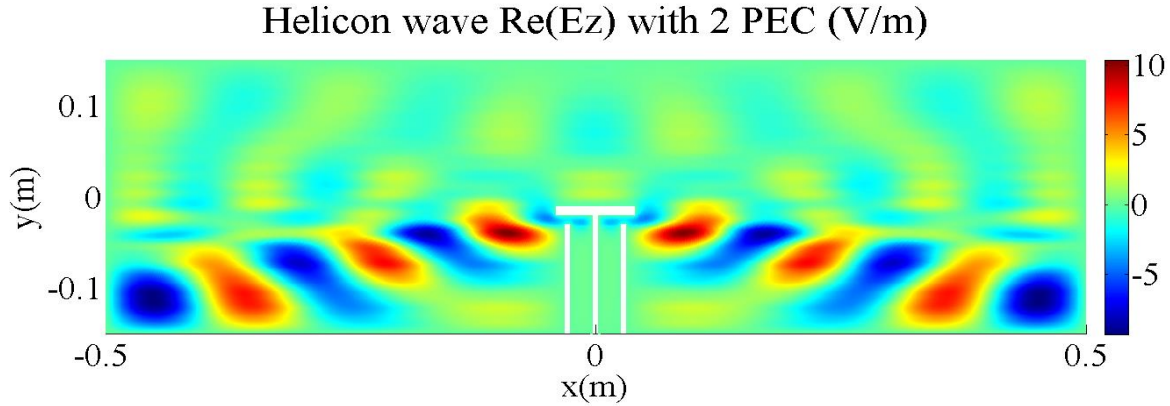
Figure 5.24. Real part of Ez field map. Two PECs are set alongside the feeder, other parameters are taken the same as Figure 5.23 (b)

Finally, it's worthwhile to mention that the field structure in *Figure 5.23* is quite sensitive to the electron-neutral collision frequency as it induces different levels of the dissipations.

5.4.2 Mesh-dependent issues near the antenna and lateral boundaries

The field structure shown in *Figure 5.23*(b) also has a convergence problem. *Figure 5.25* shows the relative difference of E_y with two mesh sizes. The field structure is mesh sensitive, especially in the region surrounding the disk antenna. This mesh-dependent behavior can be suppressed by increasing the dissipation level. The collision frequency needed to find a stable solution is around 10^7 rad/s, provided the Helicon wave frequency is $w_0=6×10^7$ rad/s. For LH wave, the relative difference is shown in *Figure 5.26*. The non-convergence behavior is also most severe around the disc, which confirms the observation in Chapter 3. By introducing the dissipation, one can greatly reduce this mesh-dependent behavior to a small level i.e. relative difference<20%. The dissipation level needed is again found to be the same scale as the wave frequency, 10^8 rad/s.

A collision frequency at the same order of the wave frequency is of course non-realistic in Tokamak edge plasma. In Aline, the maximum electron-neutral collision frequency is 10^7. But using such a high collision frequency somehow modifies the dispersion relations of the wave. The physics of the solution is thus changed. Using a smaller collision frequency than the wave frequency, the RF field is not converged to the mesh size around the antenna, which makes sheath treatment directly on the antenna boundaries problematic. This is one of the reasons why the SSWICH-FW approach is not used to conduct RF sheath simulations in Aline. The RF sheath simulation in the next section thus uses the asymptotic SSWICH-SW approach, where $E_{//}=0$ is imposed at the sheath boundaries. Another reason to use SSWICH-SW approach is that the magnetic field is totally horizontal in Aline.
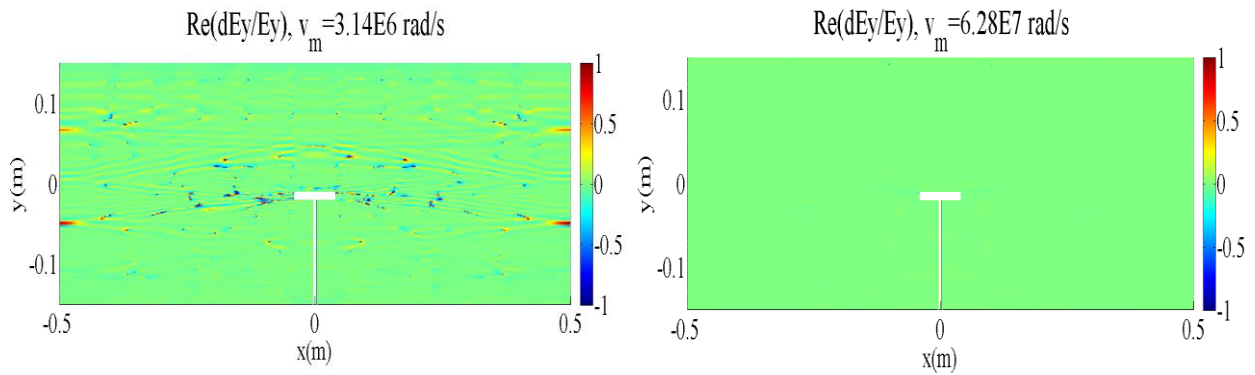
Figure 5.25. Relative variations of Ey of the Helicon wave with different dissipation; dEy/Ey=(Ey(1mm)-Ey(2mm))/Ey(2mm); Left: collision frequency $v_m=3.14\times10^6$ rad/s; Right $v_m=6.28\times10^7$ rad/s
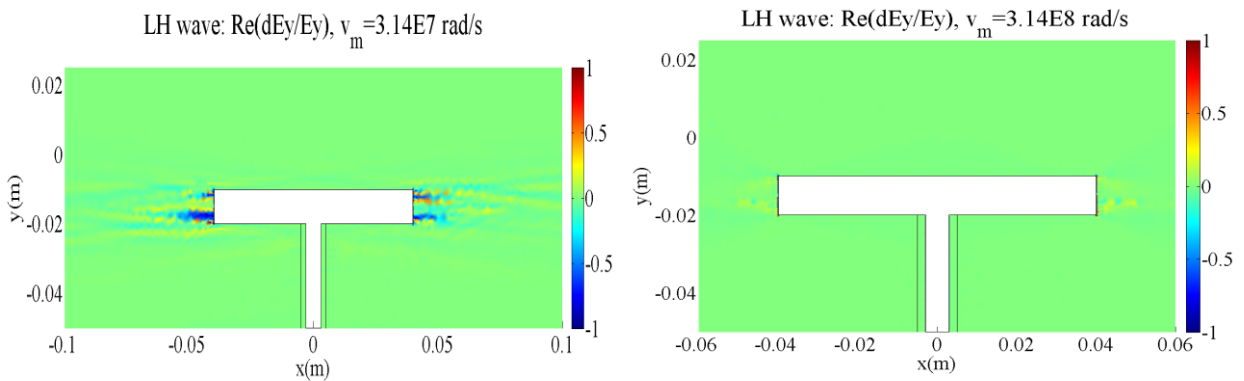
Figure 5.26. Relative variations of Ey of the LH wave with different dissipation, dEy/Ey=(Ey(1mm)-Ey(2mm))/Ey(2mm), zoom in the antenna region; Left: collision frequency $v_m=3.14\times10^7$ rad/s; Right $v_m=3.14\times10^8$ rad/s
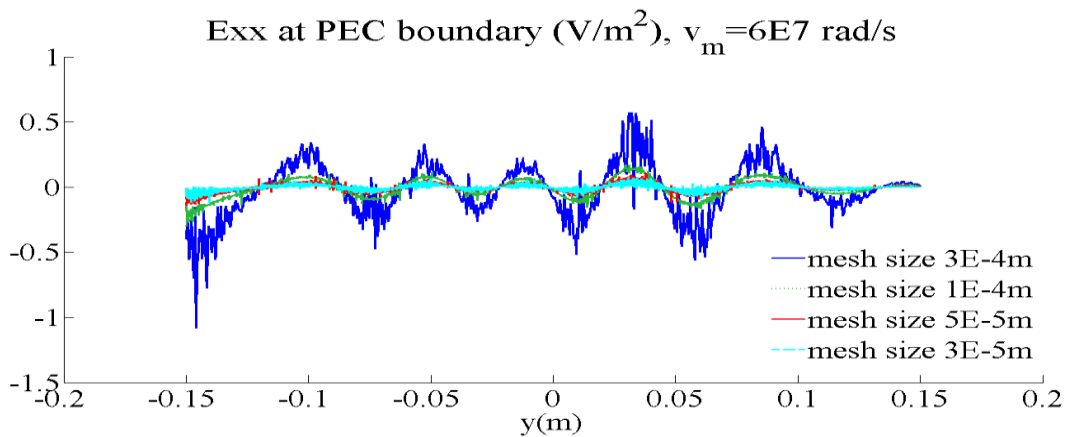
Figure 5.27. Exx at the left PEC boundary with different mesh sizes, the same plasma parameters is used as Figure 5.23(b)

It has been shown in chapter 4, the vector finite element has some problems to evaluate the derivative. Here we plot the x derivative of Ex at the left vessel boundary. We can see in *Figure 5.27*, even along the PEC boundary, the derivative is hard to converge. The small fluctuations on the E_{xx} curve were due to the fact that mesh was not regular at the boundary. Using a more regular mesh, one could obtain a smoother E_{xx}. Fortunately, at PEC boundary, the numerical instability is decreasing as the mesh size getting finer, as opposed to the behavior at the asymptotic boundary. One could believe that up to a certain limit of mesh size, the derivative at the PEC will be converged.

5.5 Comparison of 2D SSWICH-SW simulation with experimental potential map in Aline

Aline device is meant to ease the understanding of RF sheath around ICRF antennas in Tokamak. As first step to model RF sheath in Aline. The DC plasma potential by the SSWICH-SW simulation is compared to the floating potential map from the probe measurement.

The experimental floating potential map in the middle plane of the Aline is shown in *Figure 5.28*. The details of how this potential field map is obtained from the measurement can be found in [Faudot 2016]. In short, it is derived from the probe IV characteristic *Figure 2.13*. The black part is the disk antenna. The maximum value of the floating potential always locates in a region above the antenna, i.e. y=[20mm-40mm]. The plasma density from this measurement also has a peak value at y=40mm. This is probably due to the $E \times B$ drifts which transfer the particles radially. To model this process, one needs a 3D simulation and hence it is out of the scope of our current 2D version of SSWICH. In this measurement, n_e(@center)=4×10^{16}m^{-3} (the same density as in Figure 5.22), B_0=0.023T, w_0=2.2×10^{8}rad/s, gas pressure 10^{-2}mbar, one could estimate $k_{\perp,LH}^2 = 5.5 \times 10^5 m^{-2}$ ($k_{//}$=50m^{-1}) and $k_{He}^2 = 21 m^{-2}$ (α=0°). Thus the LH wave is the main propagating wave. The SSWICH-SW code only models the LH wave, which is the main propagating wave in this case. The ion cyclotron frequency under current magnetic field is about 5.5×10^4 rad/s is one order less than the ion-neutral collision frequency estimated from Eq. (4.29), which leads to v_i=5.2×10^5 rad/s. Thus the DC perpendicular conductivity proposed in Eq. (4.31) can be used in this simulation.
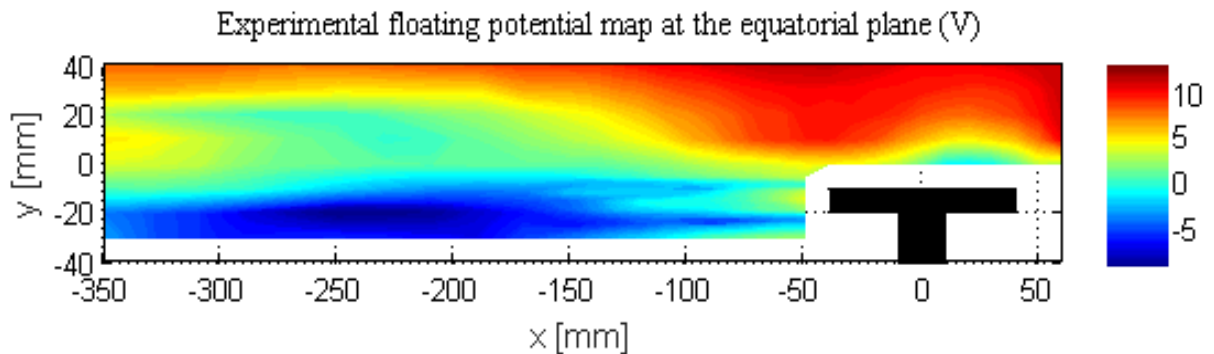
Figure 5.28. Floating potential map measured by the probe in Aline discharge [Faudot 2016], B$_0$=0.023T, w$_0$=2.2×10^{8}rad/s, gas pressure 10^{-2}mbar, antenna is grounded as it is in Tokamak

In the simulation, we shifted the density profile *Figure 5.22* rightwards to have the maximum value at y=40mm. The electric field inside the feeder still uses the rough estimation of |Ex|=900V/m. The temperature is constant all through the domain. The DC plasma potential calculated by SSWICH-SW under the same condition is shown in *Figure 5.29*. The V_{DC} is converged to the mesh size even the RF field of the LH wave has some oscillations. Unlike the experimental map, the V_{DC} from simulation is quite homogeneous at the center. The radial extension of V_{DC} depends on the perpendicular conductivity and thus the ion-neutral collision. To recover the toroidal (x direction) variations of V_{DC} structure as seen in *Figure 5.28*, one needs to lower the parallel DC conductivity in SSWICH to allow the toroidal gradient taking effect. The simplest case is a linear sheath regime where the relation $|\dfrac{e(V_b - V_{DC} + V_f)}{k_B T_e}| \ll 1$ is fulfilled. In this case, the toroidal inhomogeneity can be quantified as [Colas 2010]

$$|\frac{\delta V_{DC}(y,x)}{V_{DC}(y,x)}| \approx \frac{\sigma_\perp}{\sigma_{//}} \frac{x^2}{\lambda^2} \tag{5.12}$$

Where λ is the diffusion length that has been defined in Eq. (5.4). In this expression, x=0 corresponds to the middle plane. When $|\delta V_{DC}/V_{DC}| \ll 1$, the toroidal homogeneity is well preserved. The inhomogeneity get largest at x=±0.5.

We then progressively decrease the parallel conductivity in the simulation to find the critical value below which the toroidal homogeneity of V_{DC} breaks. In *Figure 5.29*, $\sigma_\perp = 0.02\,S/m, \sigma_{//} = 80\,S/m, \lambda = 0.08m$ at y=0, x=-0.5 so that $|\delta V_{DC}/V_{DC}|$=0.0098<<1. One can see the V_{DC} is homogenous along the toroidal direction. If we define $|\delta V_{DC}/V_{DC}(y, -0.5)|$=0.1 as the criterion level, the minimum $\sigma_{//}$ one can go is 10 times smaller provided other conditions remain the same. This is confirmed by the SSWICH simulation. As an example of toroidal inhomogeneous V_{DC}, *Figure 5.30* shows the simulation with $\sigma_{//}$ 100 times smaller than the one in *Figure 5.29*. Indeed the toroidal inhomogeneity gets larger at the edge and smaller at the center.

In reality, the density profile also has toroidal variations, these will also make a contribution to the V_{DC} toroidal inhomogeneity since the conductivities depend on the density. To recover the whole picture of *Figure 5.28*, one needs a precise 2D density profile.
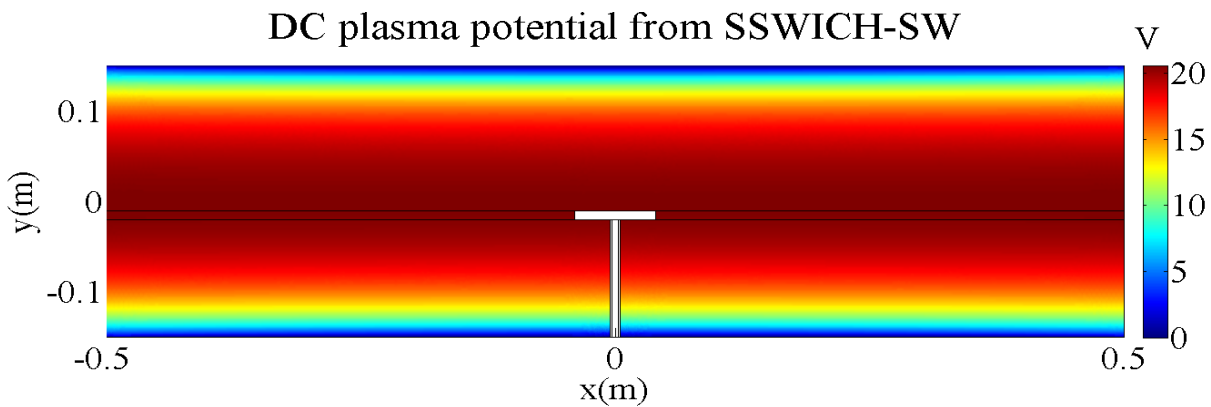
DC plasma potential from SSWICH-SW

DC plasma potential from SSWICH-SW, $\sigma_{//}/100$
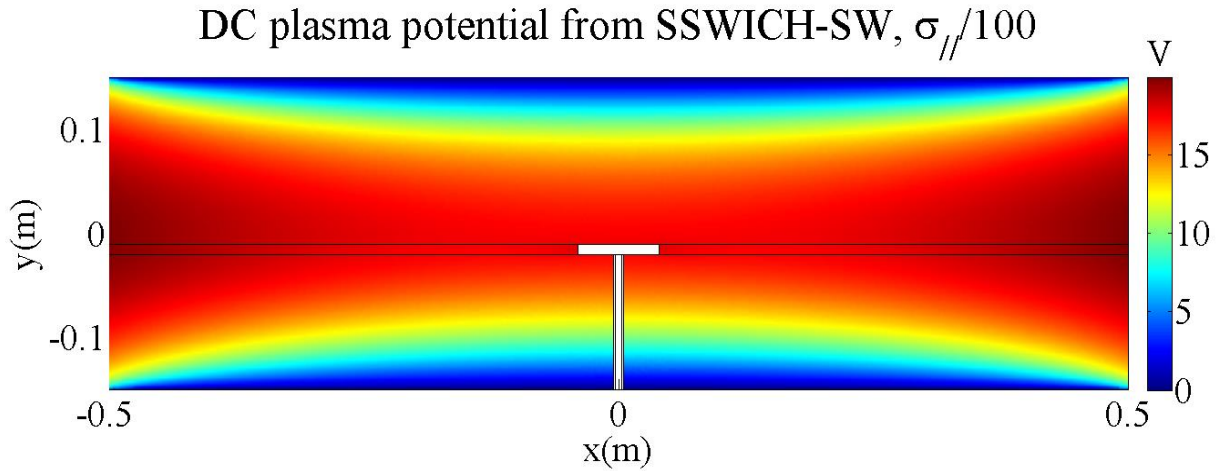
Figure 5.30. DC plasma potential with parallel conductivity 100 times less than the one used in Figure 5.29, other parameters are the same as Figure 5.29

One of the explanations of the maximum floating potential appearing above the antenna is that the ions are accelerated by the radial electric field at the antenna top surface. Thus the ions are more energetic in some specific regions above the antenna. To fully model this process, one needs to solve relevant kinetic equations. In SSWICH, we could only model this physics by artificially increasing the ion-neutral collision frequency v_i from 5×10^5 rad/s to 5×10^6 rad/s in the region y=[10mm 50mm]. The new V_{DC} map taking to account these modifications is shown in *Figure 5.31.* The peak value of V_{DC} is now slightly shifted upwards.

With the latest developed spectral method, (see Page 121), we could now conduct full wave simulation for Aline. The SSWICH-SW simulation deals with non-tilted magnetic field and ignores the poloidal (out of plane direction) derivative. In order to have a better comparison, we take the smallest magnetic tilt angle θ=0.01° in the SSWICH-FW, which still keeps the numerical accuracy of the RF field simulation as mentioned in Section 4.4.3. From Page 121, we know that $k_z=1\times10^{-3}m^{-1}$ can well approach the zero k_z case. *Figure 5.32* shows the V_{DC} by SSWICH-FW simulation. The field structure keeps almost invariant which justifies our previous assessment that the LH wave is the main wave under the present experimental conditions. However, unlike the Tokamak case where the V_{DC} magnitude increases when combing the fast wave, here the V_{DC} magnitude decreases by 20%. Thus the Helicon wave seems play a destructive rule on V_{DC} magnitude.

Go beyond these comparisons are difficult as a realistic plasma contains many physical processes that are not modelled in SSWICH. In the above simulations, we have assumed the antenna is grounded. The self-biasing of the antenna depends on the way whether it is directly connected to the ground, or through a capacitor. In the former case, the voltage at the antenna surface is similar to the Tokamak case, i.e. 0V, whereas in the latter case, it is negatively biased. This biasing can be investigated in Aline and answer the question: should the antenna structure be grounded or floating to limit the heat flux. In this part of the thesis, only the first case is studied. Although Aline has a capacitive coupling regime at this stage, it can

easily change to the inductive coupling. To be more representative to the Tokamak situation, two straps can be put side by side into the Aline chamber. Each strap forms a current loop to the feeder. This has been planned in the future experimental studies.
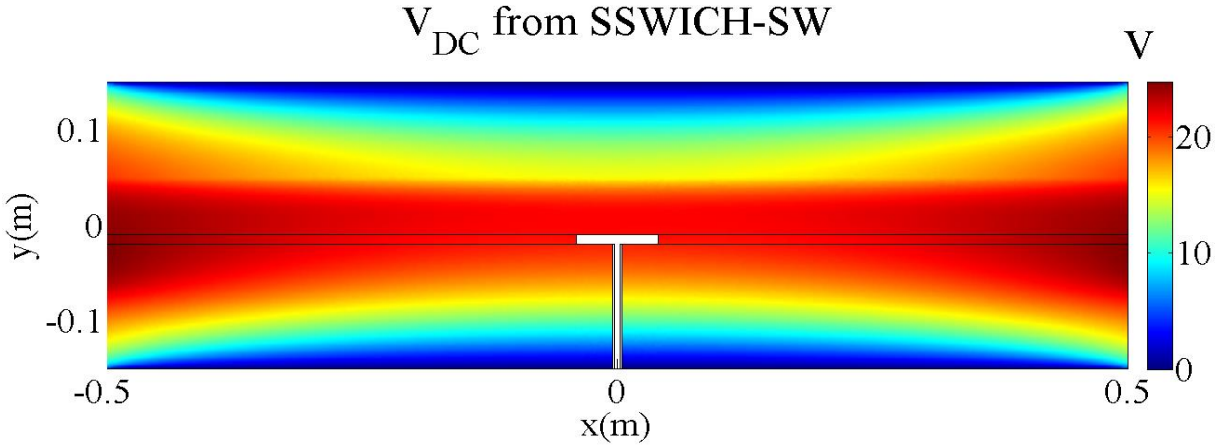
Figure 5.31. DC plasma potential map from 2D SSWICH-SW simulation with modified ion-neutral collision, parallel conductivity is divided by 100 as shown in Figure 5.30
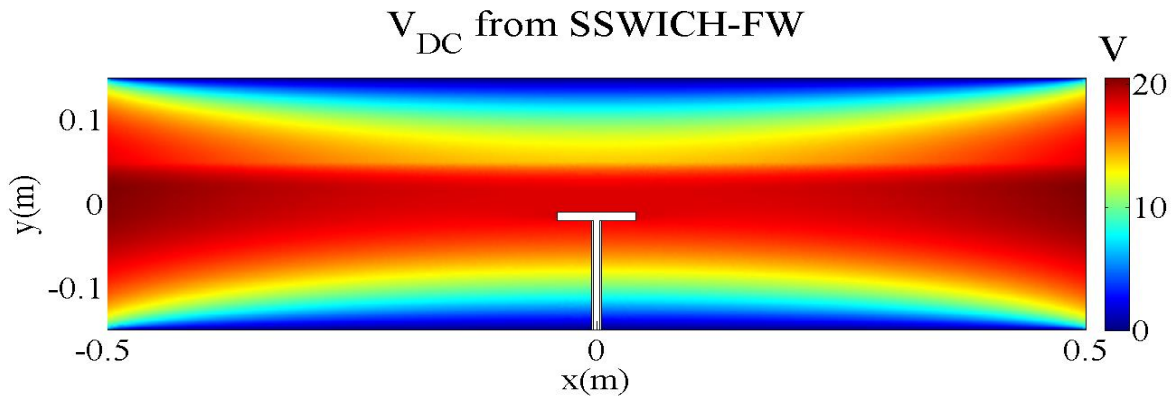
Figure 5.32. DC plasma potential map from 2D SSWICH-FW simulation using spectral approach, $k_z=0.001m^{-1}$, $\theta=0.01°$, other plasma parameters are the same as Figure 5.31

5.6 Conclusion of this chapter

This chapter firstly documented the role of the fast wave in tokamak environment. With the new 2D SSWICH-FW cod in its asymptotic version, we observed mode conversion occurring at the far SOL sheath boundaries when the geometry has a shape transition. At materials boundaries located far away from the modelled ICRF launchers, the behaviour of oscillating RF sheath voltage and DC plasma potential varying under different geometric dimensions agrees with the expected properties of the fast wave induced far field sheaths, that were totally absent in SSWICH-SW. The amplitude of V_{RF} at these remote locations remains modest in comparison with V_{RF} values induced on close objects (e.g. internal face of antenna side limiters) in the same simulations. The existence of far-field sheaths in the free SOL cannot totally explain the enhanced DC potentials measured outside antenna limiters. Decreasing the perpendicular DC plasma

conductivity significantly affects the DC plasma potential broadening even with the presence of the fast wave. This suggests the DC current transport is still the dominant mechanism in determining radial extension of the DC plasma potential peaks measured experimentally.

We have also shown that the SSWICH-FW asymptotic code could recover some key experimental results on Tokamaks, including the double-hump structure of the DC plasma potential and left-right asymmetry of the heat flux on the antenna surface. By decoupling the slow wave and the fast wave excitations, simulations reveal that the fast wave can play a significant role on the DC plasma biasing even in the vicinity of the wave launcher. The double-peak poloidal distribution of sheaths effects observed on RFA and IR thermography on Tore Supra, already present in SSWICH-SW results, is mainly attributed to the $E_{//}$ component (dominated by Slow Wave) in the RF field map for SSWICH-FW excitation.

Our simulations also revealed poloidal modulations of V_{RF} and V_{DC} that are hardly present on measurements. These modulations are attributed to the effect of Faraday screen bars in the $E_\perp$ component of the radiated RF near field (dominated by Fast wave). We speculate that the present simulations over-estimate these poloidal modulations of V_{RF} and V_{DC}. Simple assessments indeed suggest that the multi-2D approach followed so far, while being satisfactory for Slow Wave computations in tokamaks, underestimates the evanescence of Fast Waves with large poloidal wavevectors. These spectral components do not contribute much to the radiated ICRH power but are present in the RAPLICASOL near-field maps. Therefore incorporating at least some 3D effects should be envisaged in future versions of SSWICH-FW. This comes unfortunately with a numerical cost.

Besides, the SSWICH asymptotic code was also being used to conduct electromagnetic simulations for Argon plasmas in the Aline device. Our first step is to implement SSWICH-FW principles into the Aline cylindrical geometry, with equatorial plane (radial/axial) as our simulation domain. A prescribed electric field map is used as the excitation at the ceramic layer to mimic the capacitive coupling regime of Aline machine. To damp the waves, the neutral-electron collision frequency has been introduced into the cold plasma dielectric tensor. There are mainly two polarizations of waves existing in Aline, the Helicon wave and the lower hybrid wave, corresponding to the fast wave and the slow wave in Tokamak, respectively. SSWICH-FW simulations showed that at low densities the disc-shaped RF electrode in Aline excites preferentially the LH wave, while it rather emits helicon wave at large densities. The field structure however is very sensitive to the electron-neutral collision frequency, whose accurate value is unfortunately hard to know. The antenna is plugged inside the Aline chamber. A collision frequency that is comparable to the wave frequency is needed to totally resolve the mesh-dependent behaviours of the electromagnetic fields around the antenna. The 2D SSWICH-SW approach has been used to simulate RF sheath in Aline. The DC plasma potential from SSWICH-SW simulation is compared with the measured DC floating potential map during the Aline experiment. The experimental floating potential map peaks several centimetres above the antenna, this feature can be partially modelled by counting the increasing of the ion-neutral collision in the region above the antenna due to the ion acceleration by the radial electric field.

Reference

[Bobkov 2016] V. Bobkov et al, "Making ICRF compatible with a high-Z wall in ASDEX Upgrade", Proc. 43rd EPS conference, July 4-8th, 2016, KU Leuven, Belgium

[Kohno 2015] H. Kohno, J. R. Myra and D. A .D'Ippolito, "Numerical investigation of fast-wave propagation and radio-frequency sheath iteraction with a shaped tokamak wall", Phys. Plasma **22**, 072504 (2015)

[Chabert 2011] P. Chabert and N. Braithwaite. "Physics of Radio-Frequency plasmas", Cambridge University Press, Cambridge, UK, 2011.

[Corre 2012] Y. Corre et al, "Characterization of heat flux generated by ICRH heating with cantilevered bars and a slotted box Faraday screen", Nucl. Fusion **52**, 103010 (2012)

[Colas 2013] L. Colas et al, "RF-sheath patterns modification via novel Faraday screen and strap voltage imbalance on Tore Supra ion cyclotron antennae", J. Nucl. Mat. **438** S330-S333 (2013)

[Colas 2016] L. Colas, L. Lu, A. Krivska, J, Jacquot, J. Hillairet, W. Helou, M. Goniche, S. Heuraux and E. Faudot, "Spatial proximity effects of the excitation of sheath RF voltages by evanescence slow wave in the ion cyclotron range of frequencies", accepted by PPCF in October 2016

[Jacquot 2013] J Jacquot, PhD thesis, "Description non lineaire auto-coherente de la propagation d'ondes radiofrequences et de la peripherie d'un plasma magnetise", Universite de Lorraine, 2013

[Jacquot 2014] J. Jacquot, D. Milanesio, L. Colas, Y. Corre, M. Goniche, J. Gunn, S. Heuraux, M. Kubic and R. Maggiora, "Radio-frequency sheaths physics: Experimental characterization on Tore Supra and related self-consistent modeling", Phys. Plasma **21**, 061509 (2014)

[Jacquot 2015] J. Jacquot et.al, "Full wave propagation modelling in view to integrated ICRH wave coupling/RF sheaths modelling", AIP Conf. Proc, 1689, 050008 (2015)

[Faudot 2016] E. Faudot et al, "RF potential oscillations in a magnetized capacitive discharge", proc. 43rd EPS conference, July 4-8th, Leuven, Belgium, 2016

Chapter 6   Final remarks and prospects

1. Main results achieved in this thesis

Ion cyclotron resonant heating (ICRH) is one of the main heating methods used in the present-day magnetic fusion devices, i.e. Tokamak. It is also the unique way to achieve direct ion heating. The wave is launched by antennas at the edge of the Tokamak device under the typical frequency range of 30-80MHz. To achieve a sufficient plasma heating and make the heating system reliable for steady-state operation, one must understand the antenna-plasma coupling and minimize spurious edge effects of RF near field. This thesis is a part of work contributed to this subject.

Although the fusion plasma is extremely hot, the thermal effect is only important around the resonance. Out of the resonance region, it is often convenient to use the cold plasma approximation. The use of simplified dielectric tensor makes it possible to treat the cold plasma as an anisotropic dielectric. An ICRH antenna can emit two types of cold plasma waves: the fast wave and the slow wave. The former can propagate to the central plasma and play as a heating wave, while the latter is evanescent above the lower hybrid resonance and propagates below. The fast wave has notable electric field components that are perpendicular to the static magnetic field, whereas the slow wave has a large electric field in the direction parallel to the static magnetic field. Since the fast wave is the main heating wave, the ICRH antenna is often poloidally displaced to generate the fast wave. The lower hybrid resonance naturally presents in the current-day Tokamaks, i.e. inside the antenna box, however, it is often being neglected in the previous wave coupling simulations.

The first part of this thesis studied the impact of densities that decay continuously inside the antenna and across the Lower hybrid resonance on RF near field and power coupling. A 2D full wave (slow wave + fast wave) code named RAPLICASOL-2D has been developed before this thesis. Previously it had a pure toroidal magnetic field. During this thesis, it was upgraded to the tilted magnetic field configuration. The new magnetic field is now tilted in the toroidal/poloidal plane. This code considers a collisionless cold magnetized plasma without sheath, although it is flexible to add collisions and is also compatible to implement sheath boundary conditions. The code was developed based on the finite element solver of the commercial software COMSOL Multiphysics. One of the main reasons to use COMSOL is that it allows one saving the time in coding and compiling and thus the users can focus on studying the physics.

 Simulation by the new 2D RAPLICASOL code shows that at densities below the LH resonance, reaching numerical convergence is nontrivial: up to the memory limits of the adopted workstation, the field pattern changes with the grid size. A physical interpretation relies on the fact that propagating slow wave can have very short wavelength and thus it is sensitive to simulation parameters, like mesh size. The main results of this part of thesis are shown in *Figure E.1*. In this figure, we examined the dependence of the power coupling to the main plasma on the variation of the tilt angles, with finite plasma densities inside the antenna box. Interestingly and importantly, the total coupled spectrum is independent on the mesh size and is only weakly affected by the presence of the density profile inside the antenna box in dipole phasing. Dipole phasing is often used as heating phasing. One can thus drop this low density inside antenna box for the fast wave coupling studies. This justifies the simplification that most current-day wave coupling codes made, i.e. ignoring the existence of the lower hybrid wave in their simulation and only considering the fast wave. In monopole phasing, simulation shows there is a maximum 20% of power increase due to the presence of plasma. The distinction comes from the fact that the fast wave

evanescence length for low $k_{//}$ is changing. Hence modeling low $k_{//}$ scheme with antenna staying in vacuum may need to be re-considered. Simulation also shows that varying the density gradient in the fast wave evanescence region has no significant effect on wave coupling. One can thus still model the power coupling to plasma in a fairly good precision despite of some uncertainties existing in the density profile.
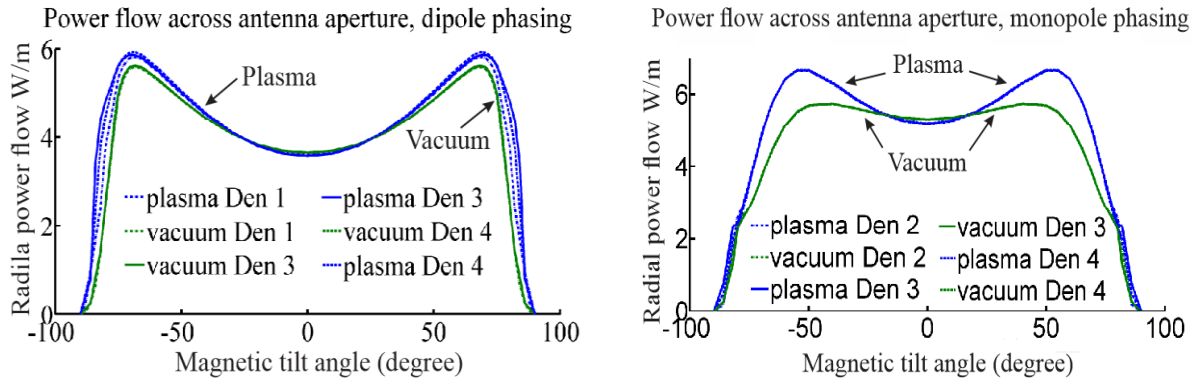
Figure E.1 behaviors of the power coupling with tilt angle and different density profiles, in dipole phasing (left) and monopole phasing (right)

Radio frequency (RF) waves can induce the sheath RF oscillations in their accessible regions. The oscillating RF sheath voltage has a net contribution to the DC plasma potential via non-linear sheath rectification. The sheath rectification is suspected to cause strong impurity sputtering and excessive heat loads on ICRF antenna surfaces and other plasma facing components. Our way to model the RF wave and sheath interaction is to solve self-consistently the RF wave propagation and DC plasma biasing with non-linear sheath boundary conditions (SBC). It adopts a three fields approach, i.e. solves the RF wave propagation, RF oscillating sheath voltage and DC plasma potential in an iterative way. The RF sheath is often modelled in the textbook by a circuit model which consists of a capacitor, revered diode and constant ion current source. Under a high sheath voltage and immobile ion regime, like the typical working conditions of the ICRF antenna in Tokamak, this model can be further reduced to a parallel-plate capacitor with a time-varying width. The formula for the RF sheath capacitance can consequently be obtained. Under an electrostatic sheath assumption, a sheath boundary condition strictly speaking valid for an immobile ions limits were proposed by Myra and D'Ippolito before this thesis. The theory of the DC sheath assumes a constant ion current with knowing the ion enters the sheath at the Bohm sound speed, while the electrons are assumed to be Maxwellian and follows the Boltzmann density distribution inside the sheath. A sheath IV characteristic can then be derived to describe the total DC current across the sheath, where the RF sheath has a non-linear contribution to the DC plasma potential via the rectification process. The thickness of the DC sheath is described by the Child-Langmuir law. With these theoretic bases, the Self-consistent Sheath and Waves for ICH (SSWICH) code was developed at CEA in 2013. The first SSWICH version adopts a simple 2D rectangular geometry and the magnetic field is either parallel or perpendicular to the wall. Under this magnetic configuration, the SBCs are only associated to the evanescent slow wave, thus it solves only the slow wave propagation in the RF field module. The slow wave field is excited by importing the field map from any other antenna code, i.e. TOPICA. An asymptotic version considering an infinite sheath width was also developed in order to ease the numerical convergence of the fully coupled SSWICH-SW. It only solves the three modules one time instead of iteratively. Tests have shown that at least in the Tore Supra configuration, the asymptotic version can already give a result fairly close to the final solution. Furthermore, A 3D version of the asymptotic SSWICH-SW was developed by taking Fourier transform in the third (poloidal) direction [Colas 2012]. Indeed, with the infinite sheath width assumption,

the sheath boundary conditions used in the first two modules become linear. This linearity guarantees that each poloidal wave number is independent to others, which allows one to run the 2D module sequentially for all the kz. With SSWICH-SW/TOPICA simulation, one can already recover the spatial proximity effect that has been observed experimentally and cannot be produced by the traditional line integral approach. However, the main heating wave, the fast wave is somehow missing in the SSWICH-SW code.

The central part of this thesis is the development and test of a new SSWICH version which should include the fast wave, a more realistic magnetic field configuration and shaped walls. Those objects are internally linked with each other. For example, under a tilted magnetic field, the fast wave is automatically coupled into the SBCs. Secondly, previously literature also indicates that under tilted magnetic field or with shaped walls, mode conversion is likely to occur between the slow wave and the fast wave, so one must also introduce the fast wave. Adding the tilted magnetic field and shaped wall is a step towards the realistic geometry.

The SSWICH-Full Wave code, still in 2D to limit the numerical cost, has a magnetic field tilted in poloidal and toroidal plane. This is not the most general case, but under this magnetic configuration, one can keep a similar simulation geometry as the previous code and at the same time introduce the fast wave coupling into code. At the beginning of this thesis, we have already envisaged that the RAPLICASOL and SSWICH should finally be generalized into one code. Thus during the development of the SSWICH-FW code, we chose a similar geometry with the 2D RAPLICASOL code, but the walls were shaped and new sheath boundary conditions were applied.

The SBCs used for the SSWICH-FW code should be valid under the tilted magnetic field. These boundary conditions did not exist before this thesis. In this thesis, more general RF SBCs were derived using all RF field components and the rectification formula was improved account for the tilted $\mathbf{B_0}$ in a simple way. Whether these formula fulfill the reality or not is still an open question and they are still under tested by more fundamental simulations. These boundary conditions were implemented along the shaped walls of the SOL region in the SSWICH-FW. The RF waves can be excited either by prescribed poloidal currents on built-in antenna straps or by prescribed external field maps. The way of imposing a current on the strap surface is not so realistic since the plasma can induce a current on the antenna surface too. Thus the field map excitation is better. SSWICH is at the present time the only code in the world able to simulate RF sheaths in tokamak environment using realistic antenna field maps.

Following the same strategy used in the development of the SSWICH-SW code, an asymptotic version of SSWICH-FW code based on the infinite sheath width assumption was developed. Asymptotic SSWICH-FW simulations using typical tokamak experimental (Tore Supra like) parameters have shown that the mode conversion from FW to SW occurring at the sharp corners where the boundary shape varies rapidly. Indeed, based on the fact that the slow wave and the fast wave have different behaviors when the Stix component evolves, we found that the field pattern appears at the leading edge of the side limiter is more likely a slow wave. The fast wave can access remote regions that are inaccessible for the slow wave. Simulation has also evidenced "far-field" sheath oscillations appearing at the shaped walls with a relatively long magnetic connection length to the antenna. These oscillations can only be excited by the propagating FW. By tuning the toroidal and radial dimensions of the SOL region, one could see that both the $|V_{RF}|$ and $|V_{DC}|$ at the shaped far SOL boundary decreases under a larger toroidal distance to the active antenna. The hypothesis behind this observation is that the fast wave contact less with the target boundary when

the SOL toroidal dimension getting larger. This can be seen by recalling the fast wave field pattern. $|V_{RF}|$ is a better indicator to examine the influence of the fast wave than $|V_{DC}|$ since the scale of V_{DC} at the far SOL is affected by both the propagating fast wave and the DC current transport. For example, increasing the toroidal magnetic connection length will increase the transversal diffusion length at far SOL and reduce the V_{DC} at the leading edge of the side limiter. Both the $|V_{RF}|$ and $|V_{DC}|$ increase under larger radial distance to the wave launcher, which is somehow counter-intuitive, especially when thinking about the spatial proximity effects. This behavior suggests that a propagating fast wave may not have the spatial proximity effects. Nevertheless, this observation agrees with the expected properties of the fast wave induced far field sheath provided the fast wave can contact more with the target boundary when the radial distance is larger. The behavior of V_{DC} at the far SOL boundary with variation of tilt angle is quite similar to the tendency of power coupling w.r.t. the tilt angle, i.e. *Figure E.1*. It further confirms that the fast wave plays a dominant role on the V_{DC} excitation in the far SOL region. The third part of simulations aims at exploring the role of the fast wave on V_{DC} radial broadening. Results show that decreasing the perpendicular DC plasma conductivity can significantly affect the V_{DC} radial broadening in the free SOL even in the presence of the fast wave. This suggests that the DC current transport is still the dominant mechanism to determine the DC plasma radial broadening.

Up to here, the results we discussed above were obtained using the current excitation by imposing poloidal currents on the build-in antennas. When comparing the simulation with the experiment, it is better to use a more realistic excitation. For example, importing field maps at the aperture from other more advanced wave coupling code. The 3D version of the RAPLICASOL code is developed in parallel to this thesis under the framework our European sheath project, thanks to the work by our Garching colleague [Jacquot 2015]. It has a very similar structure with the 2D RAPLICASOL code and the field map from this code has less noise than the previous maps we used from TOPICA. Thus further tests are carry out by the joint 3D RAPLICASOL and 2D SSWICH-FW asymptotic simulations. One of the most successful results produced by the SSWICH-SW/TOPICA simulation is the double-hump structures appearing at the 2D vertical-radial V_{DC} map at the toroidal location of the edge of side limiters. This kind of structure has been seen excessively in the experimental temperature and potential maps. SSWICH-FW/RAPLICASOL simulations have also recovered this double-hump vertical structure using multiple 2D approaches. At first, we ran the 3D RALICASOL code with the same parameter set-up as the 2D SSWICH-FW asymptotic and picked up the 2D (vertical-toroidal) electric fields at the Faraday screen of the 3D RAPLICASOL code. For each altitude (in vertical direction), the corresponding two tangential electric field components from the field map were imposed at the SSWICH aperture. The distinct polarizations of the fast wave and the slow wave allow one to decouple these two waves from the excitation, i.e. use only the perpendicular E component from the field map for the fast wave and use only the parallel E component for the slow wave. *Figure E. 2* shows the multiple-2D scan simulation results using SSWICH-FW/RAPLICASOL. The result matches better with the experimental double-hump structure when only the slow wave is accounted for. The slow wave, with a short evanescence length, is sensitive to the small modifications of the geometry in the private SOL. The curvature we introduced in the private SOL is thus important for the near field study but most probably not relevant for the fast wave coupling studies. On the other hand, the fast wave is sensitive to the 3D effect. While the slow wave has a dominant effect to excite V_{DC} in the private SOL, both of these two waves seem to play a comparable role on V_{DC} excitation in the vicinity of the wave launcher. At the last several months of this thesis period, we eventually tried a way to incorporate the 3D effect. The trick is to perform Fourier transform at the vertical direction (z direction) for the input E field map, similarly to the 3D asymptotic SSWICH-SW version, but now we consider both the two tangential

components from the 3D RAPLICASOL simulation. Then for each kz, run successively the RF field module and V_{RF} module making use of the spectral input of the RF field map and revised RF-SBCs which incorporates kz. Next, extract spectral component of V_{RF} at the sheath boundaries for each kz and perform inverse Fourier transform to V_{RF} along the vertical direction to obtain the V_{RF} solution in spatial domain at each sheath boundary. Finally run the V_{DC} module normally using the V_{RF} from the last step. Using this technique, a surface wave propagating along z direction is likely to appear at the sheath boundaries under high kz. This may due to an inconsistency between the FFT assumption and the finite size of the wave launcher. By using the Fourier transform, we imposed the periodic boundary conditions at the two ends of the vertical extension of the antenna, so these surface wave can propagates to infinite away from the antenna, whereas in reality they are reflected by the boundaries of the antenna.
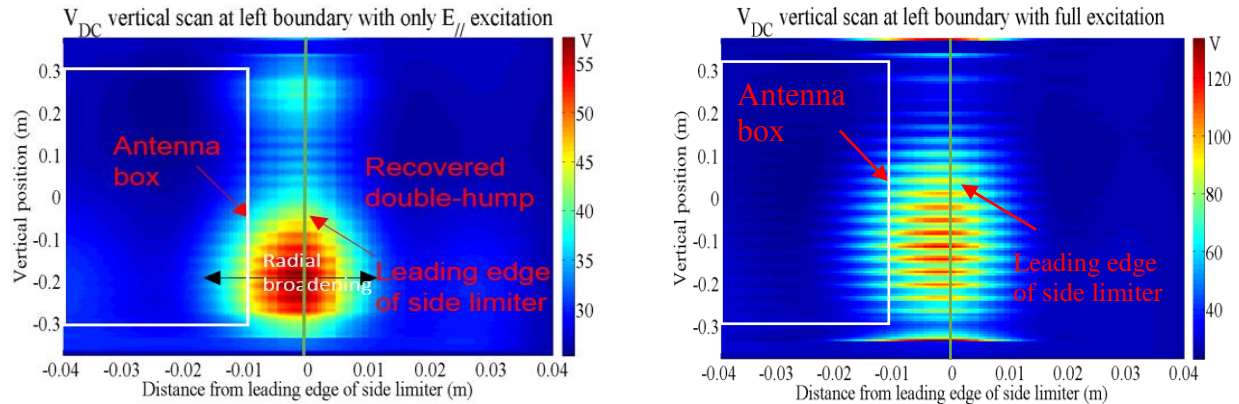
Figure E.2. Vertical-radial map of V_{DC} at the edge of the left side limiter by SSWICH-FW/RAPLICASOL simulations using multiple-2D approach, with only $E_{//}$ excitation (left), with full excitation (right). The simulation did not include the 3D effect

The left-right asymmetry of the temperature or the heat load at two opposite ends of the same magnetic field line has been observed extensively in the strap dissymmetrization experiments. This observation is a strong justification for the spatial proximity effects. With SSWICH-FW/RAPLICASOL simulations, we further evaluated the heat flux along two opposite sheath boundaries of the same antenna. Simulation successfully revealed the left-right asymmetry, suggesting that spatial proximity effects in RF sheath excitation, studied for slow wave only previously, is still important in the vicinity of the wave launcher under full wave polarizations, where both the fast wave and the slow wave are evanescent.

Initially developed for the RF sheath studies in Tokamaks, SSWICH-FW has more versatile applications. In the third part of this thesis work, we have shown how SSWICH principle can be implemented into a totally different machine than Tokamak, in terms of geometry and plasma coupling regime. The Aline device is a dedicated tool to study the basic plasma wave properties and the RF sheath. SSWICH is used as the first attempt to conduct interpretative simulations for Aline Argon plasmas. Using the asymptotic SSWICH-FW code, we have observed and studied both the LH wave and Helicon wave appearing under different Aline parameters. The LH wave normally propagates under a low density, like the slow wave in Tokamak, whereas the Helicon wave prefers a high density, similar to the fast wave in Tokamak. A major difference of the Helicon wave and the fast wave in Tokamak is that the helicon wave propagates along the magnetic field and has a resonance cone oriented along the toroidal direction. The lower hybrid wave, like the electrostatic slow wave in Tokamak, also propagates inside a resonance cone. This common property help us to identify the helicon wave and the Lower hybrid wave in the simulation. Given the

current plasma density of Aline, the Helicon wave can be observed under a very low magnetic field in Argon plasmas. In this magnetic field, the Argon ions are not really magnetized. To realize the helicon wave with a magnetized ions, it is better to use Helium. The mesh-dependent behavior of the electric fields surrounding the straps which we identified in Chapter 3 appears again in the Aline simulation. Adding collision is an efficient way to reduce this non convergence. From a pure numerical point of view, the collision frequency should be as high as the wave frequency in order to eliminate this non convergence, however, having such a high collision frequency will definitely change the physics of the waves. A better solution is clearly needed to tackle this non-convergence problem.

Since the magnetic field in Aline is totally horizontal and the fact that the "slow-wave-like" Lower Hybrid wave is the main wave that could be excited under the present status of the Aline machine, the SSWICH-SW code was used to model the RF sheath in Aline. The Spitzer conductivity was replaced by a parallel conductivity that counts for the electron-neutral collision, whereas the perpendicular DC conductivity comes from the ion-neutral collisions. There are also some other mechanisms that affects the DC conductivity, i.e. ion viscosity, ion inertial. For simplicity, those effect were neglected in the current simulations. Thanks to its easy access for diagnostic, the Aline device can provide experimental floating potential map that can be compared with the SSWICH-SW modelling. The DC plasma potential in the SSWICH-SW simulation shows a toroidal homogeneity under a high parallel conductivity, i.e. in the tokamak plasmas, whereas the experimental floating potential map measured in Aline has toroidal variations. Now with our new parallel conductivity, the toroidal inhomogeneity appeared as predicted by an analytical model. The experimental floating potential always has a peak value above the antenna whereas the SSWICH simulation shows the peak value is located at the antenna. This discrepancy was partially explained by the acceleration of the ions due to the radial electric field at the top surface of antenna, a phenomenon not present in SSWICH.

Above we have summarized the main results achieved during this thesis. We hope that we have convinced the readers that SSWICH as a numerical code can produce some reasonable results to help understand the wave/sheath problems. In the following, we will present the prospect for the future work.

2. Future work

The present 2D RAPLICASOL code we used to carry out the first part of this thesis work did not consider the parasitic damping. Our later simulation in Aline device has shown that adding collision can greatly reduce the mesh-dependent behavior. However, an accurate dissipation level is critical in these simulations but it is difficult to know the collisionality around the LH resonance. Thus a better way to solve this mesh-dependent problem is strongly needed. An ongoing mathematical work tries to reformulate rigorously the finite element method around the lower hybrid resonance, to get a converged solution across this resonance under the collisionless limits [Campos 2016]. At this moment, this method has only been proven to work efficiently for the fast wave. It may be still a promising method to tackle the slow wave, which causes the real problem. In this part of work, we only consider the case where the LH resonance locates below the straps, however, the same method can also be used to examine another extreme case when the strap is below the LH resonance and can excite directly the propagating slow wave. The 3D effect is not included in this part of work. The poloidal derivative is likely to play an important role in studying the density modification by ponderomotive forces and thus should be accounted in the wave coupling studies. Right now, we have the 3D RAPLICASOL available at hand, but running this code is highly

memory consuming. Finally, around the LH resonance, thermal effect become significant, one may thus also need to consider the finite Larmor radius corrections. These interesting topics are left for future studies.

In the current 2D SSWICH-FW code which we developed in the second part of this thesis, formulas of RF sheath capacitance and RF sheath rectification under tilted $\mathbf{B_0}$ took a simple extrapolation from the previous formula that are valid under non-tilted magnetic field configuration. These formulas will be updated when more fundamental physics on RF sheath studies get advanced. In Chapter 4, two different approaches were proposed to calculate the oscillating RF sheath voltage (V_{RF}). In our latest effort, the first method by integrating the tangential electric field to calculate V_{RF} is generalized by a spectral treatment. Throughout the code development, we spent a lot of time on deriving and implementing the second approach of V_{RF}. It is finally reserved as the secondary choice due to the numerical instability of the derivatives of the electric field at the sheath boundary. We speculate this is a numerical issue that is related to the compatibility of the asymptotic sheath boundary conditions with the setup of the finite element method used in COMSOL software. Using COMSOL allows us cutting down greatly the time we spent in the code development, but on the other hand, we are restricted from knowing and modifying the internal processing of the finite element solver. Another weakness of using COMSOL is the limited options for the boundary condition. In a home-made code based on the primary compiling language, i.e. FORTRAN, one can easily realize the DB boundary condition. But in COMSOL, it becomes tricky.

Another weakness of the current SSWICH-FW code is the use of the loosely constrained transport parameters. The scale of V_{DC} is still very sensitive to the value of the perpendicular conductivity. This problem exists already in the SSWICH-SW code and had been discussed extensively in the PhD thesis of Dr. Jacquot. At this moment, SSWICH-FW code takes similar V_{DC} model as the SW code, it thus inherits this weak point. The two ad hoc perpendicular conductivities still need to be determined more precisely from the edge turbulence analysis. Work has been started on this point [Tamain 2016], but unfortunately it was not completed before the end of this thesis.

In SSWICH-FW, the shape of geometry in the private SOL also matters. The magnitudes of V_{DC} and also the heat flux in the private SOL are sensitive to the modification of the geometry in the private SOL. The slow wave is generally believed to have a dominant contribution on V_{DC} in the private SOL. Probably due to the short wavelength of the slow wave, it was shown in the simulation that a modification of the geometry can affect the scale of V_{DC} (or heat flux) up to 30%. The next step will thus be to implement with more realistic curved components, especially in the private SOL region. Besides, in parallel to this thesis work, the 2D RAPLICASOL code has been extended to a cylindrical geometry in order to cover the full toroidal curvature of the Tokamak vessel wall and the antenna structure. A comparison of the RF near field calculated by this new 2D RAPLICASOL under the cylindrical geometry and the rectangular geometry [Jacquot 2015] shows the toroidal curvature is important for the amplitude of the parallel near field. In the future, SSWICH-FW will also have to include the toroidal curvature.

In Chapter 5, we found the 3D effects is important to evaluate the impact of the fast wave on V_{DC} excitation at the far SOL. The best way to count the 3D effect is of course to conduct a 3D simulation. In 3D, one can also have a realistic voltage excitation of the antenna. Unfortunately a full-3D SSWICH-FW simulation is presently out of reach, both by lack of appropriate formulation for the SBCs and due to the excessive memory requirements. The latter memory problem is obvious. For the former problem, we have made some progress, i.e. the formulation of the 3D sheath boundary condition (DB SBCs) has been tested

in free space but not in plasma yet. In theory, the secondary approach for V_{RF} works also in 3D if the derivative of the electric field gets numerically converged to the mesh size, but it remains to be tested numerically on a curved plane. The latest way of spectral treatment we found to include the 3D effect is so far the best method we can provide in the period of this thesis. This should be the prior point to improve the code in the future.

Our final goal with SSWICH is to implement a 3D realistic geometry, a full wave treatment and a 3D sheath boundary conditions. The 3D RAPLICASOL code solving full wave propagation without sheath is now available. It will replace the current RF module in the 3D version of SSWICH-FW code. In the future, SSWICH can work together with other codes to cover more physics. For example, the RF induced density modification and gas puffing are considered in the 3D edge transport code: the EMC3-Eirene code [Zhang 2016]. The V_{DC} map produced by 3D SSWICH-FW can be used as an input for the EMC3-Eirene code. The latter will then return a more self-consistent 3D density profile, which in turn can be imported into 3D SSWICH-FW code. These two codes can be solved iteratively until the numerical convergence is reached.

Last but not least, sputtering, heat loads and impurity radiations are among the direct consequences of the RF near field. At this stage, they are not modelled in the SSWICH, but we have shown in Chapter 5 how SSWICH results can be used to evaluate the heat flux. SSWICH-FW is an important step to model these physical processes. Studying experimentally the RF impacts on the impurity transport and radiation will be the topic of a new PhD. SSWICH-FW code could be used as a numerical tool for his thesis.

For the simulations of Aline plasma, we surely know that our work is just a start of the efforts towards a better understanding the properties of waves and sheath in a linear device. Modeling waves inside a cavity like Aline needs to introduce the collisions to act as a damping mechanism. Not surprisingly, the field structure in the simulation is very sensitive to the electron-neutral collision. The analytical equation proposed in Chabert's book is currently the best way to estimate this collision frequencies. Besides, an accurate density is also important to guarantee the simulation is comparable with the reality discharge. At this moment, the density profile used in the simulation is only inhomogeneous along the radial direction. To fully recover the toroidal variation shown in the experimental floating potential map, one must count the toroidal variation of the density.

This thesis is done within the context of nuclear fusion research, and especially dedicated to model the Tore Supra RF sheath. Tore Supra has nearly completed its upgrade to WEST and plans to launcher its first plasma by the end of this year. The 3D asymptotic SSWICH-SW code together with the field maps from TOPICA was used before to optimize the electric design of the FS of the new WEST antennas [Helou 2015]. The first of these antennas has now been delivered to CEA. In the future WEST experiment, if more simulations on the RF sheath are needed, the SSWICH-FW/RAPLICASOL can be a new choice.

Finally, SSWICH presents a methodology to model RF waves and sheath interactions. It has potential applications in the other research areas. For example, RF sheath is also present in the artificial satellites and spacecraft. The plasma in space can interacts with the satellites which uses the RF wave as information carrier. In the presence of SBC, SSWICH simulation has shown the sheath-plasma waves appears when the resonance condition [D'Ippolito 2008] fulfills. From an engineer's view, the metal-sheath-plasma region creates a waveguide where the surface waves (sheath-plasma wave) can propagate. The immediate result of these surface waves is that they make a significant contribution to the antenna impedance thus affect its performance [Laurin 1989]. Besides, they provide a mechanism for locally generated electromagnetic waves to propagate between widely separated points on large spacecraft.

These waves are likely to give rise to the electromagnetic interference problems if picked up by sensitive devices. SSWICH may help to understand these waves.

3. Proposals for the future experiments

One of the central question this thesis discussed is the role of the fast wave in RF/DC sheath excitation. With SSWICH, we have observed the FW-SW mode conversion, explored the properties of the fast wave induced far field sheath and investigated the impact of the fast wave on radial V_{DC} broadening, these features are yet to be proved through experiments. The role of the fast wave can be identified experimentally using $\dot{B}$ probe [D'Ippolito 2013]. It is a coil that measures the RF magnetic field traversing through it. By choosing the orientation correctly, it can be used to detect the time-varying of the parallel magnetic field and thus determine the transversal electric field which mainly comes from the fast wave. By comparing the fast wave component of the $\dot{B}$ probe signal with the strength of the measured plasma potential, one can find the correlation between these two quantities and then check which wave is dominant on RF sheath rectification both in the vicinity of wave launcher and at the far SOL boundaries. The other way to compare the impact of the fast wave and the slow wave on RF sheath is to excite these two waves one after the other and to see the evolution of the potential on the nearby material boundaries. To excite the slow wave on purpose maybe difficult to realize in Tokamak, but it is much easier to do in Aline. Aline device is meant to ease understanding of the RF sheath in Tokamaks. In the near future, a replacement of the current electrode is planned. It will have a similar strap antenna as in Tokamak. SSWICH-FW can provide numerical support for the design of this antenna. After the new strap antenna is installed in Aline, one can conveniently manipulate the strap orientations. For example, rotating the strap by 90°, the fast wave antenna becomes a slow wave antenna. A Faraday screen can be put in front of this strap to compare the strength of the plasma-wall interactions on the FS surface under two different strap orientations.

The spatial proximity effect has been justified by the experiments conducted in TS and AUG upgrades since it is proposed. It's generally known that the evanescent slow wave has this effect, while it is less clear whether the propagating wave or the fast wave also have this feature. We answered partially this question in the numerical test of chapter 5. At least in the Tore Supra configuration we found that the propagating fast wave does not have this feature. This result can be examined experimentally by moving radially the straps and comparing the magnitude of the electric field at the fast wave propagating region. One can further change the density to have an evanescent fast wave in the probe accessible region in Aline. Then play with the dissymmetrization experiments to see whether the evanescent fast wave has the spatial proximity effects.

Reference

[Campos-Pinto2016] M. Campos-Pinto and B. Després, "Constructive formulations of resonant Maxwell's equations", Hal Preprint online 2016, submitted to Siam J. Math. Anal.

[D'Ippolito 2008] D. A. D'Ippolito, J. R. Myra, E.F. Jaeger and L.A. Berry, "Far-field sheaths due to fast wave incident on material boundaries", Phys. Plasm. 15 (2008) 102501

[D'Ippolito 2013] D. A. D'Ippolito, J. R. Myra, R. Ochoukov and D. G. Whyte, "Modelling far-field radio-frequency sheaths in Alcator C-Mod", Plas. Phys, Cont. Fusion, **55** (2013) 085001

[Helou 2015] W. Helou, et.al, "Radio-frequency electrical design of the WEST long pulse and load-resilient ICRH launchers", Fusion. Eng. and Des, 96-97 (2015) 473-476

[Jacquot2015] J. Jacquot, V. Bobkov, L. Colas, S. Heuraux, Alena Křivská, L. Lu and J.-M. Noterdaeme, "Full wave propagation modelling in view to integrated ICRH wave coupling/RF sheaths modelling", Poster A-41, proc. 21st Conference on RF Power in Plasmas, Lake Arrowhead (California) 2015, AIP Conf. Proc. 1689, 050008-1 050008-4 (2015)

[Laurin 1989] J. J. Laurin, G. A. Morin and K. G. Balmain, "Sheath wave propagation in a magnetoplasma", v24, N3, p289, 1989

[Tamain2016] P. Tamain, C. Colin , L. Colas, C. Baudoin, G. Ciraolo, R. Futtersack, D. Galassi , Ph. Ghendrih, N. Nace, F. Schwander and E. Serre, "Numerical analysis of the impact of an RF sheath on the Scrape-Off Layer in 2D and 3D turbulence simulations", proc. 22nd International Conference on Plasma Surface Interations in Controlled Fusion Devices, Poster P.2.48 submitted to Nuclear Materials and Energy

[Zhang2016] W. Zhang, V. Bobkov, T. Lunt, J.-M. Noterdaeme, D. Coster, R. Bilato, P. Jacquet, D. Brida, Y. Feng and E.Wolfrum, "3D simulation of gas puff effects on edge density and ICRF coupling in ASDEX Upgrade", Nuclear fusion, **56**(3) 2016

A : Filamentary RF electric fields around straps in plasma-filled box as Slow Wave structures excited by poloidal RF currents

This Appendix proposes an explanation for the filamentary structures observed in simulated 2D RF field maps around poloidal current straps radiating in plasma-filled antenna box [Chapter 3][Lu 2016]. The qualitative phenomenology to be reproduced includes the following observations:

1°) "Filaments" appear mainly on the parallel and radial components of the RF electric field.

2°) Filaments feature small-scale radial structures in the immediate vicinity of the radiating straps.

3°) Filaments decrease in magnitude and change shape when the parallel dielectric constant of the medium is artificially increased in magnitude.

4°) Filaments are absent when the antenna box is in vacuum or more generally when it is filled with diagonal dielectric media.

5°) Filaments persist even when the confinement magnetic field is fully toroidal. For the sake of simplicity we will study this particular case.

Arguments 1—3 suggest that the filaments consist of highly evanescent Slow Wave electric fields. However a direct excitation of the Slow Wave by the poloidal RF currents imposed on the strap is counter-intuitive, particularly in situation 5. Besides, observation 4 demonstrates a role of the non-diagonal components in the dielectric tensor. These components are traditionally associated with the Fast Mode. Here we propose a simple semi-analytical theory for filament production by an infinitely thin poloidal current strap radiating in toroidally-bounded homogeneous gyrotropic medium with large but finite parallel conductivity. The conditions for exciting the Slow Wave are determined and compared to the phenomenology.

Monochromatic RF electric fields **E** oscillating as $\exp(+\mathrm{i}\omega_0 t)$ ("engineer convention") propagate according to the time-harmonic vectorial equation

$$\nabla \times \nabla \times \mathbf{E} - k_0^2 \boldsymbol{\varepsilon}\mathbf{E} = -\mathrm{i}\mu_0 \omega_0 \mathbf{j_{ant}} \quad (A.1)$$

In this equation $k_0 = \omega_0/c$ is the wavevector in vacuum, $\mathbf{j_{ant}}$ is an imposed current source, while the (normalized) dielectric tensor takes a gyrotropic form characteristic of cold magnetized plasmas [Stix 1992]. Using the COMSOL geometric conventions

$$\boldsymbol{\varepsilon} = \begin{bmatrix} \varepsilon_\perp & \mathrm{i}\varepsilon_\times & 0 \\ -\mathrm{i}\varepsilon_\times & \varepsilon_\perp & 0 \\ 0 & 0 & \varepsilon_{//} \end{bmatrix}\begin{matrix} y \\ z \\ x \end{matrix} \qquad (A.2)$$

In a loss-less medium the three Stix parameters $\varepsilon_\perp$, $\varepsilon_\times$ and $\varepsilon_{//}$ are real constants, and in magnetized plasmas $\varepsilon_{//}$ generally takes large negative values. When the medium is homogeneous, plane waves oscillating as $\exp(+i\omega_0 t - ik_0(n_{//}x + n_\perp y))$ are allowed to propagate. In Fourier space equation (A.1) becomes ([Stix 1992] with "engineer conventions")

$$k_0^2 \mathbf{K}\hat{\mathbf{E}} = i\mu_0\omega_0\hat{\mathbf{j}}_{\mathbf{ant}} \quad ; \quad \mathbf{K} = \begin{bmatrix} \varepsilon_\perp - n_{//}^2 & i\varepsilon_\times & n_{//}n_\perp \\ -i\varepsilon_\times & \varepsilon_\perp - n^2 & 0 \\ n_{//}n_\perp & 0 & \varepsilon_{//} - n_\perp^2 \end{bmatrix} \begin{matrix} y \\ z \\ x \end{matrix} \quad (A.3)$$

For given parallel refractive index $n_{//}$ the perpendicular refractive indices $n_\perp$ and the electric field polarisations are respectively the solutions of det($\mathbf{K}$)=0 and the associated eigenvectors. In gyrotropic media two modes can exist: the Fast Wave and the Slow Wave. In this note we use the simplified dispersion relations valid for large negative $\varepsilon_{//}$ far from the Lower Hybrid resonance $\varepsilon_\perp = 0$. However we retain the full wave polarizations, because they play a key role in filament excitation. The simplified formulas are also valid for any value of $\varepsilon_{//}$ when $\varepsilon_\times = 0$, i.e. in uniaxial media. The Fast Wave refractive index is given by equation (see also [Stix 1992], or [Brambilla1998], eq. (22.4))

$$n_{\perp F}^2 = \varepsilon_\perp - n_{//}^2 - \frac{\varepsilon_\times^2}{\varepsilon_\perp - n_{//}^2} \qquad (A.4)$$

The associated (approximate) polarization is ([Brambilla1998], eq. (22.13), with "engineer convention")

$$E_{yF} \approx -\frac{i\varepsilon_\times}{\varepsilon_\perp - n_{//}^2}E_{zF} \quad ; \quad E_{xF} \approx -\frac{n_{\perp F}n_{//}}{\varepsilon_{//} - n_{\perp F}^2}E_{yF} = \frac{i\varepsilon_\times n_{\perp F}n_{//}}{\left(\varepsilon_\perp - n_{//}^2\right)\left(\varepsilon_{//} - n_{\perp F}^2\right)}E_{zF} = P_F\left(n_{\perp F}\right)E_{zF} \quad (A.5)$$

For large $|\varepsilon_{//}|$, the Fast Wave electric field is nearly transverse to the confinement magnetic field. Yet for finite parallel conductivity and in presence of gyrotropy ($\varepsilon_\times \neq 0$) the Fast Wave carries a small E_x component. The Slow Wave refractive index is given by equation (see also ([Brambilla1998], eq. (22.5)).

$$n_{\perp S}^2 = P\left(1 - n_{//}^2 / S\right) \qquad (A.6)$$

The associated (approximate) polarization is ([Brambilla1998], eq. (22.14))

$$E_{yS} = -\frac{n_{\perp S}n_{//}}{\varepsilon_\perp - n_{//}^2}E_{xS} \quad ; \quad E_{zS} \approx -\frac{i\varepsilon_\times}{n_{\perp S}^2}E_{yS} \approx \frac{i\varepsilon_\times n_{//}}{n_{\perp S}\left(\varepsilon_\perp - n_{//}^2\right)}E_{xS} = P_S^{-1}\left(n_{\perp S}\right)E_{xS} \quad (A.7)$$

The radiated Slow Wave electric field is nearly transverse to the ignorable direction z. Yet for finite parallel conductivity and in presence of gyrotropy the Slow Wave carries a small E_z component. For $n_{//}^2 \gg |\varepsilon_\perp|$, the first equation of (A.7) reduces to $\left|\frac{E_y}{E_x}\right| \sim \sqrt{|\varepsilon_{//}/\varepsilon_\perp|}$. We now investigate wave excitation by an infinitely thin poloidal current sheet located in $y=0$, i.e. in equation (A.1) we impose

$$\mathbf{j}_{\mathbf{ant}}\left(x, y, z\right) = j_{zant}\left(n_{//}\right)\delta\left(y\right)\exp\left(i\omega_0 t - ik_0 n_{//}x\right)\mathbf{e_z} \qquad (A.8)$$

For simplicity we assume radiating boundary conditions both towards large positive y and large negative y. To incorporate a metallic wall at the back of the antenna box, one can use *a posteriori* the method of images. Under radiating conditions, the poloidal and parallel RF electric fields take the simple form:

$$E_z\left(n_{//}, y\right) = E_{zF}\left(n_{//}\right)\exp\left(-ik_0 n_{\perp F}|y|\right) + E_{zS}\left(n_{//}\right)\exp\left(-ik_0 n_{\perp S}|y|\right) \qquad (A.9)$$

$$E_x(n_{//}, y) = \text{sgn}(y)\left[P_F(+n_{\perp F})E_{zF}(n_{//})\exp(-ik_0n_{\perp F}|y|) + P_S(+n_{\perp S})E_{zS}(n_{//})\exp(-ik_0n_{\perp S}|y|)\right] \quad \text{(A.10)}$$

In these expressions either Re($n_\perp$)>0 (outgoing waves) or Im($n_\perp$)<0 (evanescent waves). In expression (A.10) sgn(y) appears since both $P_F(n_{\perp F})$ and $P_S(n_{\perp S})$ change signs when $n_\perp$ is reversed (see equation (A.5) and (A.7)). At the current sheet, we enforce the continuity of the parallel RF electric field as well as

$$\left(\partial_y E_z\right)_{y=0^+} - \left(\partial_y E_z\right)_{y=0^-} = i\mu_0\omega_0 j_{zant}(n_{//}) \quad \text{(A.11)}$$

This yields

$$P_F(+n_{\perp F})E_{zF}(n_{//}) + P_S(+n_{\perp S})E_{zS}(n_{//}) = 0 \quad \text{(A.12)}$$

$$n_{\perp F}E_{zF}(n_{//}) + n_{\perp S}E_{zS}(n_{//}) = -\frac{\mu_0 c}{2}j_{zant}(n_{//}) \quad \text{(A.13)}$$

Whence the amplitude of the Slow Wave poloidal RF field.

$$E_{zS}(n_{//}) = \frac{\mu_0 c P_F j_{zant}(n_{//})}{2(n_{\perp F}P_S - n_{\perp S}P_F)} \quad \text{(A.14)}$$

Formula (A.14) shows that poloidal RF currents can excite the Slow mode. The qualitative explanation is as follows. Poloidal currents produce RF electric fields oriented in the poloidal direction (equation (A.11)), i.e. preferentially excite the Fast wave. But the Fast mode can in turn generate a small parallel electric field. To cancel this field at the current sheet it is necessary to produce a Slow Wave component. From equation (A.12) $E_{zS}(n_{//})$=0 if P_F=0, i.e. for example if $\varepsilon_\times/\varepsilon_{//} = 0$. In other words the Slow Wave appears only in gyrotropic media with finite parallel conductivity, consistent with observations 3 and 4. Besides $n_{//}\neq 0$ is also required.

Figures A.1.a) – 1.d) illustrate the RF electric fields produced by an infinitely thin current strap radiating in a typical plasma found in the box. For these conditions all the Fast Wave modes and the Slow Wave modes of the box are evanescent, but the Slow Wave disappears over a smaller radial distance. In these conditions the radial RF field is in phase with the RF current, while the poloidal and parallel RF fields are in phase quadrature. Small-scale features, of millimetric radial extension, appear mainly in the map radial electric field, but are hardly visible for the poloidal electric field, consistent with observations 1 and 2. Across the strap, the parallel electric field swaps signs. This change is continuous but occurs over a small radial width of the same order as for the radial field. Although their spatial structures are different, the ratio of typical amplitudes for the radial and parallel electric fields is $\left|\frac{E_y}{E_x}\right| \sim \sqrt{|\varepsilon_{//}/\varepsilon_\perp|}$. Since the Fast and Slow waves can be explicitly separated in our model, we verify that the small-scale features are associated with the Slow mode. This is illustrated on *Figures A.*1.b) for the parallel electric field. Away from the strap, only the Fast Wave components of the RF fields persist.
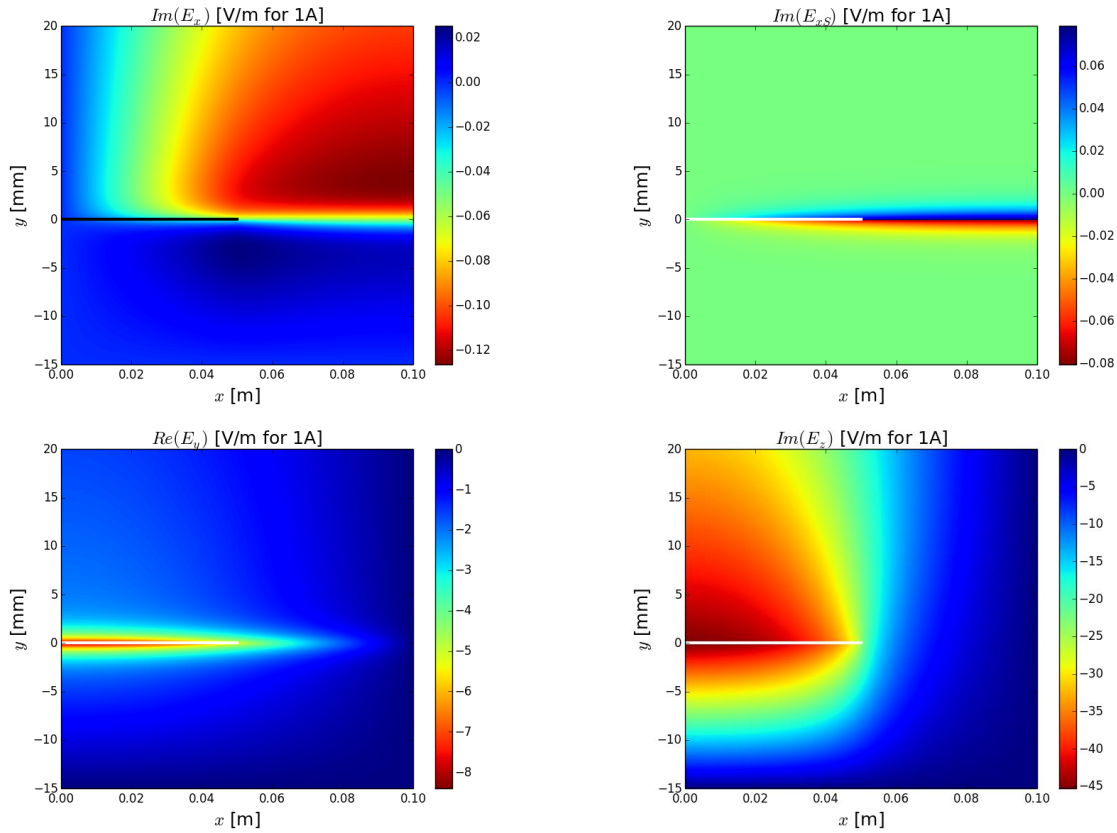
Figures A.1. 2D (toroidal/radial) maps of RF electric fields produced by an infinitely thin current strap of parallel extension l//=0.1m. The strap is fed with 1A of current distributed regularly over the strap width. The strap is enclosed in a metallic box of parallel extent L//=0.2m, with a metallic wall at y=-15mm. The box is filled with homogeneous plasma of dielectric constants $\varepsilon_{//} = -15290$, $\varepsilon_{\perp} = -3.787$, $\varepsilon_{\times} = 13.17$. a) Imaginary part of parallel RF electric field, b) idem, slow wave contribution, c) Real part of radial RF electric field, d) Imaginary part of poloidal electric field. Thick horizontal lines : sketch of strap. Only half of the box is represented. Toroidal symmetry relations: Ex(-x,y)=-Ex(x,y) ; Ey(-x,y)=+Ey(x,y) ; Ez(-x,y)=+Ez(x,y).

Figures A.2 illustrate how the near field patterns evolve when the parallel dielectric constant is divided by ten compared to *Figures A.1*. The poloidal electric field is hardly modified, consistent with the expected properties of the Fast Wave. The parallel electric fields increase in magnitude as $\sim|\varepsilon_{//}|$, while the amplitude small-scale radial fields scales as $\sim\sqrt{|\varepsilon_{//}|}$. The shape of the parallel electric field pattern hardly evolves, except close to the strap. The filamentary structures become wider radially, by an approximate factor $\sqrt{|\varepsilon_{//}|}$.

Going beyond the qualitative observations 1—5 is challenging, because the spatial pattern of Slow Wave fields likely depends on the detailed spatial distribution of strap RF currents. In our simple 2D model the strap is reduced to an imposed current sheet homogeneous in the ignorable direction. In more refined 3D models the strap is thick, the distribution of RF currents should depend on the poloidal coordinate and should be determined self-consistently.
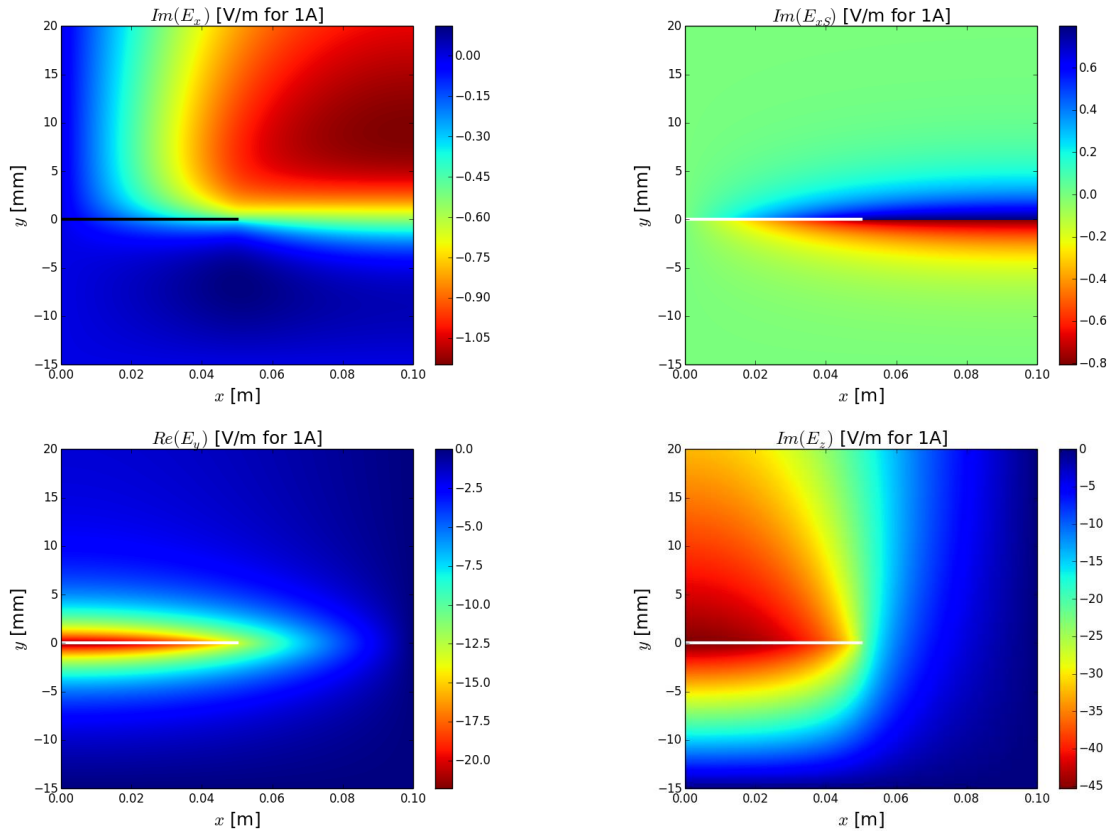
Figures A.2. Same as figures A.1, with parallel dielectric constant $\varepsilon_{//} = -1529$

B : Vector analysis using 2D curved coordinates

Let us consider a 1D curve drawn on a 2D Cartesian plane and scalar or vector fields in the vicinity of the curve. The present note aims at expressing the standard operators of vector analysis (gradient, divergence, rotational, Laplacian) in the vicinity of this 2D curve, using two "local coordinates" related to the curve, namely an arc length along the curve and an extra coordinate normal to the curve, together with field derivatives "tangential" and "normal" to the curve. A prerequisite towards this goal is to properly define these "local coordinates" as well as the tangential and normal derivatives, for points lying on the curve or located in its immediate vicinity. Some necessary conditions on the smoothness of the curve and its curvature are outlined, in order to be able to build the local coordinates.

Tangential, normal vectors and radius of curvature for a 1D curve in a 2D Cartesian plane.

Our working objects are a 2D Cartesian plane (x,y), a third out-of-plane direction z, as well as a 1D parametrized curve $C(x(t),y(t))$ drawn in the 2D plane. We assume that coordinates $x(t)$ and $y(t)$ have at least first and second order derivatives with respect to parameter t. The main notations and conventions associated with curve C are summarized on *Figure B.1*.
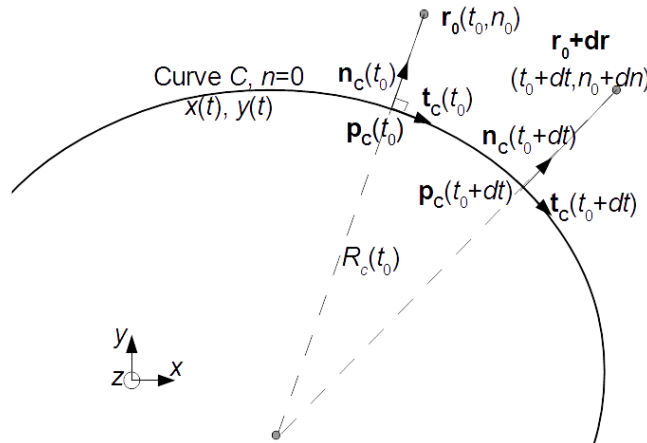
Figure B.1: Main conventions and notations adopted in the note.

Without loss of generality, parameter t can be taken as an arc length or curvilinear abscissa, i.e.

$$dx^2 + dy^2 = dt^2 \text{ for elementary displacements along the curve (B.1)}$$

In every point of curve C one can define a tangent vector $\mathbf{t_C}(t)$ as:

$$\mathbf{t_C}(t) = \left(\frac{\partial \mathbf{r}}{\partial t}\right)_C = \begin{bmatrix} (\partial x/\partial t)_C \\ (\partial y/\partial t)_C \end{bmatrix} \tag{B.2}$$

Here subscript C denotes displacements along curve C. Since t is an arc length, $\mathbf{t_C}(t)$ is a unit vector. One can also define a unit vector $\mathbf{n_C}(t)$ normal to the curve in the 2D plane as:

$$\mathbf{n_C}(t) = \mathbf{e_z} \times \mathbf{t_C}(t) \tag{B.3}$$

Where $\mathbf{e_z}$ is the unit vector in the out-of-plane direction z (independent of t). While the amplitude of $\mathbf{t_C}(t)$ is always 1, in the most general case the direction of this vector depends on arc length t, so that one can define a derivative $(\partial\mathbf{t_C}/\partial t)_C$. Since $\mathbf{t_C}$ is a unit vector one has

$$\mathbf{t_C}\cdot\left(\frac{\partial\mathbf{t_C}}{\partial t}\right)_C = \frac{1}{2}\left(\frac{\partial\mathbf{t_C}\cdot\mathbf{t_C}}{\partial t}\right)_C = 0 \tag{B.4}$$

Since $\mathbf{e_z}\cdot\mathbf{t_C}=0$, $\mathbf{e_z}\cdot(\partial\mathbf{t_C}/\partial t)_C = 0$, and consequently $(\partial\mathbf{t_C}/\partial t)_C$ is parallel to $\mathbf{n_C}(t)$

$$\left(\frac{\partial\mathbf{t_C}}{\partial t}\right)_C = -\frac{\mathbf{n_C}(t)}{R_c(t)} \tag{B.5}$$

$R_c(t)$ is an (algebraic) local radius of curvature for curve C in point t. Similarly from the definition (B.3) of the normal vector

$$\left(\frac{\partial\mathbf{n_C}}{\partial t}\right)_C = +\frac{\mathbf{t_C}(t)}{R_c(t)} \tag{B.6}$$

Tangential and normal coordinates in the vicinity of a 1D curve in a 2D Cartesian plane.

To locate a point on curve C, one single coordinate t is necessary. However two coordinates are necessary to place a point in the 2D plane (x,y). This 2D extension is necessary to define scalar and vector fields and their differential operators in the vicinity of curve C. One would therefore like to build a local system of two coordinates (t,n) such that:

- The arc length t on curve C is the first coordinate.
- n is constant on curve C, and without loss of generality, one can choose $n=0$ on C.
- For easier use the system of coordinates is orthogonal, i.e. $(\partial\mathbf{r}/\partial t)\cdot(\partial\mathbf{r}/\partial n) = 0$ everywhere. Note that here the subscript C has been dropped, since displacements are not restricted to curve C any more. Orthonormality of the coordinate system is not requested.

The choice for the set of local coordinates (t,n) is not unique. To define one such set one can proceed as follows. Given any point $\mathbf{r_0}(x_0,y_0)$ in the vicinity of C there exists a "closest point" $\mathbf{p_C}(x(t_0),y(t_0))$ on curve C whose distance to $\mathbf{r_0}$ is minimal. This requirement defines the first coordinate t_0. This definition is non-ambiguous if point $\mathbf{p_C}(t_0)$ is unique. Unicity can be a difficult issue. It is briefly discussed below and it is postulated for the moment. Let us call $\mathbf{p_C}(t_0)$ the "projection" of $\mathbf{r_0}$ onto curve C. If we exclude the extremities of curve C (another potential source of difficulty…) the definition of $\mathbf{p_C}(t_0)$ as "closest" point yields

$$\frac{\partial.}{\partial t}[\mathbf{r_0} - \mathbf{p_C}(t)]_C^2 = 2(\mathbf{r_0} - \mathbf{p_C}(t_0))\cdot\mathbf{t_C}(t_0) = 0 \tag{B.7}$$

i.e. the projection is locally normal to curve C. Consequently $\mathbf{r_0}$ writes

$$\mathbf{r_0} = \mathbf{p_C}(t_0) + n_0\mathbf{n_C}(t_0) \tag{B.8}$$

This relation defines the second coordinate n_0, whose physical meaning is an algebraic (closest) distance of point $\mathbf{r_0}$ to curve C. If $\mathbf{r_0}$ lies on curve C, it coincides with $\mathbf{p_C}(t_0)$ and $n_0=0$, as requested. While coordinates (x_0,y_0) are relatively easy to obtain as a function of (t_0,n_0), the opposite transformation is generally delicate. But only the forward formulas are necessary to express the differential operators of field calculus. Let us now consider two neighboring points $\mathbf{r_0}$ and $\mathbf{r_0}+\mathbf{dr}$ not necessarily located on curve C. $\mathbf{dr}$ can be expressed as

$$\mathbf{dr} = \mathbf{p_C}(t_0 + dt) - \mathbf{p_C}(t_0) + (n_0 + dn)\mathbf{n_C}(t_0 + dt) - n_0\mathbf{n_C}(t_0) \tag{B.9}$$

Retaining only first order quantities yields

$$\mathbf{dr} = \left(1 + \frac{n_0}{R_c(t_0)}\right)\mathbf{t_C}(t_0)dt + \mathbf{n_C}(t_0)dn \qquad\qquad (B.10)$$

One can therefore define local partial derivatives (tangential and normal) in every point $\mathbf{r_0}$ as an extension of the partial derivatives on C.

$$\frac{\partial \mathbf{r}}{\partial t}(t_0, n_0) = \left(1 + \frac{n_0}{R_c(t_0)}\right)\mathbf{t_C}(t_0) \qquad\qquad (B.11a)$$

$$\frac{\partial \mathbf{r}}{\partial n}(t_0, n_0) = \mathbf{n_C}(t_0) \qquad\qquad (B.11b)$$

as well as the local metric

$$ds^2 = \left(1 + \frac{n_0}{R_c(t_0)}\right)^2 dt^2 + dn^2 = h_t^2 dt^2 + h_n^2 dn^2 = ds_t^2 + ds_n^2 \quad (B.12)$$

Inverting relation (B.10) one also gets

$$\nabla t(t_0, n_0) = \frac{\mathbf{t_C}(t_0)}{1 + n_0/R_c} \qquad\qquad (B.13a)$$

$$\nabla n(t_0, n_0) = \mathbf{n_C}(t_0) \qquad\qquad (B.13a)$$

From equation (B.11) $(\partial \mathbf{r}/\partial t).(\partial \mathbf{r}/\partial n) = 0$, i.e. the coordinate system is orthogonal, as requested. For points $\mathbf{r_0}$ on curve C, $n_0=0$ and $(\partial \mathbf{r}/\partial t)$ coincides with $(\partial \mathbf{r}/\partial t)_C$. On the curves n_0=constant, coordinate t generally does NOT represent an arc length. Provided that the normal vector $\mathbf{n_C}(t_0)$ can be properly defined, the normal derivative is always well-behaved, i.e. $h_n>0$. This is not true for the tangential derivative: even if the tangential vector $\mathbf{t_C}(t_0)$ can be properly defined, an additional requirement for $h_t>0$ is that $n_0>-R_c(t_0)$ if $R_c(t_0)>0$, or $n_0<-R_c(t_0)$ if $R_c(t_0)<0$. Associated with the critical normal distance $n_0=-R_c(t_0)$ is a loss of unicity for the point $\mathbf{p_C}(t_0)$ "closest" to $\mathbf{r_0}$. Indeed, as sketched on *Figure B.1*, multiple projections mean $\mathbf{dr}$=0 for non-zero dt in equation (B.10), which is possible if $n_0=-R_c(t_0)$.

The local radius of curvature of curve $n=n_0$ in point $\mathbf{r_0}$ is calculated from

$$\left(\frac{\partial \mathbf{t_C}}{\partial s}\right)_{n=n_0} = -\frac{\mathbf{n_C}(t_0)}{n_0 + R_c(t_0)} \qquad\qquad (B.14)$$

Near the critical point it becomes null, preventing a clear definition of a local tangent.

If $|R_c(t_0)| \geq R_0 > 0$ for every point on curve C, then one can always define the local system of coordinates (t, n) in a neighborhood of curve C small enough such that $|n_0| < R_0$. This justifies the term "local" system of coordinates. Simple examples of the above procedure are

Straight line $y=0$

For this trivial example $t=x$, $n=y$, $R_c(t) \rightarrow \infty$, the system of coordinates can be extended throughout the 2D plane.

Circle $x^2+y^2=r_0^2$

Using the standard polar coordinates (r, θ) one can choose $t=-r_0\theta$, $n=r-r_0$, $R_c(t)=r_0$, $R_c(t)+n=r$. The system of coordinates is meaningful if $r \geq 0$ or $n \geq -r_0$.

Finally *Figure B.2* illustrates a less trivial example of coordinates built from a parabola. Near the summit of the parabola, a singularity appears in the coordinate system when *n* becomes too positive, preventing its extension to the whole 2D plane.
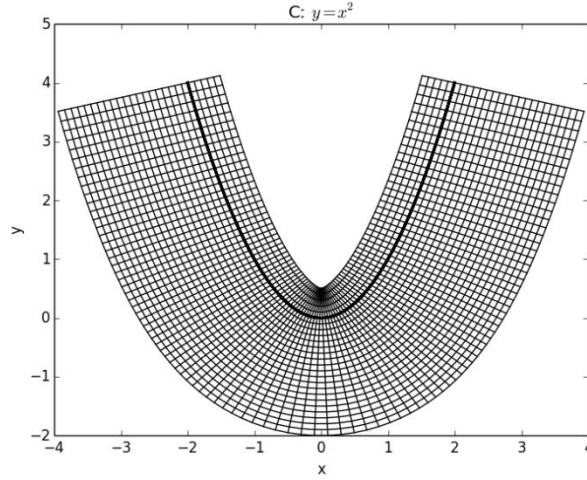

Figure B.2: local orthogonal coordinate system built from parabola C: y=x² (shown as bold curve)

Vector analysis using local coordinates.

With the newly defined local coordinate system (*t,n*) in the 2D plane (*x,y*), complemented with the usual out-of-plane coordinate *z*, one can express the standard differential operators of mathematical physics in 3D using standard tools from textbooks (e.g. [Angot1972]). As particular examples, the obtained formulas include Cartesian and cylindrical geometries.

Gradient of a scalar field

We envisage a scalar field $F(\mathbf{r})=F(x,y,z)=F(t,n,z)$ defined in 3D, in the vicinity of curve *C* for (*t,n*), as well as its partial derivatives with respect to all coordinates. The metric element associated to *z* is $h_z=1$. The gradient of ∇F in point $\mathbf{r_0}$ is such that, for infinitesimal displacement $\mathbf{dr}$

$$F(\mathbf{r_0} + \mathbf{dr}) = F(\mathbf{r_0}) + dF = F(\mathbf{r_0} + \mathbf{dr}) + \mathbf{dr}.\nabla F(\mathbf{r_0}) \qquad (B.15)$$

Vector $\nabla F(\mathbf{r_0})$ has components along tangent, normal and out-of-plane directions

$$\nabla F(\mathbf{r_0}) = [\nabla F(\mathbf{r_0})]_t \mathbf{t_c}(t_0) + [\nabla F(\mathbf{r_0})]_n \mathbf{n_c}(t_0) + [\nabla F(\mathbf{r_0})]_z \mathbf{e_z} \qquad (B.16)$$

Combining (B.15) and (B.16) with expression (B.10) for $\mathbf{dr}$ the components of the gradient write

$$[\nabla F(\mathbf{r_0})]_t = \frac{1}{h_t}\frac{\partial F}{\partial t} = \frac{1}{1+n_0/R_c(t_0)}\frac{\partial F}{\partial t} \qquad (B.17a)$$

$$[\nabla F(\mathbf{r_0})]_n = \frac{1}{h_n}\frac{\partial F}{\partial n} = \frac{\partial F}{\partial n} \qquad (B.17b)$$

$$[\nabla F(\mathbf{r_0})]_z = \frac{1}{h_z}\frac{\partial F}{\partial z} = \frac{\partial F}{\partial z} \qquad (B.17c)$$

Divergence and Rotational of a vector field

We now introduce a vector field $\mathbf{V}(\mathbf{r})=\mathbf{V}(x,y,z)=\mathbf{V}(t,n,z)$ defined in the vicinity of curve *C*, as well as its partial derivatives with respect to all coordinates. The tangential and normal components of **V** are defined

as their projections in the local tangent and normal directions $V_t(t_0,n_0,z_0)=\mathbf{V}(t_0,n_0,z_0).\mathbf{t_c}(t_0)$ and $V_n(t_0,n_0,z_0)=\mathbf{V}(t_0,n_0,z_0).\mathbf{n_c}(t_0)$. For the sake of completeness, we also assume that $\mathbf{V}(t_0,n_0,z_0)$ has a component $V_z(t_0,n_0,z_0)$ in the out-of-plane direction z. Using these components the local divergence of vector field **V** is defined as [Angot1972]

$$\text{div}(\mathbf{V}) = \frac{1}{h_t h_n h_z}\left[\frac{\partial h_n h_z V_t}{\partial t} + \frac{\partial h_z h_t V_n}{\partial n} + \frac{\partial h_t h_n V_z}{\partial z}\right] \tag{B.18}$$

$$\text{div}(\mathbf{V}) = \frac{1}{1+n_0/R_c(t_0)}\frac{\partial V_t}{\partial t} + \frac{\partial V_n}{\partial n} + \frac{V_n}{R_c(t_0)+n_0} + \frac{\partial V_z}{\partial z} \tag{B.19}$$

The 3 components of **rot(V)** are defined in 2D as [Angot1972]

$$[\mathbf{rot}(\mathbf{V})]_t = \frac{1}{h_n h_z}\left[\frac{\partial h_z V_z}{\partial n} - \frac{\partial h_n V_n}{\partial z}\right] = \frac{\partial V_z}{\partial n} - \frac{\partial V_n}{\partial z} \tag{B.20a}$$

$$[\mathbf{rot}(\mathbf{V})]_n = \frac{1}{h_z h_t}\left[\frac{\partial h_t V_t}{\partial z} - \frac{\partial h_z V_z}{\partial t}\right] = \frac{\partial V_t}{\partial z} - \frac{1}{1+n_0/R_c(t_0)}\frac{\partial V_z}{\partial t} \tag{B.20b}$$

$$[\mathbf{rot}(\mathbf{V})]_z = \frac{1}{h_t h_n}\left[\frac{\partial h_n V_n}{\partial t} - \frac{\partial h_t V_t}{\partial n}\right] = \frac{1}{1+n_0/R_c(t_0)}\frac{\partial V_n}{\partial t} - \frac{\partial V_t}{\partial n} - \frac{V_t}{R_c(t_0)+n_0} \tag{B.20c}$$

Laplacian of a scalar field

Combining the above results yields a formula for the Laplace operator of the scalar function $F(t,n,z)$ [Angot1972]

$$\Delta F = \frac{1}{h_t h_n h_z}\left[\frac{\partial.}{\partial t}\left(\frac{h_n h_z}{h_t}\frac{\partial F}{\partial t}\right) + \frac{\partial.}{\partial n}\left(\frac{h_z h_t}{h_n}\frac{\partial F}{\partial n}\right) + \frac{\partial.}{\partial z}\left(\frac{h_t h_n}{h_z}\frac{\partial F}{\partial z}\right)\right] \tag{B.21}$$

Or

$$\Delta F = \frac{1}{[1+n_0/R_c(t_0)]^2}\frac{\partial^2 F}{\partial t^2} + \frac{n_0 R_c(t_0)}{[R_c(t_0)+n_0]^3}\frac{\partial R_c}{\partial t}(t_0)\frac{\partial F}{\partial t} + \frac{\partial^2 F}{\partial n^2} + \frac{1}{R_c(t_0)+n_0}\frac{\partial F}{\partial n} + \frac{\partial^2 F}{\partial z^2} \tag{B.22}$$

In this last formula the tangent derivative of the radius of curvature enters into account, except on the curve itself (n_0=0).

C : Implement the alternative approach to solve the oscillating sheath voltage along a curve

I. Implementing equation (4.19) using COMSOL boundary PDE

The goal of this Appendix is to show how to compile Eq. (4.19) in COMSOL. Eq. (4.19) reads,

$$A_{11}\frac{\partial}{\partial s}(\frac{\partial V_{RF}}{\partial s})+(\frac{\partial A_{11}}{\partial s}+\frac{A_{21}}{R})\cdot\frac{\partial V_{RF}}{\partial s}=\frac{\partial}{\partial s}(A_{12}E_n)+\frac{\partial}{\partial n}(A_{21}E_s+A_{22}E_n+A_{23}E_z)+\frac{A_{22}E_n}{R_c} \text{ (C.1)}$$

It can be embedded into the coefficient form of boundary PDE in COMSOL, which reads [COMSOL 2012]

$$\nabla\cdot\left(-\mathbf{c}\nabla V-\boldsymbol{\alpha}V+\boldsymbol{\gamma}\right)+\boldsymbol{\beta}\cdot\nabla V+aV=f \text{ (C.2)}$$

Here, V is an unknown scalar representing the sheath voltage, $\mathbf{c}$ is a matrix, $\boldsymbol{\alpha}$, $\boldsymbol{\beta}$ and $\boldsymbol{\gamma}$ are vectors, a is a scalar, f is a source term. $\nabla=\left(\dfrac{\partial}{\partial x},\dfrac{\partial}{\partial y}\right)$ is by default defined in the Cartesian coordinate.

If equation (C.2) is solved along 1D curve, we have proved that it can be re-formulated as an ordinary differential equation defined in the curvilinear coordinate.

$$\frac{d.}{ds}\left(-c(s)\frac{du}{ds}-\alpha(s)u+\gamma(s)\right)+\beta(s)\frac{du}{ds}+a(s)u=f(s) \qquad \text{(C.3)}$$

$$c(s)\equiv\vec{e}_t.c\vec{e}_t \quad ; \quad \alpha(s)\equiv\vec{e}_t.\boldsymbol{\alpha} \quad ; \quad \gamma(s)\equiv\vec{e}_t.\boldsymbol{\gamma} \quad ; \quad \beta(s)\equiv\vec{e}_t.\boldsymbol{\beta}$$

with

$$\mathbf{c}=c(s)\begin{bmatrix}tx^2 & tx\cdot ty\\ tx\cdot ty & ty^2\end{bmatrix} \quad ; \quad \boldsymbol{\alpha}=\alpha(s)\vec{e}_t=\alpha(s)\begin{bmatrix}tx\\ ty\end{bmatrix}$$

$$\boldsymbol{\beta}=\beta(s)\vec{e}_t=\beta(s)\begin{bmatrix}tx\\ ty\end{bmatrix} \quad ; \quad \boldsymbol{\gamma}=\gamma(s)\vec{e}_t=\gamma(s)\begin{bmatrix}tx\\ ty\end{bmatrix} \qquad \text{(C.4)}$$

Compare equation C.1, it's easy to see

$$c(s)=-A_{11}, \quad \beta(s)=\frac{A_{21}}{R_c} \text{ (C.5)}$$

While the others coefficient $\alpha(s)$, $\gamma(s)$ are zeros. Note the Right-Hand side (HRS) of equation (C.1) has three items. The first term can be extended as,

$$\frac{\partial}{\partial s}(A_{12}E_n)=E_n(ty\frac{\partial tx}{\partial s}(\varepsilon_{22}-\varepsilon_{11})+tx\frac{\partial ty}{\partial s}(\varepsilon_{22}-\varepsilon_{11})+tx\cdot ty^2\frac{\partial}{\partial y}(\varepsilon_{22}-\varepsilon_{11})-ty\frac{\partial\varepsilon_{21}}{\partial y})$$

$$+A_{12}(\frac{\partial nx}{\partial s}E_x+\frac{\partial ny}{\partial s}E_y+nx\cdot txE_{xx}+nx\cdot tyE_{xy}+ny\cdot txE_{yx}+ny\cdot tyE_{yy}) \qquad \text{(C.6)}$$

Where $E_{ij} = \dfrac{\partial E_i}{\partial j}$ $i, j = x, y$ are used in COMSOL. In the derivation of C.6, we have used the chain rule

for the derivatives of electric fields and dielectric tensor: $\dfrac{\partial}{\partial s} = tx\dfrac{\partial}{\partial x} + ty\dfrac{\partial}{\partial y}$ and the fact that partial

derivatives of dielectric tensor w.r.t x are zero. For the tangential derivatives of the normal/tangential vector, COMSOL provides two build-in operators to calculate them,

$$\mathrm{dtang}(tx, y) = ty\frac{\partial tx}{\partial s}, \quad \mathrm{dtang}(ty, x) = tx\frac{\partial ty}{\partial s} \quad (C.7)$$

So the partial derivatives of the normal/tangential vector can be avoided by using 'dtang' operator, for example,

$$
A_{12}(\frac{\partial nx}{\partial s}E_x + \frac{\partial ny}{\partial s}E_y) = (-tx\cdot\mathrm{dtang}(ty, y)(\varepsilon_{22} - \varepsilon_{11}) + \varepsilon_{21}(tx\cdot\mathrm{dtang}(ty, x) + ty\cdot\mathrm{dtang}(ty, y)))E_x
$$
$$
+(ty\cdot\mathrm{dtang}(tx, x)(\varepsilon_{22} - \varepsilon_{11}) - \varepsilon_{21}(tx\cdot\mathrm{dtang}(tx, x) + ty\cdot\mathrm{dtang}(tx, y)))E_y
$$
(C.8)

The second term of C.1 can be calculated as,

$$
\frac{\partial}{\partial n}(A_{21}E_s + A_{22}E_n + A_{23}E_z) = (A_{21}\cdot tx + A_{22}\cdot nx)(nx\cdot E_{xx} + ny\cdot E_{xy}) + (A_{21}\cdot ty + A_{22}\cdot ny)(nx\cdot E_{yx} + ny\cdot E_{yy})
$$
$$
+A_{23}(nx\cdot E_{zx} + ny\cdot E_{zy}) + E_s(tx\cdot ty\cdot ny\frac{\partial(\varepsilon_{22} - \varepsilon_{11})}{\partial y} + ny\frac{\partial\varepsilon_{21}}{\partial y}) + E_n(nx^2\cdot ny\frac{\partial\varepsilon_{11}}{\partial y} + ny^3\frac{\partial\varepsilon_{22}}{\partial y})
$$
(C.9)

where the chain rule is used, $\dfrac{\partial}{\partial n} = nx\dfrac{\partial}{\partial x} + ny\dfrac{\partial}{\partial y}$ and the simplification Ez=0 at curve. Finally the third

term of C.1,

$$\frac{A_{22}E_n}{R_c} = -A_{22}E_n\,\mathrm{curv} \quad (C.10)$$

Where build-in operator 'curv' is used, R$_c$=-1/curv. So the equation C.1 becomes

$$\frac{d}{ds}(A_{11}\frac{dV_{RF}}{ds}) + \frac{A_{21}}{R_c}\frac{dV_{RF}}{ds} = \text{ Eq. (C.6)+ Eq. (C.9)+ Eq.(C.10)} \quad (C.11)$$

II.   Calculate partial derivatives of normal/tangential vector components defined in a 2D domain

This section shows how to calculate partial derivative of *nx or ny* with respect to x, y, as like they are defined in the domain instead of on the curve only. This method can avoid using 'dtang' operator.

Starting from definition $n_x = \mathbf{n.e_x}$ and performing partial derivation we have in the vicinity of curve C[x(s),y(s)].

Expanding usual derivative dx and dy in curvilinear coordinate, one gets the following relation

$$
\begin{pmatrix} dx \\ dy \end{pmatrix} = \begin{pmatrix} (1+\dfrac{n_0}{R_c})tx & nx \\[2mm] (1+\dfrac{n_0}{R_c})ty & ny \end{pmatrix} \begin{pmatrix} ds \\ dn \end{pmatrix}
\tag{C.12}
$$

Where on the curve $n_0=0$, one recovers the familiar total differential of dx and dy

$$
dx = \frac{\partial x}{\partial s} ds + \frac{\partial x}{\partial n} dn
$$
$$
dy = \frac{\partial y}{\partial s} ds + \frac{\partial y}{\partial n} dn
\tag{C.13}
$$

From equation C.12 one gets the reversal relation

$$
\begin{pmatrix} ds \\ dn \end{pmatrix} = \begin{pmatrix} \dfrac{tx}{(1+\dfrac{n_0}{R_c})} & \dfrac{ty}{(1+\dfrac{n_0}{R_c})} \\[3mm] nx & ny \end{pmatrix} \begin{pmatrix} dx \\ dy \end{pmatrix}
\tag{C.14}
$$

And the definition of R_c gives

$$
\frac{\partial \vec{n}}{\partial s} = \frac{\vec{s}}{n_0 + R_c} \tag{C.15}
$$

Thus

$$
\left(\frac{\partial n_x}{\partial x}\right)_{y=cst} = \left(\frac{\partial \mathbf{n}}{\partial x}\right)_{y=cst}.\mathbf{e_x} = \left(\frac{\partial s}{\partial x}\right)_{y=cst}\left(\frac{\partial \mathbf{n}}{\partial s}\right)_{n=cst}.\mathbf{e_x} + \left(\frac{\partial n}{\partial x}\right)_{y=cst}\left(\frac{\partial \mathbf{n}}{\partial n}\right)_{s=cst}.\mathbf{e_x} = \left(\frac{\partial s}{\partial x}\right)_{y=cst}\frac{\mathbf{s}.\mathbf{e_x}}{R_c} = \frac{t_x^2}{R_c} \tag{C.16}
$$

Here we used the properties

$$
\left(\frac{\partial \mathbf{e_x}}{\partial x}\right)_{y=cst} = 0, \ \left(\frac{\partial \mathbf{n}}{\partial n}\right)_{s=cst} = \mathbf{0}, \ \left(\frac{\partial \mathbf{n}}{\partial s}\right)_{n=cst} = \frac{\mathbf{s}}{n_0 + R_c}, \ \left(\frac{\partial s}{\partial x}\right)_{y=cst} = \frac{t_x}{1 + n_0/R_c} \text{ and } n_0=0 \text{ at curve}
$$

Similarly we get

$$
\left(\frac{\partial n_y}{\partial x}\right)_{y=cst} = \frac{t_x t_y}{R_c} \ ; \ \left(\frac{\partial n_x}{\partial y}\right)_{x=cst} = \frac{t_x t_y}{R_c} \ ; \ \left(\frac{\partial n_y}{\partial y}\right)_{x=cst} = \frac{t_y^2}{R_c} \tag{C.17}
$$

Using C.16-C.17, the first RHS term of C.1 then becomes

$$\frac{\partial}{\partial s}(A_{12}E_n) = E_n \frac{ty^2 - tx^2}{R_c}(\varepsilon_{22} - \varepsilon_{11}) + E_n \cdot tx \cdot ty^2 \frac{\partial(\varepsilon_{22} - \varepsilon_{11})}{\partial y} - E_n \cdot ty \frac{\partial \varepsilon_{21}}{\partial y}$$

$$+ A_{12}(\frac{tx}{R_c}E_x + \frac{ty}{R_c}E_y + ny^2 E_{yx} - nx^2 E_{xy} + nx \cdot ny \cdot E_{xx} - nx \cdot ny \cdot E_{yy})$$

(C.18)

Finally the equation C.1 can also be expressed as

$$\frac{d}{ds}(A_{11}\frac{dV_{RF}}{ds}) + \frac{A_{21}}{R_c}\frac{dV_{RF}}{ds} = \text{ Eq. (C.18)+ Eq. (C.9)+ Eq. (C.10)} \quad \text{(C.19)}$$

D : A possible way to realize DB boundary condition in COMSOL

I.   Analysis of the problem

In engineering design, the DB boundary condition reads:

$$n \cdot D = 0 \quad n \cdot B = 0 \tag{D.1}$$

[Lindell 2009] proved that for a TE polarized plane wave (w.r.t incidence plane), this boundary condition can be replaced by a Perfect Electric Conductor (PEC), whereas for a TM polarized plane wave, it can be seen as a Perfect Magnetic Conductor (PMC),

Indeed, consider a TE polarized wave incident in xz plane, with a PEC in the z>0 half plane. If we use engineering convention.

The incident fields writes

$$\mathbf{E}^i = e^{-j\vec{u}_i \cdot \vec{r}} \vec{e}_y$$
$$Z_c \mathbf{H}^i = -e^{-j\vec{u}_i \cdot \vec{r}} k_z \vec{e}_x + e^{-j\vec{u}_i \cdot \vec{r}} k_x \vec{e}_z \tag{D.2}$$

And reflection fields:

$$\mathbf{E}^r = -e^{-j\vec{u}_r \cdot \vec{r}} \vec{e}_y$$
$$Z_c \mathbf{H}^i = -e^{-j\vec{u}_r \cdot \vec{r}} k_z \vec{e}_x - e^{-j\vec{u}_r \cdot \vec{r}} k_x \vec{e}_z \tag{D.3}$$

Where $\vec{u}_i = k_z \vec{u}_z + k_x \vec{u}_x$, $\vec{u}_r = -k_z \vec{u}_z + k_x \vec{u}_x$, $Z_c = \sqrt{u_0 / \varepsilon_0}$. One can see at the boundary, it fulfills

$$\vec{u}_z \cdot (\mathbf{H}^i + \mathbf{H}^r) = 0$$
$$\vec{u}_z \cdot (\mathbf{E}^i + \mathbf{E}^r) = 0 \tag{D.4}$$

The same for TM polarized wave with PMC boundary.

A problem may arise for a normal incidence plane wave. In this case the plane wave naturally fulfill the vanishing of longitudinal components. So this boundary does not play a role of boundary at all. In other words, DB boundary condition is incomplete for normal incident plane wave [Bosiljevac 2011].

If we consider a 3D waveguide in free space, see Figure D.1. Plane 1 is the plane to excite fields. Plane 4 is the target plane on which we want to implement DB boundary condition. There is no direct way to implement boundary conditions other than constraint on tangential components of EH fields in COMSOL. However, this can be done through introducing two extra scalars, i.e. u and v. The definition of this two vectors are represented by introducing an extra boundary ODE (2D boundary plane in 3D space), defined on the target plane 4,

$$\mathbf{e}_a \frac{\partial^2 \mathbf{T}}{\partial t^2} + \mathbf{d}_a \frac{\partial \mathbf{T}}{\partial t} = \mathbf{f} \tag{D.5}$$

Where $\mathbf{e}_a$, $\mathbf{d}_a$ are 2*2 vectors and $\mathbf{f}$ is a 1*2 vector. $\mathbf{T} = \begin{bmatrix} u \\ v \end{bmatrix}$. Here we choose $\mathbf{e}_a$ and $\mathbf{d}_a$ equal zero, $\mathbf{f} = \begin{bmatrix} \mathbf{n} \cdot \mathbf{E} \\ \mathbf{n} \cdot \mathbf{curlE} \end{bmatrix}$, where n is the normal component of the target plane 4. $\mathbf{E}$ is the electric field on the plane, n •curl$\mathbf{E}$ gives normal magnetic field. So the solution of (D.5) must be $E_n=0$ and $B_n=0$ (which is equal to (D.1) in free space), while u and v can be any value. Now going back to wave equation, without loss of generality, we rewrite the $\mathbf{E}$ field on the boundary plane as

$$E_x = t1x * u + t2x * v$$
$$E_y = t1y * u + t2y * v \tag{D.6}$$
$$E_z = t1z * u + t2z * v$$

Where t1 and t2 are the two tangential base vector on the boundary plane. t1x is the x component of t1, et.al. The idea lies behind (D.5) and (D.6) is that by (D.5) Comsol is aware of DB boundary conditions thus all the six electrical and magnetic components of wave equation can be solved. Then the two extra scalars is uniquely determined by two of three equations in (D.6). (D.6) can be implemented in COMSOL through boundary type 'Electric field' under EMW.

II.   Tests on 3D rectangular waveguide in COMSOL

We first construct a 3D rectangular waveguide in free space. As *Figure D.1* shows, wave propagates along z direction. E field is excited in the y direction. This is done by applying an excitation port boundary condition on plane 1, which specifies the power excited from this port is 1W. Correspondingly, on plane 6 we apply a receiver port boundary condition. The boundaries on top and bottom (3, 5) are PEC. Since DB boundary condition is incomplete for normal incidence plane wave, it is reasonable to implement this boundary condition on the planes parallel to propagation direction, e.g. plane 4. The other lateral boundaries plane 2 is PMC.

One would note that in free space, DB boundary condition (D.1) requires the vanishing of the normal electric field and magnetic field. To see this, let's plot the magnetic field and electric field near plane 4. In *Figure D.2*, the electric field stays dominant in y direction whereas the magnetic field deviated from x direction to z direction. The Poynting vector thus should be normal to the DB boundary.

III.   Conclusion

Although more tests still need to be done, several conclusions can already be made. 1. DB boundary condition has an inherent drawback that it must exclude a normal incidence plane wave. 2. The kind of trick to constrain normal components presented in this report can be easily extended to constrain other components, e.g. a mixed boundary type Ey=0, Bz=0 on plane 4.
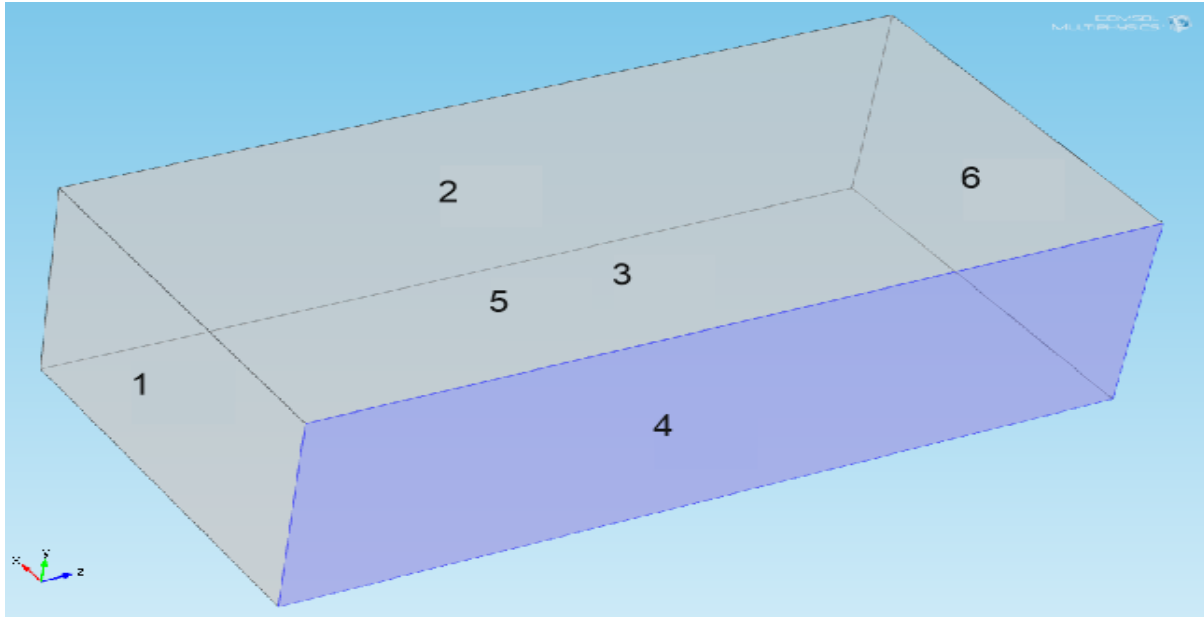
Figure D.1. 3D geometry of a simple waveguide
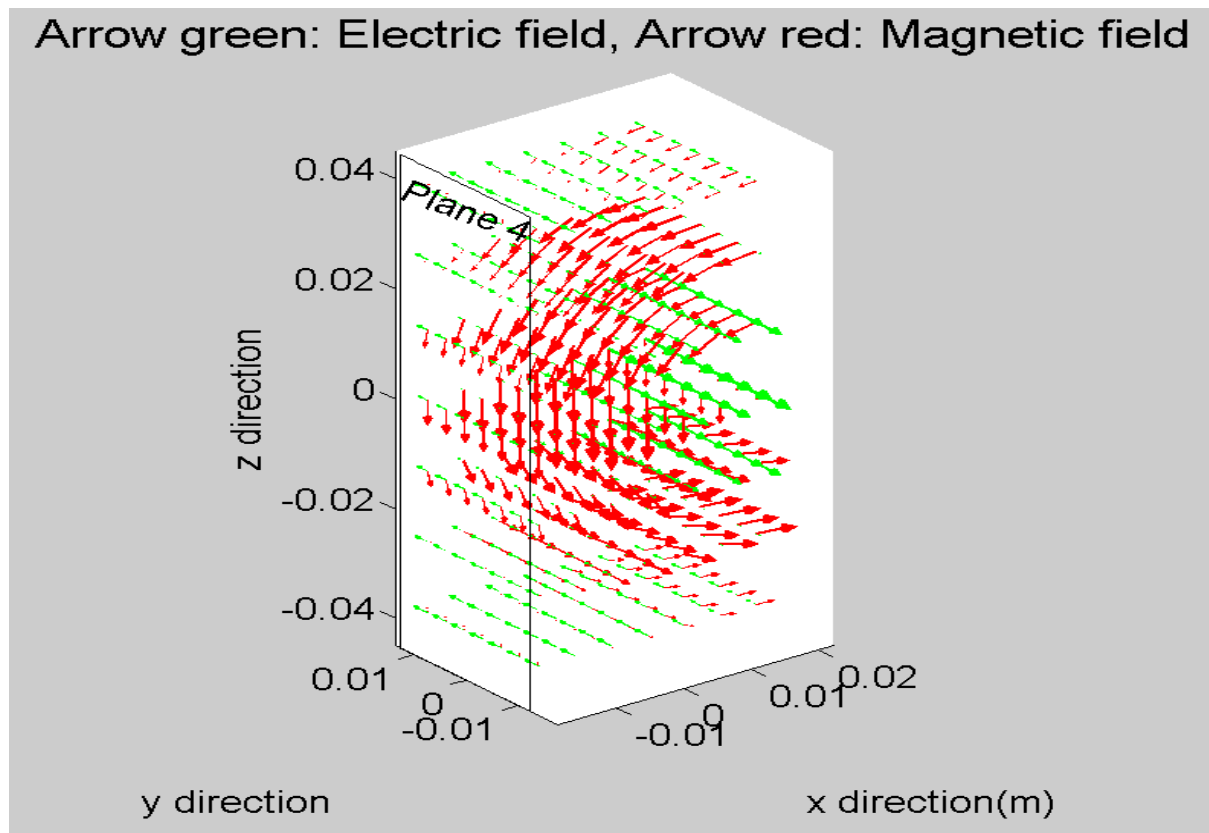
Figure D.2. Behavior of Magnetic field and electric field near the DB boundary

References

[Angot1972] A. Angot, "Compléments de mathématiques", 6th edition, Masson 1972 (in French)

[Brambilla1998] M. Brambilla, « Kinetic theory of plasma waves », Oxford science publications 1998.

[Bosiljevac 2011] M. Bosiljevac, Z. Sipus, P.S. Kildal and A. A. Kishk, "Modelling EBG surfaces using amended DB boundary conditions", Euro. Conf. on antennas and propagation, 11-15th April 2011, Rome, Italy

[COMSOL 2012] COMSOLMultiphysics Reference guide, version 4.3a, Nov, 2012

[Lindell 2009] I. V. Lindell and A. H. Sihvola, "Uniaxial IB-Medium Interface and Novel Boundary Conditions", IEEE Trans. on antennas and propagation, VOL. 57, NO. 3, MARCH 2009

[Lu 2016] L. LU et al. "Ion Cyclotron wave coupling in the magnetized plasma edge of tokamaks: impact of a finite, inhomogeneous density inside the antenna box", *PPCF, 58(5) 2016*.

[Stix 1992] T.H.Stix, waves in plasmas, AIP Press (1992)

Résumé long

1. Principaux résultats obtenus au cours de cette thèse

Les ondes dans le domaine des fréquences cyclotroniques ioniques (FCI, gamme typique 30-80MHz) sont l'une des principales méthodes de chauffage additionnel utilisées dans les dispositifs de fusion magnétique actuels, par exemple les tokamaks. Elles constituent également un moyen unique de chauffage direct des ions. Ces ondes sont excitées par des réseaux phasés de rubans poloïdaux de courant situés du bord de l'appareil. Pour obtenir un chauffage du plasma suffisant et rendre le système de chauffage fiable en régime permanent, il est nécessaire comprendre le couplage des ondes depuis ces antennes jusqu'au plasma et de minimiser des effets parasites apparaissant dans le plasma de bord, en particulier dans le champ proche radiofréquence (RF) rayonné par les antennes. Cette thèse apporte une contribution de modélisation aux recherches sur ces sujets.

Bien qu'un plasma de fusion soit extrêmement chaud (les températures typiques se chiffrent en millions de K), les effets thermiques sur le comportement des ondes FCI se font surtout sentir autour de la résonance cyclotronique et ses harmoniques pour les principales espèces présentes. Hors de ces zones de résonance, il est souvent commode d'utiliser l'approximation plasma froid, permettant de traiter le plasma comme un matériau diélectrique gyrotrope. Une antenne FCI peut émettre deux types d'ondes de plasma froid: l'onde rapide et l'onde lente. La première onde est évanescente dans le vide et en dessous d'une densité de coupure, dépendant pour une onde plane du vecteur d'onde parallèle $k_{//}$. Au-dessus de la densité de coupure, l'onde rapide peut se propager jusqu'au plasma central et contribuer au chauffage. L'onde lente est évanescente au-dessus de la résonance hybride inférieure et propagative en-dessous. L'onde rapide a des composantes notables de champ électrique qui sont perpendiculaires au champ magnétique statique, alors que l'onde lente a un grand champ électrique dans la direction parallèle au champ magnétique de confinement. L'onde rapide étant la principale onde de chauffage, les rubans excitateurs sont orientés dans la direction poloïdale pour engendrer préférentiellement cette polarisation. Dans les tokamaks actuels, la résonance hybride inférieure est naturellement présente à l'extrême périphérie de la machine, et peut-être à l'intérieur du boîtier d'antenne. Cependant, elle est souvent négligée dans les simulations actuelles de couplage d'onde.

La première partie de cette thèse a étudié l'impact sur le champ RF proche et le couplage de puissance FCI de profils densités qui décroissent continûment à l'intérieur de l'antenne et traversent la résonance hybride inférieure (résonance LH). Avant cette thèse un code de couplage 2D pleine onde (onde lente + onde rapide), RAPLICASOL-2D avait été développé. Auparavant, il avait un champ magnétique purement toroïdal. Au cours de cette thèse, le code a été amélioré pour incorporer une configuration du champ magnétique inclinée dans le plan toroïdal / poloidal. Ce code considère un plasma froid magnétisé sans collision ni gaine à l'interface plasma-paroi. Il est toutefois flexible pour ajouter des collisions et est également compatible avec des conditions aux limites de type gaines à l'interface plasma-paroi. Le logiciel a été élaboré à partir du solveur commercial d'éléments finis COMSOL Multiphysics. L'une des principales raisons d'utiliser COMSOL est qu'il permet d'économiser le temps de codage et la compilation et donc les utilisateurs peuvent se concentrer sur l'étude de la physique.

167

Le nouveau code 2D RAPLICASOL montre qu'en présence de densités inférieures à la résonance LH, il devient difficile d'atteindre la convergence numérique des simulations: dans les limites de mémoire de la station de travail adoptée, le motif de champ change avec la taille des éléments finis. Une interprétation physique repose sur le fait qu'en dessous de la résonance LH l'onde lente peut se propager à très courte longueur d'onde et donc est sensible aux paramètres de simulation, comme la taille du maillage. Les principaux résultats de cette partie de la thèse sont présentés à la figure E.1. Pour une configuration de plasma et d'antenne typique de Tore Supra, cette figure trace la puissance FCI couplée au plasma principal avec 1A de courant RF sur 1m de ruban rayonnant, en fonction de l'angle d'inclinaison du champ magnétique, pour différents profils radiaux de densité plasma à l'intérieur de la boîte d'antenne. Fait intéressant et important, le spectre en nombre d'onde toroïdal k_{tor} de la puissance couplée est indépendant de la taille des mailles et n'est que faiblement affecté par la présence du profil de densité à l'intérieur de l'antenne, lorsque les deux rubans de courant considérés oscillent en opposition de phase (phasage « dipôle », le plus souvent utilisé comme configuration de chauffage sur Tore Supra). On peut donc ignorer la faible densité à l'intérieur de la boîte d'antenne pour les études de couplage d'onde rapide. Cela justifie la simplification adoptée par les principaux codes de couplage actuels: ignorer l'existence de la résonance hybride basse dans leur simulation et ne considérer que l'onde rapide. En phasage « monopôle », lorsque les deux rubans oscillent en phase, la simulation montre qu'il y a au maximum 20% d'augmentation de puissance couplée due à la présence de plasma dans la boîte. La distinction vient du fait que la longueur d'évanescence pour l'onde rapide à faible k_{tor} est en train de changer, contrairement aux k_{tor} plus élevés du dipôle. Ainsi l'hypothèse du vide dans la boîte nécessite peut-être d'être ré-examinée pour modéliser des systèmes rayonnant aux faibles k_{tor}. La simulation montre également que la variation du gradient de densité dans la région d'évanescence de l'onde rapide n'a aucun effet significatif sur le couplage d'onde. On peut donc modéliser encore le couplage de puissance à un plasma avec une assez bonne précision en dépit de certaines incertitudes sur le profil de densité mesuré.
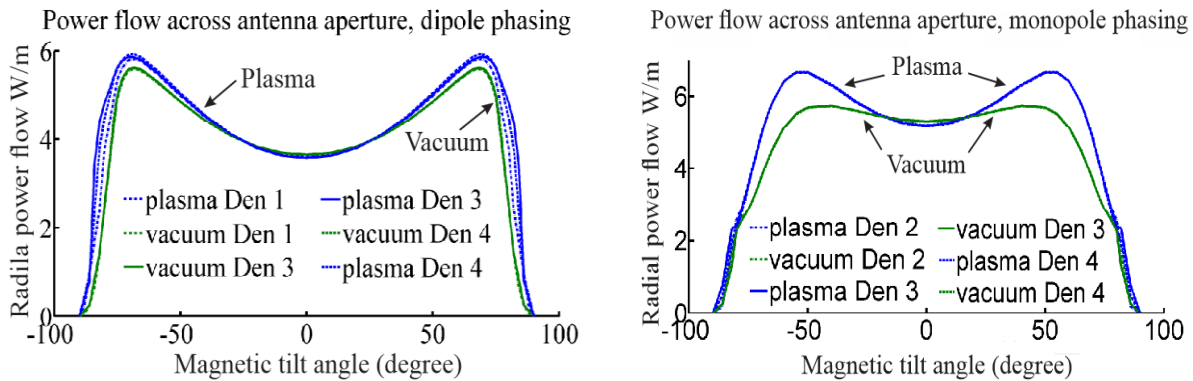
Figure E.1 : Puissance transmise au plasma central, pour 1A dans 1m de ruban, en fonction de l'angle d'inclinaison du champ magnétique par rapport à la direction toroïdale, pour différentes formes de profils de densité dans la boîte d'antenne. (a) Simulation pour deux rubans de géométrie Tore Supra dont les courants RF oscillent en opposition de phase (phasage « dipôle ») ; (b) idem pour des courants RF en phase (phasage « monopôle »)

Dans les régions qui leur sont accessibles, les ondes RF peuvent induire des oscillations RF de la couche limite à l'interface entre le plasma et la paroi de la machine, appelée « gaine ». La gaine pouvant être vue comme un composant électrique non-linéaire, des oscillations de sa tension induisent une contribution

nette au potentiel continu (DC) du plasma *via* un processus non-linéaire de rectification. On attribue à la rectification de gaine, la génération d'impuretés par pulvérisation de la première paroi, et des flux de chaleur excessifs sur les surfaces d'antenne FCI exposées au plasma, et sur les autres composants de la machine en regard. Notre façon de modéliser l'interaction des ondes RF et de la gaine est de résoudre de manière auto-cohérente la propagation des ondes RF et la polarisation DC du plasma, couplées par l'intermédiaire de conditions aux limites non-linéaires RF et DC de type gaines (SBC) appliquées à l'interface plasma-paroi. On adopte une approche couplant de manière auto-cohérente trois quantités physiques. On résout de manière itérative jusqu'à convergence la propagation du champ électrique vectoriel RF (**E**), l'excitation de tension oscillante de la gaine (V_{RF}) et la modification du potentiel DC du plasma (V_{DC}). Dans les manuels la gaine RF est souvent modélisée par un circuit électrique constitué d'un condensateur, d'une diode et d'une source constante de courant ionique. Sous une tension de gaine élevée et dans un régime d'ions immobiles, la partie RF de ce modèle peut être réduite à un condensateur à plaques parallèles. La formule pour la capacitance RF de la gaine peut donc être obtenue en fonction de la largeur moyenne de gaine. Sous cette hypothèse électrostatique, une condition aux limites RF de type gaine valable dans la limite des ions immobiles a été proposée par Myra et D'Ippolito avant cette thèse. La théorie de la gaine DC considère un courant d'ions constant pénétrant la gaine à la vitesse du son (vitesse de Bohm), tandis que les électrons sont supposés avoir une distribution maxwellienne tronquée et suivent une distribution de densité de type Boltzmann à l'intérieur de la gaine. Le courant électronique dépend de manière exponentielle de la tension appliquée à la gaine. A l'aide de ces contributions élémentaires, une caractéristique courant-tension moyennée dans le temps (I_{DC}-V_{DC}) peut être établie pour la gaine, pour décrire le courant continu total à travers la gaine, en fonction de la tension continue à ses bornes. Par l'intermédiaire du processus non-linéaire de rectification, la présence d'oscillations RF de la tension de gaine modifie cette caractéristique I_{DC}-V_{DC} moyennée. L'épaisseur moyenne de la gaine est décrite par la loi de Child-Langmuir et dépend du potentiel DC. Ainsi la capacitance RF, qui influe sur la réflexion des ondes RF aux parois, dépend de V_{DC}. Ces bases théoriques ont été utilisées pour développer au CEA en 2013 le code SSWICH (Self-consistent Sheaths and Waves for Ion Cyclotron Heating). La première version de SSWICH (SSWICH-SW) adoptait une géométrie 2D simple formée de blocs rectangulaires où le champ magnétique était soit parallèle soit perpendiculaire aux parois. Dans cette configuration magnétique, les conditions aux limites gaine font uniquement intervenir l'onde lente. Dans son module de champ RF, SSWICH-SW résout seulement la composante parallèle du champ, associée l'onde lente. Le champ RF est excité en imposant à une limite externe du domaine de simulation une carte du champ RF parallèle issue d'un code d'antenne extérieur. Afin d'initier la résolution itérative de SSWICH-SW, on utilise dans le module RF une version asymptotique des conditions aux limites RF de type gaine, qui ne dépend plus de la largeur de gaine. Des tests ont montré qu'au moins dans la configuration Tore Supra, cette version asymptotique dite « gaines larges » peut déjà donner un résultat assez proche de la solution finale après convergence. En outre, une version 3D du code SSWICH-SW asymptotique a été développée en traitant la troisième direction (poloidale) de manière spectrale. En effet, dans l'approximation « gaines larges », les deux premiers modules de SSWICH deviennent linéaire. Cette linéarité garantit que chaque nombre d'onde poloidal k_z est indépendant des autres, ce qui permet de faire fonctionner le module 2D séquentiellement pour chaque k_z. Avec la simulation SSWICH-SW, on a déjà reproduit un effet de proximité spatiale entre émetteur d'onde et gaines, qui a été observé expérimentalement.

L'onde rapide, principale onde de chauffage, est absente du code SSWICH-SW. Dans la partie centrale de cette thèse nous avons développé une nouvelle version de SSWICH incluant l'onde rapide (FW), une

configuration plus réaliste de champ magnétique et des parois courbes. Ces nouvelles propriétés sont intrinsèquement reliées. Par exemple, dans un champ magnétique incliné, l'onde rapide intervient dans les conditions aux limites gaines (SBCs). La littérature indique alors que, par réflexion sur un mur incliné par rapport au champ magnétique, une conversion de mode est susceptible de se produire entre l'onde lente (SW) et l'onde rapide (FW). L'ajout du champ magnétique incliné et des murs courbes est une étape vers la géométrie réaliste. Le code SSWICH-Full Wave, toujours en 2D pour limiter le coût numérique, a un champ magnétique incliné dans le plan poloïdal et toroïdal. Ce n'est pas le cas le plus général, mais sous cette configuration magnétique, on peut garder une géométrie de simulation similaire à celle du code précédent et en même temps d'introduire le couplage d'onde rapide dans le code. Au début de cette thèse, nous avons déjà envisagé que RAPLICASOL et SSWICH devraient à terme être généralisés en un seul code. Ainsi lors de l'élaboration du code SSWICH-FW, nous avons choisi une géométrie similaire au code RAPLICASOL 2D. Mais les parois ont été courbées et des conditions aux limites de type gaine plus générales ont été utilisées.

Les conditions aux limites DC et la capacitance RF utilisés dans SSWICH-FW doivent être valables dans le champ magnétique incliné. Ces conditions n'existaient pas avant cette thèse. Dans cette thèse, des SBCs RF plus générales ont été formulées en utilisant tous les composants de champ RF et la formule de rectification DC a été améliorée pour prendre en compte de manière simple le champ magnétique incliné. Que ces formules simples reproduisent la réalité ou non est encore une question ouverte et elles sont encore en cours de test dans des simulations plus fondamentales. Les ondes RF peuvent être excitées soit par des courants poloïdaux imposés sur des rubans dans l'antenne ou par des cartes de champ (composantes toroïdales et poloïdales) issues d'un code d'antenne 3D extérieur et imposées à la bouche de l'antenne. Imposer un courant sur la surface des rubans est moins réaliste car on incorpore moins de détails de la géométrie d'antenne. Aussi, pour reproduire des expériences il est actuellement préférable d'utiliser une excitation par cartes de champ. SSWICH est à l'heure actuelle le seul code dans le monde capable de simuler des gaines RF dans un environnement tokamak en utilisant des cartes de champ d'antenne réalistes.

Selon la même stratégie utilisée dans SSWICH-SW, une version asymptotique du code SSWICH-FW basée sur l'hypothèse « gaine large » a été développée. Les simulations SSWICH-FW asymptotiques utilisant des paramètres typiques d'expériences tokamak (comme Tore Supra) ont montré une conversion de mode de FW à SW se produisant aux angles vifs où la forme des parois varie rapidement. En effet, sur la base du fait que les ondes lentes et rapides ont des comportements différents lorsque les différentes constantes diélectriques du plasma varient, nous avons constaté que des motifs de champ apparaissant au sommet des limiteurs latéraux d'antenne sont probablement associés à l'onde lente. L'onde rapide peut accéder à des régions du plasma éloignées de l'antenne, qui sont inaccessibles à l'onde lente évanescente. Les simulations pleine onde ont mis en évidence des oscillations de gaine dans ce "champ lointain", apparaissant sur des parois courbes loin de l'antenne. Compte tenu de la distance antenne/gaine ces oscillations ne peuvent être excitées que par une onde rapide propagative. En variant les dimensions toroïdale et radiale de la paroi, on a pu voir que les deux quantités $|V_{RF}|$ et $|V_{DC}|$ dans ce champ lointain diminuent avec la distance toroïdale à l'antenne active. Par contre $|V_{RF}|$ et $|V_{DC}|$ augmentent avec la distance radiale au lanceur d'onde. C'est à première vue contre-intuitif, surtout par comparaison aux les effets de proximité spatiale gaine/émetteur observés en champ proche. Ce comportement suggère qu'une onde rapide propagative peut ne pas produire de tels effets de proximité spatiale. Néanmoins, cette observation est cohérente avec la proximité spatiale de la paroi où se développent les gaines avec

le lobe de propagation de l'onde rapide devant l'antenne. Les variations de V_{RF} dans la SOL lointaine avec l'angle d'inclinaison sont assez similaires à celles du couplage de puissance, à savoir la figure E.1. Cela confirme que l'onde rapide joue un rôle dominant sur l'excitation V_{RF} dans la SOL lointaine. La troisième série de simulations visait à explorer le rôle de l'onde rapide sur l'extension radiale de la région à V_{DC} élevés dans la SOL libre. Les résultats montrent que la diminution de la conductivité perpendiculaire DC du plasma peut affecter de manière significative cette largeur, même en présence de l'onde rapide. Cela donne à penser que le transport de courant continu est toujours le mécanisme dominant pour déterminer l'extension radiale de la zone polarisée par les ondes.

Jusqu'ici, les résultats dont nous avons parlé ci-dessus ont été obtenus en imposant des courants poloïdaux sur des rubans implantés dans l'antenne. Lorsque l'on compare la simulation avec l'expérience, il est préférable d'utiliser une excitation plus réaliste: imposer à la bouche d'antenne des cartes de champ importées d'un code de couplage d'onde avec une géométrie d'antenne plus détaillée. Une version 3D du code RAPLICASOL a été développée en parallèle à cette thèse grâce au travail de J. JACQUOT à Garching. Il a une structure très similaire au code 2D RAPLICASOL et la carte du champ issue de ce code a moins de bruit numérique que les cartes précédentes. L'un des résultats produis par la simulation SSWICH-SW / TOPICA est une structure verticale en double bosse pour V_{DC} au niveau du bord d'attaque des limiteurs d'antenne. Ce type de structure a été vu expérimentalement sur des images infrarouges de la température de surface des limiteurs, ainsi que sur des cartes 2D du potentiel mesuré par sondes. Les simulations SSWICH-FW / RAPLICASOL ont également reproduit cette structure verticale à double bosse en utilisant une approche multi-2D. Dans un premier temps, nous avons utilisé le code 3D RALICASOL avec les mêmes paramètres plasma que la simulation 2D SSWICH-FW asymptotique et déduit du code d'antenne des cartes 2D (vertical-toroïdal) des champs électriques à l'écran de Faraday. Pour chaque altitude (dans la direction verticale), les deux composantes tangentielles du champ électrique de la carte de champ ont été imposées à la bouche d'antenne dans SSWICH. Les polarisations distinctes de l'onde rapide et l'onde lente permettent de découpler partiellement ces deux ondes dans l'excitation. En utilisant uniquement la composante $E_\perp$ de la carte du champ on excite préférentiellement l'onde rapide. En utilisant uniquement $E_{//}$ on excite préférentiellement l'onde lente. La figure E. 2 montre les résultats de la simulation multi-2D utilisant SSWICH-FW / RAPLICASOL. Le résultat correspond mieux avec la structure à double bosse expérimentale quand seul $E_{//}$ est utilisé. L'onde lente, avec une longueur d'évanescence courte, est sensible aux petites modifications de géométrie dans la SOL privée. La courbure de la paroi introduite dans le SOL privée se révèle importante pour l'amplitude du champ proche, mais très probablement non pertinente pour les études de couplage d'onde rapide. D'autre part, l'onde rapide est probablement sensible à des effets 3D. Alors que l'onde lente a un effet dominant pour exciter V_{DC} dans la SOL privée, ces deux ondes semblent jouer un rôle comparable sur V_{DC} dans le voisinage du lanceur d'onde. Au cours des derniers mois de cette période de thèse, nous avons finalement testé un moyen d'intégrer des effets 3D dans les simulations. L'astuce consiste à traiter la direction verticale (direction z) de manière spectrale dans les deux premiers modules de SSWICH, de manière similaire à la version 3D asymptotique SSWICH-SW, en considérant maintenant les deux composantes tangentielles du champ issues de RAPLICASOL 3D. Enfin on exécute le module V_{DC} en multi-2D en utilisant le V_{RF} de la dernière étape. En utilisant cette technique, et pour certains vecteurs d'ondes poloidaux k_z, une onde de surface se propageant dans la direction z est susceptible d'apparaître au niveau des parois où existent des gaines. Cela peut être dû à une incompatibilité entre les conditions aux limites périodiques et la taille finie du lanceur d'onde. En utilisant des transformées de Fourier, nous avons implicitement imposé des conditions aux limites périodiques aux deux extrémités verticales du domaine de simulation, de sorte que ces ondes de surface

peuvent se propager à l'infini de l'antenne, alors qu'en réalité elles sont peut-être réfléchies aux extrémités des limiteurs d'antenne.
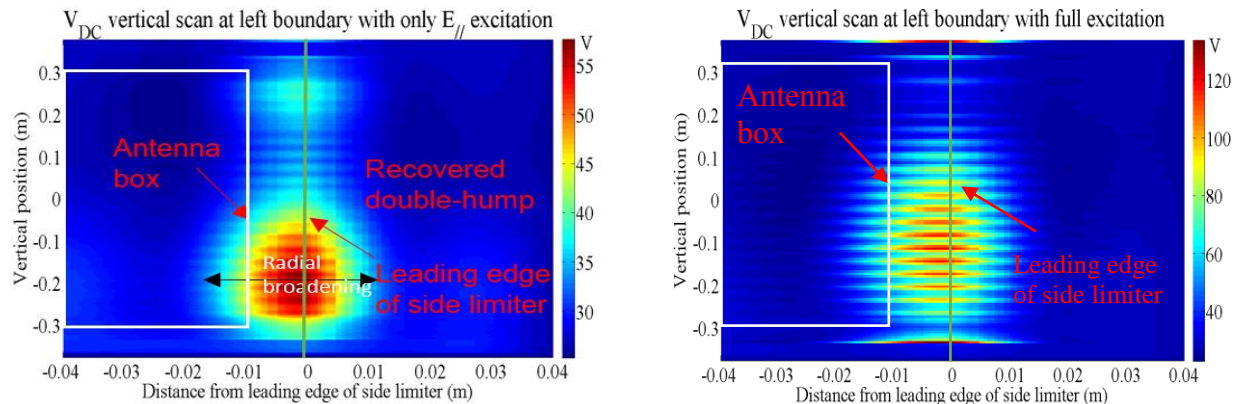

Figure E.2. Carte Verticale-radiale de V_DC à l'extérieur du limiteur d'antenne gauche, pour 1 MW couplés, simulations SSWICH-FW/RAPLICASOL multi-2D, sans inclure d'effet 3D. (Gauche) simulations excitées uniquement avec la composante E_//, de la carte de champ RF issue RAPLICASOL 3D. (Droite) simulations réalisées avec toutes les polarisations de la carte de champ RF.

Une asymétrie gauche-droite de la température de surface ou des flux de chaleur a été observée en détail entre les deux extrémités opposées de la même ligne de champ magnétique dans des expériences où les deux rubans des antennes Tore Supra n'étaient pas alimentés avec la même puissance. Cette observation est une justification solide pour les effets de proximité spatiale dans l'excitation des gaines RF. Avec SSWICH-FW et RAPLICASOL, nous avons simulé le flux de chaleur sur les deux limiteurs aux deux extrémités de la même antenne. La simulation pleine onde a reproduit avec succès l'asymétrie gauche-droite des flux de chaleur, ce qui suggère que les effets de proximité spatiale, étudiés précédemment uniquement pour l'onde lente, sont toujours valables en présence de toutes les polarisations d'onde dans le voisinage de l'antenne, où à la fois l'onde rapide et l'onde lente sont évanescentes.

Initialement développé pour les études de gaine RF dans les tokamaks, SSWICH-FW a des applications plus polyvalentes. Dans la troisième partie de ce travail de thèse, nous avons montré comment le principe de SSWICH peut être mis en œuvre dans une machine totalement différente du Tokamak, en termes de géométrie et régime de couplage onde/plasma. Le dispositif ALINE est une décharge plasma cylindrique magnétisée dédiée à l'étude des propriétés de base des ondes de plasma et des gaines RF. SSWICH a été utilisé dans une première tentative de simulations interprétatives pour les plasmas d'ALINE en Argon. En utilisant le code SSWICH-FW asymptotique, nous avons observé et étudié à la fois l'onde hybride basse (LH) et l'onde Hélicon, apparaissant dans différents régimes de paramètres d'Aline. L'onde LH se propage normalement à une faible densité, comme l'onde lente des Tokamak, alors que l'onde Hélicon existe préférentiellement à densité élevée, comme l'onde rapide dans un Tokamak. Une différence majeure entre l'onde Hélicon et l'onde rapide Tokamak est que l'onde hélicon se propage le long du champ magnétique et a un cône de résonance orienté selon la direction toroïdale. L'onde LH, comme l'onde lente électrostatique des Tokamak, se propage aussi à l'intérieur d'un cône de résonance. Cette propriété commune nous aide à identifier l'onde Hélicon et l'onde hybride inférieure dans la simulation. Compte tenu de la densité actuelle du plasma d'ALINE, l'onde Hélicon peut être observée uniquement avec un très faible champ magnétique dans les plasmas d'argon. Dans ce champ magnétique, les ions argon ne sont pas vraiment magnétisés. Pour produire l'onde hélicon avec ions magnétisés, il est préférable d'utiliser l'hélium. La sensibilité des champs électriques au maillage du domaine au voisinage des structures

excitatrices, identifiée précédemment en tokamak, apparaît également dans les simulations ALINE. Ajouter des collisions est un moyen efficace de réduire cette sensibilité. D'un point de vue purement numérique, la fréquence de collision doit être aussi élevée que la fréquence d'onde afin d'éliminer cette non-convergence avec le maillage. Cependant, avoir une fréquence de collision aussi élevée va certainement changer la physique des ondes. Une meilleure solution est clairement nécessaire pour résoudre ce problème de non-convergence.

Étant donné que le champ magnétique dans ALINE est totalement horizontal et que l'onde LH est la principale onde qui pourrait être excitée dans l'état actuel de la machine Aline, le code SSWICH-SW a été utilisé pour modéliser les gaines RF dans ALINE. La conductivité DC Spitzer des tokamaks a été remplacée par une conductivité parallèle prenant en compte les collisions électrons-neutres, tandis que la conductivité DC perpendiculaire du plasma provient des collisions ions-neutres. D'autres mécanismes sont susceptibles d'affecter la conductivité DC effective du plasma: la viscosité ionique, l'inertie des ions. Par souci de simplicité, ces effets ont été négligés dans les simulations actuelles. Grâce à son accès facile pour les diagnostics, le dispositif ALINE peut fournir une carte expérimentale du potentiel flottant de sondes de Langmuir qui peut être comparée à la modélisation SSWICH-SW. Le potentiel de plasma DC dans la simulation SSWICH-SW présente une homogénéité toroïdale lorsque la conductivité parallèle du plasma est élevée, comme c'est le cas dans les plasmas de tokamak. La carte mesurée dans Aline montre des variations parallèles du potentiel flottant. Avec une conductivité parallèle plus faible, une inhomogénéité toroïdale apparaît également dans nos simulations, comme le prédit un modèle analytique. Le potentiel flottant expérimental a toujours une valeur maximale au-dessus de l'antenne tandis que la simulation de SSWICH indique une valeur crête localisée à l'antenne. Cet écart est actuellement expliqué par l'accélération d'ions par le champ électrique radial au niveau de la surface supérieure de l'antenne, un phénomène non présent dans SSWICH.

Nous avons ici résumé les principaux résultats obtenus au cours de cette thèse. Nous espérons avoir convaincu que le code numérique SSWICH peut produire des résultats raisonnables pour aider à comprendre les problèmes d'ondes et de gaines RF au bord des plasmas magnétisés. Dans ce qui suit, nous allons présenter des perspectives pour des travaux futurs.

2. Travaux futurs

Le code 2D RAPLICASOL actuel, utilisé pour réaliser la première partie de ce travail de thèse, n'a pas tenu compte d'un éventuel amortissement parasite des ondes dans le bord. Notre simulation dans le dispositif ALINE a montré que l'ajout de collisions peut réduire considérablement la sensibilité des résultats au maillage. Cependant, le niveau de dissipation précis est critique dans ces simulations, et il est difficile de connaître la collisionalité autour de la résonance de la LH. Aussi, une meilleure façon de résoudre ce problème est fortement nécessaire. Un travail mathématique en cours tente de reformuler rigoureusement la méthode des éléments finis autour de la résonance hybride inférieure, pour obtenir une solution convergente à travers cette résonance dans la limite non-collisionnelle. Jusqu'à présent, cette méthode n'a été testée que dans des cas plus simples que notre géométrie. Dans notre première partie nous n'avons considéré que le cas où la résonance de LH est localisée derrière les rubans de courant. Cependant, la même méthode peut également être utilisée pour examiner un autre cas extrême, lorsque le ruban est en-dessous de la résonance de LH et peut exciter directement l'onde lente propagative. Les effets 3D n'étaient pas inclus dans cette première partie de notre travail. Une dérivée poloidale est susceptible de jouer un rôle important dans l'étude de la modification de la densité par les forces

pondéromotrices et doit donc être prise en compte dans les études de couplage d'onde. A présent une version 3D de RAPLICASOL est disponible, mais l'exécution de ce code est très consommatrice de mémoire. Enfin, autour de la résonance de LH, les effets thermiques deviennent importants, et peuvent nécessiter des corrections pour tenir compte des effets dus au rayon de Larmor fini.

Dans le code 2D SSWICH-FW actuel, développé dans la deuxième partie de cette thèse, les formules de capacitance RF de la gaine et de rectification en champ magnétique incliné ont pris la forme d'une simple extrapolation des formules antérieures, valides en champ magnétique normal aux parois. Ces formules seront mises à jour au vu d'études plus fondamentales de la physique des gaines RF. Deux approches différentes ont été proposées pour calculer la tension de gaine RF oscillant (V_{RF}). Dans notre dernier effort, notre première approche de calcul V_{RF} par une méthode intégrale a été généralisée par un traitement spectral. Tout au long du développement de code, nous avons passé beaucoup de temps pour mettre au point une méthode alternative utilisant des dérivées spatiales du champ RF pour calculer V_{RF}. Finalement cette deuxième approche n'a pas été privilégiée, en raison de l'instabilité numérique des dérivées du champ électrique aux parois où on applique les SBCs. Nous pensons que c'est une question numérique liée à la compatibilité des conditions aux limites de la gaine asymptotique avec la mise en place de la méthode des éléments finis utilisés dans le logiciel COMSOL. L'utilisation de COMSOL nous permet de réduire considérablement le temps de développement et de compilation du code, mais d'autre part, nous restreint dans notre capacité à connaître et modifier le traitement interne du solveur d'éléments finis. Une autre faiblesse de COMSOL est une limitation relative des options pour les conditions aux limites. Dans un code fait maison basé sur le langage de compilation primaire, à savoir FORTRAN, on peut facilement implémenter les conditions aux limites souhaitées.

Une autre faiblesse du code SSWICH-FW actuel est l'utilisation des paramètres de transport faiblement contraints. L'extension radiale de V_{DC} est toujours très sensible à la valeur de la conductivité DC perpendiculaire. Ce problème existait déjà dans le code SSWICH-SW et avait été discutée en détail dans la thèse de doctorat de J. Jacquot. Actuellement, le module pour le calcul de V_{DC} utilisé dans le code SSWICH-FW est très similaire à celui du code SW, et il hérite donc ce point faible. Les deux conductivités perpendiculaires ad hoc doivent encore être déterminées plus précisément a partir de l'analyse des turbulences. Un travail sur ce point a été initié par P. TAMAIN, mais malheureusement, il n'a pas été achevé avant la fin de cette thèse.

Dans SSWICH-FW, la forme de la géométrie des parois dans la SOL privée est également importante. L'amplitude de V_{DC} et aussi le flux de chaleur dans la SOL privée sont sensibles à la modification de la géométrie dans cette région. Généralement, on attribue à l'onde lente une contribution dominante sur V_{DC} dans le SOL privé. Probablement en raison de la courte longueur d'évanescence de l'onde lente, il a été montré par la simulation d'une modification de la géométrie peut influer sur l'amplitude de V_{DC} (ou des flux de chaleur) jusqu'à 30%. La prochaine étape sera donc d'implanter avec des composants incurvés plus réalistes, en particulier dans la région de la SOL privée. D'ailleurs, en parallèle à ce travail de thèse, le code 2D RAPLICASOL a été étendu à une géométrie cylindrique afin de rendre compte la courbure toroïdale du champ magnétique, des parois du Tokamak et la structure d'antenne. Une comparaison du champ proche RF calculé par cette extension 2D RAPLICASOL en géométrie cylindrique avec le résultat obtenu en utilisant la géométrie rectangulaire montre que la courbure toroïdale importe pour l'amplitude du champ proche parallèle. À l'avenir, SSWICH-FW devrait également inclure la courbure toroïdale.

Dans le chapitre 5, nous avons trouvé que les effets 3D sont importants pour évaluer l'impact de l'onde rapide sur l'excitation des gaines dans la SOL. La meilleure façon de prendre en compte les effets 3D est bien sûr de procéder à une simulation 3D complète. En 3D, on peut aussi avoir une excitation de tension réaliste de l'antenne. Malheureusement, une simulation complète 3D SSWICH-FW est actuellement hors de portée, à la fois par l'absence de formulation appropriée pour les SBC et en raison des exigences excessives de mémoire Le problème de la mémoire est évident. Pour le premier problème, nous avons fait des progrès, à savoir la formulation en 3D de la condition aux limites de la gaine (DB SBCs) n'a pas encore été testée dans le plasma mais dans l'espace libre. En théorie, l'approche secondaire pour V_{RF} fonctionne également en 3D si la dérivée numérique du champ électrique converge en changeant le maillage, mais il reste à la tester numériquement sur un plan incurvé. Le traitement spectral de la direction poloidale est actuellement la meilleure méthode pour incorporer des effets 3D que nous pouvons proposer à l'issue de cette thèse.

Notre objectif final avec SSWICH est de mettre en œuvre une géométrie 3D réaliste, une propagation pleine onde et des conditions aux limites de type gaine valables en 3D. Le code 3D RAPLICASOL est maintenant disponible pour résoudre la propagation pleine onde complète sans gaine. Il remplacera le module RF courant dans la version 3D du Code SSWICH-FW. À l'avenir, SSWICH peut être couplé avec d'autres codes pour couvrir plus de physique. Par exemple, la modification de la densité induite par la RF et une modélisation de l'injection locale de gaz sont considérés dans le code de transport de bord 3D EMC3-Eirene. La carte de V_{DC} produit par SSWICH-FW 3D pourrait être utilisée comme une entrée pour le code EMC3-Eirene. Ce dernier pourrait alors retourner une distribution 3D de densité plus auto-cohérente, qui à son tour pourrait être importée dans le code 3D SSWICH-FW. Ces deux codes peuvent être résolus de manière itérative jusqu'à convergence numérique.

Enfin, la pulvérisation, les flux de chaleur et le rayonnement des d'impuretés sont parmi les conséquences directes des effets de gaine RF. A ce stade, ces phénomènes ne sont pas modélisés dans le code SSWICH, mais nous avons montré comment les résultats de SSWICH peuvent être utilisés pour évaluer des flux de chaleur. SSWICH-FW est une première étape importante pour modéliser ces processus physiques. Étudier expérimentalement les impacts des ondes sur les impuretés sera le sujet d'un nouveau doctorat sur la nouvelle machine WEST et le tokamak chinois EAST. Le code SSWICH-FW pourrait être utilisé comme un outil numérique pour interpréter les mesures.

Pour les simulations plasma dans ALINE, nous sommes conscients que notre travail est juste une première étape pour une meilleure compréhension des propriétés des ondes et des gaines dans une machine linéaire. La modélisation des ondes dans une cavité comme ALINE doit comporter des collisions comme mécanisme d'amortissement. Sans surprise, la structure du champ dans la simulation est très sensible aux collisions électrons-neutres. L'équation analytique proposée dans le livre de Chabert est actuellement la meilleure façon d'estimer cette fréquence de collision. En outre, une densité précise est également importante pour garantir que la simulation est comparable à la décharge réelle. A ce moment, le profil de densité utilisé dans la simulation est seulement inhomogène le long de la direction radiale. Pour reproduire entièrement la variation toroïdale présente dans la carte expérimentale de potentiel flottant, il faut certainement incorporer une variation toroïdale de la densité. En outre, la simulation actuelle de gaine RF ne comporte que l'onde hybride inférieure. Les effets de l'onde hélicon sur l'excitation de gaines RF sont encore à explorer.

Cette thèse se fait dans le contexte de la recherche sur la fusion nucléaire, et elle est particulièrement dédiée à la modélisation de gaine RF dans Tore Supra. Tore Supra a presque terminé sa mise à niveau vers WEST et prévoit de produire son premier plasma d'ici la fin de cette année. Le Code SSWICH-SW 3D asymptotique avec les cartes champ de TOPICA a été utilisé pour optimiser la conception électrique des écran de Faraday des nouvelles antennes WEST. La première de ces antennes a maintenant été livrée au CEA. Dans l'avenir, SSWICH-FW / RAPLICASOL pourra être utilisé pour interpréter les expériences dans WEST.

Enfin, SSWICH présente une méthodologie pour modéliser les ondes RF et les interactions de la gaine. Elle a des applications potentielles dans les autres domaines de recherche. Par exemple, des gaines RF sont également présentes dans les satellites artificiels et des vaisseaux spatiaux. Le plasma dans l'espace peut interagir avec les satellites qui utilisent des ondes RF pour leurs transmissions. En présence de SBC, la simulation SSWICH a montré que des ondes gaine-plasma apparaissent le long des parois. Du point de vue d'un ingénieur, la région métal-gaine-plasma crée un guide d'onde où les ondes de surface (ondes gaine-plasma) peuvent se propager. Le résultat immédiat de ces ondes de surface est qu'ils apportent une contribution significative à l'impédance de l'antenne et affecte ainsi sa performance. En outre, ce mécanisme permet aux ondes électromagnétiques générées localement de se propager entre les points largement séparés sur un grand vaisseau spatial. Ces ondes sont susceptibles de donner lieu à des problèmes d'interférences électromagnétiques si elles sont collectées par des dispositifs sensibles. SSWICH pourait aider à comprendre ces ondes.

3. Propositions pour les futures expériences

Une question centrale de cette thèse est le rôle de l'onde rapide dans l'excitation de gaines RF. Avec SSWICH, nous avons observé une conversion de mode FW-SW, exploré les propriétés des gaine RF en champ lointain produites par l'onde rapide et étudié l'impact de l'onde rapide sur l'extension radiale des pics de V_{DC}. Ces caractéristiques ne sont pas encore été observées expérimentalement. L'onde rapide peut être identifiée expérimentalement en utilisant une bobine qui mesure le champ magnétique RF la traversant. En choisissant correctement l'orientation de la bobine, on peut détecter le champ magnétique RF parallèle qui provient principalement de l'onde rapide. En comparant la composante d'onde rapide du signal de la sonde avec la force du potentiel du plasma mesurée, il est peut-être possible de trouver une corrélation entre ces deux grandeurs et vérifier quelle onde est dominante sur la rectification de gaine RF à la fois à proximité du lanceur d'onde et plus loin dans la machine. L'autre façon de comparer l'impact de l'onde rapide et l'onde lente sur la gaine RF est d'exciter ces deux ondes les unes après les autres et de voir l'évolution du potentiel sur les parois matérielles à proximité. Exciter préférentiellement l'onde lente peut être difficile à réaliser dans Tokamak, mais est plus facile à réaliser dans ALINE. ALINE est destiné à faciliter la compréhension de la gaine RF dans les Tokamaks. Dans un futur proche, il est prévu un remplacement de l'électrode de courant actuelle par une antenne ruban similaire à celle des Tokamaks. SSWICH-FW peut fournir un support numérique pour la conception de cette antenne. Lorsque la nouvelle antenne ruban aura été installée dans ALINE, on pourrait facilement manipuler son orientation par rapport au champ magnétique. Une rotation de 90° du ruban transforme l'antenne d'onde rapide en antenne excitant préférentiellement l'onde lente. Un écran de Faraday peut être mis en face du ruban pour comparer la force des interactions plasma-paroi sur la surface de l'écran pour deux orientations différentes du ruban.

Un effet de proximité spatiale entre émetteur d'onde et gaine a été proposé pour interpréter des expériences de déséquilibre droite-gauche menées dans Tore Supra et ASDEX-Upgrade. Il est généralement connu que l'onde lente évanescente peut produire cet effet. Il est moins clair de savoir si l'onde rapide, évanescente ou propagative, peut produire un effet analogue. Nous avons répondu en partie à cette question dans nos tests numériques. Au moins dans la configuration Tore Supra nous avons constaté que l'onde rapide propagative ne possède pas cette propriété. Ce résultat peut être examiné expérimentalement en déplaçant radialement les rubans et en comparant l'amplitude du champ électrique au niveau de la région de propagation d'onde rapide. On peut en outre modifier la densité pour avoir une onde rapide évanescente dans la région accessible à la sonde dans ALINE. Ensuite, reprendre des expériences de dissymétrisation des antennes pour voir si l'onde rapide évanescente produit des effets de proximité spatiale.

Abstract

Ion Cyclotron Resonant Heating (ICRH) by waves in 30-80MHz range is currently used in magnetic fusion plasmas. Excited by phased arrays of current straps at the plasma periphery, these waves exist under two polarizations. The Fast Wave tunnels through the tenuous plasma edge and propagates to its center where it is absorbed. The parasitically emitted Slow Wave only exists close to the launchers. How much power can be coupled to the center with 1A current on the straps? How do the emitted radiofrequency (RF) near and far fields interact parasitically with the edge plasma *via* RF sheath rectification at plasma-wall interfaces? To address these two issues simultaneously, in realistic geometry over the size of ICRH antennas, this thesis upgraded and tested the Self-consistent Sheaths and Waves for ICH (SSWICH) code. SSWICH couples self-consistently RF wave propagation and Direct Current (DC) plasma biasing *via* non-linear RF and DC sheath boundary conditions (SBCs) at plasma/wall interfaces. Its upgrade is full wave and was implemented in two dimensions (toroidal/radial). New SBCs coupling the two polarizations were derived and implemented along shaped walls tilted with respect to the confinement magnetic field. Using this new tool in the absence of SBCs, we studied the impact of a density decaying continuously inside the antenna box and across the Lower Hybrid (LH) resonance. Up to the memory limits of our workstation, the RF fields below the LH resonance changed with the grid size. However the coupled power spectrum hardly evolved and was only weakly affected by the density inside the box. In presence of SBCs, SSWICH-FW simulations have identified the role of the fast wave on RF sheath excitation and reproduced some key experimental observations. SSWICH-FW was finally adapted to conduct the first electromagnetic and RF-sheath 2D simulations of the cylindrical magnetized plasma device ALINE.

Résumé

Le Chauffage Cyclotron Ionique (ICRH) par des ondes dans la gamme 30-80MHz est couramment utilisé dans les plasmas de fusion magnétique. Excitées par par des réseaux phasés de rubans de courant à la périphérie du plasma, ces ondes existent sous deux polarisations. L'onde rapide traverse le bord ténu du plasma par effet tunnel puis se propage à son centre où elle est absorbée. L'onde lente, émise de façon parasite, existe seulement à proximité des antennes. Quelle puissance peut être couplée au centre avec 1A de courant sur les rubans? Comment les champs radiofréquence (RF) proches et lointains émis interagissent-ils avec le plasma de bord par rectification de gaine RF à l'interface plasma-paroi? Pour répondre simultanément à ces deux questions, en géométrie réaliste sur l'échelle spatiale des antennes ICRH, cette thèse a amélioré et testé le code numérique SSWICH (Self-consitent Sheaths and Waves for ICH). SSWICH couple de manière auto-cohérente la propagation des ondes RF et la polarisation continue (DC) du plasma *via* des conditions aux limites non-linéaires de type gaine (SBC) appliquées à l'interface plasma / paroi. La nouvelle version SSWICH-FW est pleine onde et a été développée en deux dimensions (toroïdale/radiale). De nouvelles SBCs couplant les deux polarisations d'ondes ont été obtenues et mises en œuvre le long de parois courbes inclinées par rapport au champ magnétique de confinement. Avec ce nouvel outil en l'absence de SBCs, nous avons étudié l'impact d'une densité décroissant continuement à l'intérieur de la boîte d'antenne en traversant la résonance hybride basse (LH). Dans les limites mémoire de notre poste de travail, les champs RF au-dessous de la résonance LH ont changé avec la taille de maille. Par contre spectre de puissance couplée n'a que très peu évolué, et n'était que faiblement influencé par la densité à l'intérieur de l'antenne. En présence de SBCs, les simulations SSWICH-FW ont identifié le rôle de l'onde rapide sur l'excitation de gaines RF et reproduit certaines observations expérimentales clés. SSWICH-FW a finalement été adapté pour réaliser les premières simulations 2D électromagnétiques et de gaine-RF de la machine plasma cylindrique magnétisée ALINE.